On the Playability of Stringed Instruments

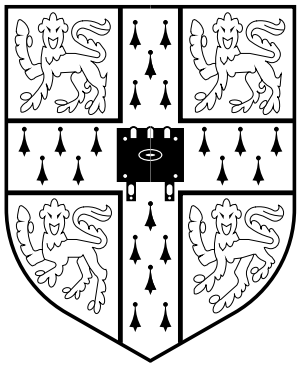

This dissertation is submitted for
the degree of Doctor of Philosophy

3 October 2003

Paul M Galluzzo, Trinity College

Supervisor: Professor J Woodhouse

To Mom

ACKNOWLEDGEMENTS

In the period between October 2000 and September 2003, I have had the good fortune to have as supervisor Professor J. Woodhouse, to whom very special acknowledgement is due for his most valuable advice and encouragement.

Other individuals who at some point contributed to the production of this thesis or the research presented herein include: Hugh, Srikanth, Garreth, Len, Paresh, Dan, Jonathan, Paul R., Frank, David M., Robin, Glenn, Mom and Dad, Philippe, Jan, Simon, Ken, Sondipon, Derek, David T., Susannah, James, Andrew, Tim, Peter, Malcolm, Keith, Jo, Andrew P., Andrew G., Hannah, and of course Eleanor and Beatrice[1]. And finally, Clare G. deserves a special mention for bravely volunteering the use of her cello in this project.

This project was financially supported by the Engineering and Physical Sciences Research Council. The ongoing love and support of Rachel underpins the writing of this dissertation and the research behind it.

[1]For future reference: Hugh Hunt (lecturer, PhD advisor), Srikanth Phani (DVRO), Garreth Ryder (technician), Len Howlett (technician), Paresh Date (control group), Dan Auger (control group), Jonathan Paxman (control group, anti-windup), Paul Roberts (control group, floating point precision, optical encoder), Frank Dolman (technician), David Miller (chief technician), Robin Langley (professor, head of DVRG), Glenn Vinnicombe (lecturer, control group), Mom and Dad, Philippe Duffour (DVRO), Jan Maciejowski (lecturer, now head of control group), Simon Smith (technician, electronics), Ken Johnson (professor, tribology), Sondipon Adhikari (DVRO), Derek Smith (lecturer, experiment), James Talbot (DVRO), Andrew Pick (DVRO), Andrew Grime (DVRO), Tim Love (computing), Peter Clarkson (computing), Malcolm Smith (lecturer, control group), Keith Glover (control group, now head of dept.), David Trippett (pianist), Susannah Ticciati (cellist), Jo Moodie, Andrew Moodie, Hannah Moodie, and of course Eleanor and Beatrice Outram (daughters of Martin Outram, who chose creative names for the robot). And finally, Clare Gilmour.

FOREWORD

As first noticed by Helmholtz, strings vibrate in a “V-shape” when they are bowed correctly and a full tone is produced, where the vertex of the “V” shuttles back and forth along the visible envelope of the string’s motion. If the instrument is bowed incorrectly, i.e. the instrument does not “speak”, then this “Helmholtz motion” is not produced, and the shape of the string as it vibrates will be quite different. The goal of this research is to gather experimental data from a stringed instrument and use it in the on-going development of a theoretical model of the mechanics of the bowed string, which can be used to investigate which aspects of the violin, strings or bow influence the ease with which this “Helmholtz motion” can be produced.

The design, testing and application of a robotic bowing machine are described, which has allowed the speed and force of a bow as it plays a cello to be controlled. Extensive measurements of various aspects of the motion of a cello string being bowed by the bowing machine are presented, and compared with predictions from nominally similar theoretical models. Although certain models do reflect the qualitative behaviour seen in experiment under some conditions, all show vast room for improvement.

Aspects of theoretical predictions that are at odds with experimental results, and would therefore impede efforts to use theoretical modelling in the design of a more “playable” violin, are subsequently described. Shortcomings of each model are attributed to physical defects of the theories underpinning them, and various modifications are discussed and tested.

This dissertation is the result of my own work and includes nothing which is the outcome of work done in collaboration except where specifically indicated in the text.

CONTENTS

LIST OF FIGURES

NOMENCLATURE

β	Non-dimensional bow position, defined as (bow-bridge distance)/(string length)
Δ	Tracking delay of force controller
$\delta(t)$	Dirac delta function
$\delta_\nu(P_i, P_j)$	ν-gap metric between systems P_i and P_j
δ_r	Thickness of the contact patch between bow and string
$\dot{m}$	Mass flow rate of rosin into or out of the contact patch
γ	Viscosity of rosin
λ	Equivalent "dashpot rate" for the position controller, i.e. its differential gain
λ_b	Equivalent dashpot rate used to model losses at the bridge
μ	Coefficient of friction, equal to f/N
μ_d	The approximate value of coefficient of friction during sliding
μ_s	Maximum possible coefficient of friction, at the limit of static friction
ω	Frequency, in rad/s
ω_c	Low pass cut-off frequency for the differential term of the position controller
ω_k	Natural frequency (in rad/s) of the k^{th} mode in the vibrational frequency response function
ω_{LP}	Low pass roll-off frequency of force controller
ω_n	Natural frequency of closed loop position controller, equal to $\sqrt{k/M}$
Π_{input}	Dimensionless group used to describe friction
Π_{time}	Dimensionless group used to describe transient time scale of string vibration
ρ	Position of bow; the bow speed v_b equals $\dot{\rho}$
ρ_r	Density of rosin
Θ	Temperature of the rosin in the contact patch
ζ	Damping coefficient
A	Area of physical contact between bow and string
a	Bow acceleration, equal to $\dot{v}_b$

a_k Amplitude of the k^{th} mode in vibrational frequency response function

A_{tot} Macroscopic area of contact patch between bow and string

$b_{P,C}$ Generalized stability margin for plant P and feedback controller C

c Propagation speed of transverse waves

$C(j\omega)$ Frequency response of a feedback controller

c_θ Propagation speed of rotational waves

c_{jg} Constant of proportionality for junction growth model

c_n Damping coefficient of closed loop position controller, equal to $\lambda/2\sqrt{kM}$

c_{pr} Thermal heat capacity of rosin

D Diameter of the string

E Effective Young's modulus of the string

f Friction force exerted on the string by the bow

f_c Low-pass frequency (in Hz) of feedback controller

$g(t)$ Green's function for thermal heat conduction

h_1 Bridge-side reflection function

h_2 Finger-side reflection function

$h_{\theta 1}$ Bridge-side torsional reflection function

$h_{\theta 2}$ Finger-side torsional reflection function

k Equivalent "stiffness" of position controller, i.e. its proportional gain

k_b Approximate stiffness of bridge, with respect to transverse motion

k_E Wave-number of evanescent transverse waves on string

k_I Integral gain of position controller

k_P Wave-number of propagating transverse waves on string

k_{str} Static transverse stiffness (force/displacement) of the cello string

k_y Shear yield strength of rosin

L Length of string

L_{str} Distance from the bow/string contact to the clamp attaching the bow to the linear motor

L_x Distance from the inflexion point in the leaf spring to the clamp attaching the bow to the linear motor (see Figure 2.17)

M Mass of moving parts of bowing machine, scaled to units of Volts per unit acceleration

m Mass (in kg) of moving parts of bowing machine

m_s Mass per unit length of the string

N Normal force with which the bow presses into the string

P Tension of the string

$P(j\omega)$ Frequency response of a system being controlled, by feedback or otherwise

q Shear stress in bow/string contact patch, equal to f/A

Q_k	Q-factor of the k^{th} mode in vibrational frequency response function
r	Demand signal for bowing machine controller
T	Time period of oscillation of the string in its fundamental transverse mode
T_θ	Time period of oscillation of string in its first rotational mode, equal to $2L/c_\theta$
u	Control effort for the speed controller, i.e. the input to the linear motor
u_{max}	Saturation limit for linear motor
u_{OL}	Output from the open-loop speed controller
v	Velocity of the string at the bowing point
$v_{\theta i1}$	Magnitude of torsional velocity wave approaching the bowing point from the bridge side
$v_{\theta i2}$	Magnitude of torsional velocity wave approaching the bowing point from the finger side
$v_{\theta o1}$	Magnitude of torsional velocity wave sent towards the bridge from the bowing point
$v_{\theta o2}$	Magnitude of torsional velocity wave sent towards the finger from the bowing point
v_θ	Velocity of the edge of the string, caused by rotation about its centre
v_b	Velocity of the bow
v_h	Combined magnitude (in m/s) of waves impinging on the bowing point of the string
v_{i1}	Magnitude of transverse velocity wave approaching the bowing point from the bridge side
v_{i2}	Magnitude of transverse velocity wave approaching the bowing point from the finger side
v_{o1}	Magnitude of transverse velocity wave sent towards the bridge from the bowing point
v_{o2}	Magnitude of transverse velocity wave sent towards the finger from the bowing point
V_r	Volume of rosin in the contact patch between the bow and the string
y	dA/dt is assumed to be proportional to $(1 - A/A_{tot})^y$
Z	Impedance of the string to transverse velocity waves, equal to $Z_T Z_\theta/(Z_T + Z_\theta)$
z	Power to which loading time is raised, to be proportional to dA/dt
Z_H	Impedance of bow hair
Z_T, Z_θ	String's impedance to transverse motion by linear and rotational excitation, respectively
CLTF	Closed-loop transfer function

Chapter 1
BACKGROUND

INTRODUCTION

The cornerstone of modern research on the physics of the bowed string is the discovery, by Helmholtz 130 years ago [1], that the string forms a "V-shape" when bowed correctly, with the vertex of the "V" travelling back and forth along the string. This motion, subsequently dubbed "Helmholtz motion", cannot be seen by the naked eye because it is too rapid; a violinist looking at the string would see a blurred version as illustrated in Figure 1.1.

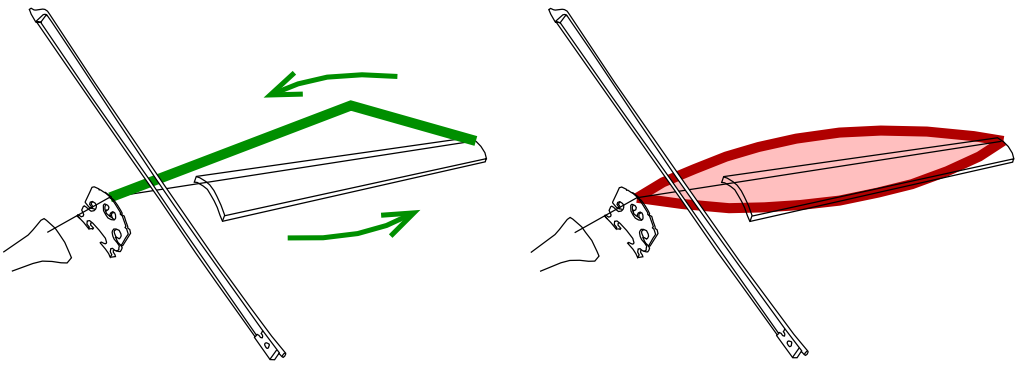

(a) (b)

Figure 1.1: The motion of the string during Helmholtz motion: (a) the instantaneous shape of the string, (b) what a player looking at the string sees. The sharp bend in the string seen in (a) travels back and forth at a sufficiently high speed that only a blurred outline of its motion is visible to the naked eye. The string sticks to the bow at all times except when the bend is between the bow and the bridge. The transverse scale of the string motion is shown greatly exaggerated.

Importantly, Helmholtz motion is unique and distinctive, causing the force acting on the bridge (which excites the body to produce sound waves) to have a recognizable spectrum. Players associate the resulting sound with "speaking", whereas its alternatives include "crunching", "whistling" and other noises. The production of Helmholtz motion is the goal for the vast majority of musical bow-strokes.

With this in mind it is natural to identify two inherent qualities in a violin which, if measurable, would provide a sound basis for the evaluation of an instrument:

(1) The "playability" of the violin, i.e. the ease with which a clean tone may be produced from a violin. In quantitative terms, this may be expressed as the range of bowing gestures that a player may use which results in Helmholtz motion within an acceptably short time.

(2) The "richness", or "beauty", of the tone produced by the violin, once Helmholtz motion has indeed been achieved.

Whilst the second of these relies on the subjective opinion of the listener, the distinctiveness of Helmholtz motion makes the first, "playability", amenable to deterministic measurement: Helmholtz motion either has or has not been produced, and if it has, it took a specific amount of time to do so. The reduction of playability to these simple terms means that theoretical models of the bowed string which predict the formation of Helmholtz motion could be used to find out what makes some instruments easier to play (i.e. more playable) than other instruments.

This would make it possible therefore to identify means by which manufacturers of violins (or indeed of strings, bows, or rosin) could improve this important quality of their instruments. Whereas past improvements to the design of the violin have taken place slowly, largely due to the often contradictory results of trial and error investigation, this deterministic approach promises the inception of irrefutable improvements. This thesis represents a step towards this goal.

In the remainder of this chapter, the existing level of understanding of the physics of the the bowed string will be presented, laying the foundations for the remaining chapters. An overview of the structure of this thesis follows. It should be understood throughout that this research pertains to all members of the stringed instrument family, even though the violin is referred to most frequently.

1.1 LITERATURE REVIEW

Considerable research effort has been directed at the study of the mechanics and kinematics of the bowed string, not to mention the numerous other topics under the general guise of "musical acoustics". Those strands of research that directly impact this dissertation are outlined in this section.

1.1.1 MODELLING THE BOWED STRING

The concept of "Helmholtz motion", discussed in the Introduction, provided the inspiration for serious attempts over the last 130 years to describe the physics governing the action of the bowed string. Helmholtz himself [1] noted that the rapidly moving "kinks" which appear in the string are caused by the stick-slip nature of the bow/string contact: slipping occurs if a kink is between the bow and the bridge, whereas sticking occurs if the kink (or kinks) are on the opposite side of the bow. Hence Helmholtz motion, consisting of only one kink travelling back and forth along the whole length of the string, corresponds to one stick and one slip per period. Any large kinks in the string have subsequently been nicknamed "Helmholtz corners".

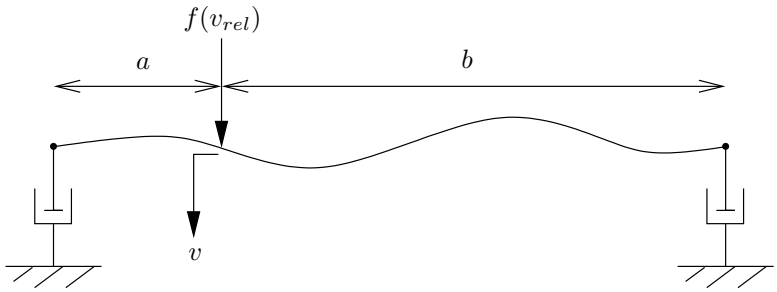

Figure 1.2: The model used by Raman [2]. String terminations are assumed to behave like pure mechanical resistances, the string itself is a perfectly flexible stretched string (with no torsion), and the applied force follows a prescribed function of relative sliding velocity, $f(v_{rel})$. With the ratio a:$(a+b)$ equal to that of two coprime integers, so that the model of the string can be reduced to a difference equation, and hence solved by hand.

Helmholtz himself did, however, concede that "No complete mechanical theory can yet be given for the motion of strings excited by the violin-bow, because the mode in which the bow affects the motion of the string is unknown" [1, Ch.V4]. Attempting to rectify this situation, Raman [2] was the first to attempt to describe the transient vibration of the string. Handicapped by a lack of computer-aided calculation in the early part of the twentieth century, Raman made several simplifying assumptions in order to reduce the motion of the string to a difference equation which could be exactly solved by hand. Specifically, Raman modelled the bowed string as a perfectly flexible string, stretched between terminations having reflection coefficients less than unity, excited

by a velocity-dependent force applied at a single point an integer fraction of the string length away from the bridge. Raman found that certain combinations of bow force (N), bow speed (v_b) and bow position ($\beta = \frac{\text{bow-bridge distance}}{\text{string length}}$) eventually led to Helmholtz motion.

Friedlander [3] and Keller [4] used the same model as Raman but with rigid string terminations, and found the surprising result that all periodic waveforms are unstable under those conditions. This situation, which obviously conflicts with the experience of playing a real violin, occurs if the power input from the friction force is not dissipated, as discussed in greater detail in [5, 6]. (Various modifications to the model which allow periodic motion to exist will be discussed later on.)

Friedlander, in his analysis of periodic motion, proposed a graphical construction for relating the velocity v at the bowing point to the friction f there. Noting that $f \propto v$ for an infinite string (with no reflections), and that $f \propto (v - v_h)$ for a string of finite length (where v_h is the velocity of the returning waves as they meet the bowing point), the values of f and v can be obtained as the solution of two simultaneous equations:

$$f = 2Z_T(v - v_h), \tag{1.1a}$$

$$f = f(v - v_b), \tag{1.1b}$$

where Z_T is the transverse characteristic impedance of the string ($Z_T = \sqrt{Pm_s}$, where m_s is the mass per unit length of the string and P is the tension of the string), v_b is the bow speed and $f(v - v_b)$ represents the functional dependence of friction on relative sliding speed (often referred to as the "friction curve"). The solution is given by the intersection of the two equations when plotted on the same graph, as shown in Figure 1.3.

It is worth noting in passing that McIntyre and Woodhouse [7] demonstrated that Equation (1.1a), used by Friedlander to describe ideal strings, is also a good approximation for real strings which have finite bending stiffness.

ROUNDED CORNER MODELS, AND THE FORMATION OF SECONDARY WAVES

The existence of sharp-cornered waves on strings (as in for example Figure 1.1(a)) seems dubious in the face of effects such as bending stiffness [8] and damping [9]. The idea of modifying Helmholtz motion by "smoothing out" the Helmholtz corner was first explored by Cremer and Lazarus [10, 11], and later by Cremer [8, 12]. Cremer studied the change in shape undergone by rounded waves as they pass underneath the bowing point, and found that the shape change depends on the magnitude of the normal force N exerted by the bow on the string. Previous models, notably Raman's, only allow sharp corners whose shape is independent of bow force.

Considering a "sharp corner" as causing a step change in transverse string velocity as it passes a point along the string, and a "rounded corner" as causing a gradual ramp up (or down) in velocity,

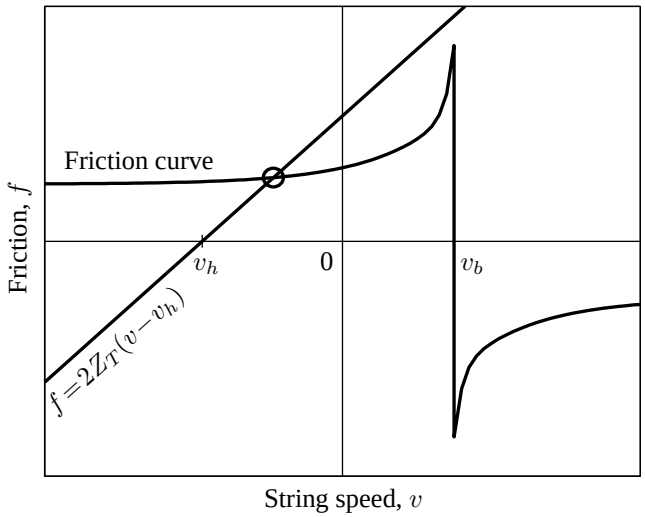

Figure 1.3: Friedlander's graphical construction for the calculation of f and v, comprising the two equations (1.1a) and (1.1b). The latter of these equations, the so-called "friction curve", implies that the friction is only a function of the relative sliding speed, $v_b - v$, between the bow and the string. Typically, the friction curve itself comprises two positive-sloping curves separated by a vertical line as above; this general form implies that the magnitude of the friction can vary up to some limit provided the string is sticking to the bow (implying the vertical portion of the friction curve given by $v = v_b$), but that it is progressively less as the relative sliding speed increases (implying the curved portions). The solution to Equations (1.1a) and (1.1b) is given by the intersection of the two, as shown here with a circle.

Cremer [12] argued that a rounded Helmholtz corner approaching a sticking bow will only induce slipping once the velocity has reached $\mu_s N/2Z_T$, where μ_s is the maximum static friction coefficient. Thus, there is a delay between the time when the wavefront reaches the bow and the time when the wave travels past the bow, and this time delay increases as N is increased from zero. Similarly the opposite is true when sticking re-commences; only part of a rounded Helmholtz corner approaching a slipping bow will have passed the bow before sticking ensues — the corner is in this case "hurried on" somewhat.

Lazarus [13] and Cremer [12, 14, 15] pointed out that the friction force rises to its largest possible value $\mu_s N$ when the string is released and to a large value again when it is recaptured, giving rise to the so-called "rabbit ears" in plots of friction against time. Apparently independently, Schelleng [16, §II.J] and Cremer [8] demonstrated how these sudden changes in friction force generate waves, commonly referred to as "Schelleng ripples", which are superimposed on Helmholtz motion as first observed by Kohut and Matthews [17]. These ripples consist of waves reflecting between the bow and the bridge or between the bow and the finger, causing a disturbance of period βT at the bowing point, where T is the time period of oscillation of the string.

HYSTERESIS IN THE FRICTION-VELOCITY PLANE, AND THE FLATTENING EFFECT

McIntyre and Woodhouse [7] studied the asymmetry of nonlinear frictional excitation, and concluded that the delay in the travel time of the Helmholtz corner at release (from slipping) outweighs the advance at recapture. This causes a net time delay in the round trip of the Helmholtz corner, leading to a lowering of the vibration frequency; this corresponds to what a musician would understand as a "flattening of pitch"[1]. This surprising flattening behaviour, whose existence had been known of for some time (see for example [2, p.135]), has since received more attention by various investigators [18, 19, 20, 21].

In the process of exploring the cause of pitch flattening, McIntyre and Woodhouse [7] resolved the ambiguity which arises when obtaining friction and velocity using Friedlander's construction. As shown in Figure 1.4, there exists a region where Equations (1.1a) and (1.1b) yield three possible solutions. McIntyre and Woodhouse generalized earlier results due to Friedlander [3] and Schelleng [16] to show that the middle solution is always unstable, whereas the outer two are always stable. Hence, with v_1 and v_2 as defined in Figure 1.4, if the string is already sticking (i.e. the solution is already on the vertical portion of the friction curve) then it will remain sticking until $v_h < v_1$, or if already slipping (i.e. the solution is already on the curved portion of the friction curve) then it will remain slipping until $v_h > v_2$.

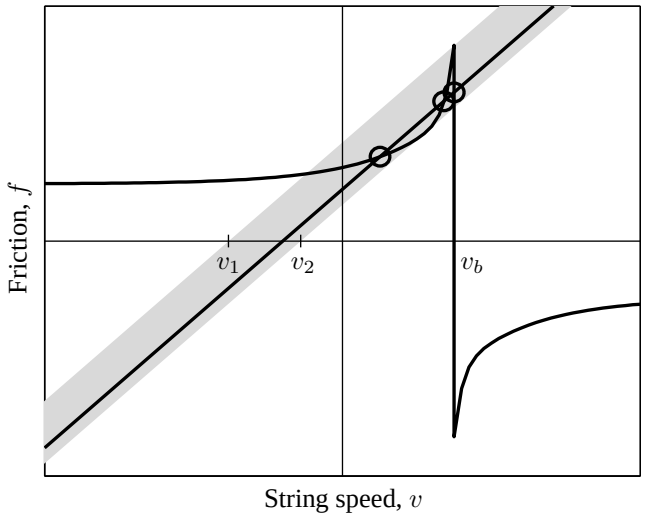

Figure 1.4: Friedlander's ambiguity. The straight sloping line has three intersections with the friction curve whenever it lies in the shaded region described by $v_1 < v_h < v_2$; hence in these circumstances Equations (1.1a) and (1.1b) have three solutions. Of the three solutions, indicated here by circles, the middle one is always unstable, whereas the outer two are always stable. If $v_h < v_1$ or $v_h > v_2$ then there is only one solution, as in Figure 1.3.

[1] Interestingly, many violinists are more aware of "pitch wavering" than "pitch flattening" as such, due to the twitchiness of the flattening effect.

REFLECTION FUNCTIONS, AND TIME-STEPPING SIMULATIONS

An obvious way to compute the time-varying response of the string, whose motion may be described by second and fourth order linear differential equations [22] and is therefore linearly dependent upon excitation force, is to use the "Green's function" method: the force input is calculated at a given time step according to some friction law (e.g. a function of relative sliding velocity such as the friction curve in Figures 1.3 and 1.4); the resulting time history of force is convolved with the impulse response of the string to give the string velocity at the next time step; a new value of friction is hence calculated, and so on. However, because the impulse response of the string takes several seconds to decay away in practice (easily confirmed by plucking the string of an instrument), this convolution integral is computationally extremely cumbersome. This method was demonstrated by Woodhouse [23] and, for the particular case of periodic waveforms, by Schumacher [24].

As suggested by McIntyre and Woodhouse [7], from a computational point of view it is far more efficient to make direct use of Equation (1.1a), the characteristic equation of a string of finite length. To do so, one need only calculate the combined magnitude v_h of waves returning from the ends of the string, which depends only on waves generated at the bowing point at times of around βT and $(1-\beta)T$ previously, where T is the string's fundamental time period of oscillation. As such, the convolution integral is considerably shortened; whereas the Green's function method required convolution with the entire history of the string's motion, this method only requires the motion from the last period or so, since a wave returning to the bow is subsequently replaced by the next outgoing wave travelling in the same direction. This method is illustrated in Figure 1.5.

Assuming for the moment that the bow and string meet at a point, that the bow itself is rigid, and that the string only exhibits transverse motion (not torsional motion), the procedure for McIntyre and Woodhouse's method of simulating bowed strings at each time step is thus as follows:

1. Calculate the magnitudes of incoming waves (labelled $i1$ and $i2$ in Figure 1.5) by convolving recent outgoing waves with a "reflection function" for the relevant portion of string (i.e. the bridge side or the finger side of the bow). A reflection function, in its most general mathematical form, smooths waves (i.e. rounds corners) and delays them according to the time taken to travel from the bowing point to the end of the string and back.

2. Calculate the combined velocity of waves returning to the bowing point, $v_h = v_{i1} + v_{i2}$ (see Equation (1.1a)).

3. Determine the new values of f and v using Friedlander's construction (described previously).

4. Calculate the new outgoing waves (labelled $o1$ and $o2$ in Figure 1.5): $v_{o1} = v_{i2} + f/2Z_T$ and $v_{o2} = v_{i1} + f/2Z_T$. The velocity v of the string at the bowing point is equal to $v_{i1} + v_{o1}$, or equivalently $v_{i2} + v_{o2}$.

5. Repeat steps 1-4 at subsequent time steps.

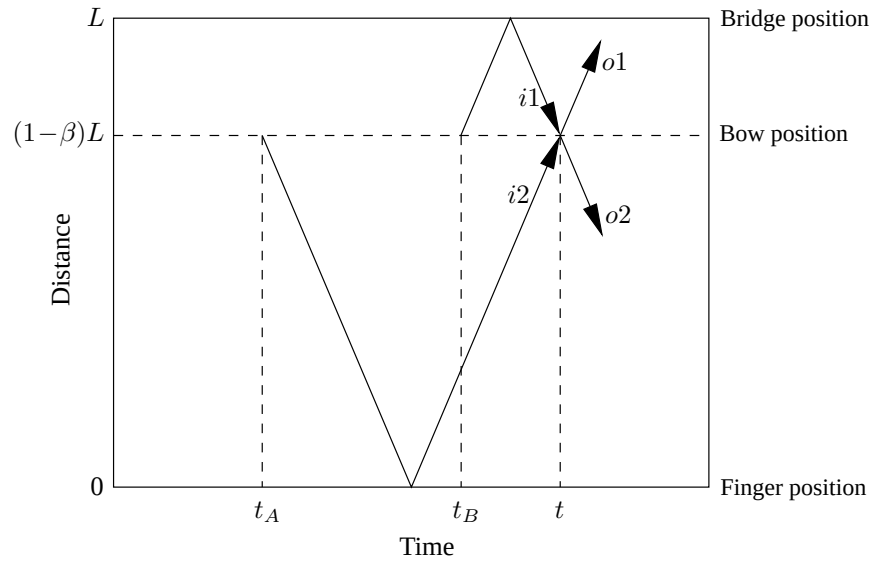

Figure 1.5: Space-time diagram of travelling waves sent out from the bowing point towards the finger and bridge at times t_A and t_B respectively, arriving back at the bowing point at time t. The combined velocity v_h of waves returning to the bowing point equals $v_{i1} + v_{i2}$, where v_{i1} and v_{i2} are the magnitude (in m/s) of the waves $i1$ and $i2$; hence the friction f and velocity v at the bowing point at time t can be calculated using Friedlander's construction (Equations (1.1a) and (1.1b)). The magnitudes v_{o1} and v_{o2} of the new outgoing waves are hence $v_{i2} + f/2Z_T$ and $v_{i1} + f/2Z_T$ respectively. To allow for realistic effects such as corner rounding due to damping or dispersion, McIntyre et al. [7, 25] and Woodhouse [26] proposed calculating v_{i1} and v_{i2} (and hence v_h) by convolving the waves generated at the bowing point at a range of times surrounding t_B and t_A (respectively) with appropriate reflection functions.

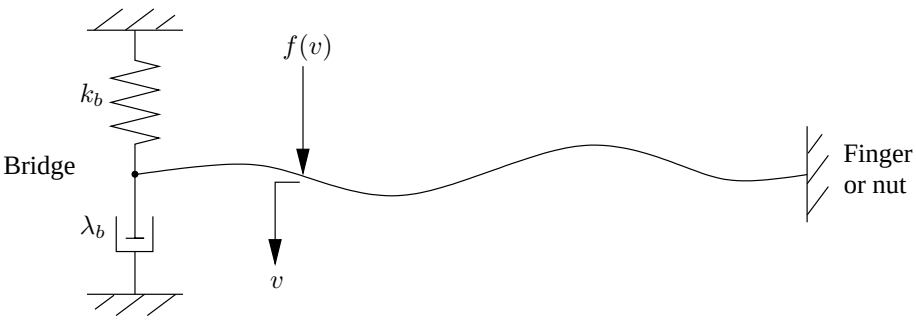

Figure 1.6: Cremer's string model. The finger is assumed to act as a rigid boundary, and the bridge is assumed to behave like a dashpot in parallel with a spring. The dashpot is responsible for absorbing energy from the string, and the spring prevents the end of the string from drifting progressively under the action of the DC component of the friction force.

A simple model used to describe reflections from the ends of the string was proposed by Cremer [10, 22], and is illustrated in Figure 1.6. It differs from Raman's (see Figure 1.2) in that all of the damping is located at the bridge end of the string, and that a spring is included to prevent the dashpot from gradually drifting away (bearing in mind that the dashpot's resistance to motion falls to zero if the motion is very slow). Defining k_b and λ_b as the spring constant and dashpot rate

respectively, the reflection functions for the string are [26]:

$$h_1(t) \;=\; \frac{(Z_T - \lambda_b)}{(Z_T + \lambda_b)}\,\delta(t - \beta T) \;-\; \frac{2k_b Z_T}{(Z_T + \lambda_b)^2}\,e^{-\frac{k_b}{(Z_T+\lambda_b)}(t-\beta T)}, \tag{1.2a}$$

$$\text{and} \quad h_2(t) \;=\; \delta(t - (1-\beta)T), \tag{1.2b}$$

where $\delta(t)$ is the unit delta function, T is the period of oscillation of the string in its fundamental mode, and the subscripts 1 and 2 refer to the bridge side and finger side of the bow, respectively. Hence, using the nomenclature of Figure 1.5, the velocities of incoming waves are:

$$v_{i1}(t) = \int h_1(\tau)\, v_{o1}(t-\tau)\, d\tau, \tag{1.3a}$$

$$v_{i2}(t) = \int h_2(\tau)\, v_{o2}(t-\tau)\, d\tau. \tag{1.3b}$$

TORSIONAL MOTION

Somewhat complicating matters, the friction force from the bow acts tangentially on the surface of the string, causing it to twist as well as deflect laterally. Although torsional string motion may not be responsible for significant sound waves emitted from the body of the instrument, its importance has been underlined by previous investigators [8] who have suggested that the conversion of transverse waves to torsional waves, which are relatively highly damped, accounts for a major part of energy dissipation during bowing. More strikingly perhaps, it has even been suggested [8] that this energy dissipation is responsible for suppressing the instability that Friedlander predicted (described on page 4).

To incorporate torsional waves into the time-stepping simulation, it is convenient to speak of the angular velocity $\dot{\theta}$ of the string in terms of an equivalent "rolling velocity" v_θ at the surface of the string:

$$v_\theta = a_s \dot{\theta}, \tag{1.4}$$

where a_s is the radius of the string. In this way, if v is the velocity of the string at its surface, then the velocity of the centre of the string is $v - v_\theta$. The impedance Z of the string to transverse motion is given by a combination of the translational impedance Z_T and the torsional impedance Z_θ:

$$\frac{1}{Z} = \frac{1}{Z_T} + \frac{1}{Z_\theta}, \tag{1.5}$$

where, for example for a cello D-string, Z_T and Z_θ are around 0.55 Ns/m and 1.8 Ns/m respectively [21]. To accommodate rotational motion, Z_T in Equation (1.1a) should now be replaced with Z.

McIntyre and Woodhouse's time-stepping simulation model can now be extended to allow for the effect of torsional waves on the value of v_h. The solution to this problem, first presented in [25, App.B], is illustrated in Figure 1.7: the combined magnitude of incoming waves v_h is now equal to

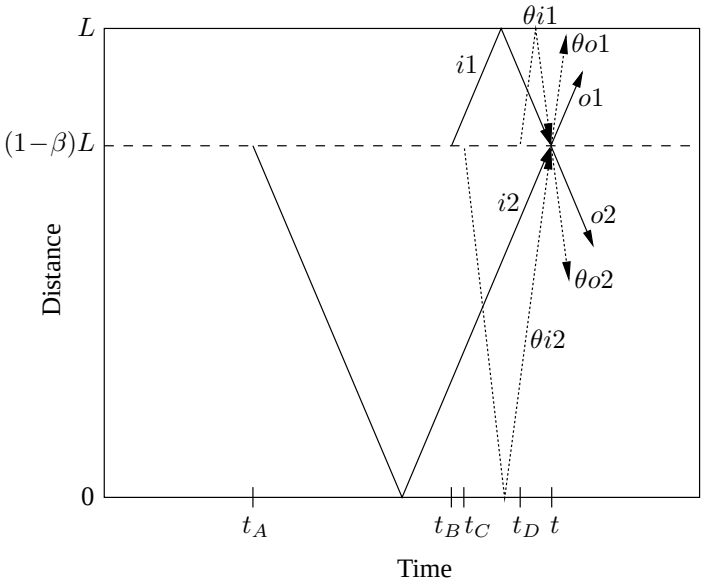

Figure 1.7: Space-time diagram of transverse waves (solid lines) and torsional waves (dotted lines) impinging on the bowing point at time t. The incoming transverse waves, labelled $i1$ and $i2$, departed from the bowing point at times t_B and t_A respectively (as they did in Figure 1.5); the incoming torsional waves, labelled $\theta i1$ and $\theta i2$, departed from the bowing point at times t_D and t_C respectively, and have a clearly larger propagation speed. These four waves contribute to the velocity of the surface of the string at the bowing point at time t, and in simulations the sum of the contributions from each is used to obtain v_h in order that Friedlander's construction may be used. The outgoing waves, $o1$ and $o2$ (transverse), and $\theta o1$ and $\theta o2$ (torsional), are perturbations of the incoming waves as described in Equations (1.9a)–(1.9d).

the sum of the velocity of the two incoming transverse waves v_{i1} and v_{i2} and the equivalent linear velocity of the two incoming rotational waves $v_{\theta i1}$ and $v_{\theta i2}$. To calculate these four quantities, we generalize (1.3) by having a total of four convolution integrals with four corresponding reflection functions:

$$v_{i1}(t) = \int h_1(\tau)\, v_{o1}(t-\tau)\, d\tau, \tag{1.6a}$$

$$v_{i2}(t) = \int h_2(\tau)\, v_{o2}(t-\tau)\, d\tau, \tag{1.6b}$$

$$v_{\theta i1}(t) = \int h_{\theta 1}(\tau)\, v_{\theta o1}(t-\tau)\, d\tau, \tag{1.6c}$$

$$v_{\theta i2}(t) = \int h_{\theta 2}(\tau)\, v_{\theta o2}(t-\tau)\, d\tau, \tag{1.6d}$$

with the subscripts $\theta i1$, $\theta i2$, $\theta o1$ and $\theta o2$ as shown in Figure 1.7. On the basis of measurements of the torsional impulse response of a selection of cello strings, Woodhouse and Loach [27] argued that $h_{\theta 1}$ and $h_{\theta 2}$ should encapsulate frequency-independent non-dispersive spatially uniform torsional damping, such that rotational waves of (temporal) frequency ω travelling along a string at speed c_θ decay according to

$$\text{angular displacement}(x,t) = e^{i\omega(t-x/c_\theta)} e^{-\omega\zeta x/c_\theta}, \tag{1.7}$$

where t is time, x is distance travelled, and ζ is a damping coefficient (assumed constant) which takes a value of around 0.01 [27] or more [28] for cello strings, compared to an equivalent of around 0.001 for transverse waves on the same strings [21]. Defining T_θ as the time taken for a rotational wave to travel from one end of the string to the other end and back (i.e. $T_\theta = 2L/c_\theta$), the resulting expressions for $h_{\theta 1}$ and $h_{\theta 2}$ are approximately thus [27]:

$$h_{\theta 1}(t) = \begin{cases} \frac{\zeta\beta T_\theta}{\pi((t-\beta T_\theta)^2+(\zeta\beta T_\theta)^2)} & \text{for } t \geq 0 \\ 0 & \text{for } t < 0 \end{cases}, \tag{1.8a}$$

$$h_{\theta 2}(t) = \begin{cases} \frac{\zeta(1-\beta) T_\theta}{\pi((t-(1-\beta)T_\theta)^2+(\zeta(1-\beta)T_\theta)^2)} & \text{for } t \geq 0 \\ 0 & \text{for } t < 0 \end{cases}. \tag{1.8b}$$

With v_h calculated according to these reflection functions as $v_{i1} + v_{i2} + v_{\theta i1} + v_{\theta i2}$, one may still proceed to use Friedlander's construction to calculate f and v. Finally, the outgoing waves are:

$$v_{o1} = v_{i2} + \frac{f}{2Z_T}, \tag{1.9a}$$

$$v_{o2} = v_{i1} + \frac{f}{2Z_T}, \tag{1.9b}$$

$$v_{\theta o1} = v_{\theta i2} + \frac{f}{2Z_\theta}, \tag{1.9c}$$

$$v_{\theta o2} = v_{\theta i1} + \frac{f}{2Z_\theta}. \tag{1.9d}$$

BENDING STIFFNESS

Unlike an "ideal string", real strings have some bending stiffness, or resistance to curvature, which in the words of Schelleng [16, §III.B] "endangers the beautiful simplicity of the flexible string". The additional elastic potential energy due to bending stiffness is naturally more and more significant as frequency increases because the wave-number, and hence curvature, of transverse waves increases with frequency. This additional potential energy causes the natural frequencies of the string to increase by an amount proportional to to the square of the harmonic number [7, 29, 30], so that the natural frequency of the n^{th} mode is proportional to $n(1+\varepsilon n^2)$, where ε is a small positive number. Schelleng [16] proposed that this harmonic distortion is audible in cases where the dimensionless ratio ED^4/PL^2 is greater than around 0.0002, where E is the effective Young's modulus of the string, D is the diameter of the string, P is the string tension and L is the length of the string.

Bending stiffness also has an effect on the point impedance, Z, of the string. Pitteroff and Woodhouse [31] demonstrated that the expression previously used for Z, $Z_T Z_\theta/(Z_T + Z_\theta)$, should be replaced by

$$\frac{Z_\theta Z_T(1 - k_P/k_E)}{Z_\theta + Z_T(1 - k_P/k_E)}, \tag{1.10}$$

where k_P and k_E are the (frequency-dependent) wave-numbers of propagating and evanescent waves, respectively. (k_P and k_E are hence the real and imaginary roots, respectively, of the fourth-order differential equation for a freely vibrating stiff string. Note, if the string has no bending stiffness then the ratio k_P/k_E is zero, and the above expression reduces back to $Z_T Z_\theta/(Z_T + Z_\theta)$.) A similar result was derived previously by Cremer [8, 32, 33] (see alternatively [22, Ch.7]) in the context of reflection and transmission coefficients for transverse waves travelling along a stiff string impinging on a sticking bow.

In addition to the above, bending stiffness also causes wave dispersion, which in this case means that higher frequency waves propagate along the string slightly more quickly than lower frequency waves. This affects the reflection functions h_1 and h_2 introduced on page 7, as discussed by Woodhouse [26, App.]. Woodhouse derived an approximation for the reflection function corresponding to an impulse travelling to and from the end of a slightly stiff string. When this function is convolved with the reflection function for a damped flexible string with compliant terminations, the resulting function corresponds to the "completed" reflection function, i.e. the reflection function corresponding to an impulse travelling to and from the end of a damped slightly stiff string with compliant terminations.

REAL BOWS: FINITE WIDTH BOWS, AND BOW HAIR COMPLIANCE

While real strings have bending stiffness and allow torsional motion, the bundle of bow hair in real bows has a ribbon-like finite width as well as some degree of compliance. The latter quality of real bow hair means that large amounts of friction will stretch the hair, and the former implies that the bow contacts the string at a range of points rather than at a single point. Raman himself [2, p.115] pointed out that, during Helmholtz motion, "while it is possible for a single point on the string to have absolutely the same velocity as the bow during every part of its forward motion [i.e. during sticking], kinematical theory shows that it is not possible for every element on a finite region to have absolutely the same velocity as the bow in every part of its forward motion." The reason for this is that the portion of string under the bow must rotate during sticking as demonstrated in Figure 1.8, and hence some points along the finite width contact region must slip to accommodate this.

McIntyre et al. [34] undertook the first serious exploration of this "kinematical" incompatibility and its effects on the motion of the string and the sound of the instrument. For the sake of simplicity, they studied the case where the bow contacts the string at two points as illustrated in Figure 1.9 (whereas most analytical theory assumes a single point contact), and found that slipping was prone to occur at the contact nearer the bridge while sticking continued at the other contact. They found that the resulting irregular vibration of the string between the bow and the bridge excited the instrument to produce an audible "fuzzy" noise, in both theory and experiment.

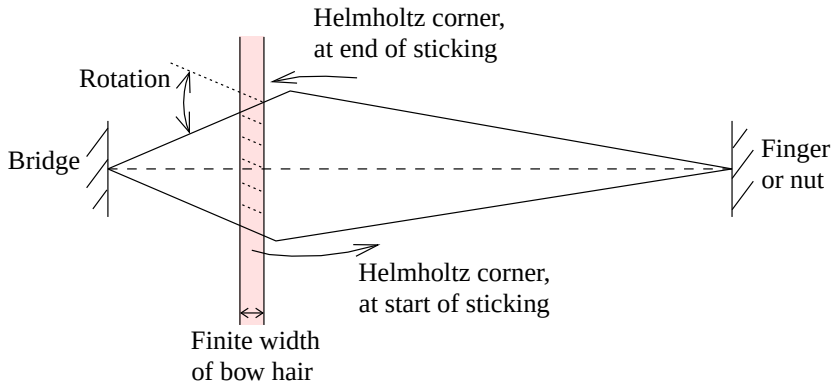

Figure 1.8: Illustration of the cause of "differential slipping." Between the time when the Helmholtz corner has just passed the bow and the time when it returns from the finger, the string near the bridge is "swept," and hence rotated. However, the bow does not rotate, and so the string must slip at one point or a range of points while still sticking at other points.

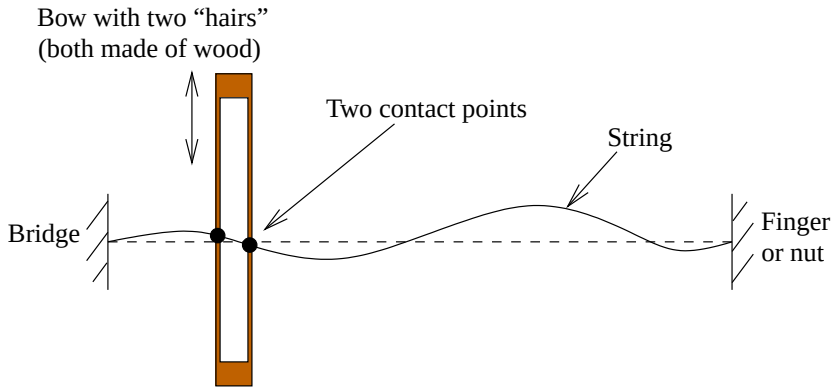

Figure 1.9: McIntyre et al.'s "two-haired bow" [34]. In their experiments this comprised a rosined wooden rod with a groove cut along its length to leave two wooden "hairs"; in simulations this was modelled as simply two point contacts instead of the customary one.

A more comprehensive analysis of the effects of a finite width bow-string contact patch was subsequently presented by Pitteroff and Woodhouse [31, 35, 36], who in the same analysis included the influence of torsional motion, string bending stiffness (described already) and bow hair compliance. They firstly demonstrated that, if the bow and string are assumed to contact each other only at a point, then the effect of bow hair compliance on the point impedance, Z, of the string is to transform the expression given in Equation (1.10) into the following:

$$\frac{Z_\theta Z_T (1 - k_P/k_E)}{Z_\theta + Z_T (1 - k_P/k_E)(1 + 2Z_\theta/Z_H)}, \tag{1.11}$$

where Z_H is the impedance of the bow hair. (Note, Z_H is infinite if the hair is assumed to be rigid, in which case Eq. (1.11) reduces to Eq. (1.10).) Pitteroff and Woodhouse derived two alternative analytical models for Z_H, one based on a simple spring-dashpot model and the other based on a

viscoelastic continuum model (see Figures 1.10(a) and 1.10(b)). Contrary to expectations, they found that the first of these models led to more accurate predictions of the reflection and transmission behaviour of transverse waves impinging on a sticking bow; on this basis, and bearing in mind that it is the simpler of the two models, they recommended that the spring-dashpot model should be used.

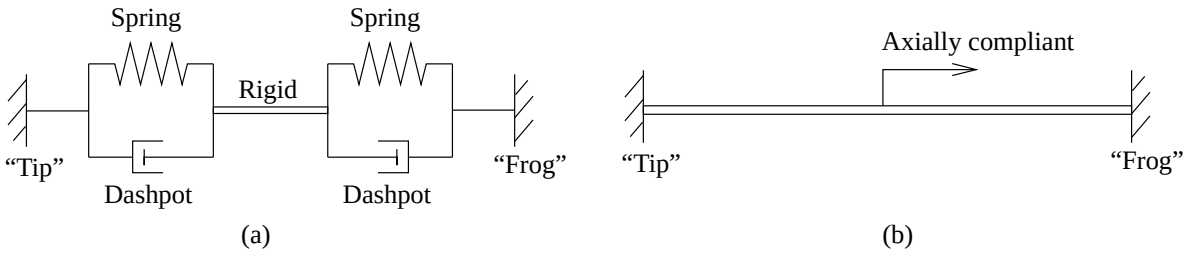

Figure 1.10: Two alternative physical models used by Pitteroff and Woodhouse [31] to find an expression for bow hair impedance Z_H. (a) spring-dashpot model; (b) continuum model, comprising the damped axial vibration of a solid bar.

Previous authors (most notably Cremer [22]) had assumed that Z_H was constant, or equivalently that the bow hair behaves like a lone dashpot, and had based the value of Z_H on that given for a single hair by Schumacher [37]. An interesting discovery of Pitteroff and Woodhouse was that Schumacher's published value of 0.6 kg/s for a single hair was misprinted; the value of 0.15 kg/s was intended instead. Indeed, this considerably smaller value of impedance is in accordance with Pitteroff and Woodhouse's own predictions. Cremer's assessment [22] that bow hair compliance is of little consequence, and aspects of the work of other authors [38, 39], were hence refuted by Pitteroff and Woodhouse.

Returning to the problem of including a finite-width contact patch in simulations of real bows, Pitteroff and Woodhouse [35] proposed a numerical solution, whereby the point-excited ideal string equation, $f = 2Z(v - v_h)$, is replaced by a finite difference implementation of the fourth-order differential equation of a stiff string for the portion of string under and near the bow; the waves travelling to and from the ends of the string (outside the finite difference region) are still evaluated using the method of reflection functions. Bow hair compliance and the friction law (assumed by Pitteroff and Woodhouse to be the "friction curve" described in Figure 1.3) are enforced as boundary conditions in the finite difference region. Pitteroff and Woodhouse demonstrated that this numerical solution could be simplified back down to the point contact problem if the contact patch was very small, and hence that it represents a generalization of Friedlander's method (described on page 4).

VALIDATION OF STRING MODEL, AND DOUBTS OVER THE FRICTION CURVE MODEL

It is worth noting at this stage that the theoretical concepts described up to this point have been reasonably well corroborated by experimental results, with the exception of Equation (1.1b) — the

assumption that friction depends only on relative sliding velocity — and, to a lesser extent, the exact numerical value of Z_θ (c.f. [27]). The basic parts of the model of the bowed string are not dissimilar to theoretical models from other branches of mechanical engineering (see for example [40]), and so it comes as little surprise that the model can predict, for example, the plucked response of the string very accurately [41, Fig.2].

The area of greatest concern is the theoretical model of rosin used to calculate the friction force. The so-called "friction curve model", described above, uses a single curve to describe the dependence of friction coefficient on relative sliding velocity, as sketched for example in Figure 1.3. Until recently, all published work on the bowed string has assumed such a model, with the shape of the curve taken from the work of Lazarus [42] and Smith and Woodhouse [43], who measured the coefficient of friction between two rosined surfaces in a steady sliding apparatus. However, whereas under these steady sliding conditions friction can only depend upon relative sliding speed, in general there is no reason to dismiss the possibility that other state variables might also influence rosin's tribological behaviour.

Confirming this suspicion, a large body of evidence has been reported recently to suggest that friction coefficient is dependent upon variables other than just relative sliding speed. Smith and Woodhouse [43, 44] measured the friction and relative sliding speed between a rosined rod and a wedge under dynamically varying conditions and found that their locus, plotted in the friction-velocity plane, was considerably at odds with the result of the simpler steady sliding measurements. Woodhouse et al. [41] deduced the friction and velocity of an actual bowed string at its bowing point by monitoring the forces exerted by the string on the two terminations and working backwards from a knowledge of the impulse response of the string; they too found that the friction could not be accounted for by a simple "friction curve" model.

The conclusion is that although the linear elements of the model are known to perform well, there is a clear need for a new, more sophisticated, model for the frictional behaviour of rosin.

THE INFLUENCE OF TEMPERATURE ON ROSIN FRICTION

Based on their observations, Smith and Woodhouse [43] suggested that the temperature of the rosin plays a central role in the friction force exerted by the bow on the string; indeed, they noted, rosin is already close to its glass transition point at room temperature. In general terms, they proposed that rosin is softer when hotter, and that sufficient heat is generated during slipping to raise the rosin's temperature. Hence, during a typical stick-slip cycle, hysteresis in the friction-velocity plane may be explained by the following course of events:

1. During sticking, no heat is generated through sliding, and heat is conducted away from the bow-string contact patch. This allows the rosin to cool down, and the shear strength of the rosin to rise.

2. When slipping starts, heat is generated at a rate equal to the product of friction force and relative sliding velocity. This heat rapidly raises the temperature of the rosin, and the shear strength drops.

3. The dynamics of the vibrating string cause the relative sliding velocity to diminish, and hence sticking to re-commence. However, the rosin is still hot from the heat generated during slipping, and so the friction coefficient at the start of sticking is still low.

This hysteretic behaviour, caused by thermal time lags, is sketched in Figure 1.11, and qualitatively agrees with Smith and Woodhouse's [43] and Woodhouse et al.'s [41] observations.

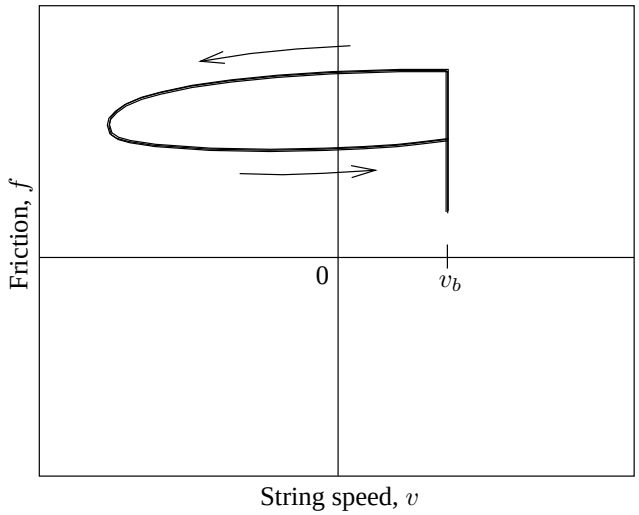

Figure 1.11: Sketch of the friction and string velocity during one stick-slip cycle, including (qualitatively) the effects of temperature on friction. During sticking, the operating point lies on the vertical portion of the curve on the right; slipping causes the operating point to move to the left; and heat generation softens the rosin, causing the operating point to move downwards. The rosin is still hot when sticking is re-established, hence the operating point rejoins the vertical part of the curve below the position where it departed initially. This type of hysteretic behaviour is incompatible with the concept of a single "friction curve", but was observed in a range of stick-slip situations involving rosin by Smith and Woodhouse [43] and Woodhouse et al. [41].

To describe the thermodynamics of heat flow through the contact patch, Smith and Woodhouse argued that the heat generated through friction is counterbalanced by convection, absorption and conduction, according to the following law [43]:

$$\overbrace{\mu N(v_b - v)}^{\text{rate of doing work}} = \overbrace{\dot{m}_{out}c_{vr}\Theta_{out} - \dot{m}_{in}c_{vr}\Theta_{in}}^{\text{convection}} + \overbrace{\rho_r V_r c_{pr}\frac{d\Theta}{dt}}^{\text{absorption}} + \overbrace{\int_{-\infty}^{t} g(t-\tau)\Theta(\tau)d\tau}^{\text{conduction}}, \qquad (1.12)$$

where $\dot{m}_{in}$ and $\dot{m}_{out}$ are the mass flow rates of rosin in and out of the contact patch, c_{vr} is the effective specific heat capacity (assumed constant) of rosin, Θ is the temperature of the rosin, ρ_r is the density of rosin, V_r is the volume of the contact patch, and $g(t)$ is a suitable Green's function for

the heat diffusion problem. This formulation can be implemented in time-stepping simulations to calculate the temperature, by substituting the relevant terms with finite difference representations.

TEMPERATURE-DEPENDENT ROSIN MODELS: VISCOUS AND PLASTIC

With the temperature known from Equation (1.12), it remains to devise a model for how the friction at the bow-string contact depends on temperature. Smith and Woodhouse [43] proposed two alternative models: the "thermal viscous model" and the "thermal plastic model". In the first of these, the rosin is assumed to behave like a viscous liquid, whose viscosity decreases as temperature increases, according to rheometer measurements of viscosity at a range of temperatures. In the thermal plastic model, the rosin is treated as a perfectly plastic solid, which will only deform (i.e. allow slipping) once the shear stress reaches the shear yield strength k_y of rosin. In this case, k_y is assumed to be temperature-dependent.

For the viscous model, the shear force acting per unit area of the contact patch is the product of temperature-dependent viscosity $\gamma(\Theta)$ and velocity gradient $(v_b - v)/\delta_r$ (assumed uniform), where δ_r is the thickness of the rosin layer between bow and string. Hence the total friction force f is

$$f = A\,\gamma(\Theta)\,\frac{(v_b - v)}{\delta_r}, \tag{1.13}$$

where A is the area of the contact patch. For a given temperature, the operating point must lie along a straight line of slope $-A\gamma/\delta_r$ in the f vs. v plane such as that of Figure 1.12(a). The Friedlander construction can still be used with this model, as shown in Figure 1.12(b).

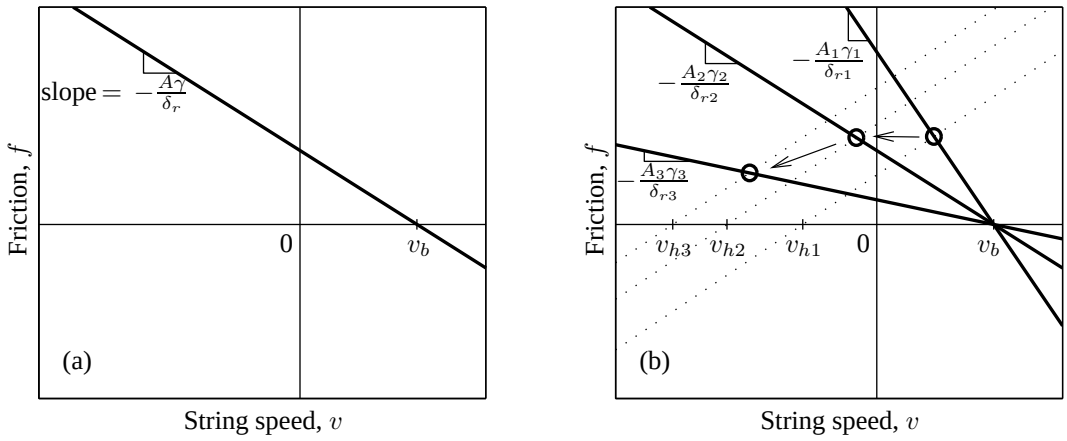

Figure 1.12: The "thermal viscous model" of friction. The rosin is modelled as a viscous liquid, whose viscosity γ depends on temperature. Hence, at a given temperature the friction must lie along a line such as that in (a). Friedlander's construction can still be used to obtain f and v, bearing in mind that the viscosity may change between time steps. To illustrate the use of Friedlander's construction in this instance, three successive operating points are indicated by circles in (b), corresponding to the three load lines indicated by dotted lines.

In the same spirit of simplicity, the second thermal friction model proposed by Smith and Woodhouse assumes that the dynamic friction coefficient is governed by a temperature-dependent shear yield strength $k_y(\Theta)$, so that at a given temperature the dynamic friction coefficient is rate-independent, as illustrated in Figure 1.13(a). Defining $\text{sgn}(v - v_b)$ as $(v - v_b)/|v - v_b|$, the friction is given by the step-wise function

$$f = A\, k_y(\Theta)\, \text{sgn}(v - v_b). \tag{1.14}$$

A relationship between k_y and Θ was chosen which ensures that Equations (1.12) and (1.14) predict the same amount of friction during steady sliding as Smith and Woodhouse measured in steady sliding tests. The usage of Friedlander's construction in conjunction with this model is illustrated by Figure 1.13(b).

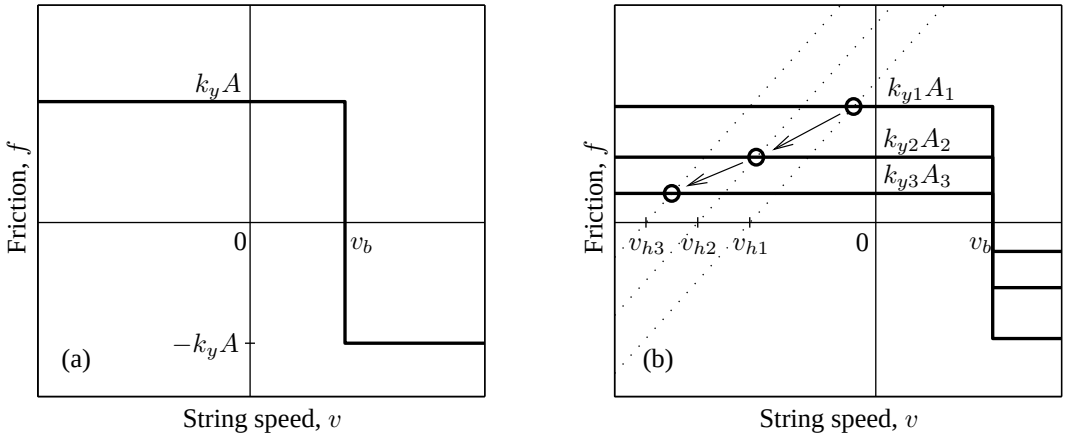

Figure 1.13: The "thermal plastic model" of rosin friction. The rosin is modelled as a perfectly plastic solid, whose shear yield strength k_y depends on temperature. Hence, at a given temperature the friction must lie along a line such as that in (a). Friedlander's construction can again be used to obtain f and v, bearing in mind that k_y may change between time steps. To illustrate the use of Friedlander's construction in this instance, three successive operating points are indicated by circles in (b), corresponding to the three load lines indicated by dotted lines.

Smith and Woodhouse tested each of these two thermal friction models and found that while the plastic model qualitatively predicted the stick-slip motion seen in their experiments, the viscous model did not and that it should be discarded. Furthermore, they showed that the plastic thermal model predicted hysteresis similar to that of Figure 1.11. The important conclusions of Smith and Woodhouse's work were hence that temperature influences rosin, and that the thermal plastic model is among the simplest methods of incorporating thermodynamics into the calculation of friction between rosin-coated objects in a way that reflects qualitative trends in experiment.

1.1.2 APPLICATION OF THEORY TO PLAYABILITY

Although the study of the mechanical properties of the violin and bow is fascinating in its own right, it is ultimately a means for understanding which aspects of a violin affect the duration of pre-Helmholtz motion transients. Furnished with such an understanding based on deterministic physical analysis, one could proceed to explore changes to the design of a violin, a string, or rosin that a manufacturer could make, which would shorten these transients, thus improving the instrument's "playability". Similarly, one could possibly suggest changes to the method of playing a violin which a player could instigate, which for less advanced players at least would promote an improvement in clarity of tone.

Various speculative efforts have been made in similar directions already, based mainly on simulations using the earlier "friction curve model" for the mechanics of the bowed string. It is hoped that further theoretical developments would allow such research to be expanded upon; indeed, these past research efforts, described below, provide guidelines for future investigations into playability.

MAXIMUM AND MINIMUM BOW FORCE LIMITS

Schelleng [16] famously set the precedent for examining the physics of the bowed string from the perspective of a player. He examined the conditions required to maintain Helmholtz motion in the steady state and derived an upper limit for the amount of force that a player may use before Helmholtz motion breaks down. Schelleng's limit, in terms of the instantaneous bow speed v_b, the bow's position β along the string, the transverse impedance Z of the string and the coefficients of friction μ_s for the limit of static friction and μ_d during slipping, is:

$$N_{max} = \frac{2Zv_b}{(\mu_s - \mu_d)\beta}. \tag{1.15}$$

Schelleng noted that Raman [2, p.151] had previously derived an analogous lower limit for normal force during Helmholtz motion under the assumption that the bridge behaves like a dashpot (as in for example Figure 1.2) and that β is sufficiently small that the short section of string between the bow and the bridge may be assumed to be without curvature. The latter assumption has since been shown to have little effect on the result [24, 26] (c.f. also [45, Fig.2]). Defining λ_b as the corresponding dashpot rate, Raman's limit is:

$$N_{min} = \frac{Z^2 v_b}{2\lambda_b(\mu_s - \mu_d)\beta^2}. \tag{1.16}$$

Noting that the ratio of these two limits is proportional to β and hence that the player has more freedom when playing further from the bridge, Schelleng plotted the range of forces available to a player during Helmholtz motion as a function of β. Schelleng's original diagram [16], which has since become known as the "Schelleng diagram", was similar in principle to Figure 1.14.

Schelleng's motivation behind this work was to provide a scientific explanation for players who, like Schelleng himself, had noticed a variation in N_{max} and N_{min} as the bow is moved away from

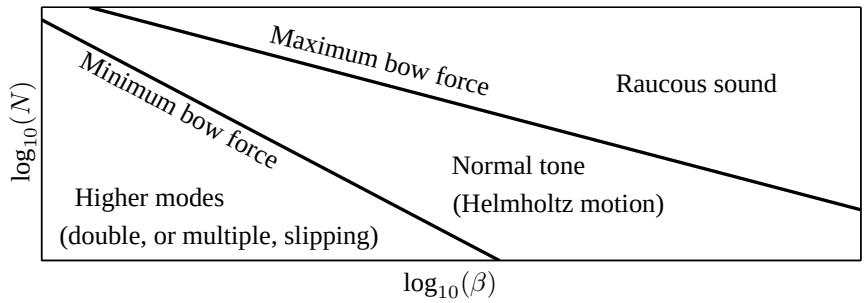

Figure 1.14: "Schelleng diagram". Schelleng plotted his upper limit and Raman's lower limit for bow force during Helmholtz motion, to demonstrate that they become closer together as the bow approaches the bridge (i.e. as β decreases). If the force is less than the lower limit (whose slope in the log-log plane is -2), then a second slip per period appears — Schelleng called the subsequent motion "higher modes", although other authors have coined the term "double slipping motion". If the force exceeds the upper limit (whose slope is -1), then the Helmholtz corner is prevented from completing its round trip of the string, causing the periodic stick-slip action of Helmholtz motion to give way to a more scratchy "raucous" sound.

the bridge. However, it is also apparent from Equations (1.15) and (1.16) that, if the assumptions used to derive N_{max} and N_{min} are valid, then one could manipulate the properties of the bridge (to modify λ_b) or the string (to modify Z), in order to alter N_{max} and N_{min} to suit the needs of the player [46]. Indeed, there have been some attempts to measure minimum bow force ([47, Fig.3], [48, Table VIII], [22, Fig.4.5]), but the only solid conclusion from these measurements is that old Italian violins such as those of Guarneri have no intrinsic advantages over nominally inferior instruments such as Saunders' "$5.00 fiddle" [48] in this sense.

However, if indeed we are to divert our attention away from qualitative limits which confine a player and focus instead on the playability of a violin, then we must take into account that the experience of most violinists is that an instrument's "playability" manifests itself most noticeably at the start of notes rather than after the note has been produced. Whereas any violinist can eventually produce Helmholtz motion on any held note, it is strikingly difficult on some instruments compared with others to perform a passage of many fast notes and achieve a "clean attack" (that is, nothing but Helmholtz motion) on each one. Psychoacoustical research [49] indicates that players and listeners are sensitive to pre-Helmholtz motion noises lasting even just a few hundredths of a second.

And so, while Schelleng's work is illuminating to the player, thus fulfilling its intended purpose, investigations of playability should focus upon the transient motion of the string. Can "playability" be rigorously defined in terms of how consistently a given set of bowing gestures produce short pre-Helmholtz motion noises? What determines the duration of these noises, and can a player avoid them altogether?

CONSIDERATION OF INITIAL TRANSIENT, AND PRE-HELMHOLTZ MOTION DURATION

Drawing inspiration from Schelleng, Woodhouse [46] undertook the first serious exploration of the role of transient vibration in determining the playability of a violin. Whereas the "Schelleng diagram" describes the range of bow force a player can use to maintain Helmholtz motion, Woodhouse plotted the range of force which, with the string starting from rest in a simulation model of the bowed string, eventually led to Helmholtz motion. Importantly, by taking the transient vibration of the string into account, this contrasts Equations (1.15) and (1.16): due to the nonlinear dependence of the string's vibration on initial conditions [50], some levels of bow force which lie within Schelleng's limits never led to Helmholtz motion at all. Indeed, Woodhouse found that the least possible bow force that could be selected which led to Helmholtz motion was almost two orders of magnitude greater than the minimum bow force predicted by Equation (1.16) for the same bow speed during steady state motion.

Following Woodhouse's example, Schumacher and Woodhouse [51, 52] proceeded a step further by plotting the time taken to achieve Helmholtz motion from the start of a bowing gesture; as such, regions in Woodhouse's plot which indicate the production of Helmholtz motion are now divided into regions where Helmholtz motion was produced after very little delay and regions where it took longer to achieve Helmholtz motion. Treating the size of regions where Helmholtz motion was achieved rapidly as an indicator of the playability of the violin, Schumacher and Woodhouse examined the effect on this area of altering certain parameters in the model of the bowed string. As such, their investigation was tantamount to a computer-aided empirical analysis of playability, equivalent in many ways to the more traditional trial and error investigations of playability and tone quality by violin makers and string/rosin manufacturers.

Not having been extensively validated by experimental data, Schumacher and Woodhouse's model of the bowed string was too tentative for them to draw any firm conclusions regarding how a violin could be beneficially altered. A separate but intriguing finding in both [51] and [52] was that, in simulations which use the "friction curve" rosin model, contours along which the duration of pre-Helmholtz motion transients are the same coincide almost exactly with contours where the initial values of bow force and velocity are constant. No explanation for this unexpected observation was offered, and it would seem to be an interesting subject for future investigation.

PERFECT TRANSIENTS, AND THE FORCE-ACCELERATION PLANE

Arriving at this subject as a player like Schelleng, Guettler [45] pointed out that the "switch on" transients upon which most of the above work was based, in which the velocity and force both suddenly change from zero to a non-zero value with the string initially at rest, cannot be achieved in practice. He suggested that, for the first few tenths of a second or so at least, either the bow force or the bow speed (or both) must start from zero and increase approximately uniformly with time, with the other of the two remaining constant; for a "string crossing" or for "*spiccato*" (or

"bouncing bow") the force increases from zero as the bow comes into contact with the string, whereas for probably all other "bowing attacks" it is the velocity that would increase from zero. Leaving the first of these two aside, Guettler argued that the parameters most relevant to players are hence bow force N and bow acceleration a, and that regions of Helmholtz motion are most usefully viewed in the N vs. a plane.

Besides running computational bowed-string simulations and plotting the time taken to achieve Helmholtz motion at a grid of points in the N vs. a plane, Guettler sought analytical expressions for the upper and lower bounds of the regions containing "perfect transients", i.e. combinations of force and acceleration which produce Helmholtz motion (or more generally one stick and slip per period) without any delay whatsoever. Guettler derived four necessary conditions for the production of a perfect transient, given several simplifying assumptions: the effects of wave dispersion or other sources of "corner rounding" were ignored, the ends of the string were treated as dashpots, torsional motion was ignored, the effect of temperature on rosin was ignored, the bow was assumed to contact the string only at a point, the bow hair was assumed to be stiff, and finally $1/\beta$ was required to be an integer. However, before citing Guettler's four conditions, it is helpful (for later reference also) to review the vibration pattern of a bowed string in the first few moments of a theoretical "perfect transient", following a similar approach to the same problem by Cremer [53]. Figures 1.15(a)–(g) illustrate the chain of events that would occur in a perfect transient, and are described as follows:

(a) Before the first slip the bow may be thought of as pulling the string outwards quasi-statically.

(b) The first time the string slips, two waves (labelled "1" and "2" in Figure 1.15) are sent outwards from the bowing point. At this stage the string's motion is similar to what it would be if it had been plucked [22, §2.2].

(c) The first slip is terminated when wave "2" passes over the bowing point having first reflected from the bridge. Shortly after the end of the first slip, waves 1 and 2 are both travelling away from the bow towards the far end of the string (the finger or nut side). The dashed line shows the shape that the string would have at this point if it had indeed been plucked.

(d) Waves 1 and 2 are both inverted when they reflect off the far end of the string, and travel back towards the bow.

(e) Wave 1 is of the opposite sign required to induce slipping, and hence reflects off the (sticking) bow.

(f) Wave 2 is however of the same sign as a "Helmholtz corner", and hence induces slipping when it reaches the bowing point. Hence, while wave 1 continues to travel away from the bow towards the nut, wave 2 travels past the bowing point towards the bridge.

(g) The second slip stops when wave 2 passes back over the bowing point. Because wave 1 reflected off the bow whereas wave 2 travelled the extra distance $2\beta L$ to the bridge and back, the two waves are now a total distance $4\beta L$ apart.

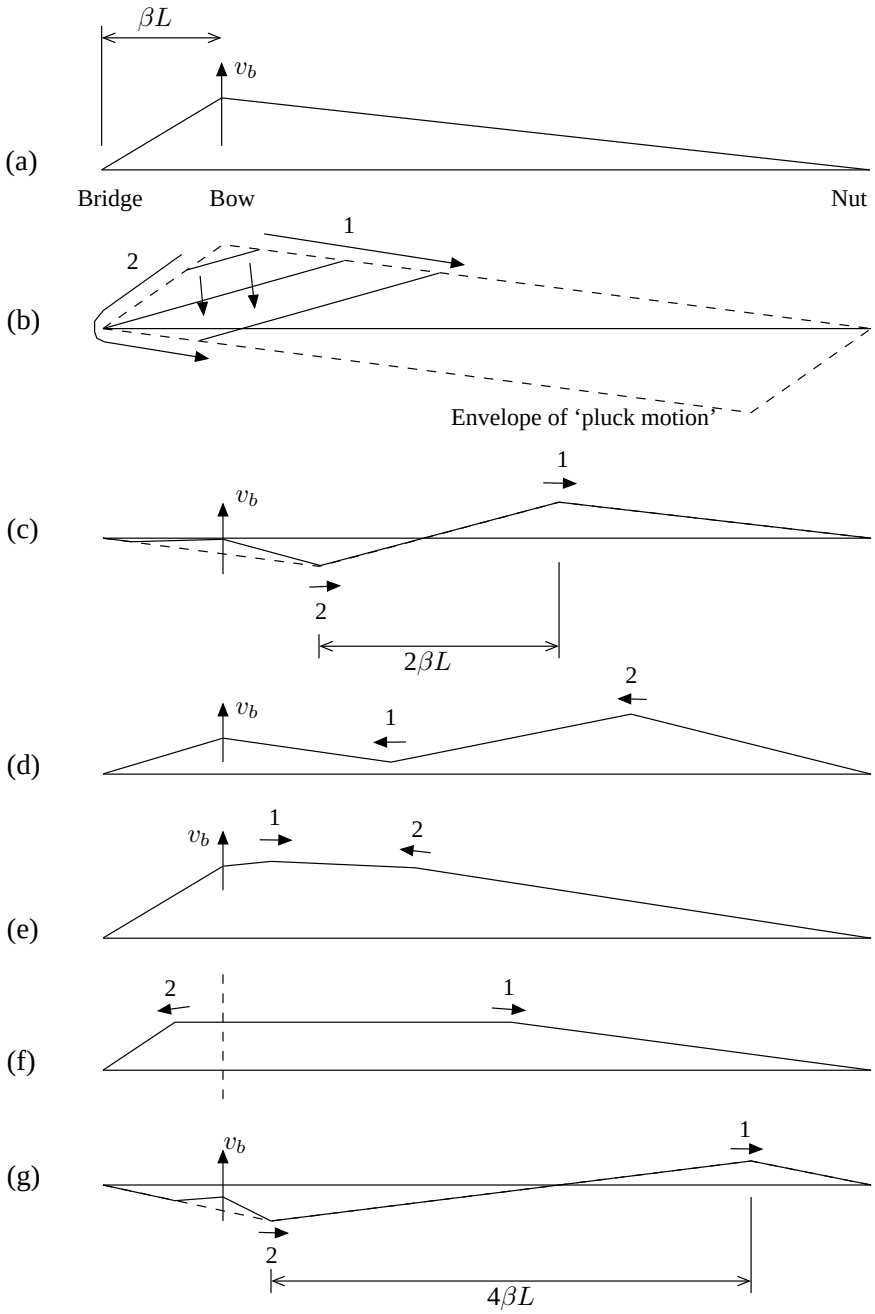

Figure 1.15: The shape of the string during various early stages of the "perfect transient", i.e. one in which the string sticks and slips once per period: (a) shortly before the string first slips, (b) during the first slip — the two waves, labelled "1" and "2", are sent outwards from the bow in a similar fashion to a plucked string [22, §2.2], (c) shortly after the first slip, at which time both waves are on the nut-side of the bow — the dashed line again shows the shape of the string if it had been plucked, (d) both waves have reflected off the nut, and hence inverted, (e) the first wave reflects off the bow, (f) the second wave transmits past the bow, inducing a second slip, (g) following the second slip, the two waves are spaced twice as far apart as previously. The general pattern between (c) and (g) subsequently repeats, increasing the distance between waves 1 and 2 by $2\beta L$ each time. Schelleng [16, §II.F] was the first to point out that of the two waves created at the onset of slipping in (b), only wave 2 is in the same sense as the "Helmholtz corner" associated with Helmholtz motion, and that the subsequent growth of this wave is therefore responsible for whether or not a transient will evolve into Helmholtz motion. Guettler's four conditions [45] for this to happen without any interruption to the cyclic stick-slip pattern are described in the text.

Each of these stages in the early part of the "perfect transient" is illustrated in Figure 1.15. Guettler identified four potential pitfalls in this chain of events, and defined four corresponding threshold tests that must be passed in order for the "perfect transient" to occur:

1: Resolving forces at the bowing point we find that, during (c) and (d) above (corresponding to Figures 1.15 (c) and (d)), the friction force required from the bow increases steadily until wave 1 meets the bow, at which point it drops. The first pitfall is hence that the bow must press into the string with enough force to be able to supply this friction, which is at its greatest in the moment immediately before wave 1 reflects from the bow.

2: The second slip should be induced when wave 2 meets the bow between (e) and (f); the second potential pitfall is therefore that the bow must press against the string sufficiently lightly that wave 2 can overcome static friction and transmit past the bowing point.

3: As illustrated in Figure 1.15, wave 2 reflects back and forth between the bridge and the nut (total distance L), whereas wave 1 reflects back and forth between only the bow and the nut (total distance $(1-\beta)L$); hence each time wave 2 passes the bowing point the separation between the two waves increases by a distance $2\beta L$. This is more easily seen in the space-time diagram of the two waves in Figure 1.16. As the two waves become further and further apart, the next reflection of wave 1 starts to approach wave 2 from behind (one may think of wave 2 undergoing a 360° phase change). Their separation after k reflections of wave 2 from the bridge is $(2L - 2(k+1)\beta L)$, and hence if β is the reciprocal of an integer they exactly coincide after $k = 1/\beta - 1$ reflections. Bearing in mind that they are of opposite signs (see Figure 1.15), Guettler pointed out that wave 1 is in danger of cancelling out wave 2 at this point, to the extent that the $1/\beta^{\text{th}}$ slip may not occur: this is Guettler's third pitfall.

   Hence, Guettler stipulated that wave 2 must be stronger than wave 1, and that the bow force must not be so great as to prevent the combined wave from penetrating past the bow. This gives rise to a new upper limit on bow force.

4: Guettler observed that, with the model which he used for the bowed string, the amount of friction required from the bow on the string in order to achieve the perfect transient (that is one stick and slip per period) sometimes reaches a large value after around $1/(3\beta)$ reflections of wave 2 off the bridge. Assuming that the friction peaks between the $1/(3\beta)^{\text{th}}$ and the $(1 + 1/(3\beta))^{\text{th}}$ reflection, and using the same string model as before, Guettler derived a lower limit for bow force: if the bow force fails to exceed this limit, the rise in friction may induce a second slip if it reaches the limiting static friction $\mu_s N$. In relation to the other three conditions for the production of a "perfect transient", this fourth one applies at a time in the transient after the first two, but before the third.

These four conditions for a perfect attack, expressed in analytical form by Guettler, were found to agree with the results of simulations using a Raman-type model, and as such to complement Schelleng's original ideas; interestingly, Schelleng himself [16, §II.F] predicted that "wave 2" in

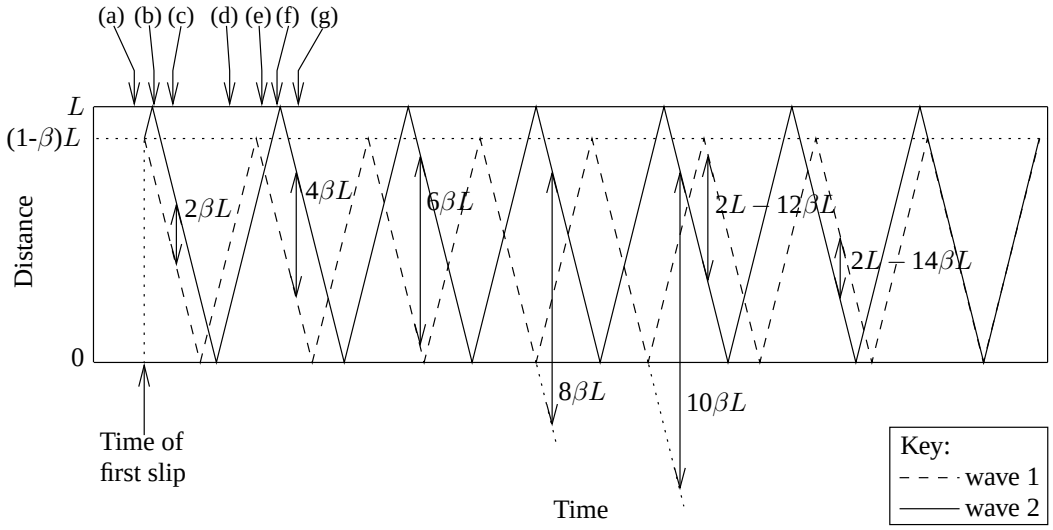

Figure 1.16: Space-time diagram of the two waves (labelled "1" and "2" in Figure 1.15) generated at the start of a "perfect transient". Wave 1 is represented by a dashed line and wave 2 is represented by a solid line. The times of the snapshots (a)–(g) in Figure 1.15 are indicated at the top; β is the same in both figures. After each reflection of wave 2 off the bridge, the separation between the two waves increases by a distance $2\beta L$, although the separation between wave 2 and the next reflection of wave 1 is $(2L - 2(k{+}1)\beta L)$ after k reflections, as shown. Hence in this case, where β is exactly 1/8, the two waves meet each other after wave 2 has reflected from the bridge seven times (i.e. $k = 1/\beta - 1$).

figures 1.15 and 1.16 should grow into a "Helmholtz corner". It is indeed the case that with low frequency strings (such as the C string of a cello or any string of a double bass), where the period length is in excess of a hundredth of a second, almost any interruption to the regular stick-slip pattern of Guettler's "perfect transient" will be audible [49]. For such cases, Guettler's limits for bow force in terms of acceleration provide a guide to the player on what is allowable. Conversely, the construction of the strings, rosin or instrument could be manipulated in order to alter the magnitudes of Guettler's limits to suit the needs of a player. For example, one would expect added damping in the string to smooth out wave 1 more than wave 2, since wave 2 is "sharpened" each time it passes under the bow [5, 7], whereas wave 1 never passes under the bow; this would relax Guettler's third condition to some extent [45, §4].

However, as already mentioned, the exact formulation of Guettler's four conditions is based on several simplifying assumptions, and as such their applicability in practice may be open to question. Indeed, a "perfect transient" may be too harsh a requirement for some instances where a "good transient" in some sense would suffice. Certainly, if the string's natural frequency is high (which it would be for example on a violin), and hence the period length is short, a non-periodic initial "noise" may be tolerable for the duration of several period lengths [49].

DEFINING PLAYABILITY

Although the idea that "playability" is linked to ease of production of Helmholtz motion has been around for some time now [54], playability as such has essentially evaded quantitative definition. Most mentions of this quality of an instrument are vague, usually referring to general behavioural patterns in one parameter space or another. Cremer himself [22, p.2] was driven to write that "only one goal remains elusive: that of deriving credible, objectively measurable criteria for the evaluation of instruments."

Only Schumacher and Woodhouse [51, §IV.B] have ventured to discuss algorithmic techniques which might be employed if one were to quantify playability. Upon observing the spatial patterns of plots of time taken to achieve Helmholtz motion in various parameter spaces, they suggested that a measure of playability could be constructed based on the extent of regions of different "types of terrain" in each parameter space. For example, a region of parameter space which has a mixture of "good" and "bad" transients (in the sense that Helmholtz motion was achieved quickly, or after a significant delay, respectively) might seem "unreliable" to the player, and should therefore be minimized; conversely, a region in which Helmholtz motion is produced quickly and consistently would be desirable to the player, and efforts should be directed at augmenting this region. In the first case, the plot of time taken to achieve Helmholtz motion would appear to be "speckled", whereas in the second case it would appear "smooth". Schumacher and Woodhouse suggested that the task of classifying regions of parameter space would be made easier with the help of automatic image-processing techniques. Certainly no attempt has ever been made to bring these concepts to fruition, and indeed they may be subject to fundamental change as new theoretical models predict visibly different spatial patterns [21].

Finally, because this research area remains in its infancy, there exists a notable lack of psychoacoustical tests illustrating the simple difference between a "playable" violin and an "unplayable" violin. The driving force behind this concept currently relies instead on the widespread view that, on some instruments more than others, one must "work hard" to make the instrument speak. A formal player rating test, in which two or more violins of theoretically contrasting playability were tested by human violinists, would underline the importance of research into the playability of stringed instruments.

1.2 AIM AND STRUCTURE OF THESIS

The research described up to this point has brought the level of knowledge of the mechanics of the bowed string to a stage where many aspects of the bowed string can be described with qualitative accuracy, with the path towards research into "playability" itself beginning to be uncovered. The most conspicuous absentee amongst existing research in this area is a thorough experimental validation of the theoretical models used to describe the bowed string.

The aspect of theory that requires the most attention is the model used to describe the frictional behaviour of rosin. Nearly all investigators up to now have assumed the classical "friction curve model", but this model is incompatible with Smith and Woodhouse's [43] and Woodhouse et al.'s [27] measurements of friction. Smith and Woodhouse [43] suggested the alternative "plastic thermal model", but the physics of this model is intentionally simple, and based in part on tentative measurements of the properties of rosin.

There exists an imminent need for a facility for performing parallel simulations and experiments, in which the string is bowed identically in both cases. With such a facility, details of the simulated and measured string vibration can be compared, with a view towards making whatever changes to the theory that are necessary in order to achieve detailed agreement between the two.

In Chapters 2 and 3, the design and construction of a computer-controlled bowing machine is described that has allowed such measurements to be made. The steps taken to ensure that the bow force, bow speed and bow position are controlled to within tight tolerances are described in detail, and the resulting performance capabilities of the bowing machine are presented.

In Chapter 4, a broad range of experimental data is presented that was obtained as the bowing machine bowed a cello using a perspex rod. A perspex rod was chosen in the first instance because it contacts the string at a point rather than across a finite range of positions, and is rigid; as such, the effects of "real bows" discussed on page 12 can be ignored. A "Schelleng diagram" is presented that shows the range of bow force that a player may use to sustain Helmholtz motion; the results are directly compared with Schelleng's [16] analytical predictions. A series of "Guettler diagrams" are also presented, which demonstrate the effect of altering the bow force and acceleration on the time taken to produce Helmholtz motion, and as such reflect the playability of the cello used in experiment. A range of individual string vibration waveforms are shown that illustrate the transient and steady state behaviour of the bowed string, and aspects of these waveforms that hold information about the frictional behaviour of rosin are highlighted. A variety of evidence is presented that illustrates the "repeatability" of measurements of transient string vibration.

In Chapter 5, a wide range of results from simulations of the bowed string are presented that are nominally similar to the experimental results of Chapter 4, using both the "friction curve model" and the "plastic thermal model" of rosin. Results from the friction curve model are presented based on two contrasting friction curves: the first is the friction vs. sliding speed relation obtained by Smith and Woodhouse [43] from steady sliding tests, and the second is a new f-v relation derived from experimental data in Chapter 4. In keeping with the use of a perspex rod in the experiments in Chapter 4, all simulations ignore the effects of the finite width and compliance of real bows. Neither the results from the friction curve model with either of the two friction curves, nor the results from the thermal plastic model, are observed to agree with the experimental results in great detail, although the plastic thermal model is seen to be the most successful in this respect.

Possible explanations for many of the differences between simulation and experiment are discussed in Chapter 6, and various ways in which the simulations could be improved in order to alleviate

each difference are suggested. A review of some of the evidence of Chapter 4 suggests that the contact area between bow and string can increase under sustained tangential loads. The function proposed by Smith and Woodhouse [43] to describe the dependence of friction coefficient on the temperature of the rosin coating the bow is shown to be the probable source of various anomalies in simulations based on the plastic thermal model. The possibility that the string never truly sticks to the bow, but rather "creeps" under tangential loads while apparently sticking, is suggested based on a range of experimental evidence.

Results obtained from bowing the cello used in Chapter 4 with a real bow instead of a perspex rod are presented in Chapter 7. Guettler diagrams and individual string vibration waveforms are again used to illustrate the general behaviour of the string, several aspects of which are seen to be indistinguishable from the behaviour observed when using the perspex rod. The few exceptions include some new features of the string's transient vibration waveform that appear only when the bow is close to the bridge, and a tendency for the limiting static coefficient of friction to decrease towards zero at small values of normal force.

The findings of this thesis, and suggestions for future investigation, are summarized in Chapter 8.

Chapter 2

EXPERIMENT I: APPARATUS AND FEEDBACK CONTROL

INTRODUCTION

A detailed description of the design and functionality of the computer-controlled bowing machine used in this project is presented in this chapter, which is structured as follows:

- overall design concept underpinning the bowing machine
- details of the feedback compensators used to control bow force and bow speed
- techniques used to measure the speed and force
- mechanical design of the bowing machine, with emphasis on how its individual mechanical features improve the performance of the feedback controllers

The resulting performance capabilities of the machine, and some methods employed to boost them, will be presented in the following chapter.

2.1 ALTERNATIVE DESIGN CONCEPTS

The construction of a mechanical device which plays a violin is a task which various researchers have undertaken over the last hundred years or so. The basic design concepts of past bowing machines, as well as the objectives of the underlying research, have differed widely. Müller and Völker [22, p.48], for example, used a moving rosin-coated belt to "play" the violin, whereas Saunders [55] and Bladier [56] both used hard rosin-coated rotating discs (see Figure 2.1). Other researchers have strayed even further from the use of a conventional bow; in the bowing machine of Weinreich et al. [57, 58, 59], the string is not touched by any kind of bow at all — it is excited by an electromagnet instead.

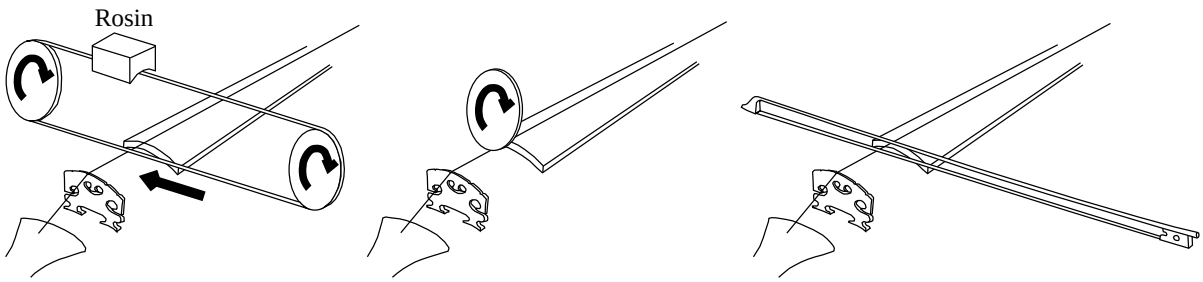

(a) Belt design (b) Disc design (c) Bow design

Figure 2.1: Some alternative design concepts for the bowing machine: (a) a tensioned belt is continuously drawn over a block of rosin and the surface of a string; (b) a rosin-coated disc rotates such that it continuously touches the string; (c) a real bow, or a rosin-coated rod is drawn across the string.

In addition to these, a number of bowing machines have been developed in which a conventional bow was used to play a violin. Lawergren [60] for example attached each end of a bow to a wagon driven by a DC motor, and used a screw jack to press a violin against it. Pickering [61] devised a similar arrangement, but pressed the bow into the string using a weighted wheel. Investigators in India in the first half of the twentieth century (especially Kar et al. [47], and even Raman himself [62]) followed similar lines, in spite of the limited technology available to them.

The objectives of the present research project suggest the necessity of a bowing machine which closely mimics the action of a human violin player: in particular this project aims to understand the influences on a violin's playability, which is inextricably linked to the way the violin is played. It would be inappropriate at this stage therefore to assume that certain aspects of the bow, such as the way it is held, are unimportant to playability.

The design concept shown in Figure 2.1(c) was therefore chosen for the bowing machine, because it most resembles a human violinist. It is intended that accurate control (and therefore also knowledge) of the bow speed, force, and position will facilitate computational simulations of the bowed string which run in parallel to, and which can be compared with, experiments.

2.2 DESIGN STRATEGIES FOR FEEDBACK CONTROLLERS

2.2.1 DESIGN REQUIREMENTS

The task of the bowing machine is to be able to monitor and control the normal force with which the bow is pressing against the string and the speed with which it is drawn across the string; furthermore, it should be capable of reproducing the sort of bowing gesture that a human player might use. The principal objective of the feedback compensators used to control force and speed is therefore to enforce that the actual bow speed and force closely follow a pre-defined trajectory; this is referred to as "tracking a demand signal" in the control literature.

The configuration used for feedback control throughout this section is as shown in Figure 2.2. The closed-loop transfer function (CLTF), i.e. the ratio of y (the output) to r (the input), is:

$$\text{CLTF} = \frac{P(j\omega)C(j\omega)}{1 + P(j\omega)C(j\omega)}, \tag{2.1}$$

where $P(j\omega)$ is the frequency response of the system being controlled, and $C(j\omega)$ is that of the controller.

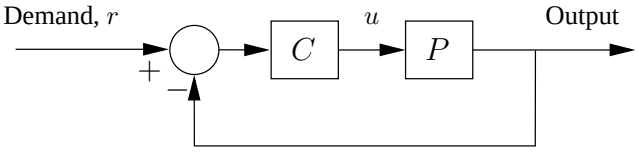

Figure 2.2: Configuration used for feedback control: P is the system to be controlled ("plant"), and C is the controller. Both are single-input/single-output.

Due to inevitable bandwidth limitations of the hardware used, it is necessary that for both force and speed control, the controller be effective only up to a certain frequency f_c (which may be different in the two cases), beyond which it should have no response (i.e. CLTF$(j\omega) \to 0$ for $\omega > 2\pi f_c$). This can be accomplished by including the factor, or frequency weighting, $2\pi f_c/(j\omega + 2\pi f_c)$ in C. Also, to ensure good tracking performance we may include the factor $2\pi f_c/j\omega$ in C because, from (2.1), this achieves CLTF$(j\omega) \approx 1$ for $\omega < 2\pi f_c$. The controllers would neither attempt to control, nor excite, vibrations at frequencies above f_c.

The work of Askenfelt [63, 64] indicates that the frequency f_c might reasonably be taken as being of the order 10 Hz, implying that any significant bow dynamics in the range 0–10 Hz would need to be compensated for. An example of the type of bowing gesture that might be expected from the bowing machine is shown in Figure 2.3, in which the bow speed exponentially increases from zero and the force exponentially decreases from some initial value in a manner not dissimilar to a *martelé* bowing attack.

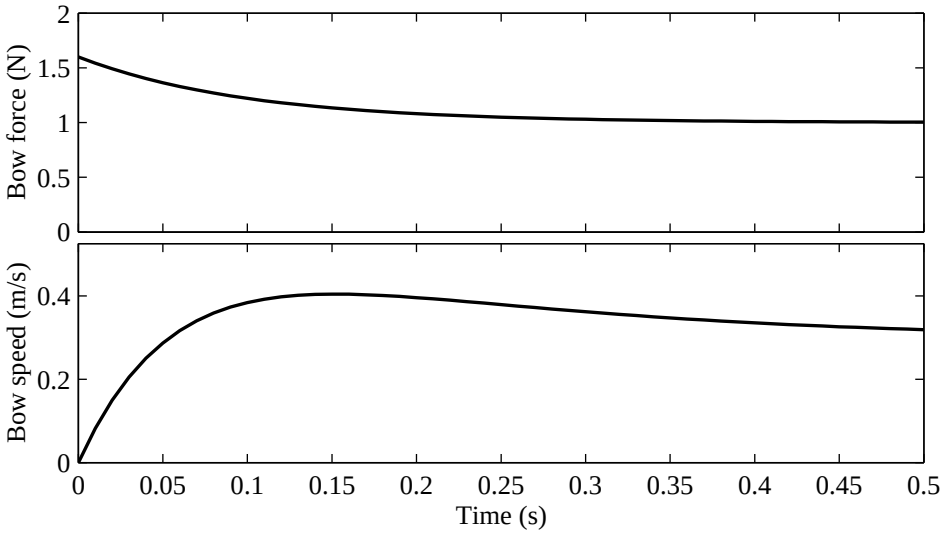

Figure 2.3: Example of the type of bowing gesture which will be required from the bowing machine.

2.2.2 FORCE CONTROL

IDENTIFICATION OF SYSTEM TRANSFER FUNCTION

When the bow is stationary, its dynamics are linear and time-invariant; the ratio of bow/string contact force to excitation force takes the form of a standard mechanical frequency response $\left(\sum_{k=1}^{\infty} \frac{a_k}{\omega_k^2+(\omega_k/Q_k)j\omega-\omega^2}\right)$, where a_k, ω_k and Q_k are the amplitude, natural frequency and Q-factor of the k^{th} mode respectively.

The impulse response method was used to measure the frequency response of the bow: a short pulse was input to the amplifier driving a shaker every one second, and the response was measured for one second. By measuring from the start of one pulse up to the beginning of the next, the measurements were truly periodic, hence preventing spectral leakage [65, §11.6]. The frequency response of the bow was obtained as the ratio of the discrete Fourier transform of the response to the discrete Fourier transform of a pulse.

Circle fitting [66, §4.3.3], non-linear least squares [66, §4.4.2], and rational fraction polynomial methods [66, §4.4.3] were all used to obtain initial estimates of the coefficients a_k, ω_k, and Q_k. However, the high level of modal overlap in the system (as large as 0.5) made manual iterations necessary to obtain accurate values of these parameters. Typically, two to four modes would be fitted in the range 0–400 rad/s in order to capture all significant resonances and anti-resonances in the range 0–100 rad/s. Figure 2.4 shows a representative example of measured and reconstructed transfer functions: values of Q-factor (Q_k) tend to be in the region of 5 or 10, and the lowest natural frequency (ω_1) is of the order of around 50 rad/s.

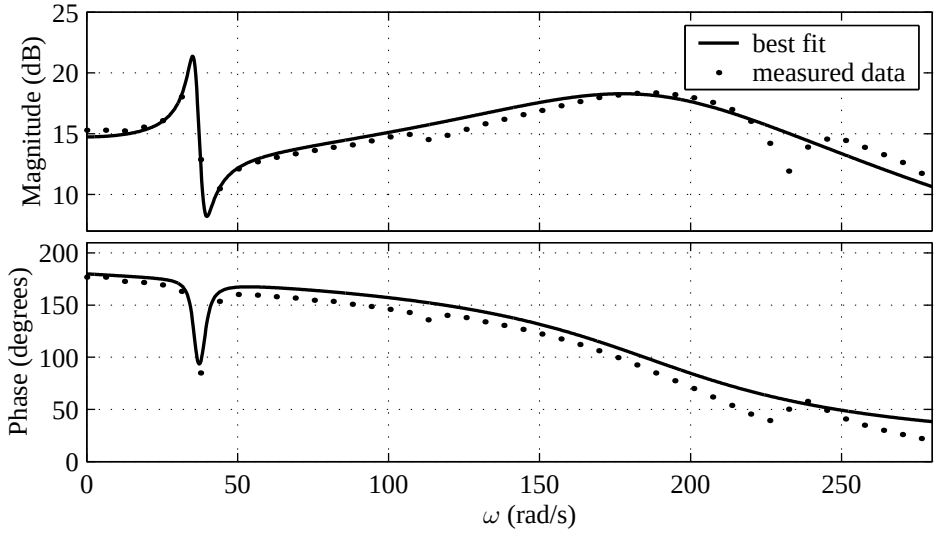

Figure 2.4: A typical example of the use of the transfer function identification technique; experimental measurements are shown with dots, and the modal fit is shown with a solid line. Clearly, no attempt was made to include the small and rather heavily damped mode at around 250 rad/s in the best fit model, as it does not significantly affect the frequency response below around 200 rad/s. This figure is representative of the compromise between ignoring small peaks and retaining important resonances and anti-resonances.

ALTERNATIVE DESIGN STRATEGIES

Importantly, the bow's frequency response depends on the location of the bow/string contact point; moving it along the length of either the bow or the string will significantly alter the modal parameters (modal amplitudes, frequencies, and damping factors). Therefore a feedback controller which makes use of prior knowledge of the bow's frequency response would need to make provisions for its dependance upon contact location. Problems similar to this have been solved before (see especially [67]) under the guise of "parameter-dependent feedback control", where in this case the "parameter" would be the location of the bow/string contact. Methods of tackling parameter-dependent feedback control problems include the following:

- Design a feedback controller with a certain level of "robustness" guaranteed, by using the standard $\mathcal{H}_\infty$ loop-shaping procedure; robustness implies insensitivity to general changes in the frequency response (call this P) of the system being controlled. This method is only realistically good for systems with small parametric uncertainty (specifically those for which $\inf_i \sup_j \delta_\nu(P_i, P_j) \lessapprox 0.15 : P_i, P_j \in \{\text{our parametric set}\}$, i.e. the smallest worst case ν-gap metric should not exceed more than about 0.15, albeit after frequency weighting has been used). ("Linear parameter-varying" and "μ-synthesis" design techniques were deemed impractical for the present application, and controllers designed using the "Linear Quadratic Gaussian" method do not give sufficient robustness guarantees [68, §14.10].)

- Use the "extended $\mathcal{H}_\infty$ loop-shaping procedure" of Vinnicombe [69], which caters specifically for parametric uncertainty problems. This method is used to calculate precisely that controller C_{opt} which satisfies $\inf_{P\in\mathcal{P}} b_{P,C_{opt}} = \sup_{C} \inf_{P\in\mathcal{P}} b_{P,C}$ where $\mathcal{P}$ is our parametric set and $b_{P,C}$ is the generalized stability margin — i.e. we can calculate C_{opt}, which is the controller that gives the best (and most robust) performance over the whole parametric range. As a rule of thumb for the present application, one could expect the value of $\inf_{P\in\mathcal{P}} b_{P,C_{opt}}$ to be in the region of 0.25, if $\inf_i \sup_j \delta_\nu(P_i, P_j) \lessapprox 0.3 : P_i, P_j \in \mathcal{P}$, which is considerably better than ordinary $\mathcal{H}_\infty$ loop-shaping. Disadvantages of extended $\mathcal{H}_\infty$ loop-shaping compared with ordinary $\mathcal{H}_\infty$ loop-shaping include the potential complexity of the resulting controller, as well as the user-intensive nature of the design procedure.

  [It is understood in both of the above two cases that the set of transfer functions $\mathcal{P}$ have been weighted in the frequency domain, e.g. by filtering out high frequencies.]

- In cases where the system response is extremely sensitive to parametric uncertainty (say $\inf_i \sup_j \delta_\nu(P_i, P_j) \gtrapprox 0.5 : P_i, P_j \in \mathcal{P}$), one may be forced to design separate feedback controllers for different regions of the parameter space, and to switch between them according to real-time measurement of the parameter.

  For example, in the case of the bow force controller required for this project, where bow-string contact position is "the parameter", one would divide the full range of possible contact positions into two or more smaller intervals, and design a controller for each. When the force controller is activated, only the particular controller designed for the present contact location would have its output connected to the input of the amplifier driving the shaker; all other controllers (corresponding to other contact regions) would be disconnected until the contact location is changed.

  The main disadvantage associated with using a switching technique is the challenge of making the switching process smooth; it would be unacceptable to have a "bump" or "jolt" as we switch from one controller to the next — put simply, this situation could arise if the different controllers had different gains. Methods of enforcing "bumpless transfer" include gain scheduling [70] or the normalized coprime factorization implementation technique of Kothare et al. [71]. Another disadvantage of switching techniques is the numerically intensive requirement that the output of all controllers must be calculated (even though only one is used at a time).

- It is sometimes possible to physically change the system that is to be controlled, to make it easier to control. For example in a mechanical application (say, controlling the position of a flexible structure), if control is required within only a certain bandwidth, then it would be sensible to modify its dynamic properties (if feasible) to ensure that no clear resonances or anti-resonances exist within that bandwidth; this equates to keeping system poles and zeros away from the imaginary axis (or real frequency axis). Ironically, it is often easier to modify

the system itself than to design a complicated feedback controller which takes into account every detail of the system's frequency response; see [67] for example.

Improving the dynamics of a system in this way can in some cases avoid any need to use extended $\mathcal{H}_\infty$ loop-shaping or switching, making the controller both simpler to design and easier to implement.

(Mathematical and nomenclatural background for the control theory mentioned above may be found in [69].)

INITIAL DESIGN OF FORCE CONTROLLER

The methodology initially used to design the force controller was tailored towards the limitations of the original mechanical design, which consisted simply of a perspex rod mounted on a plain 2 mm thick mild steel leaf spring, pressed against the string by a shaker as shown in Figure 2.5.

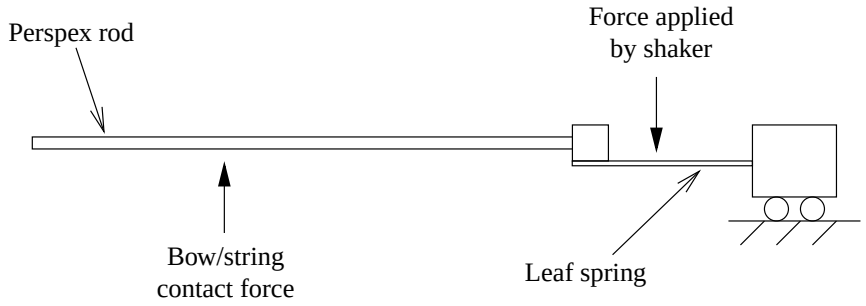

Figure 2.5: The initial mechanical design, consisting of a plain perspex rod mounted on a strip of mild steel. The "bow" is mounted in a cantilever arrangement, where a force applied by a shaker presses the perspex rod into the string.

The main problem associated with this set-up is that its resonant frequencies ω_1, ω_2 etc were sufficiently low that at every possible contact location at least one resonance fell below 10 Hz; consequently the force controller (requiring a bandwidth of around 10 Hz) required a non-trivial frequency response in order to damp out these resonances. Furthermore, the details of each mode (Q_k, ω_k and a_k) fluctuated severely as the contact location was changed, causing the "parametric uncertainty" to be so large that even extended $\mathcal{H}_\infty$ loop-shaping would not on its own be sufficient: a switching technique of some kind was required. Figure 2.6 shows the bow's frequency response at a selection of contact positions, demonstrating this variability.

Once the decision had been made to rely on switching, it was found that ordinary $\mathcal{H}_\infty$ loop-shaping was sufficient to provide the necessary frequency dependance of each individual controller; the added effort required to use the extended $\mathcal{H}_\infty$ loop-shaping procedure outweighed the small advantage that fewer controllers (approximately five instead of around eight) would need to be designed

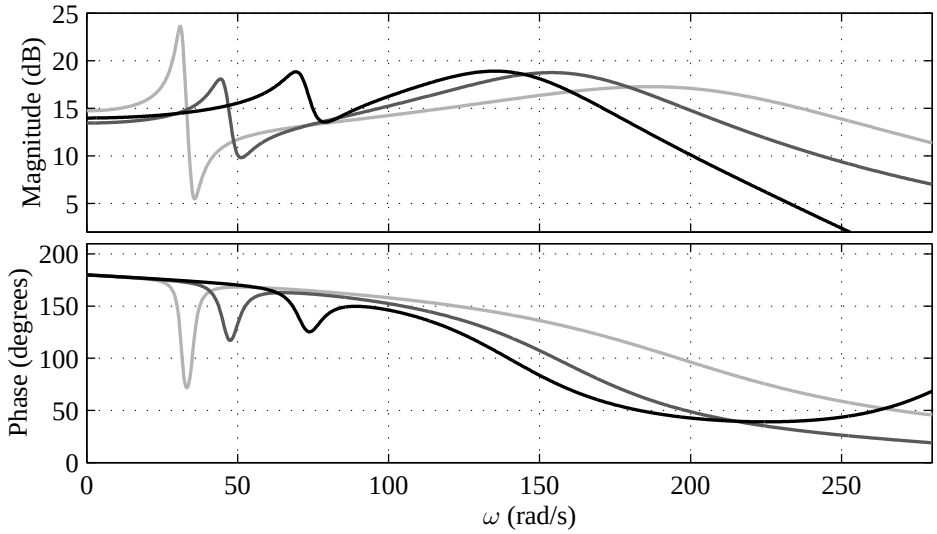

Figure 2.6: Frequency response (strain gauge response per unit pre-shaker amplifier input) at a variety of contact locations, with the original perspex rod bow design. The lowest frequency moves significantly within the control bandwidth (70 rad/s).

and switched between. Hence, eight $\mathcal{H}_\infty$ controllers were designed for each of eight bow/string contact regions, and a gain-scheduling technique was used to switch between them. The resulting level of performance was adequate by the standards of Section 2.2.1.

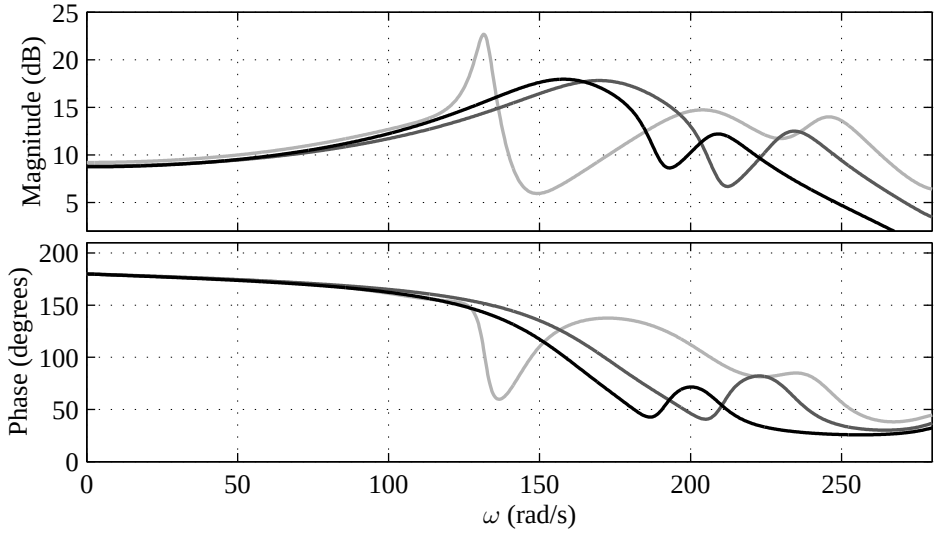

Figure 2.7: Frequency response (strain gauge response per unit pre-shaker amplifier input) at the same selection of contact locations used for Figure 2.6, after stiffening the perspex rod. Significantly, with the new bow design there is little variation in the frequency response inside the required control bandwidth. Compare with Figure 2.6.

FINAL DESIGN OF FORCE CONTROLLER

The necessity of a complete repetition of the above design procedure for every physical change made to the bowing machine (and therefore its frequency response) made this approach alarmingly impractical. The dynamical properties of the bowing machine were consequently changed in an effort to raise its natural frequencies and naturally bolster the force controller's bandwidth; in particular the perspex rod ("bow") and its holder were stiffened and lightened — this will be described in detail in Section 2.4.

The results of this effort are shown in Figure 2.7, which may be compared with Figure 2.6: the first natural frequency has been shifted from around 8 Hz to around 25 Hz, below which the frequency response is constant. The frequency response below the first mode is flat because its flexural behaviour there is quasi-static; now that the rod has been stiffened, its deflection shape remains unchanged up to a higher frequency. Notice also in Figure 2.7 that the low frequency response is largely uninfluenced by the bow/string contact location.

This new-found low-frequency insensitivity to contact location affords the force controller considerable simplification: not only does one controller suffice for the whole range of contact positions, but this one controller can be quite basic. The controller can now be of the form

$$C = k_C \frac{(\omega_{LP})^2}{j\omega(j\omega + \omega_{LP})}, \tag{2.2}$$

where k_C is used to scale $|P(\omega_{LP})\,C(\omega_{LP})|$ to 1. (In fact, the controller in Equation (2.2) is arrived at if the $\mathcal{H}_\infty$ loop-shaping procedure is employed using the weights described in Section 2.2.1 (setting $\omega_{LP} = 2\pi f_c$), on a system whose response is flat with respect to frequency, for which "integral action" [72, §4.2.2] is required.)

Hence we can now control the bow/string contact force using the configuration shown in Figure 2.8. A pre-compensator converts a force demand signal into a strain demand signal using Equation (2.7) (derived in Section 2.3.1), and the feedback loop actually controls the strain gauge signal. Importantly, by converting the force demand signal into a strain demand signal outside the feedback loop we preserve the sensitivity function, $1/(1 + PC)$, which is a measure of the controller's performance [72, §6.9.1].

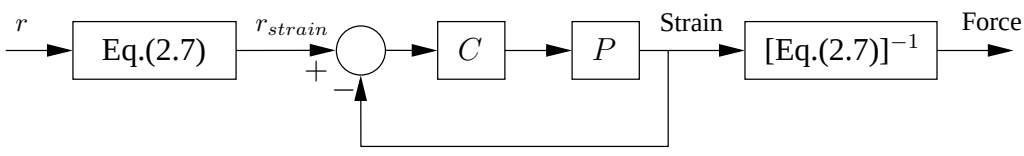

Figure 2.8: The force controller in its final form comprises a *strain* controller and a pre-compensator which converts force demand signals into strain demand signals. The details of the conversion of force into strain, i.e. Equation (2.7) will be described in Section 2.3.1.

2.2.3 SPEED CONTROL

As discussed in the last section, the force controller requires knowledge of the exact position of the bow at all times in order that the force demand signal can be converted to an appropriate strain demand signal. It is imperative therefore that the *position* of the bow be controlled, rather than its speed; although position is equal to the integral of speed, the inevitable low frequency drift problems associated with numerical integration would increasingly obscure the result of such an integral. A feedback compensator, whose task is to control the speed, would not have any objections if the bow had mistakenly moved ten feet in one direction, provided its speed equaled that of the demand signal at that instant. Compounding matters, if the position of the bow does not remain within certain bounds, the bow will either collide with the instrument it is meant to be playing, or it will make the instrument so far away as to render the force transducer incapable of actuating the bow force.

For these reasons the position ρ of the bow will be considered the control variable in the remainder of this section, rather than speed v_b (equal to $\dot{\rho}$).

CONTROL STRATEGY

The moving parts of the bowing machine are mounted on a platform which runs smoothly along a linear track (see Fig. 2.14); force is applied to accelerate or decelerate it using a linear induction motor. As such, from a feedback control perspective it can be viewed as a mass on wheels, as shown in Figure 2.9, for which $u \propto \text{force} = m\ddot{\rho}$, where ρ is its displacement, m is its mass, and u is the voltage input to the amplifier driving the linear motor. Defining M as m multiplied by the number of Volts input to the amplifier required to achieve 1 N of force, we have $u = M\ddot{\rho}$.

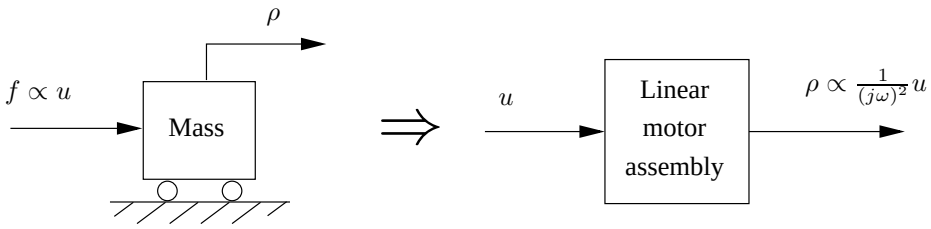

Figure 2.9: The moving parts of the bowing machine can be treated as a mass on wheels: the displacement ρ is $-1/m\omega^2$ times the applied force, $f(= Fe^{j\omega t})$.

Therefore from Equation (2.1), the use of controller C in the feedback configuration shown in Figure 2.2 would give a closed loop response function from r, the demand signal, to ρ, the position, as:

$$\text{CLTF}(j\omega) = \frac{(-1/M\omega^2)\, C(j\omega)}{1 + (-1/M\omega^2)\, C(j\omega)}. \tag{2.3}$$

Using a controller C of the form $k + j\omega\lambda$ gives

$$\text{CLTF}(j\omega) = \frac{2c_n\omega_n j\omega + \omega_n^2}{-\omega^2 + 2c_n\omega_n j\omega + \omega_n^2}, \tag{2.4}$$

where $\omega_n = \sqrt{k/M}$ and $c_n = \lambda/2\sqrt{kM}$, which conveniently describes the mechanical system shown in Figure 2.10: a spring and dashpot (whose respective coefficients are k and λ) tether the moving parts to the desired position, r.

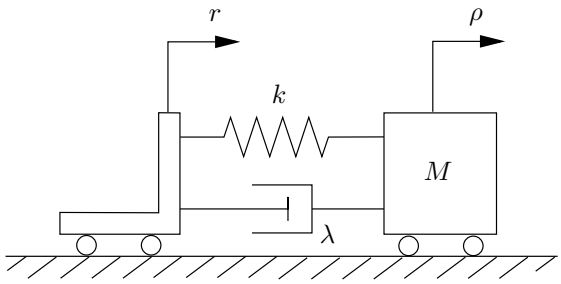

Figure 2.10: A controller C of the form $k + j\omega\lambda$ is equivalent to a spring and a dashpot joined to a trolley at the desired location r. From a mechanical perspective this is in a sense "optimal", provided sensible values of k and λ are chosen.

Two further features were incorporated into the position controller for practical reasons. First, an additional term $k_I/j\omega$ (an integrator) was added to C, to prevent small amounts of friction from affecting the dc gain (steady state response). Second, low-pass filtering was used to ensure the properness of the controller (i.e. $C(j\omega \to \infty)$ should be finite). Viewing C as a "PID" controller (with k, k_I, and λ the proportional, integral, and derivative constants respectively), the derivative term $j\omega\lambda$ increases without limit as $\omega \to \infty$; therefore this term must be low-pass filtered before being implemented. Hence the final expression for the position controller, C, is:

$$C(j\omega) = M\left(2c_n\omega_n j\omega\frac{\omega_c}{\omega_c + j\omega} + \omega_n^2\right) + \frac{k_I}{j\omega}. \tag{2.5}$$

Multiple-order low-pass filtering (to further suppress external disturbances) tends to introduce lightly damped poles in the closed-loop transfer function, which is obviously detrimental. The resulting need for in-built high frequency noise insensitivity in the derivative term calls for a careful choice of position measurement technique. The digital sensor chosen for this reason will be described in Section 2.3.2.

2.2.4 CONTROLLER IMPLEMENTATION ENVIRONMENT

The controllers designed for the bowing machine are sufficiently complex that it would be impractical to implement them using analogue circuitry. Consequently the dSpace DS1102 controller board was used to implement them digitally via a PC. The DS1102 uses the TMS320C31 floating-point

digital signal processor, which has a 33.33 ns single cycle instruction execution time. Controllers designed in Matlab are downloaded to the DS1102 board using the Real-Time Workshop software package, where they run in real time.

Besides the digital signal processor, the controllers make use of the DS1102's four on-board D/A converters, four A/D converters, one of two available incremental position decoders, and a 16 bit parallel digital input/output port. Two of the D/A converters are 16 bit successive-approximation register (SAR) converters with integrated sample/hold circuits, with a maximum sampling rate of 250 kHz (conversion time is 4 μs). The other two D/A converts are 12 bit SAR-type converters with conversion times of 1.25 μs, corresponding to a maximum sampling rate of 800 kHz. The four A/D converters have a 12 bit range, and a ± 10 V output span. The incremental decoders used to support optical position sensors will be described in the context of position measurement on page 43.

2.3 MEASUREMENT TECHNIQUES

The purpose of the bowing machine is to control the speed with which a bow is drawn across a string, and the normal force with which it presses against the string. The methods used to measure these quantities are described below.

2.3.1 MEASUREMENT OF BOW/STRING CONTACT FORCE

A major influence on several design features of the bowing machine is the fact that bow force cannot be directly measured; the necessary direct contact between bow and string makes the insertion of a force transducer (e.g. [73]) impossible. Possible solutions for indirectly measuring the contact force include:

- inserting force transducers into the body of the violin underneath where the string is supported, and combining them (one for each end of the string) to give the contact force,
- mounting the whole violin (or cello) on a large force transducer, in the style of Kar et al. [47] or Lawergren [60],
- inserting a system of strain gauges inside the bow, like Askenfelt [63, 64],
- attaching strain gauges to the structure holding the bow.

Each of the above is theoretically possible: however, in this case the latter is the most practical. Strain gauges glued into the position shown in Figure 2.11, orientated parallel to the rod, measure

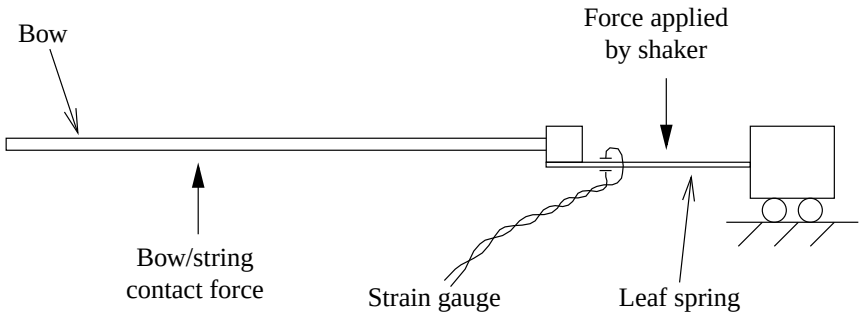

Figure 2.11: The position of the strain gauges used to indirectly measure bow/string contact force; they are placed on the structure holding the bow, between the bow and the forcing point as shown.

the bending strain at that point. Therefore, by considering a "free-body diagram" of the bow and its holder up to the position of the strain gauges we find

$$\begin{aligned}(\text{strain gauge signal}) &\propto (\text{bending moment}) \\ &= (\text{contact force}) \times (\text{distance from strain gauge to contact point}).\end{aligned} \tag{2.6}$$

Importantly, the strain gauges have been positioned within, or very near to, the line of action of the friction force acting between bow and string; the effect of friction on the strain gauge readings can hence be ignored. This is illustrated in Figure 2.12.

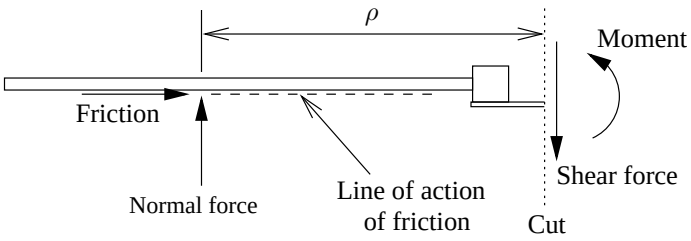

Figure 2.12: "Free-body diagram" of the bow and its support up to the position of the strain gauges. Equation (2.6) arises from the fact that the only force acting on the portion of bow shown is the reaction force of the string; the tangential component (friction) can be ignored since its line of action passes very near to the strain gauges. The geometry of the clamp holding the rod (c.f. Figure 2.18) ensures that this is still true when the line of action of friction moves due to bending in the rod.

The strain gauges are connected to a bridge amplifier (Fylde FE-641-CA). This energizes the strain gauge circuitry with a 10 kHz carrier signal and demodulates the transducer output to produce a voltage which is proportional to bending strain for frequencies up to 2 kHz.

The strain gauge and its amplifiers were calibrated using a system of weights and pulleys; results are shown in Figure 2.13, which demonstrate the accuracy of Equation (2.6). From Figure 2.13, we find

$$\big(\text{strain gauge signal (V)}\big) = 0.550 \times \big(\text{contact force (N)}\big) \times \big(\text{distance (m)}\big). \tag{2.7}$$

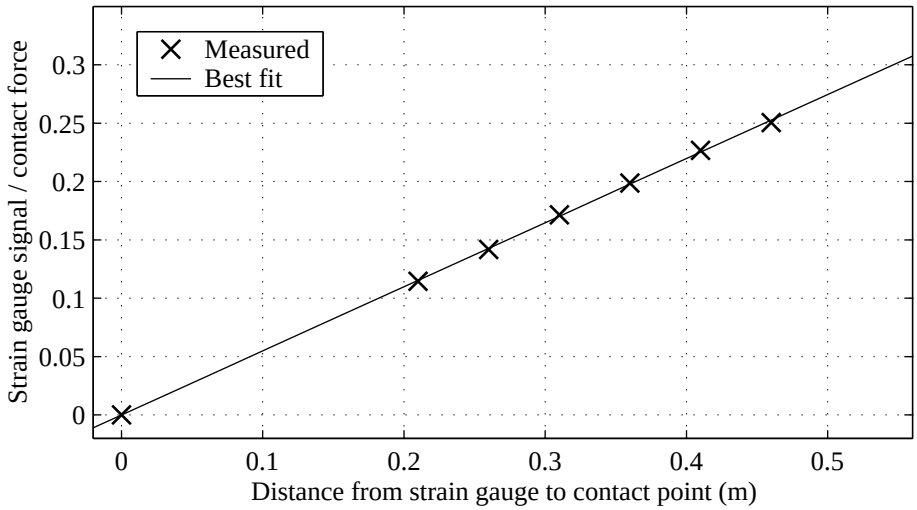

Figure 2.13: Calibration results for the strain gauge. The clear linearity justifies the assumption that the strain gauge signal is proportional to the product of the contact force and the distance between the string and the strain gauge.

2.3.2 SPEED MEASUREMENT

The position of the bow was measured using an incremental encoder; speed was obtained by calculating the time-differential of position. Knowledge of the position of the bow is as important as that of speed, because it is constantly required for the evaluation of Equation (2.7). It would not therefore be viable to determine position by integrating the output from a velocity transducer (or double-integrating the output from an accelerometer) because of the inevitable low frequency errors involved in integration.

In the present application, a digital encoder has two crucial advantages over analogue methods of measuring position (e.g. an LVDT, or a rack-and-pinion potential divider). Firstly, drift problems are completely avoided; digital encoders are impervious to issues such as temperature sensitivity or (in the case of rack-and-pinion methods) mechanical imperfections. Secondly, and equally importantly, the position measurement from an encoder is free from high frequency noise; analogue position measurement techniques require a delicate trade-off between multiple-order low-pass fil-

tering and the retention of bandwidth — the derivative term in the speed controller described in Section 2.2.3 is particularly sensitive to high frequency noise.

The single-ended optical encoder selected for use in this investigation resolves position into 5 μm intervals, and is rigidly attached to the linear motor as shown in Figure 2.14. The square waves it produces are read by one of the two incremental decoders contained in the dSpace DS1102 controller board. The decoder passes the square waves through a digital noise pulse filter (which eliminates noise pulses shorter than 80 ns), before transmitting them to a quadrature decoder which converts them into count-up and count-down pulses; a 24 bit counter with a 24 bit output latch circuit holds the current position of the sensor. The maximum count frequency of the decoder is 8.3 MHz which, for the 5 μm encoder used, implies a maximum speed of 41.7 m/s (or 93 mph), and the 24 bit position counter allows the position to vary by up to 84 m: these are both obviously adequate.

2.4 DETAILED MECHANICAL DESIGN

The essential elements of the chosen design are shown schematically in Figure 2.14. The bow is mounted in a cantilever arrangement, with a shaker pushing it against the string. The whole system is pulled back and forth using a linear motor, causing the instrument to be “played”.

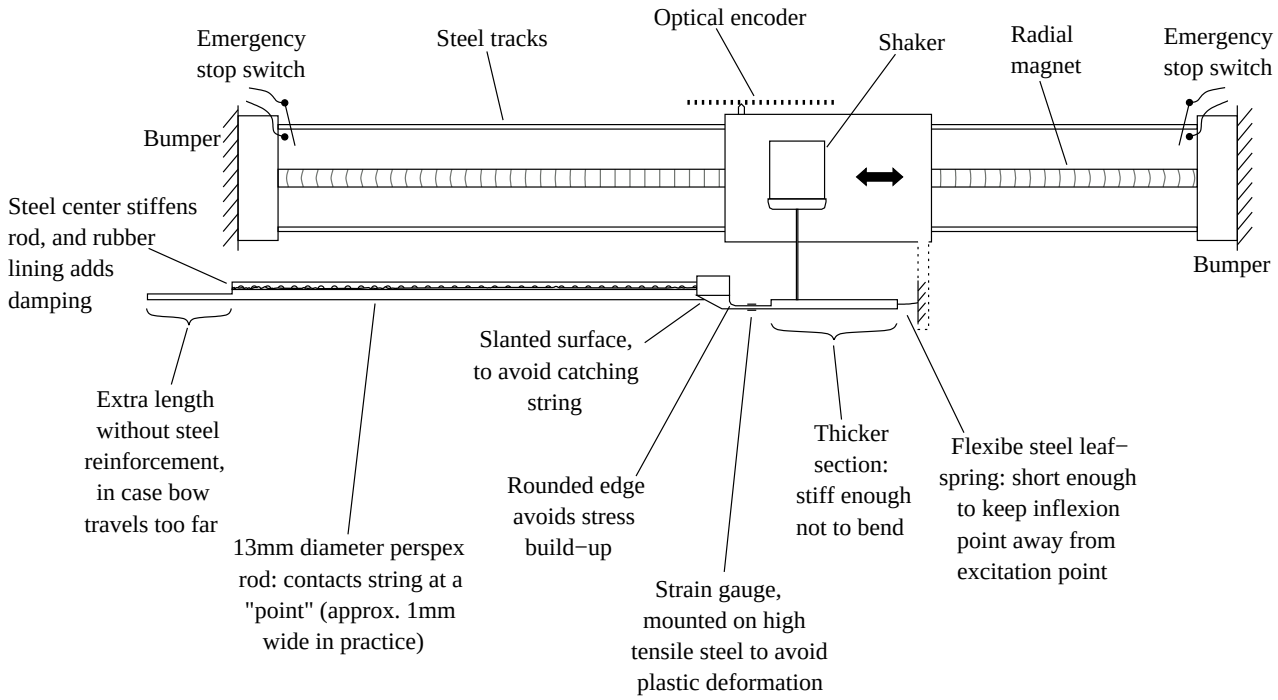

Figure 2.14: Drawing (not to scale) showing the essential features of the bowing machine.

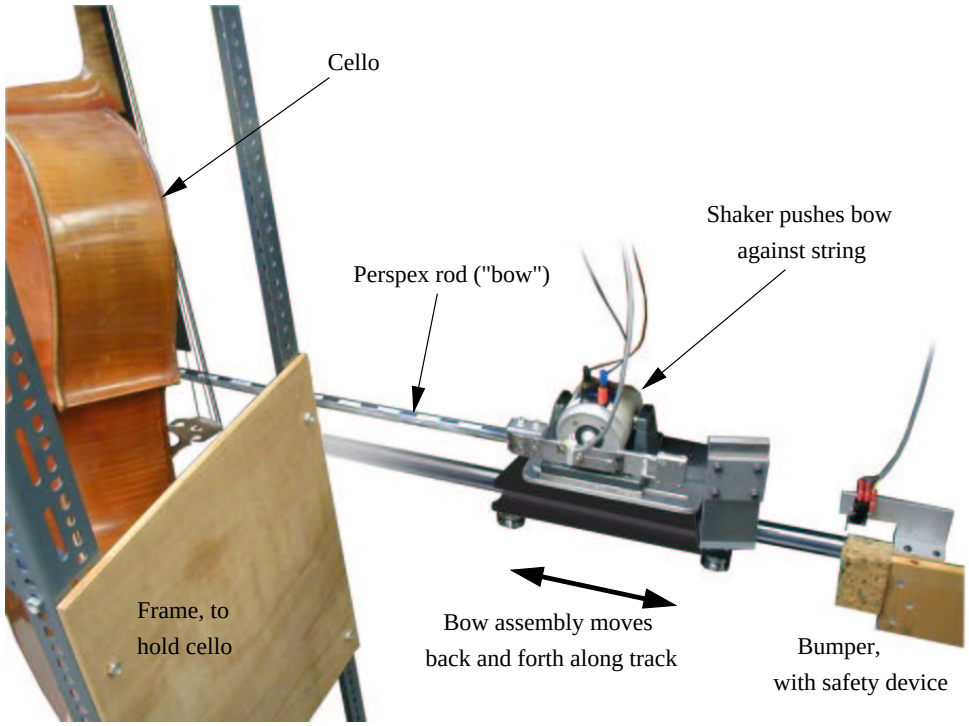

Figure 2.15: Photograph of the bowing machine — see also Figure 2.18.

SHAKER/LEAF SPRING ARRANGEMENT

The first feature of Figure 2.14 to note is the use of a leaf spring rather than a pin joint or hinge. This arrangement of a shaker and leaf spring as a means of applying torque, rather than simply a torque motor, was used in order to minimize the number of sliding contacts in the design; friction was found to be a major hindrance when controlling the bow/string contact force. However, the limitation of the shaker (the maximum dc force output of the Ling V201 shaker selected for this experiment is approximately 14 Newtons) meant that the leaf spring needed to be carefully designed, in order to ensure that as much shaker force as possible is transmitted to the violin itself.

The leaf spring was designed to be flexible enough not to resist the action of the shaker (ideally it would mimic a perfect hinge as the shaker pushes the bow into the string). For this purpose, its torsional stiffness (defined as torque / angular displacement) must be $\ll k_{str} L_{str}^2$, where k_{str} is the static transverse stiffness (force/displacement) of the violin/cello string (of the order 2500 N/m), and L_{str} is the distance from the leaf spring to the point of contact (of the order 0.3 m); this principle is illustrated in Figure 2.16. In the final design the torsional resistance of the leaf spring was 1.8 Nm/rad, allowing over 99% of the force from the shaker to be transmitted to the string.

In a further effort to mimic an ideal hinge and maximize the effectiveness of the shaker, the length of the leaf spring must be kept to a minimum. When the bow/rod deflects under the action of a force supplied by the shaker, an inflexion point will appear along the leaf spring provided it is sufficiently flexible (see Figure 2.17). If we consider a “free-body diagram” of the rod, from its free

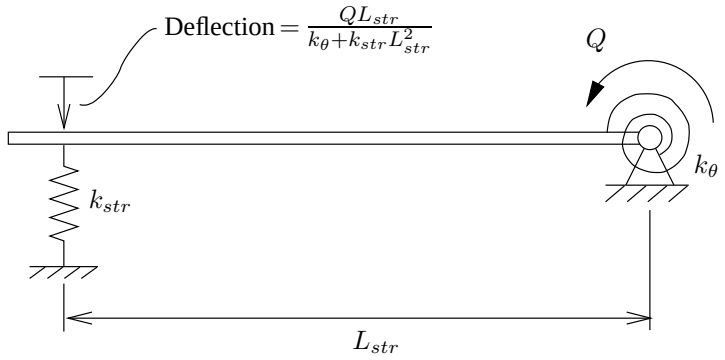

Figure 2.16: The leaf spring must be flexible enough that applied forces (from the shaker) are resisted by the cello string, rather than by the leaf spring itself. This diagram illustrates why, more specifically, the torsional stiffness k_θ should be much less than $k_{str}L_{str}^2$, where k_{str} is the static transverse stiffness of the string, and L_{str} is the distance from the leaf spring to the bow/string contact point. Q represents an applied torque.

end up to the inflexion point in the leaf spring, we find that $F_{str}/F = (L_{str} - \rho - L_x)/(L_{str} - L_x)$, where L_x is the distance from the clamp to the point of inflexion and F_{str}/F is the ratio of the force transmitted to the string to the force supplied by the shaker. Noting that $L_x < L_{str} - \rho < L_{str}$, the ratio F_{str}/F, which we seek to maximize, is therefore made larger if L_x is made smaller. Therefore since the length L_x will be roughly half the length of the leaf spring, the leaf spring should be kept as short as possible. To preserve the moment arm of the shaker whilst remaining sufficiently flexible, the leaf spring was made out of a 23 mm length of 19 mm $\times$ 0.5 mm spring steel.

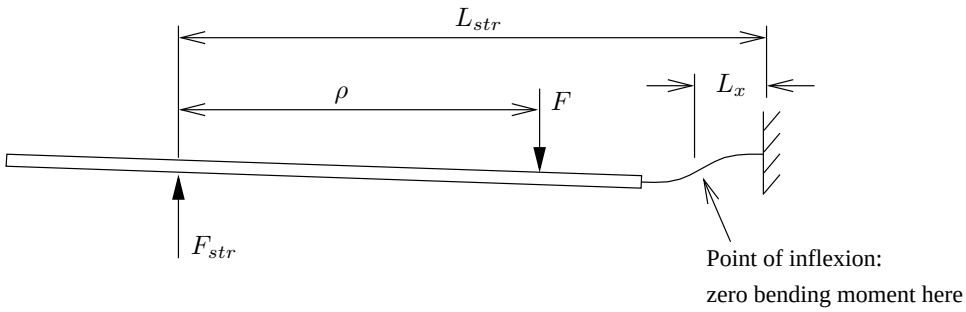

Figure 2.17: Sketch of the deflection shape of the rod and leaf spring, showing the point of inflexion. Considering torsional equilibrium about the point of inflexion, the moment arm of the shaker is $(L_{str} - \rho - L_x)$, so L_x should be kept small.

The shaker is driven by a power amplifier whose output current is proportional to its input voltage up to frequencies well beyond the bandwidth of the force controller; this proportionality, together with the linear dependence of shaker force on current, allows the use of linear feedback control (see Section 2.2.2).

SHAKER/STRAIN GAUGE/BOW MOUNTING ASSEMBLY

Another component of the bowing machine requiring special attention is the area between the leaf spring and the bow itself. This component is required to hold the bow, receive the shaker force, have strain gauges attached for force measurement, and be stiff and light to maximize the natural vibration frequencies of the cantilever system. (The natural frequencies determine the bandwidth of the force controller, so keeping them high allows quicker response times.)

In all, the design constraints for this section of the bowing machine can be summarized as follows:

- the strain gauge must be mounted between the shaker and the rod, allowing the contact force to be simply determined from the strain gauge signal using the relation to be presented in Eq. (2.7),
- the component must be flexible enough that the strain gauges give an adequately high signal-to-noise ratio,
- internal stresses of a non-linear variety such as those due to differential slipping at the edge of a clamp should be avoided, because they can affect the strain gauge signal,
- the distance from the shaker to the leaf spring must be made as long as possible to maximize the shaker's moment arm (see page 44),
- the component must be as stiff and light as possible, to keep the natural frequencies of the system as high as possible.

The design chosen to meet these criteria is shown in Figure 2.18. The component is made from high-tensile steel (heat-treated ground flat stock tool steel, conforming to BS4659 B01) in order to avoid plastic deformation and creep in the area surrounding the strain gauges. The thickness of the steel under the strain gauges is 2 mm, which was found to be as thick (and hence stiff) as possible whilst still allowing a good signal-to-noise ratio for the strain gauge signal.

Two further steps were taken to guarantee linearity (i.e. strain gauge signal $\propto$ bending moment). Firstly, the 38 mm long ($= 1.5 \times$ the width) region surrounding the strain gauges was kept bare, to allow internal stress concentrations a chance to decay away (by the St Venant effect). Secondly, excessive surface stress concentration at the join with the bow clamp were avoided by making the join there smooth.

To save weight, the size of the clamping region was minimized (its length is 40 mm), and the clamp itself was made from aluminium alloy. To additionally save weight from the point where the shaker is attached up to the point where the leaf spring is attached, the material is 3 mm thick steel or 5 mm thick aluminium, which was found to be as thin (and hence light) as possible whilst being stiff enough to keep the point of inflexion discussed on page 44 within the leaf spring.

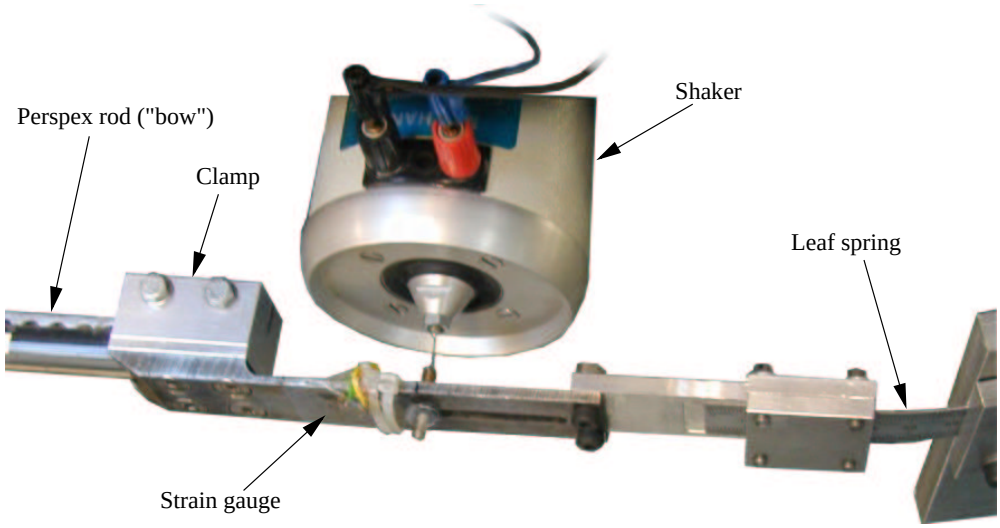

Figure 2.18: Photograph of shaker/strain gauge/bow clamp assembly; see text for details.

PERSPEX ROD ("BOW")

Most computational simulations of the bowed string have used the assumption that the bow only contacts the string at a point (rather than a finite region as would be the case for a conventional violin bow), in order to simplify the simulations. As a means of reproducing such conditions experimentally, the ordinary violin bow was replaced in the first series of experiments by a circular rod, which only contacts the string in a narrow (of the order of 0.5 mm wide) region. Perspex was used in preference to a metal for this application due to its lower thermal conductivity, necessary for the application of rosin [43, §4.2].

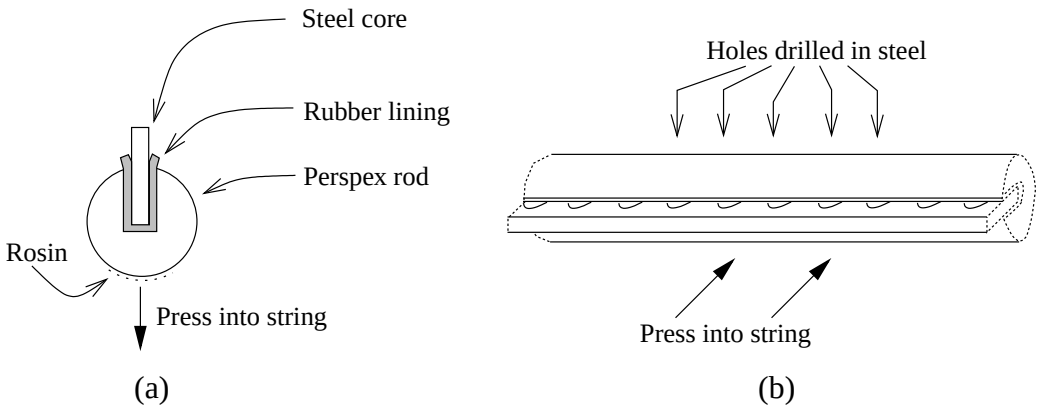

Figure 2.19: Diagram of the rod used in place of a bow: (a) drawing of cross-section (b) perspective view.

However, it was found that a plain 13 mm diameter perspex rod was too flexible, with the consequence that its natural frequencies were too low. (The natural frequencies largely determine the bandwidth of the force feedback compensator, as described in Section 2.2.2.) Hence the rod was

stiffened using a steel strip lined with rubber, as shown in Figure 2.19; the rubber absorbs some energy, thus adding damping in order to help prevent contact force fluctuations due to vibrations. In order to further raise the rod's natural frequencies, its mass was reduced by drilling holes along the length of the steel strip. The steel strip also served to prevent the rod from sagging under its own weight, as was observed with a plain perspex rod. As one might expect from Figure 2.15, any curvature in the bow will affect the distance from the bridge to the bow.

LINEAR MOTOR

To provide the back and forth movement of the bow (or perspex rod) necessary to play the violin, the rod, leaf spring and shaker are all mounted onto a linear induction motor. The advantages of using a linear induction motor over alternative methods of actuating linear motion (such as a pneumatic system or a pulley system) are that it is virtually silent when operated, as well as powerful, capable of supplying around 1 kN of thrust. The sole draw-back of linear induction motors is the "bumpiness", which is a consequence of the space (about one inch) between magnetic pole pieces of the "stator" magnet, and the finite length of the "rotor" platform. However, feedback compensation, as described in depth in this chapter and in the next, has proven sufficient for the purpose of smoothing out the motion of the motor, and hence the bow.

SAFETY PRECAUTIONS

With the delicate nature of the stringed instruments used by the bowing machine, as well as the price of them and other hardware used, several measures were taken to avoid accidental damage.

The linear motor described above can deliver up to approximately 1 kN of force, which is not only enough to crush a cello or violin, but is also enough to sever trapped cables, or to cause structural damage to the rig. It was therefore important to install bumpers (as can be seen in Fig. 2.14), particularly for those times when the position feedback controller was under development.

The shaker and the linear motor are both electromagnetic devices which can overheat if too much current is passed through them. A limit on the amount of current supplied to each was enforced within the software used for feedback control, but also an emergency power-cutout switch was embedded in each of the bumpers (also shown in Fig. 2.14).

To additionally protect the instrument being played, an extra 200 mm length of perspex was machined onto the end of the perspex rod in case the bowing machine ran past its end; in such a case, the additional perspex would keep the rod above the string, instead of allowing it to sweep below the strings. Also, the part of the bowing machine holding the bow was kept smooth on the side facing the string (for example by using countersunk Allen screws rather than ordinary screws), in case the bowing machine travelled beyond the end of the bow. These features are visible in Figures 2.14 and 2.18.

2.5 SUMMARY

A bowing machine has been constructed to play a violin or any other stringed instrument in a human-like way, using a perspex rod "bow". The use of feedback compensation was required to regulate the force with which the bow presses into the string as well as the speed with which it is drawn across the string. Having tried various standard feedback control techniques, a combination of tailor-made strategies was employed to control the bow speed and force.

Because force is not directly measurable, the force controller instead controls the signal from a strain gauge mounted near the clamp holding the bow. Demand signals for bow force are converted to demand signals for strain using measurements of the position of the bow. The task of designing a force controller was made considerably easier by modifying the dynamics of the bowing machine itself; the resulting controller has a bandwidth of about 10 Hz although its frequency response is only a second order transfer function.

The ideal speed controller for this application was found to be a quasi-PID position controller designed to simulate a tuned spring and dashpot. Digital position measurements were found to have significant advantages over analogue position measurements for this application, due to their far superior signal-to-noise ratio and their immunity to drift problems.

The capabilities of the bowing machine will be examined in the next chapter. It will be seen that the feedback controllers presented here are a good first step — indeed that they exceed the capabilities of human string players. However, various techniques will be presented which were used to boost the performance of the force and speed controllers to around the limit achievable given the hardware used.

The extra steps required to use a real bow rather than a stiffened perspex rod in the bowing machine will be described in Chapter 7.

Chapter 3

EXPERIMENT II: ANALYZING/IMPROVING PERFORMANCE

INTRODUCTION

The performance capabilities of the bowing machine described in the last chapter are studied in this chapter, and various methods which have been used to enhance them are presented. The bow speed controller is discussed first, with focus on the performance of the feedback compensator and the subsequent benefit from additional open-loop compensation and anti-windup measures. The performance of the bow/string contact force controller is then analyzed, demonstrating its sensitivity to the position of the bow (as controlled by the speed controller), and hence explaining the necessity of implementing a position predictor.

With the mechanical features and feedback controllers described in the last chapter, and the additional features mentioned above, the overall performance of the bowing machine, defined essentially as its ability to control the bow speed and force, will be shown to be easily adequate for its intended purposes.

3.1 PERFORMANCE OF SPEED CONTROLLER

The feedback compensator used to control bow position (and hence speed) was designed to mimic a spring and a dashpot; the resulting frequency response resembles that of a PID controller. From (2.5), setting $k = M\omega_n^2$ and $\lambda = 2Mc_n\omega_n$, its frequency response can be written as

$$C(j\omega) = k + \lambda j\omega \frac{\omega_c}{\omega_c + j\omega} + \frac{k_I}{j\omega}. \tag{3.1}$$

The performance of this controller is analyzed in this section, and a number of methods of improving it are presented.

3.1.1 VELOCITY AND ACCELERATION STEP RESPONSES

Computational simulations of the bowed string frequently use "switch-on transients", in which the bow starts from rest before suddenly acquiring a constant level of either velocity or acceleration. A step increase in acceleration requires the application of an (approximately) steady force, since bow acceleration is approximately proportional to the thrust provided by the linear motor (see Section 2.2.3). A step increase in velocity is however not achievable in practice, since it requires an instantaneously infinite acceleration to change velocity. The two tasks of the speed controller are therefore (1) to exactly achieve a step increase in acceleration, and (2) to get as close as possible to achieving a step increase in velocity, given the constraints of the hardware used in the bowing machine.

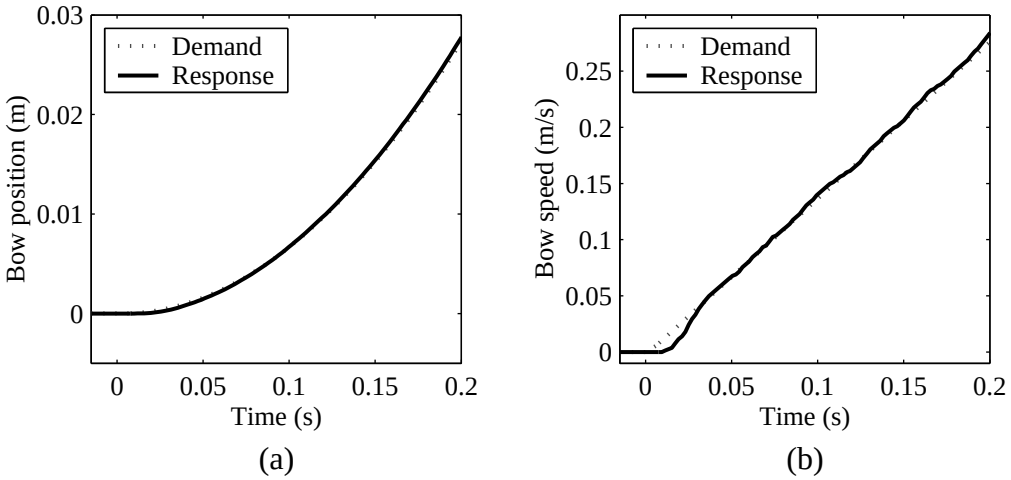

Figure 3.1: Response of the feedback controller alone to a step in the bow acceleration demand signal, whereby the bow begins accelerating from rest at a rate of 1.394 m/s^2; (b) shows the bow speed (demand and response), and (a) shows the corresponding bow position. The feedback controller is seen here, more clearly in (b) than (a), to achieve the desired bow speed after about 0.03 s.

The ability of the feedback compensator alone to actuate step changes in acceleration or velocity is demonstrated in Figures 3.1, 3.2 and 3.3. In the first of these figures, the demand signal is seen

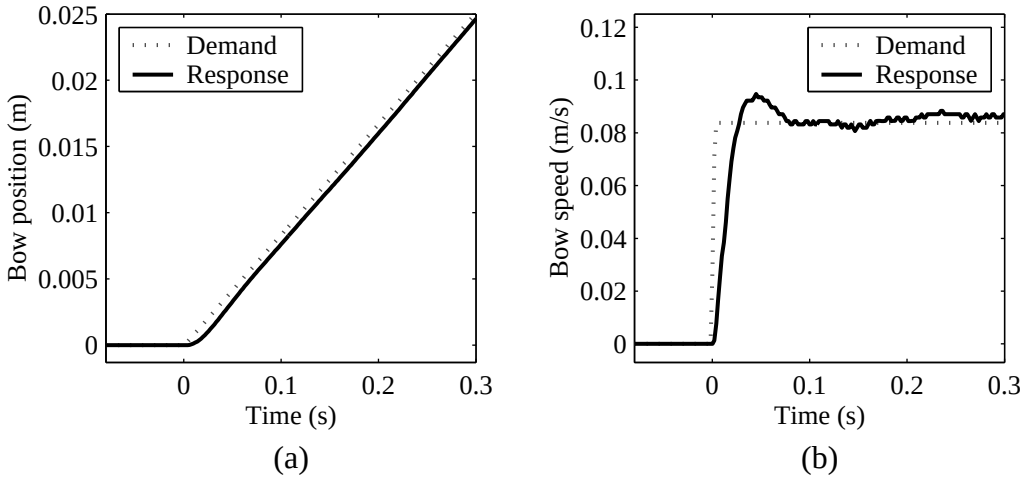

Figure 3.2: Response of the feedback controller alone to a moderate step (of 0.084 m/s) in the bow speed demand signal; (b) shows the bow speed (demand and response), and (a) shows the corresponding bow position. This figure demonstrates that the feedback controller described in the previous chapter is a good first step; it tracks the demand signal with a rise time of around 0.03 s, and over-shoots by up to 20%.

to accelerate from rest at a uniform rate of 1.394 m/s^2, with the feedback-controlled bow following with an initial delay of around 0.03 s. In Figures 3.2 and 3.3, the controller tries to actuate a step change in velocity of 0.084 m/s and 0.6 m/s respectively. In the first case (Figure 3.2), the controller takes about 0.03 s to reach its target velocity of 0.084 m/s, and then briefly overshoots this value by about 20%. This inevitable overshoot is caused by the proportional term k in (3.1) "springing" the bow forward to compensate for the initial deficit in bow position. In the second case (Figure 3.3), where the target velocity takes the more severe value of 0.6 m/s, this initial position deficit is considerably pronounced, causing an accentuated overshoot (of around 40%) in speed. This increase in position deficit occurs when the controller saturates, i.e. its output u exceeds a maximum allowable magnitude and hence is clipped; the controller outputs this maximum allowable value ($u = u_{max}$) until saturation ceases, by which time the bow has acquired too much velocity. This problem is referred to as "windup" in the feedback control literature.

In each case the feedback control is already quicker than is possible for a human violin player [74], although it is not as quick or as accurate as possible given the hardware used (comprising the digital signal processor, the linear motor and the position sensor). Various strategies have been employed to improve the performance of the speed controller:

- the values of k_I, λ, k and ω_c in Eq. (3.1) may be modified for the specific purposes of speed control and disturbance rejection,
- open-loop compensation may used to reduce the response time of the controller,
- "anti-windup" techniques may be used to reduce the effects of controller saturation.

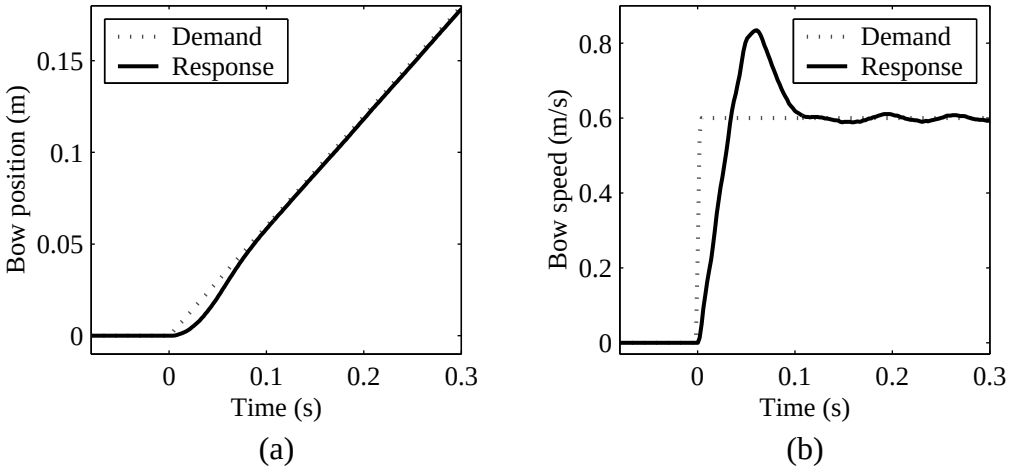

Figure 3.3: Response of the feedback controller alone to a large step (of 0.6 m/s) in the bow speed demand signal; (b) shows the bow speed (demand and response), and (a) shows the corresponding bow position. This figure demonstrates the pitfalls associated with larger step demand signals, and may be compared with Figure 3.2. Here, the feedback compensator output is greater than the maximum permissible voltage input to the linear motor in the period $0 < \text{time} < 0.05$ s, causing the controller output signal to be clipped (known as "saturation" in certain literature). The consequence in this case is the large and prolonged overshoot (up to 40%) in the bow speed, caused by the reaction of the proportional term ("virtual spring") to the resulting deficit in position. Notice in (b) the linear increase in velocity during controller saturation, corresponding to the largest achievable linear acceleration (see for example Figure 2.9), around 18 m/s^2.

3.1.2 FINE-TUNING THE EXISTING FEEDBACK CONTROLLER

SAMPLING RATE

The large bandwidth of this controller (around 100 Hz) compared with the sampling rate of the digital controller (around 500 Hz) made the controller sensitive to numerical instabilities associated with the time-stepping o.d.e. solver used by the digital signal processor. The digital signal processor stores data as single-precision floating-point data, causing larger numbers to be less precise than small numbers. This most notably affects calculations which involve the value of run-time, most notably low-pass filters with a large cut-off frequency. To combat this, allowing ω_c in Equation (3.1) to be increased, the sampling rate of the o.d.e. solver was specified as an integer power of two, namely 512 ($= 2^9$) Hz.

SPRING AND DASHPOT PARAMETERS, k AND λ

The parameters k and λ in Equation (3.1) were initially chosen to critically damp oscillations in the bow position. k and ω_c were chosen to be as large as possible given the sampling rate of the digital controller, and λ was hence chosen as $2c\sqrt{kM}$, with $c = 1$; these values were used to generate Figures 3.1, 3.2 and 3.3.

However, whilst large values of k improve the ability of the controller to reject low frequency disturbances (which are invariably present due to the non-uniformity of the radial magnetic field in the linear motor), they also increase the amount by which the bow speed overshoots its target value: this is illustrated in Figure 3.2. This is a particular drawback following periods of controller saturation (when u exceeds the maximum achievable value u_{max}) due to the associated deficit in bow position; this is illustrated by Figure 3.3. (The same conclusion is reached by considering the bow position controller to be a bow speed controller, and hence by considering the proportional term to be an integral term, with all the usual problems associated with integrator windup [72, §4.2.7].)

The value of k was therefore decreased by 20%, and the value of c was increased to 2.5, representing a 123% increase in λ. Both of these changes signify a compromise. The new value of λ is as large as possible without significantly magnifying high frequency noise — the large increase in value is made possible by the fact that the digital method of measuring position is mostly free from noise, as discussed in Section 2.3.2. The new value of k was chosen to be large enough to enable the feedback controller to reject low frequency disturbances effectively, but small enough that the overshoot in bow speed should never exceed 10%, even in the very worst case.

The controller's response to the worst case demand signal is shown in Section 3.1.5.

3.1.3 ANTI-WINDUP TECHNIQUES

Saturation ($u = u_{max}$) is inevitable when the controller is made to track large step changes in bow velocity. The integral term in the controller, $k_I/j\omega$ (see Equation (3.1)), is an obvious source of controller windup, because it needlessly continues integrating when the controller is saturated. The gain k_I was hence made variable; while the bow moves, k_I is set to zero (this makes no appreciable difference to the motion), whereas when the bow is at rest k_I is increased in order to overcome friction. (In fact, the integrator is then zeroed approximately one second before every bow stroke, to avoid low frequency offsets which would, among other things, make open-loop control more difficult.)

More subtly, however, the proportional term in the controller, k (again see Equation (3.1)), also causes windup. The reason for this, as discussed on page 52 in connection with Figure 3.3, is that the "spring action" of the controller (see Section 2.2.3) causes the bow to spring forward in response to differences between the position of the bow, ρ, and the position demand signal, r. A small difference is inevitable whenever the bow accelerates (unless open-loop control is used), but large differences arise when the controller saturates, as shown for example in Figure 3.3.

Standard techniques for dealing with controller windup problems like this, most notably the co-prime factorization approach (see for example [75]), would generally in this case cause a degradation in the performance of the feedback controller. This is because — for example in the case of a

sudden change in bow speed — they would tend to terminate the saturation before the bow speed has reached its target value, thus failing to make use of the largest possible control level u_{max}, and hence elongating the rise-time of the controller.

With the objective of controlling bow speed in mind, an ideal ad-hoc solution would be to add an offset δ to the control law which, at the moment when the bow speed reaches its target level, immediately rises from zero to the the current value of $r - \rho$, which in the time domain would be as follows:

$$u = k\,(r - \rho - \delta) + \lambda\,(\dot{r} - \dot{\rho}) \tag{3.2}$$

In this scheme, the proportional term can be thought as a spring of stiffness k which is "relaxed" at the moment when the actual bow speed equals the speed of the demand signal ($\dot{\rho} = \dot{r}$).

3.1.4 OPEN-LOOP CONTROLLER USED TO BOOST RESPONSE TIME

Although the feedback compensator used to control bow speed has a response time of only 0.03 s — representing a sufficiently high bandwidth to reject practically all disturbances — for most bowing gestures the bow speed should be under control even more quickly. The period of oscillation of a cello D-string for example is only 0.0068 s, and it has been shown that the motion of a bowed string is very sensitive to the bowing conditions inside the first few periods [52].

Open-loop control has been used as a means of achieving a nearly instantaneous step response, which in principle means guessing the value required for controller output, whilst then allowing the feedback controller to compensate if the value is not quite accurate. The open-loop and feedback controllers work in parallel, and are hence implemented as shown in Figure 3.4.

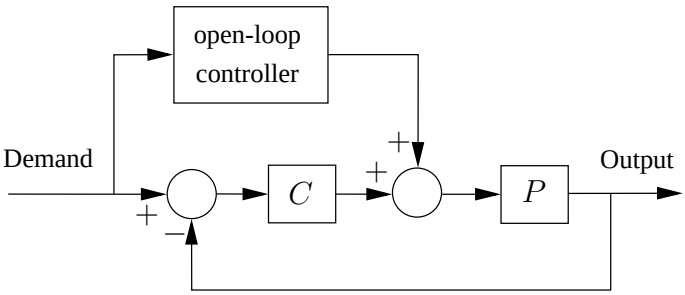

Figure 3.4: Configuration used for the open-loop speed controller: the open-loop controller and the feedback controller are implemented in parallel, such that their outputs are added before they are input to the plant.

In this case the open-loop controller design was based on the assumption that the bow assembly may be treated as a mass on wheels with some friction. Hence u_{OL}, the output from the open-loop controller, is:

$$u_{OL} = \text{offset} \times \frac{\dot{r}}{|\dot{r}|} \;+\; \text{gain} \times \ddot{r} \tag{3.3}$$

where r is the position demand signal, and "offset" and "gain" take the values 0.035 and 0.0556 respectively, based on trial and error tests. The first term in (3.3) is designed to overcome friction (modelled as Coulomb friction) and the second term accounts for the bow assembly's inertia.

It is clear from (3.3) that the open-loop controller should output a step function when actuating a step change in acceleration, and an impulse function when actuating a step change in velocity. The performance benefit of this scheme when a sudden rise in bow acceleration is required is demonstrated by Figure 3.5, in which open-loop compensation is seen to practically eliminate the initial time delay associated with the finite bandwidth of the feedback controller.

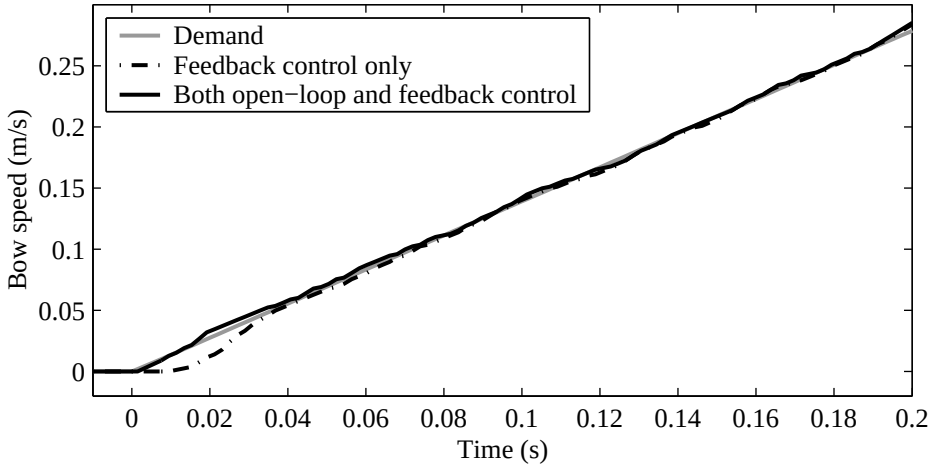

Figure 3.5: The effect of combining open-loop compensation with the feedback control already in place. In this figure the demand signal for the position controller is such that velocity increases linearly with time at a rate of 1.394 m/s^2 (as shown); the response is shown both with and without open-loop control. The difference between the two cases is evidenced by the response at time < 0.04 s: open-loop control has eliminated the time lag in the response.

When the controller is required to actuate a sudden change in bow speed however, implementing open-loop compensation is more complicated. In principle, the open-loop compensator should output a very large value for a very short period of time, because the sudden change in momentum requires an impulsive force. Due to the finite bandwidth of the controller, the limits on how much force the linear motor can exert and the risks associated with inductive surges in the motor, this is not possible in practice.

A close approximation to an impulse function, given these constraints, is shown in Figure 3.6(a), whereby the impulse is spread over roughly 0.01 s. Letting the output of the open-loop controller take this form, centered over time $t = 0$, the step response of the controller is modified to look like Figure 3.7, which should be compared with the response to the same demand signal without open-loop compensation in Figure 3.2. Several features of Figure 3.7 are notable: Firstly, the bow speed can be seen to increase at almost exactly the same time as the demand signal (at $t = 0$), thus eliminating the previous time lag. Secondly, the rise in bow speed is quicker than it was in Figure

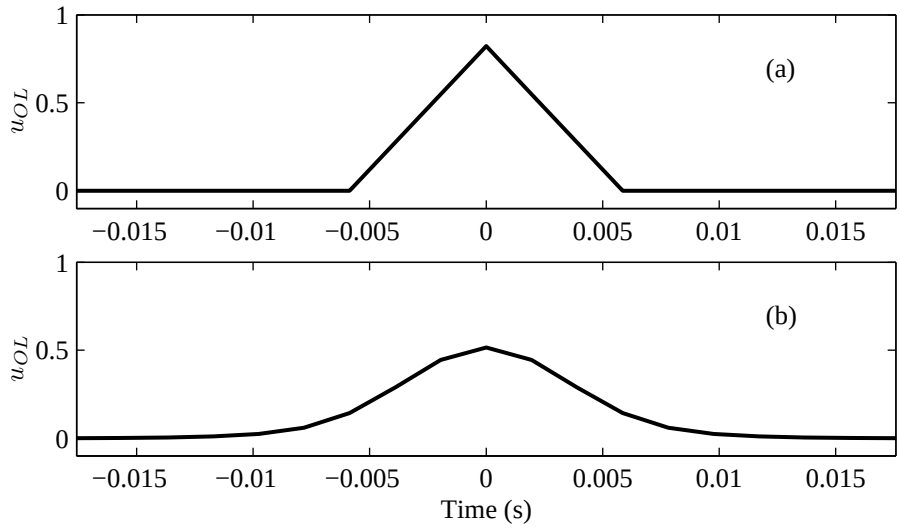

Figure 3.6: Two alternative quasi-impulse functions used by open-loop controller to actuate a rapid change in bow velocity. The triangular function in the top plot was used to produce Figure 3.7, before the more rounded function in the bottom plot was used to produce Figure 3.8; the bottom function is a low-pass filtered version of the top function.

3.2. Thirdly, the abruptness of the open-loop controller output (seen in Figure 3.6(a)) causes a high frequency mode of the experimental rig to be excited (at roughly 75 Hz). Of these three new features of the step response, the first two are desirable, but the third is undesirable.

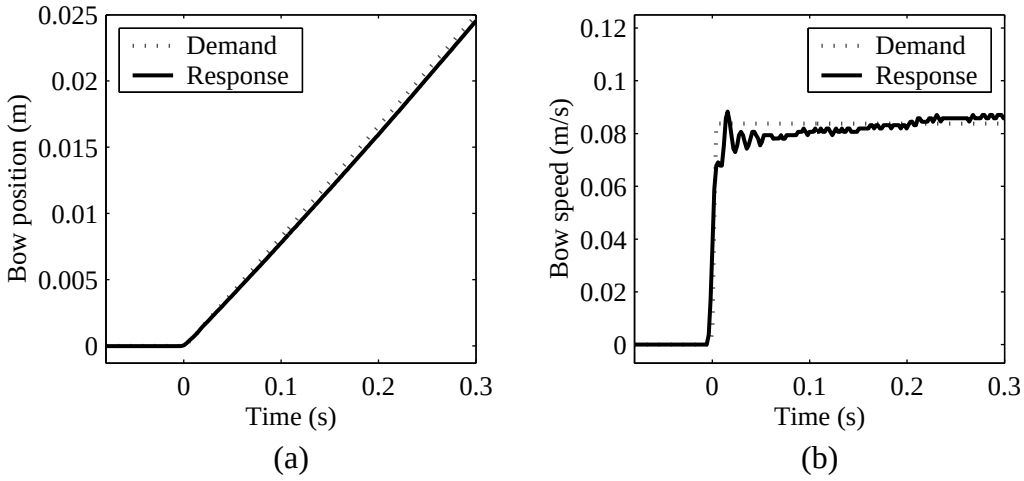

Figure 3.7: Response to a step of 0.084 m/s in the demand signal — as in Figure 3.2 — with open-loop compensation given by Figure 3.6(a). Although this open-loop control strategy is seen here to quicken the step response, it also causes a high frequency mode of the experimental rig to be visibly excited.

A compromise was found by rounding off the open-loop controller output as shown in Figure 3.6(b), by passing it through a low-pass filter (although care was taken to keep it symmetrical

about $t = 0$. The resulting step response is shown in Figure 3.8; the removal of high frequency content from u_{OL} has slightly slowed the rate at which the speed reaches its target value, but the high frequency mode is no longer significantly excited. With this open-loop controller, the time taken to change speeds is hence only 0.01 s, which is of the order of a tenth of the time taken by a human to do the same [74].

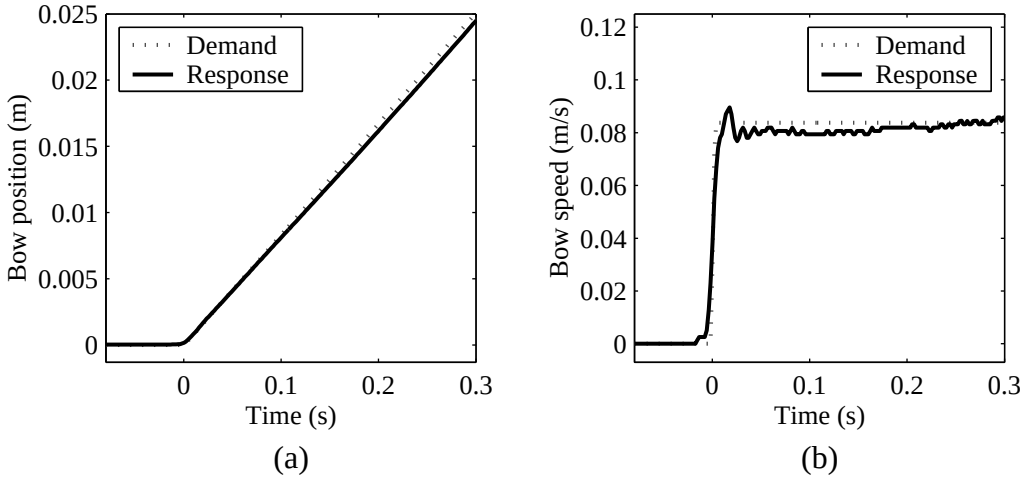

Figure 3.8: Same as Figure 3.7, but with less high frequency content in the open-loop controller output; the open-loop compensation is now based on Figure 3.6(b). The rise time of the controller is essentially preserved, but the high frequency vibration visible in Figure 3.7 has been suppressed.

It is noted that the output from the feedback controller was scaled down when the open-loop controller was active, by an amount proportional to u_{OL}, in the cases where the controller was required to actuate a sudden change in bow speed. "Turning down" the feedback controller was necessary in these cases because the feedback controller otherwise resists the open-loop controller, particularly when u_{OL} starts before time $t = 0$ (as shown for example in Figure 3.6).

3.1.5 THE WORST CASE

The most difficult type of demand signal for the speed controller to follow is a jump in bow speed, and the largest amount of bow speed is determined by the ratio of the length of the bow to the time needed to take meaningful measurements. Given the geometry of this problem, and the nature of the measurements taken, the largest jump in bow speed that the bowing machine would be expected to achieve is 0.6 m/s.

The electric motor used to actuate bow motion can deliver enough force to accelerate the bow at a rate of up to 18 m/s^2, and the controller has a rise time of around 0.01 s, which means that the controller will saturate for speeds greater than approximately 0.18 m/s. The largest required bow

speed, 0.6 m/s, will certainly therefore cause saturation, and it was proposed in Section 3.1.2 that even under these circumstances the bow speed should not overshoot by more than 10%.

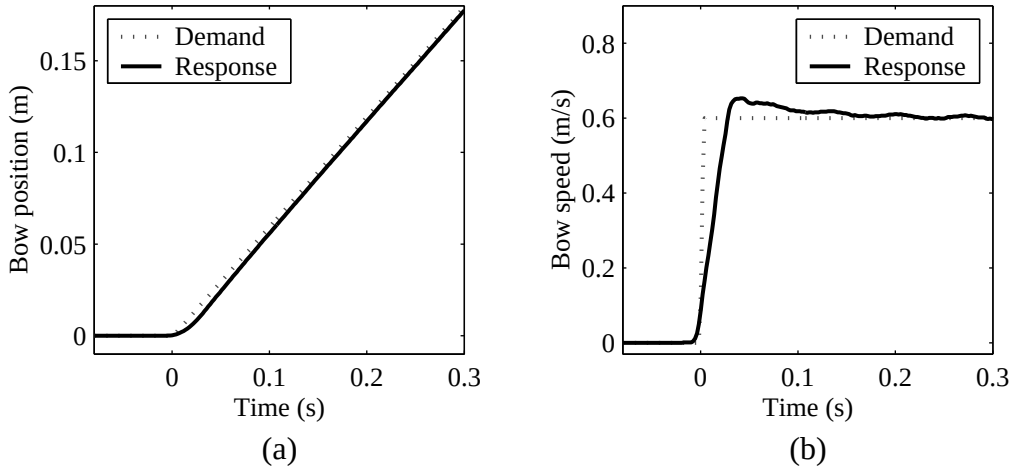

Figure 3.9: Response of the modified controller, including open-loop and feedback compensation, to a large step (of 0.6 m/s) in the bow speed demand signal; (b) shows the bow speed (both demand and response), and (a) shows the corresponding bow position. This figure represents the worst case scenario for the bowing machine, since a jump of 0.6 m/s is the most demanding possible demand signal. Comparison with Figure 3.3 reveals the effectiveness of the measures described to improve upon the feedback controller described in the previous chapter; the rise time is now quicker, and the overshoot is far smaller.

The response of the bowing machine to this most extreme demand signal is shown in Figure 3.9. It shows a period of saturation of around 0.03 s, followed by an overshoot in velocity of 8.8%, which is within the target set in Section 3.1.2.

3.2 PERFORMANCE OF FORCE CONTROLLER

The resonant frequencies of the perspex rod (used in place of a bow) were raised by maximizing its stiffness and lowering its inertia, under the premise that the feedback controller used to govern the bow-string contact force could thus be simplified. The performance capabilities of the resulting design are examined in this chapter. It will be seen that the force controller is affected by rapid changes in bow position, although measures are presented which were used to combat this effect.

3.2.1 FORCE CONTROLLER STEP RESPONSE

A measure of the performance of the feedback compensator used to control bow force is the closed loop step response. A force transducer was constructed to directly measure the bow force especially for this purpose, to confirm the indirect measurements from the strain gauges in the bow assembly. The force transducer, positioned temporarily in the place of the violin or cello, was designed such

that its output signal was proportional to normal force but independent of tangential components of bow force; a diagram of this force transducer is shown in Figure 3.10.

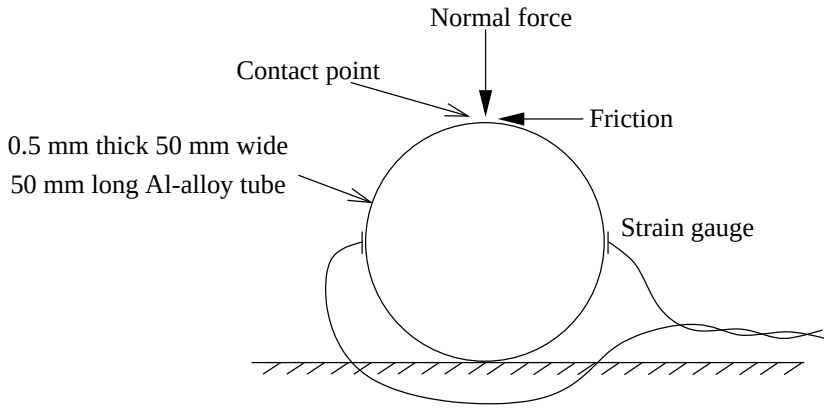

Figure 3.10: Force transducer used to validate the force controller, consisting of a thin-walled aluminium tube with strain gauges. The position of the strain gauges and the aspect ratio of the tube allow the gauges to be connected together in such a way that only normal forces, and not tangential forces, influence the measurement. This force transducer is used in the place of the violin (or cello), to validate indirect measurements of the force controller.

Figure 3.11 shows the step response of the force controller, measured firstly using the force transducer, and secondly using the indirect method described by Equation (2.7). Both measurements agree with each other, suggesting that Equation (2.7) is sufficiently accurate for monitoring the bow/string contact force. The response time of the feedback controller is, from Figure 3.11, approximately 0.1 s.

3.2.2 MAINTAINING CONSTANT FORCE DURING POSITION VARIATION

The purpose of the force controller is to calculate the appropriate level of strain gauge signal at the current contact location for the required level of bow/string contact force using Equation (2.7), and to use feedback control to ensure that the strain matches this demand. Recalling that the amount of strain required is inversely proportional to the distance, ρ, from the strain gauge to the string, as the bow is moved in the "down-bow" direction (i.e. ρ increasing) the strain must increase. Inevitably, the finite bandwidth of the feedback loop means that there is a delay when responding to changes in contact location; hence a gradual increase in ρ would lead to a deficit in contact force, and vice versa. The extent, Δ, of this time delay can be shown [72, §4.3.1] to be

$$\Delta = \frac{1}{\lim\limits_{\omega \to 0} \big(j\omega P(j\omega) C(j\omega) \big)}, \tag{3.4}$$

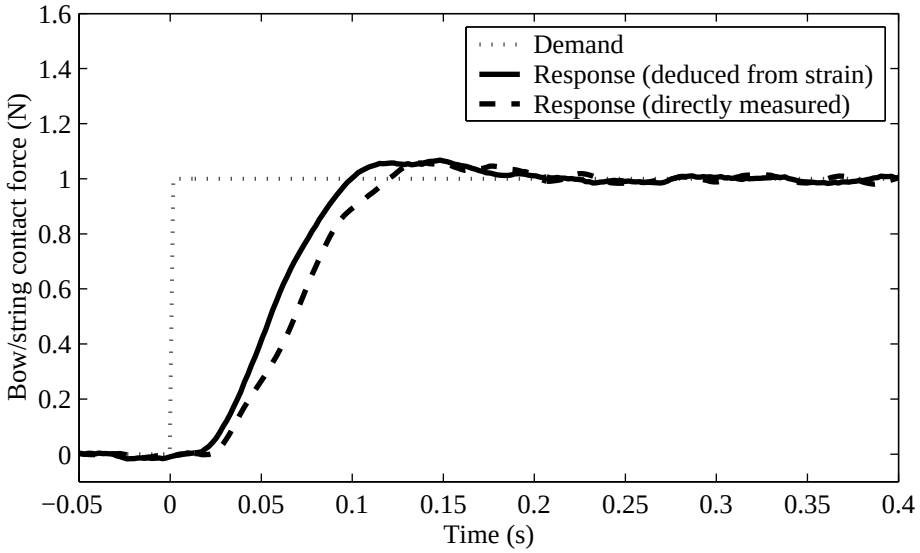

Figure 3.11: Step response of the feedback compensator used to control the bow/string contact force. The demand signal and the response (both directly measured using the force transducer described in Figure 3.10 and deduced using Equation (2.7)) are shown. The response time of the force controller, apparent from both measurements, is approximately 0.1 s.

which in this case (see Section 2.2.2) equals 0.044 ± 0.005 s. For the case where the force demand signal, r, is constant, the block diagram in Figure 2.8 can be used to show that

$$\frac{\text{normal force}}{\text{demand signal}} = \frac{N(t)}{r} \approx \frac{\rho(t-\Delta)}{\rho(t)} \approx \frac{\rho(t) - \dot{\rho}\Delta}{\rho(t)}, \tag{3.5}$$

where $\rho(t)$ is the distance from the contact point to the strain gauge at time t. So for example if $\rho(t) = 0.25$ m and $\dot{\rho} = 0.2$ m/s, then $N(t)/r = 0.965 \pm 0.004$, suggesting that one might expect an error of approximately 3.5%.

The actual situation is shown in Figure 3.12, which shows the bow force (deduced using Equation (2.7)) as the bow accelerates from rest at a rate of 2.71 m/s^2, alongside the predictions of Equation (3.5). The time-lag model predicts the correct trend, and correct order-of-magnitude values, for the deficit in bow force caused by the "down-bow". (The minor differences between prediction and measurement in Figure 3.12 arise from the fact that Equation (3.5) strictly only applies when $\frac{d^2}{dt^2}(\textit{strain demand signal}) \ll \frac{d}{dt}(\textit{strain demand signal})/\Delta$, i.e. when $\ddot{\rho} \ll \dot{\rho}/\Delta$, as well as the severity of the acceleration (2.71 m/s^2 is considered large), which causes the first mode of vibration of the perspex rod to be slightly excited.)

USING POSITION PREDICTIONS TO IMPROVE FORCE CONTROL

To counter-balance the delay associated with the feedback loop and thereby hold the force constant in the face of position variation, we can predict the position of the bow when calculating the strain

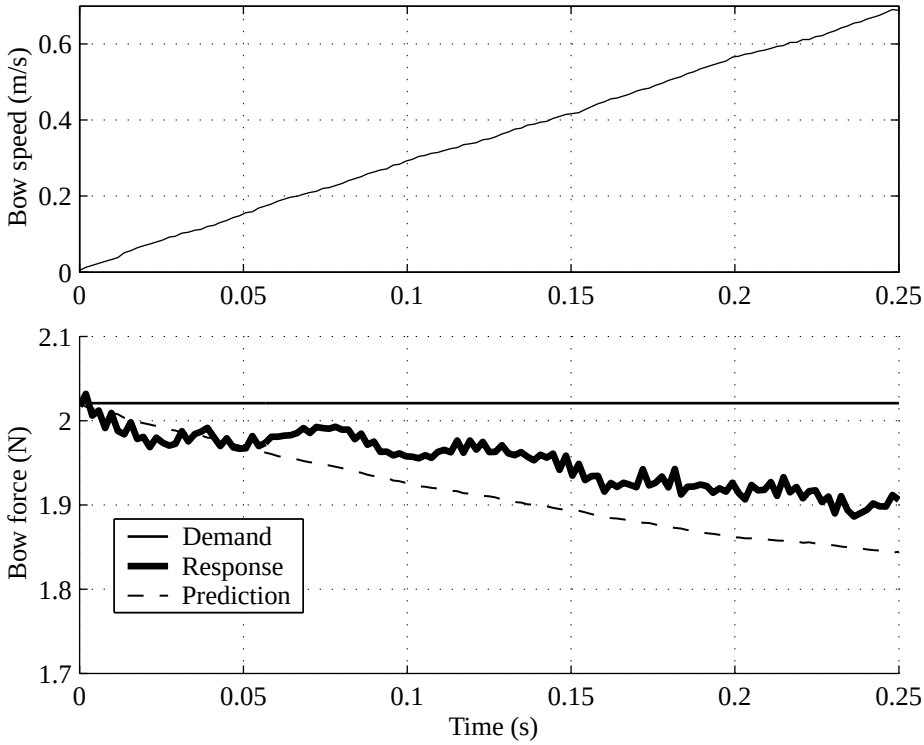

Figure 3.12: The effect of bow speed (top plot) on the bow/string contact force (bottom plot) when only the feedback controller of page 37 is used to control force; the finite bandwidth (and hence time delay) of the feedback controller is apparent from the error in contact force at larger bow speeds. Note, bow force in this figure is calculated from the strain gauge signal using Equation (2.7), which applies for frequencies below the first natural frequency of the rod. The predicted bow force is calculated using Equation (3.5), which is seen in this figure to adequately describe the effect of contact position on bow force.

demand signal. Position can be readily predicted, since it is actively controlled using the same digital signal processor as force; hence we can calculate the strain demand signal based on the bow's position a time Δ_p in the future. It was found that replacing $\rho(t)$ in Equation (2.7) with a first order Taylor expansion for $\rho(t+\Delta_p)$, i.e. $\rho+\dot{\rho}\Delta_p$, was a sufficiently effective method of executing this strategy.

Figure 3.13 shows the improvement in performance caused by implementing this scheme for three different values of Δ_p, with the case $\Delta_p = 0$ (as in Figure 3.12) included for reference. As expected, increasing Δ_p reduces the deficit in contact force until, for values greater than around 0.1, the deficit is reversed and becomes an surplus. Following trial and error tests under a range of conditions, the value $\Delta_p = 0.06$ s was chosen for the final design. The resulting percentage error in bow force with this value was found to remain less than approximately 0.2% for all of the operating conditions used in subsequent experimental work.

The resulting level of performance is within the standards set by solutions to similar problems in the control literature [67, Fig.13(a)], and satisfies the overall objectives of Section 2.2.1.

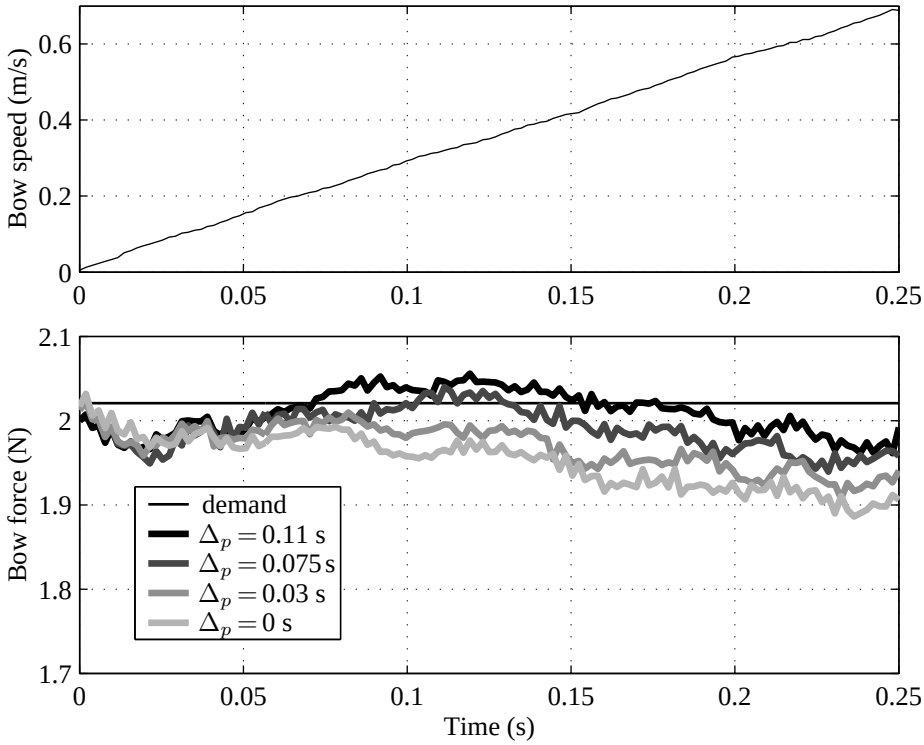

Figure 3.13: Demonstration of the strategy used to nullify the effect of position variation (top) on bow/string contact force (bottom), for three non-zero values of Δ_p. Setting $\Delta_p = 0.06$ s was found to be the best compromise under a wide range of conditions. In this figure as in Figure 3.12, contact force was deduced from the strain gauge signal using Equation (2.7).

3.3 SUMMARY: COMBINED PERFORMANCE

The performance of the bowing machine's feedback controllers, one to control the bow/string normal contact force, the other to control the bow speed, has been studied in this chapter. Although they alone already control the bow as quickly and accurately as a human string player, the hardware used by the bowing machine is theoretically capable of an even higher level of performance.

Various ad-hoc strategies have been employed to boost the performance of the speed and force controllers. To improve speed control, an open-loop controller was implemented in parallel with the existing feedback controller, measures were taken to limit the effects of controller windup, and the feedback controller was modified to reflect a compromise between bandwidth and disturbance rejection. To improve bow/string force control, a pre-compensator was implemented which anticipates the demand signal by an amount associated with the time delay of the controller.

The bowing machine should ideally be able to execute the same bowing gestures that computational simulations have been based on. Traditionally the bow velocity and bow/string contact force have been assumed to "switch on", with the string initially at rest; in practice this requires the speed to increase suddenly from zero. With the feedback compensators described in the previous chapter,

and the various additional strategies described in this chapter, the bowing machine has been shown to be capable of changing the bow speed in around 0.01 s, which is of the order of a single period of transverse string vibration, and very close to the limit of what is possible given the hardware used by the bowing machine. The more recently popular "constant acceleration bowing gesture" is naturally easier to execute in practice, and has been shown to be readily achievable by the bowing machine.

Applications of this bowing machine are numerous, ranging from theory validation studies to sophisticated playability measurements. In the next chapter, a wide range of measurements made using this machine will be presented, that will subsequently be compared with the nominally similar simulation results.

Chapter 4

EXPERIMENTS WITH RIGID POINT BOW

INTRODUCTION

Experimental results are presented in this chapter, which are intended to demonstrate the general vibrational behaviour of the string when it is bowed by the automatic bowing machine, with a perspex rod in place of a bow.

Following a description of the method used to acquire and process experimental data, measurements of the range of bowing gestures that lead to the production of Helmholtz motion are presented. These include the first ever experimental measurements of a "Schelleng diagram" (see page 20) and of a "Guettler diagram" (i.e. a plot of pre-Helmholtz motion delay in the bow force vs. acceleration plane — see page 21), and a map of vibration waveform in the bow force vs. bow velocity plane. To probe at the detailed behaviour of the bowed string, several individual string vibration measurements are presented and analyzed.

All experimental results in this chapter were measured with the bow replaced by the stiffened perspex rod, as described on page 47. Correspondingly, the nominally similar simulations presented in the next chapter ignore the effects of the finite width and compliance of ribbons of bow hair. This simplifying assumption is abandoned in Chapter 7, in which the same experiments are repeated with a real bow.

4.1 EXPERIMENTAL SETUP

The method of using the automatic bowing machine to investigate the transient vibration of the string is described in this section. All results in this chapter were generated with the perspex rod described on page 47 in place of an actual bow, to achieve the "rigid point contact" model used in most previous simulations; as such, effects caused by the finite width and compliance of bow hair can be ignored.

DESCRIPTION OF CELLO AND STRING USED IN EXPERIMENT

The bowing machine described in previous chapters can play any member of the stringed instrument family including violins, violas or cellos. A full-sized cello (with a flat metal wrapped stranded nylon core Thomastik "Dominant" D string in particular) was chosen for use in the bowing machine for three reasons:

(1) The comparatively large size of cellos makes the spatial tolerance of, for example, the distance from the bow to the bridge greater than it would be for a violin.

(2) Cello strings vibrate at a lower frequency than violin strings, allowing the bandwidth of the data acquisition hardware used to record the vibration of the string to be be lower.

(3) The torsional and transverse impedances, wave speeds and damping factors of a Thomastik "Dominant" cello D-string were measured by past researchers [21, 27]; this data can be used by simulations of the bowed string designed to be as similar to experiment as possible.

The cello is supported by a steel and wooden frame, with foam pads to simulate a player's knees as shown in Figure 4.1; the cello is thus held in roughly the same way as it would be by a human cello player. The cello can be rotated in the frame in order to present the required string for bowing, and moved vertically using screw jacks in order that the bow meets the string at the required distance from the bridge (hence fixing β). The bow-bridge distance can be adjusted to within approximately ± 0.5 mm, such that all recorded values of β are accurate to within ± 0.0007. When in use, the cello is aligned such that its strings are perpendicular to the plane containing the bow speed and normal force vectors.

METHOD OF APPLICATION OF ROSIN

The results in this chapter were generated with a perspex rod used in place of a conventional bow. The rod was rosined by rubbing it with a block of rosin with a semi-cylindrical groove cut along its length to fit the outside of the rod. It was found that the rubbing action was sufficient on its own to transfer a layer of rosin onto the surface of the rod, as it would be with an ordinary bow. Following a fresh coating of rosin, it was found that two or three minutes of long bow strokes was sufficient

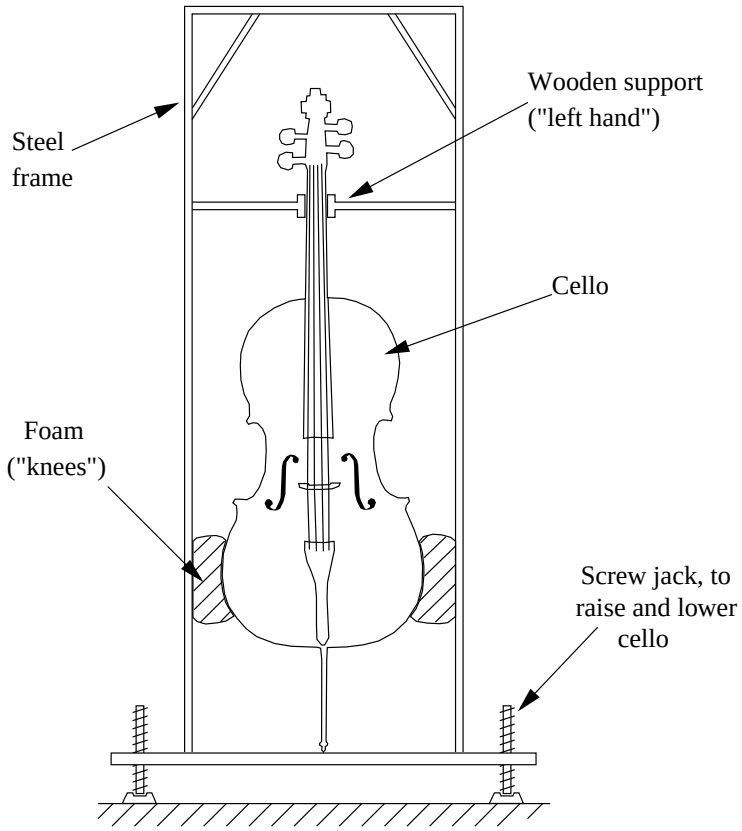

Figure 4.1: Diagram of the apparatus used to hold the cello as it is played. The configuration of the bowing machine relative to the cello is shown in Figure 2.15.

to "play in" the new rosin: the contact between the rod and the string leaves a visible track along the rod, approximately 0.5 mm wide, which has less rosin than the rest of the surface of the rod. The rosin used in all experiments described in this chapter is Hidersine "Junior" Violin Rosin, No. 12 V.

4.2 BRIDGE FORCE MEASUREMENT

The vibration response of the bowed string was measured using a piezo-electric force transducer located in the bridge under the string (after Reinicke [9]). The piezo-electric crystals are aligned such that they are only sensitive to the component of the string's tension in the transverse direction, as illustrated in Figure 4.2. This quantity, referred to as the "bridge force", is intuitively important because it is this time-varying force that excites the bridge, and in turn the body of the instrument, to produce sound waves. (The strings themselves act as dipoles and are narrow compared to the wavelength of the sound waves of relevant frequency, and are hence virtually silent). Also, each vibration regime (e.g. Helmholtz motion or double slipping motion) causes a unique pattern in the bridge force waveform, making it possible to detect whether or not Helmholtz motion has been

achieved at any given instant: these unique patterns will be reviewed in the next section.

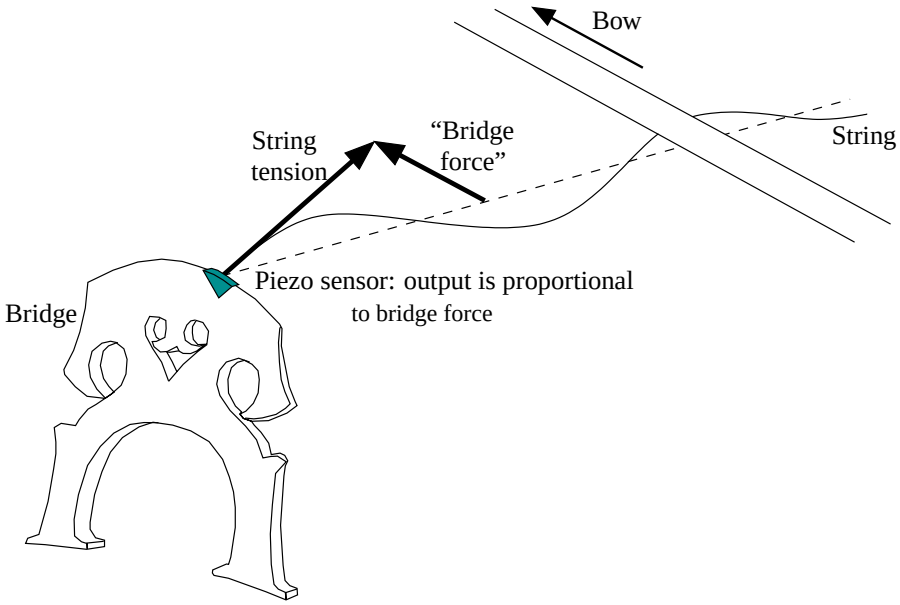

Figure 4.2: Piezo-electric force transducer mounted in the bridge of the cello; the piezo-electric crystals are aligned such that only the component of the string's tension in the transverse direction parallel to the bow, the "bridge force", is detected.

The output from the piezo-electric sensor is fed to a Birchall CA/04/NH charge amplifier with a low-pass cut-off frequency 0.53 Hz (measured) and a high-pass cut-off frequency 100 kHz (as quoted by the manufacturer). The mass of the sensor is sufficiently small that its effect on the vibration of the bridge (and the string) may be ignored.

4.2.1 DATA ACQUISITION

Bridge force data, after being amplified by the charge amplifier, was input to a PC using a NI 6024E data acquisition device. The sampling rate for all measurements was 10 kHz, except for those shown in Figure 4.34, where in order to capture some very fine details it was 160 kHz. The analog-to-digital converter of the data acquisition device allowed bridge force to be measured in steps of 0.009 N. The NI 6024E device gathers data into a circular buffer, allowing the timing of each measurement to be coordinated with the bowing machine using a pre-triggering technique: each time the bowing machine begins a bowing gesture, it sends a trigger signal to the data acquisition system, which records and saves the bridge force for 0.25 s following the trigger, and saves the bridge force that it had recorded during the 0.1 s preceding the trigger.

MAINS ELECTRICITY PICKUP

In cases where the trigger pulse coincides with the start of the string motion, the bridge force acquired during the 0.1 s preceding the trigger is theoretically zero. In practice however, the bridge force is subject to mains electricity leakage, appearing equally in the portions of bridge force before and after the trigger pulse. Hence, the extent of the mains electricity leakage is measured in the 0.1 s of pre-trigger data as a periodic disturbance whose fundamental frequency is 50 Hz. The result is then subtracted from the rest of the bridge force data after the trigger pulse.

It is noted, however, that this technique is only feasible in cases where the string is at rest before the trigger pulse; it was therefore used in all of the measurements presented in Sections 4.3.2 and 4.3.3, but in none of the measurements presented in Section 4.3.1.

RESET POSITION OF STRING BEFORE MEASUREMENT

Virtually all simulations assume that the string has no displacement at the start of every bowing gesture. In practice however, the bowing machine pulls the string aside as it moves into the required starting position for each measurement. Hence, each time the bow reaches the relevant starting position, it is lifted off the string for a half of a second, giving the string a chance to spring back to its equilibrium position. After placing the bow back on the string, the bowing machine waits for a period of around five or ten seconds before starting the next bowing gesture. This is for two reasons: it allows enough time for the PC to finish processing the data from the previous measurement, and it ensures that the bow has had time to come to rest after being lifted off the string, as the bow often bounces slightly after being placed back on the string.

4.2.2 BRIDGE FORCE "SIGNATURE" WAVEFORMS

Before describing the algorithm used to measure the time taken to produce Helmholtz motion, it is helpful to review the different types of motion which can occur, and their distinctive appearances in the bridge force signal. The list below summarizes the most common types of motion, corresponding to the plots of bridge force shown in Figures 4.3 (a)–(f):

Helmholtz motion: One slip per period, corresponding to a single "Helmholtz corner" travelling back and forth along the string (see Figure 1.1). Whenever the Helmholtz corner reflects from the bridge, the bridge force abruptly drops, following which it gradually rises back up again (c.f. also Figure 4.2). Hence, the bridge force waveform associated with Helmholtz motion is a saw-tooth wave.

Multiple slipping motion: More than one slip per period, equivalent to multiple Helmholtz motions superimposed on each other; hence there are multiple "Helmholtz corners" travelling

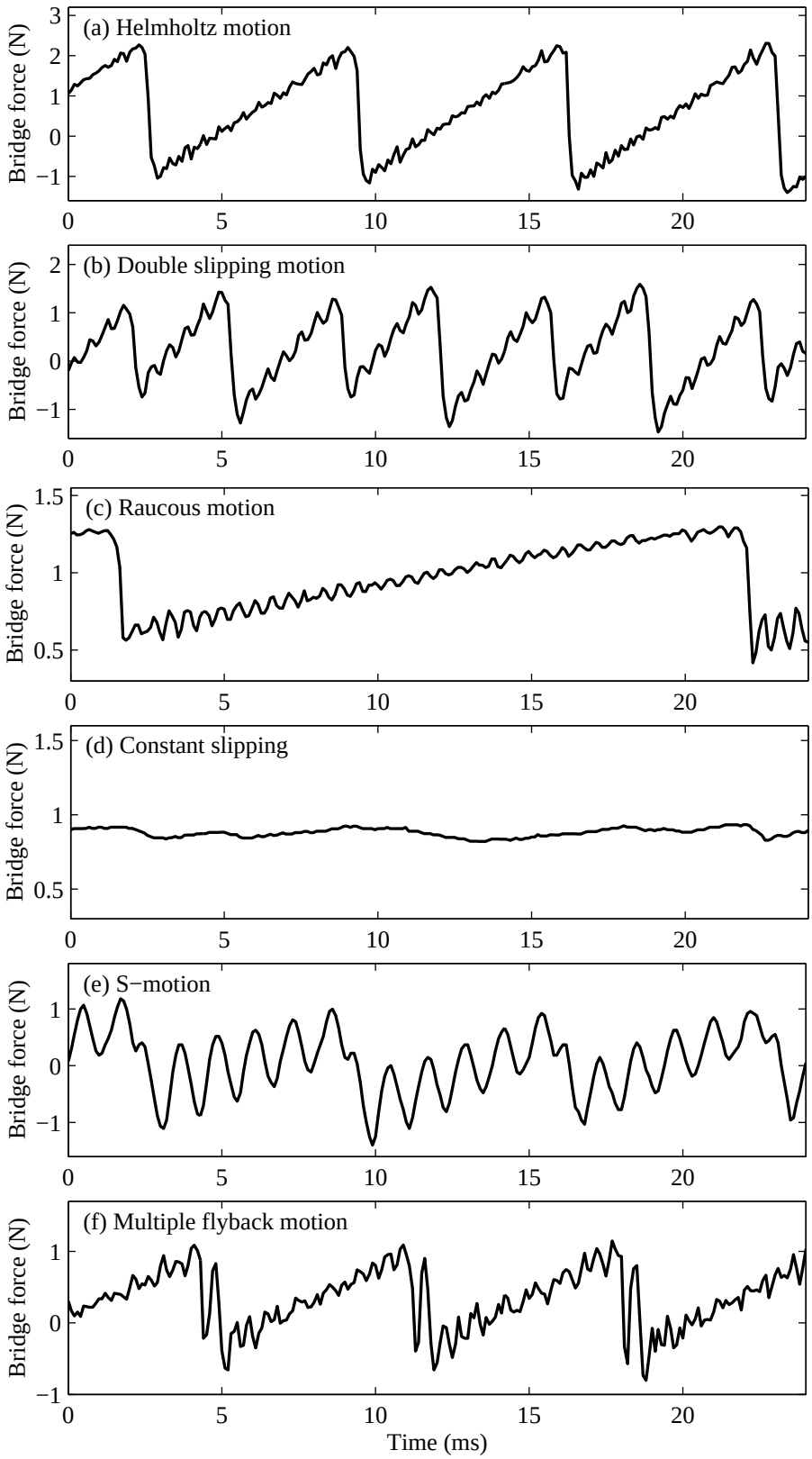

Figure 4.3: Typical examples of the six most common types of motion seen in experiment. (a) Helmholtz motion manifests itself as a saw-tooth wave; (b) double slipping motion as a double saw-tooth wave; (c) raucous motion as a prolonged or irregular saw-tooth wave; (d) constant slipping as a generally flat and featureless signal; e) S-motion as very large ripples superimposed on a saw-tooth wave; and (f) multiple flyback motion as a saw-tooth wave with two (or sometimes more) flybacks. The horizontal scales of the above plots are the same, although the vertical scales are not. "Schelleng ripples" [16, §II.J], of period βT, can be seen for example in (b), in which $\beta T = 0.544$ ms.

back and forth along the string. When each corner reflects from the bridge, it causes the bridge force to abruptly drop, and hence the resulting motion is a "multiple saw-tooth wave". Double slipping is one example of multiple slipping.

Raucous motion: Non-periodic motion, in which the Helmholtz corner is prevented from smoothly passing the bowing point due to an excessive bow force. The bridge force waveform associated with raucous motion is an elongated and enlarged, and usually irregular, saw-tooth wave. Occasionally the bow force falls within a certain range whereby the Helmholtz corner repeatedly passes the bow at the second attempt; i.e. it reflects back towards the finger the first time it meets the bow, but is sufficiently strong to induce slipping (and hence pass the bow) when it next reaches the bow. Such cases have been classified as "Anomalous Low Frequency" motion [76, 77] (see also [78, Fig.T14]), since the stick-slip triggering is periodic but less frequent than it would be for Helmholtz motion.

Constant slipping motion: Complete absence of sticking, which occurs when the bow force is very low.

S-motion: One stick and slip per period (as with Helmholtz motion) and hence one main Helmholtz corner, but with large ripples also present on the string. These ripples typically exist only when the bow is placed near a nodal point of one of the first few modes of the string — hence β must be approximately an integer ratio [60, 79]. If the bow is placed near a nodal point of the n^{th} transverse mode of the string, then the ripples will comprise contributions from the n^{th}, $2n^{\text{th}}$, $3n^{\text{th}}$, etc. harmonics of the string. It can be shown [60, 79] that this motion is equivalent to the presence of $n+1$ Helmholtz corners, and hence equivalent to one of Raman's "higher types" [2].

Multiple flyback motion: Two sticks and slips per period, but three Helmholtz corners instead of two, where all three corners are of the same magnitude, but where the middle corner is of the opposite sign as the outer two. The time delay between the first and second corners, and between the second and third corners, is $\beta T/2$. Hence the string deforms into a "W" shape rather than the "V" shape associated with Helmholtz motion. With this arrangement, the first corner induces slipping when it passes the bowing point travelling towards the bridge, whereas the second corner (of opposite sign) induces sticking when it passes the bowing point travelling towards the bridge. The third corner meets the bowing point travelling towards the bridge as the first corner meets the bowing point having just reflected from the bridge, and so the first and third waves cancel each other out at the bowing point and reflect from the bow. The state of sticking is hence preserved, until the second wave reflects from the bridge and passes the bowing point; the string continues to slip until the third wave has also passed the bowing point, having now reflected twice from the bridge. This general pattern is best understood by considering a space-time diagram, as illustrated by McIntyre and Woodhouse [50]. A similar pattern occurs when there are five or seven corners of equal magnitude and alternating sign, separated by a time lag of $\beta T/2$, with the outer pairs always responsible for causing the string to slip; in all such cases there are only two sticks and slips per period.

An illustrative example of the bridge force waveform corresponding to each of the above types of motion is shown in Figure 4.3. The upwards-sloping portions of bridge force in the first three, corresponding to episodes of sticking, can be shown [22, §3.4] to increase at a nominal rate of $2v_bZ_T/\beta T$ Newtons per second, where Z_T is the transverse impedance of the string (equal to the square root of the product of string tension and mass per unit length). "Schelleng's ripples" [16, §II.J] are evident in Figures 4.3(a)–(c); they are the result of vibration of the portion of string between the bow and the bridge during sticking [22, Fig.6.8].

Although there are other types of motion not mentioned above which exist (such as "Helmholtz crumples" [2] or "whistling" [80]), those which are most commonly seen in experiment are listed above. Indeed, the automatic pattern recognition algorithm described in the next section only looks for these five types of motion.

4.2.3 STRING VIBRATION WAVEFORM IDENTIFICATION ALGORITHM

Clearly, the bridge force waveforms associated with each of the types of motion listed above are distinctive, and it is nearly always possible to judge which motion has occurred by simply looking at the bridge force with the naked eye. However, to ensure that the same judgement is made for both simulated and experimental waveforms, an automatic pattern recognition algorithm has been developed, based on the algorithm described by Woodhouse [21, App.]. The procedure for evaluating the type of motion is essentially as follows:

- The rate of increase of the bridge force during sticking is proportional to bow speed, $v_b(t)$, and so to normalize the bridge force, it is firstly scaled by a factor $v_{\text{known}}/v_b(t)$, where v_{known} is a known velocity (say 1 m/s); all upwards-sloping regions of bridge force subsequently have the same slope, $2\,v_{\text{known}}Z_T/\beta T$.

- The function $(2\,v_{\text{known}}Z_T/\beta T) \times t$ is subtracted from the bridge force, to make the regions corresponding to episodes of sticking horizontal instead of upwards-sloping; the resulting waveform resembles a "staircase". The grey line in Figure 4.4(a) shows a typical example.

- The possibility of S-motion is accounted for at this point by searching for any instances where the bridge force rapidly rises back up again after having fallen. Noting the difference between Figures 4.3(a) and 4.3(e), S-motion causes the staircase-like function to periodically rise and fall in between times of slips (or "steps" in the staircase).

- To reduce the magnitude of the Schelleng ripples, the staircase-like signal is digitally filtered using a rectangular filter, whose duration, βT, is theoretically the same as one Schelleng ripple. Thus, the new signal is the average of the old signal over the last βT seconds, so as to produce a smoothed version of the "staircase" waveform. The black line in Figure 4.4(a) shows a typical example, which can be compared with the accompanying grey line.

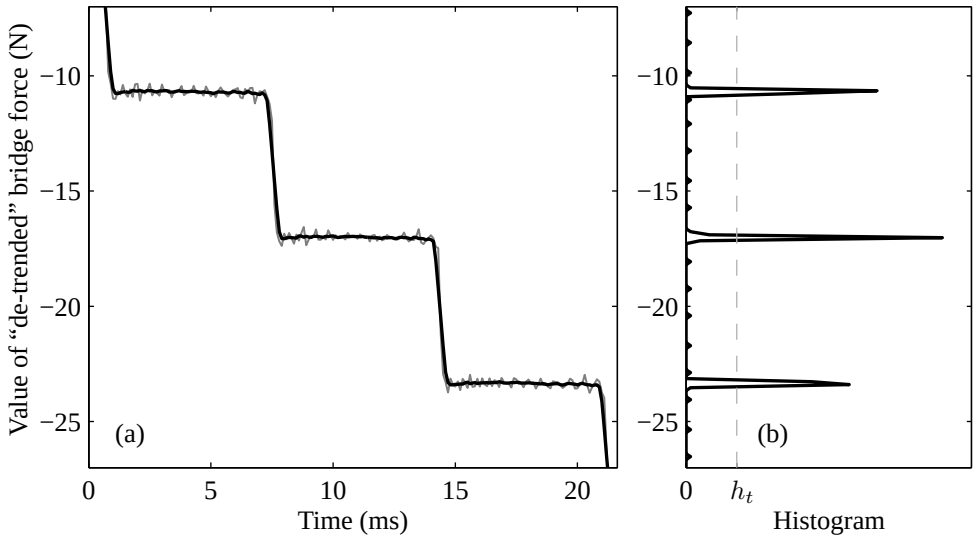

Figure 4.4: Typical output from the string vibration waveform identification algorithm. (a) shows the same bridge force waveform that was shown in Figure 4.3(a), after having been normalized and "de-trended" as described in the text; the gray and black lines show the result before and after being filtered, respectively. (b) shows the histogram of the data, with the same vertical scale; the three peaks in the histogram correspond to the three "steps of the staircase" in (a). The dashed gray line in (b) indicates the threshold which the algorithm uses to decide whether or not the peak is large, and hence whether there has been a significant sticking episode. If the spacing between the peaks is uniform, and approximately equal to $2\,v_{\text{known}} Z_T/\beta$, then the waveform is Helmholtz motion, as indeed it is in this case. If the spacing between peaks is less than $2\,v_{\text{known}} Z_T/\beta$ then it is multiple slipping motion, and if it is more then it is raucous motion. A total absence of peaks indicates constant slipping motion. The data in this figure corresponds to Helmholtz motion, and may be compared with Figure 4.5, which shows double slipping.

- A histogram of the resulting waveform is calculated; each "stair of the staircase" causes a peak in the histogram, as shown for example by the black line in Figure 4.4(b). Peaks are formally defined as any part of the histogram that exceeds some threshold h_t, indicated by the dashed grey line in Figure 4.4(b).

- The spacing between the peaks of the histogram is hence the magnitude of the "fly-back", which for Helmholtz motion is theoretically equal to $2\,v_{\text{known}} Z_T/\beta$. Hence, if the spacing between consecutive peaks is significantly less than this quantity then the motion is deemed to be multiple slipping motion. If the spacing is significantly more than $2\,v_{\text{known}} Z_T/\beta$ and the peak is itself particularly large then the motion is deemed to be "raucous motion". An example of double slipping motion is shown in Figure 4.5, and may be compared with Figure 4.4, which shows Helmholtz motion.

- Multiple flyback motion, which comprises two slips per period, causes a small peak in the histogram halfway between each consecutive pair of large peaks, because the digital filtering smooths the multiple flybacks into a steady value, and all episodes of steady values cause peaks in the histogram. Multiple flyback motion is therefore classified by the algorithm at

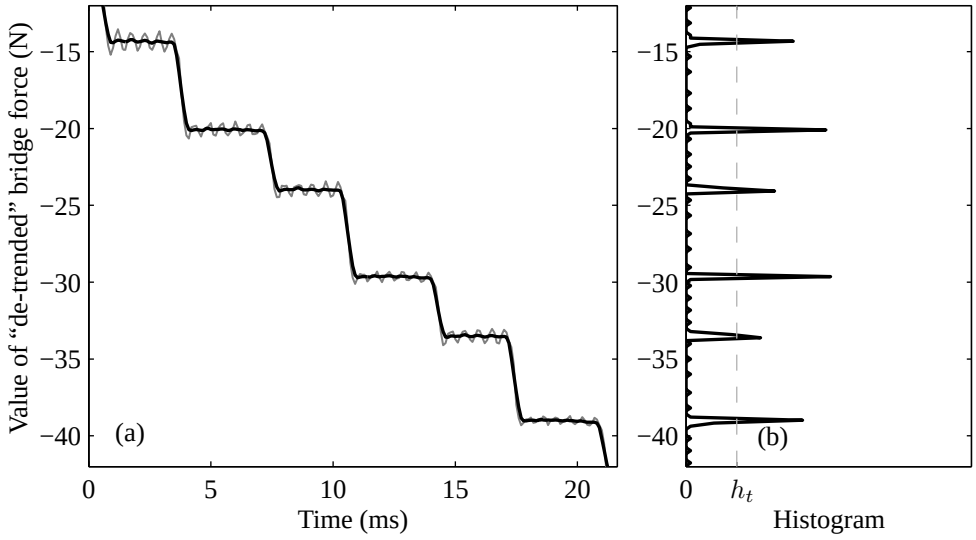

Figure 4.5: Output from the string vibration waveform identification algorithm, when the string is in double slipping motion. Hence, while Figure 4.4 shows results from Helmholtz motion, this figure shows the histogram pattern associated with the double saw-tooth waveform of double slipping: in particular, the histogram contains twice as many peaks. The identification algorithm would treat this increased density of peaks as evidence of multiple slipping.

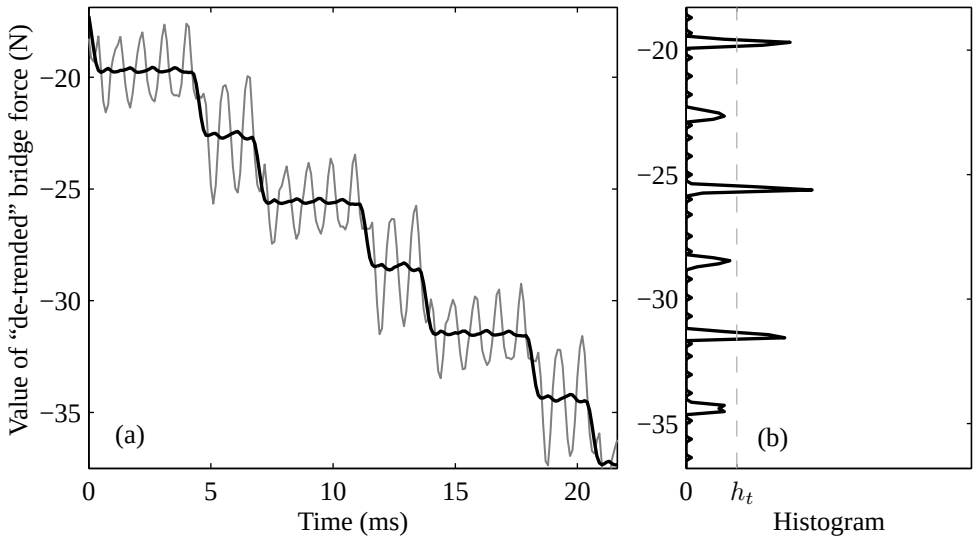

Figure 4.6: Output from the string vibration waveform identification algorithm, when the string is in multiple flyback motion. The most noticeable feature of this example is the effect of the digital filtering: the large ripples (whose period is approximately βT) are approximately smoothed out. Two peaks in the histogram are clearly caused by the bridge force waveform per period, and as such the identification algorithm would treat this as multiple slipping.

this point as multiple slipping motion. A typical histogram from multiple flyback motion is shown in Figure 4.6.

- Frequently, the string will stick and slip once per period (i.e. exhibit Helmholtz motion) for a short period of time before lapsing into a different vibration regime; hence it is insufficient to conclude that Helmholtz motion has been permanently established as soon as it has been identified for the first time in a bridge force waveform. Permanent Helmholtz motion is therefore only deemed to have been achieved if each of the remaining peaks in the histogram is of the correct spacing and magnitude for Helmholtz motion.

Several special cases, too numerous to list, were found which the above algorithm failed to deal with correctly, and for each of which a necessary modification was made to the spotting procedure. The resulting waveform identification algorithm was found to evaluate the time taken to achieve Helmholtz motion as accurately as any experienced human could at least 99% of the time, in both experimental and simulated waveforms.

EXAMPLES OF THE USE OF THE ALGORITHM

Three illustrative examples of the use of the "spotting algorithm" are shown in Figures 4.7, 4.8 and 4.9. In each case, the time of first slip is indicated by a vertical dashed line, the type of string motion is indicated by an appropriate symbol ("□" denotes Helmholtz motion, "×" denotes double slipping, and "+" denotes raucous motion), and the end of the pre-Helmholtz motion transient is indicated by a vertical arrow.

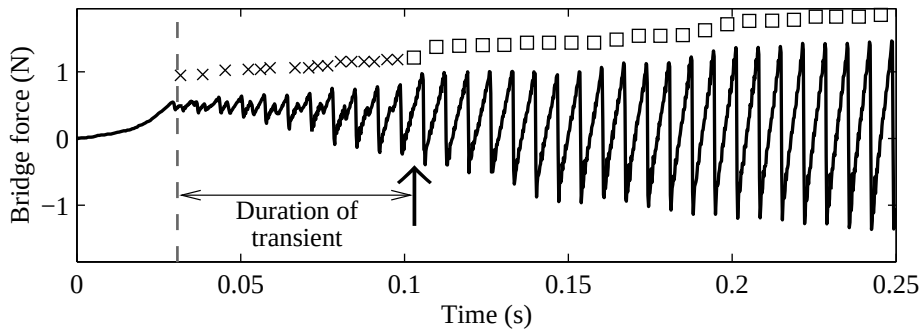

Figure 4.7: The output from the string vibration regime identification algorithm, over the course of an entire vibration transient. The algorithm has plotted an "×" symbol at the times where it detected multiple slipping, and a "□" symbol at times where it detected Helmholtz motion. Accordingly, it has plotted a vertical arrow at the time (0.1028 s) where the pre-Helmholtz motion transient concluded. The vertical dashed line indicates the time of first slip (0.0307 s), which is also automatically detected by the algorithm. Hence, the time taken to achieve Helmholtz motion, relative to the first slip, is 0.072 s in this case. This concurs with the visible pattern of saw-tooth and double saw-tooth waves in the bridge force waveform.

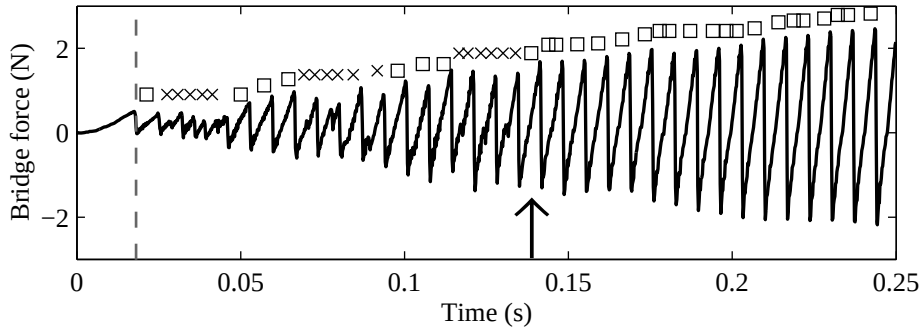

Figure 4.8: Another example of the output of the identification algorithm. The vibration transient shown here, like the one shown in Figure 4.7, consists of a combination of double slipping and Helmholtz motion. However, in this case, the string swaps between the two types of motion a number of times. Throughout the transient, the algorithm has plotted the correct symbols ($\times$ for multiple slipping and $\square$ for Helmholtz motion), and has appropriately waited until 0.1387 s to plot the vertical arrow that indicates the time when Helmholtz motion has been permanently achieved.

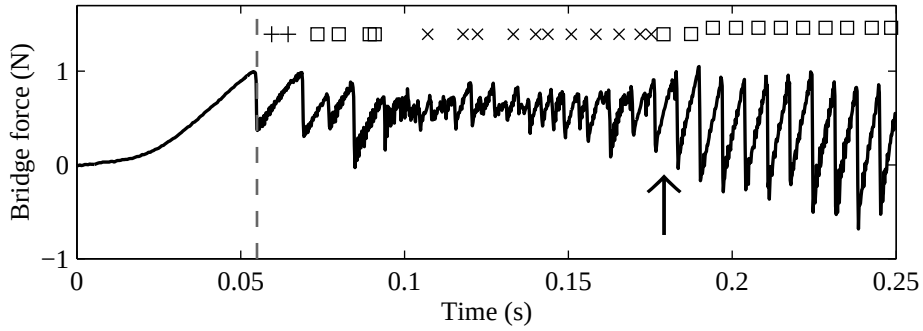

Figure 4.9: Another example of the output of the identification algorithm. In this case, the vibration transient begins with a brief episode of raucous motion, evidenced by the prolonged period of uninterrupted sticking just after the first slip. This brief occurrence of raucous motion was successfully detected by the algorithm, which uses the symbol "$+$" to indicate raucous motion: there are two $+$'s at the appropriate time of around 0.062 s. Subsequently, the algorithm is again successful in waiting until the entire pre-Helmholtz motion transient has concluded before plotting the vertical arrow, at 0.1790 s.

Each of the three examples shown demonstrates a different aspect of the algorithm. Figure 4.7 illustrates the general principle of locating the time of the first slip, searching through the remainder of the bridge force waveform to find occurrences of Helmholtz motion, and denoting the "pre-Helmholtz transient length" as being the time delay between the first slip and the time where Helmholtz motion has been found. Figure 4.8 demonstrates the ability of the algorithm to wait until Helmholtz motion has been permanently established before coming to the conclusion that the pre-Helmholtz transient has concluded. Figure 4.9 shows the spotter's ability to identify the correct string motion in cases where several different types of motion occur; in Figure 4.9, the string undergoes raucous motion, Helmholtz motion, multiple slipping motion, and finally Helmholtz motion again, with the algorithm correctly diagnosing the motion in each case.

USING PERIODICITY FOR STEADY STATE WAVEFORMS

In cases where the string has been given sufficient time to settle into a steady state vibration waveform, it is illuminating to examine the detailed response of the string at high bow force. It becomes clear that a number of different things may go wrong with Helmholtz motion, any of which would sound unacceptable in a musical context, and in that sense determine a "maximum bow force". Some examples are:

- Prolonged sticking, sometimes leading to Anomalous Low Frequency motion [76, 77].
- Non-uniformity of slips, or of flybacks in the bridge force. Often, sticking resumes prematurely, i.e. before the Helmholtz corner has completed its round trip to the bridge, due to a large bow force; this has the knock-on effect of making the next slip particularly large, hence increasing the magnitude of the next flyback in the bridge force. This type of chain of events was frequently observed in experiment to produce an audibly "noisy" sound from the cello.
- If a bow of finite width is used, then according to McIntyre et al. [34] the growth of excessive "spikes" in the bridge force due to differential slipping (see page 12) causes an audible "fuzzy" noise.

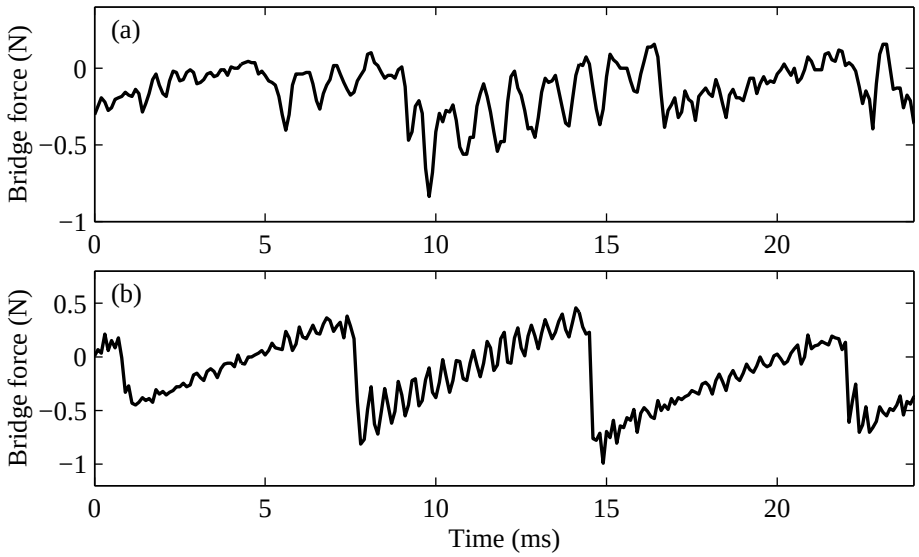

Figure 4.10: Two examples of string vibration waveforms that qualify as "raucous motion" due to a lack of periodicity rather than any particularly prolonged sticking periods. The waveform shown in (a) is visibly non-periodic, whereas the waveform in (b) is less so, but both are audibly "noisy", and were classified as "raucous" by the vibration regime identification algorithm.

Consequently, in steady state vibration measurements, the string vibration identification algorithm measures the periodicity of the waveform (by computing its autocorrelation function [81, §11.7]), and dismisses the motion as "raucous" if it is not sufficiently periodic, or if the period length is

sufficiently different from the fundamental period of the string. Two examples of audibly non-periodic waveforms are shown in Figure 4.10, which were classed as "raucous" by the algorithm. The first example, in Figure 4.10(a), is visibly non-periodic; whereas the second example, in Figure 4.10(b), suffers from a lack of uniformity of flybacks.

4.3 MAPS OF VIBRATION WAVEFORM

In this section, the pattern recognition algorithm described previously is used to explore the range of bowing gestures that are compatible with the production of Helmholtz motion. The first parameter space to be explored is the bow force vs. bow position plane, as suggested originally by Schelleng [16].

4.3.1 SCHELLENG DIAGRAM: VIBRATION REGIME IN THE N-β PLANE

METHOD

In keeping with Schelleng's original intentions, the bowing machine was used to establish an initial condition of Helmholtz motion, before bowing steadily to observe whether Helmholtz motion could be sustained at a given combination of bow speed, bow force and bow position. Hence, to generate a single data point on the Schelleng diagram, the bowing machine performs a quasi-*martelé* bowing attack and then holds a constant bow force and speed: the bow is initially pressed into the string while being accelerated from rest, then pulled away and accelerated further until the required force and velocity have been obtained, and finally held at this force and velocity for two seconds. Whilst in every case the steady bowing speed v_b was set to 0.05 m/s, the steady bow force N and bow position β were incremented in twenty logarithmically-spaced steps each. This scheme of varying bow force and bow speed with time is illustrated in Figure 4.11.

At the end of each two second period of steady bowing, the bridge force was measured for a tenth of a second, and the string motion identification algorithm was used to deduce the string's vibration regime. It was found in all cases that two seconds was a sufficient amount of time for the string to settle into a steady state motion, and so the algorithm was able to treat periodicity as a pre-requisite for Helmholtz motion as discussed previously. At the start of each bowing gesture, it was ensured that the string achieved one stick and one slip per period by the start of the two seconds of steady bowing, although in some cases this required slight adjustments to the force and velocity profiles shown in Figure 4.11. However, although periodic sticking and slipping was ensured in all cases, no bowing scheme was found that could reliably avoid the creation of S-motion in preference to Helmholtz motion (both of which involve a single stick and slip per period). Hence, many cases in which S-motion was reported were unintentionally initiated with S-motion instead of Helmholtz motion.

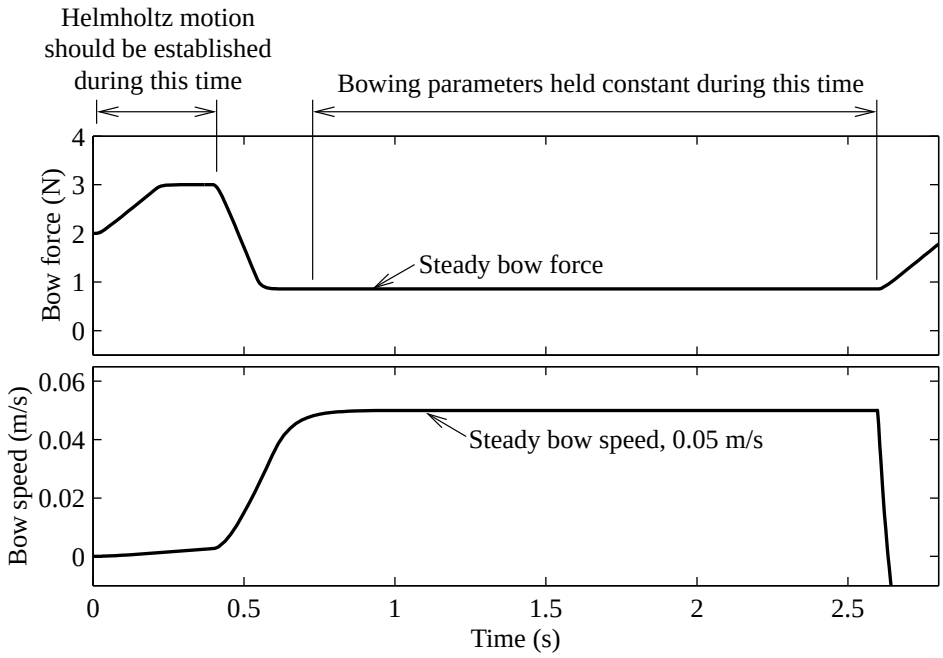

Figure 4.11: Illustration of the bowing gesture used by the bowing machine to generate each point in the Schelleng diagram. For the first 0.4 seconds, the bow is pressed firmly against the string with a low bow speed in order to achieve Helmholtz motion; then the force and speed are adjusted to their steady state values, and held at these values for two seconds. The bridge force is monitored only at the end of this time, to see whether Helmholtz motion has withstood the two seconds of steady bowing. In the case shown here, the steady state value of bow force is 0.857 N, whilst in all cases a steady bowing speed of 0.05 N was used. For the duration of each bowing gesture, β is constant.

RESULTS

The resulting "Schelleng diagram" is shown in Figures 4.12 and 4.13. In Figure 4.12, the combinations of bow force and bow position which allowed Helmholtz motion to be sustained through steady bowing are indicated by white pixels at the corresponding position in the N vs. β plane; grey pixels indicate that the string exhibited S-motion, and black pixels indicate either raucous motion or multiple/constant slipping. Figure 4.13 shows the same data plotted using the symbolic convention of Woodhouse [21]: the result of each measurement is represented by a symbol, with squares ($\square$) denoting Helmholtz motion, crosses ($\times$) denoting multiple slipping motion, pluses ($+$) denoting raucous motion, dots ($\cdot$) denoting constant slipping, and stars ($\bigstar$) denoting S-motion. Thus, while Figure 4.12 is somewhat clearer, Figure 4.13 provides more detail.

The general structure of this Schelleng diagram is qualitatively similar to the predictions of Schelleng himself (see page 20). There is a coherent region of Helmholtz motion in the centre of the plot, bordered by raucous motion (at larger forces) and multiple slipping (at lower forces). This is summarized by the schematic illustration of the experimental results in Figure 4.14.

In addition however, there are three "columns" of S-motion interspersed in the upper-right corner

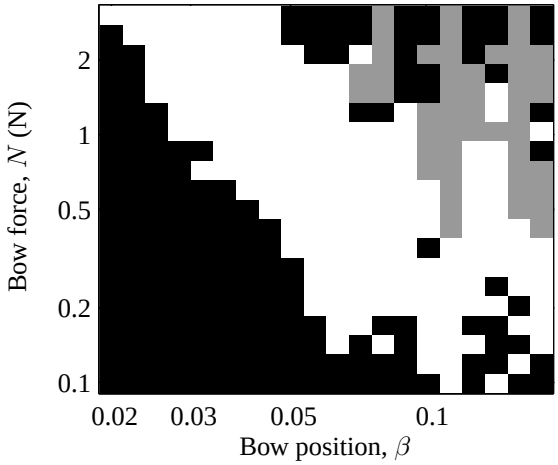

Figure 4.12: Schelleng diagram, from experimental measurements. Here, the shade of a given pixel indicates whether Helmholtz motion was sustainable at the combination of force and position corresponding to the position of the pixel. White pixels indicate that Helmholtz motion was still in evidence at the end of the steady bowing period (see Figure 4.11); black pixels indicate that it was not; and grey pixels indicate that S-motion was observed. All black pixels *above* the central white region correspond to raucous motion, and all black pixels *below* the white region correspond to what players refer to as "surface sound", i.e. multiple slipping or constant slipping. The bow speed is 0.05 m/s in all cases.

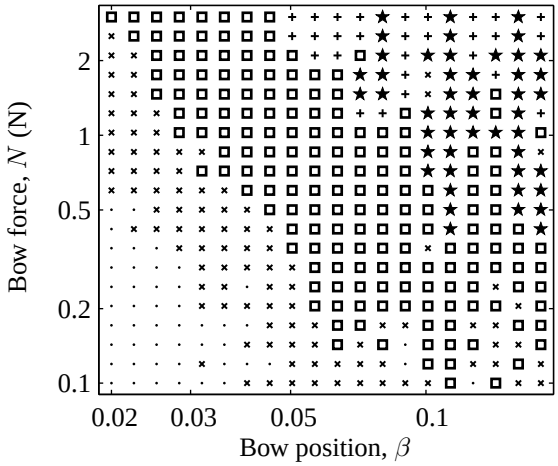

Figure 4.13: Schelleng diagram from experimental measurements, with string vibration regime indicated by symbols. Squares (□) indicate that Helmholtz motion was sustained throughout the period of steady bowing; crosses ($\times$) indicate that the string lapsed into multiple slipping motion; pluses ($+$) indicate raucous motion; dots ($\cdot$) indicate constant slipping; and stars ($\star$) indicate S-motion.

of the plot; the columns are located at values of β that are close to 1/12, 1/8, and 1/6. It is interesting to compare this pattern with the "refined Schelleng diagram" proposed by McIntyre and Woodhouse [50]. McIntyre and Woodhouse successfully predicted the existence of columns of S-motion when β is close to an integer ratio, but predicted that these columns would begin

at the boundary between Helmholtz motion and raucous motion and extend downwards (i.e. to lower bow forces). Instead, they appear to start from somewhere slightly below the boundary between Helmholtz motion and raucous motion, and extend upwards (i.e. to higher bow forces). This association of S-motion with large bow forces is in accordance with Lawergren's observation [60] that one tends to require large bow forces in order to elicit S-motion. Indeed, the fact that S-motion regions generally extend beyond the maximum bow force limit for Helmholtz motion is to be expected, if one combines Schelleng's argument [16] for the breakdown of the periodic sticking and slipping at large bow forces with Lawergren's suggestion [60, 79] that the string slips for a shorter period of time per cycle during S-motion: the shorter slipping time gives rise to a larger slipping velocity, and hence the velocity wave responsible for inducing slipping has a greater magnitude, and is thus better equipped to penetrate past the bowing point at large bow forces. This may be thought of in practice as increasing Schelleng's maximum bow force limit (described on page 19) for cases where Helmholtz motion has given way to S-motion.

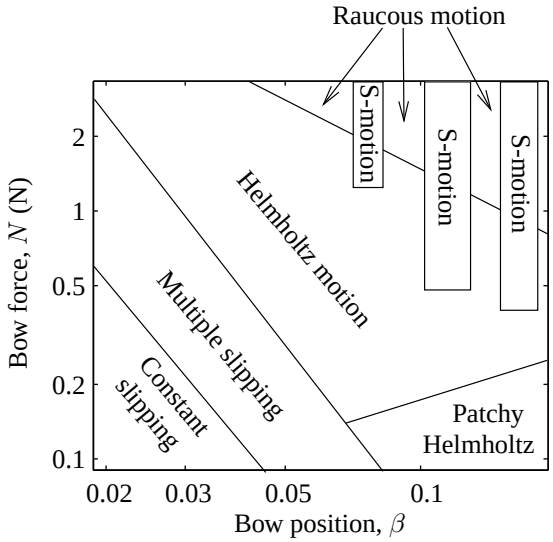

Figure 4.14: Schematic illustration of the results presented in Figures 4.12 and 4.13. The boundaries separating different vibration regimes are represented here by straight lines in around the appropriate positions. The region labelled "patchy Helmholtz" refers to the unreliability of Helmholtz motion in the corresponding region of Figures 4.12 and 4.13, which appears visually "speckly".

It is worthy of note, however, that the scheme used to produce Helmholtz motion as an initial condition (described in Figure 4.11) was only successful in so far as it produced *either* Helmholtz motion *or* S-motion at the start of any given bowing gesture. Therefore, since Helmholtz motion was not necessarily strictly established in cases where S-motion was reported, one can not conclude that Helmholtz motion ever evolved into S-motion. Avoiding S-motion in preference to Helmholtz motion under all conditions is beyond the capability of the bowing machine used in this project, because β cannot be varied during a bow stroke; this is probably the method that a human player would choose.

Another visible feature of the results is that the Helmholtz motion region begins to fade into multiple slipping towards the lower right corner of the Schelleng diagram. This is visible in both Figures 4.12 and 4.13, and is indicated in the lower-right corner of the sketch in Figure 4.14. While the boundary between Helmholtz motion and multiple slipping motion is otherwise clear-cut, this "patchy" region indicates that the boundary is not so well defined at low bow forces.

COMPARING EXPERIMENTAL RESULTS WITH SCHELLENG'S BOW FORCE LIMITS

The upper and lower force limits that Schelleng derived [16] for the sustenance of Helmholtz motion were cited in Chapter 1 (see page 19). He predicted that the boundary between Helmholtz motion and raucous motion — the upper force limit — is proportional to $1/\beta$, and that the boundary between Helmholtz motion and multiple slipping motion — the lower force limit — is proportional to $1/\beta^2$. Approximate best fit representations of these limits were found to be $0.13/\beta$ and $0.00086/\beta^2$ respectively, and are superimposed in Figures 4.15 and 4.16 on the experimental results shown previously.

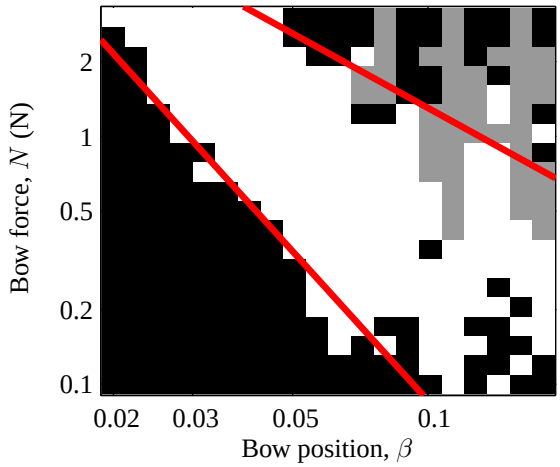

Figure 4.15: Schelleng diagram (same as Figure 4.12), with Schelleng's force limits superimposed as diagonal lines. The upper force limit, $0.13/\beta$, and the lower force limit, $0.00086/\beta$, were chosen by eye to fit the edges of the Helmholtz motion region, which is white in this figure. The proportionality to $1/\beta$ and $1/\beta^2$ was proposed by Schelleng (see Equations (1.15) and (1.16) on page 19).

Both limits appear to capture the essence of the Helmholtz motion region of the Schelleng diagram, although the upper limit is obscured by the appearances of S-motion, and the lower limit eventually gives way to a different limit defined by the "patchy region" discussed previously. While the boundary between Helmholtz motion and raucous motion is unclear, and in any case affected by the vibration identification algorithm's exact definition of "raucous motion", the position of the lower limit can be used to infer the coefficient of Schelleng's lower force limit. With reference to

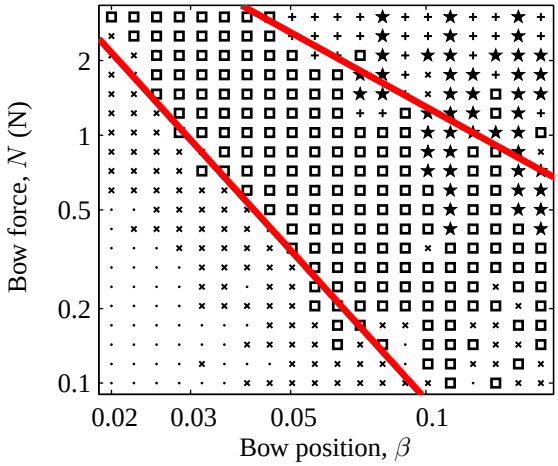

Figure 4.16: Symbolic representation of the Schelleng diagram (same as Figure 4.13), with Schelleng's force limits superimposed as diagonal lines. The upper force limit is proportional to $1/\beta$, the lower force limit is proportional to $1/\beta^2$, and the constants of proportionality are as they were in Figure 4.15.

Equation 1.16 on page 19, we find that:

$$\frac{Z^2 v_b}{2\lambda_b(\mu_s - \mu_d)\beta^2} \sim \frac{0.00086}{\beta^2}. \tag{4.1}$$

With $Z^2 v_b/2$ approximately equal to 0.009 kg^2 m s^{-3} in this case, we find that the value of $\lambda_b(\mu_s - \mu_d)$ is of the order of 10 kg s^{-1}. Hence, one would expect the dashpot rate λ_b to be of the order of 20 N s m^{-1}.

EXAMPLES OF BRIDGE FORCE WAVEFORMS FROM EACH CATEGORY

To illustrate the behaviour of the string in the different regions of the Schelleng diagram defined in Figure 4.14, a representative sample of the bridge force waveform from each region is presented in Figures 4.18(a)–(e). The values of N and β for each sample are shown in Figure 4.17.

In Figure 4.18(a), we see the usual saw-tooth waveform of Helmholtz motion; this bridge force waveform is taken from somewhere near the centre of the Helmholtz motion region of Figure 4.14. In Figure 4.18(b), which shows data from the multiple slipping region, we see an example of "triple slipping motion", whereby the three fly-backs in the bridge force correspond to three slips. In Figure 4.18(c), which shows data from the raucous motion region, we see an example of non-periodic raucous motion. Differing magnitudes of fly-backs at each slip, as seen in this example, is the most common source of non-periodicity, and hence the most common reason for the identification algorithm to label a waveform as raucous motion. In Figure 4.18(d), taken from near the bottom left corner of the Schelleng diagram, we see a typical example of constant slipping motion, whereby the string's motion has faded into an almost sinusoidal waveform. And Figure

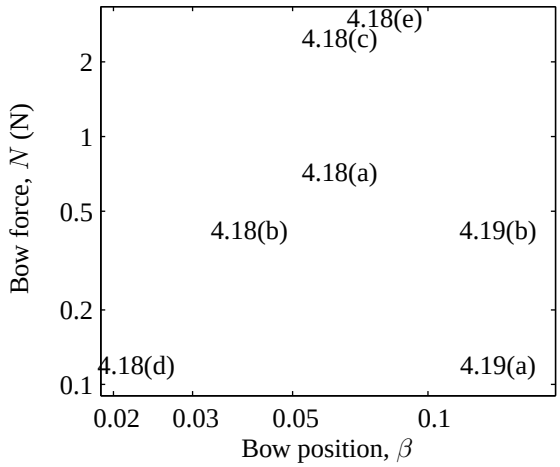

Figure 4.17: Location in the N vs. β plane of the force and position used to generate the individual bridge force waveforms shown in Figures 4.18 and 4.19. Each label in this figure is vertically and horizontally centered over the coordinates of the corresponding waveform. The bow speed was 0.05 m/s in all of the above cases.

4.18(e) shows a typical example of S-motion, taken from the top of the first of the three "columns" of S-motion (at $\beta \approx 1/12$).

Bridge force waveforms from inside and above the region labelled "patchy Helmholtz" in Figure 4.14 are shown in Figures 4.19 (a) and (b) respectively, plotted with the same vertical scale. Figure 4.19(a) shows a typical example of the breakdown of motion often seen at very low bow forces in the "patchy Helmholtz" region. Clearly the amplitude of the motion is greatly reduced, with the upwards-sloping sticking episodes fading into slipping episodes. The amplitude of the motion in both Figures 4.19(a) and 4.19(b) is very small; even in the latter case the amplitude of transverse motion at the midpoint of the string is only approximately 0.4 mm.

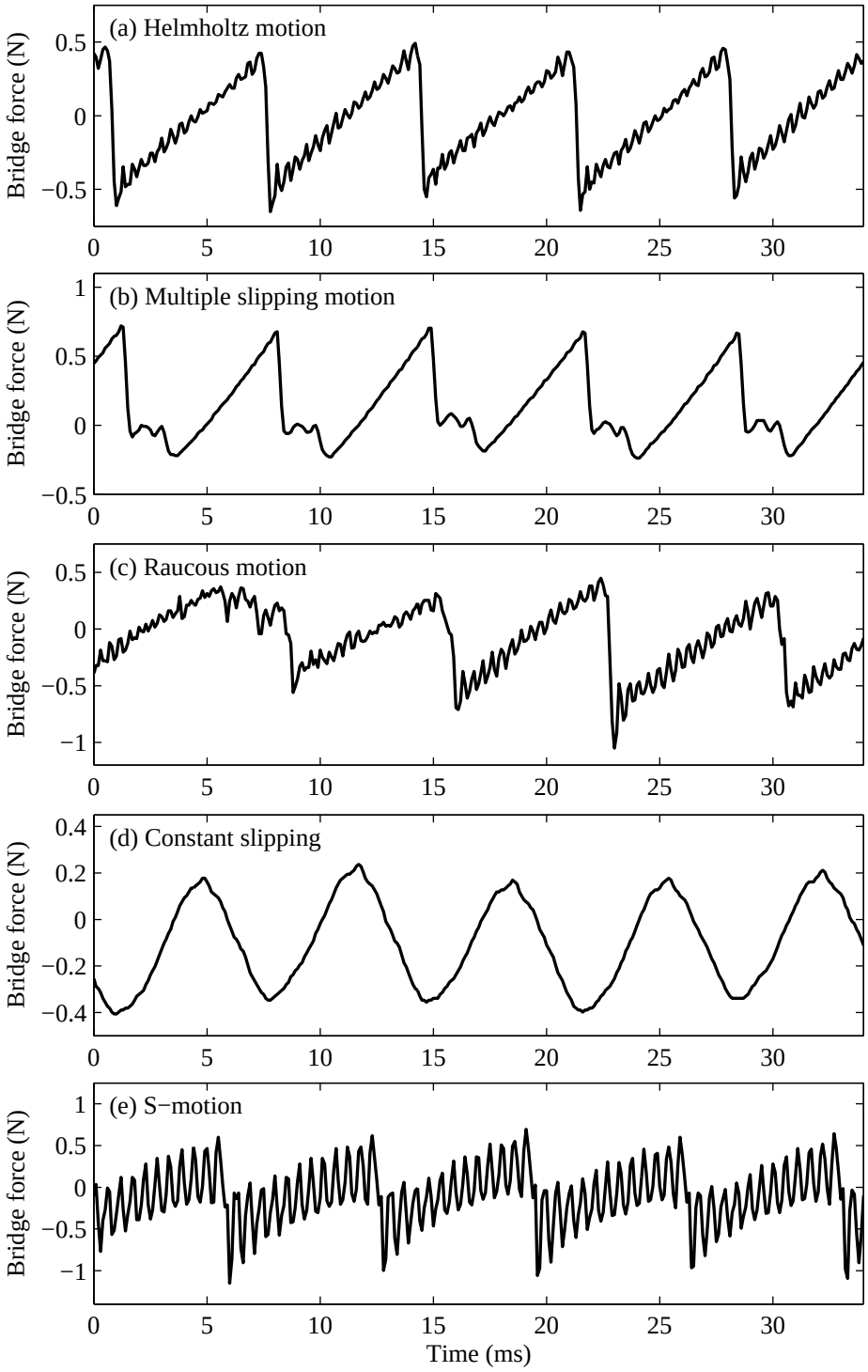

Figure 4.18: Examples of bridge force waveforms from each of the regions of the Schelleng diagram, as denoted in Figure 4.14 (except for the region labelled "patchy Helmholtz", which is treated separately in Figure 4.19). The values of bow force and position for each waveform are given in Figure 4.17, and the bow speed is 0.05 m/s in all cases.

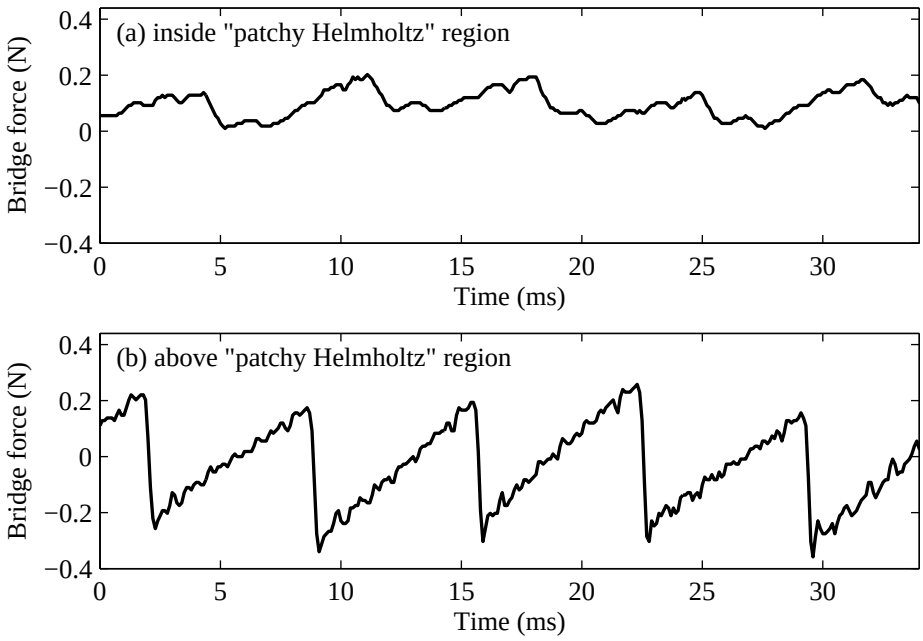

Figure 4.19: Examples of the bridge force waveforms in and around the region marked "patchy Helmholtz" in Figure 4.14. The top plot was deemed to show multiple slipping by the identification algorithm and is hence one of the black pixels in the Schelleng diagram in Figure 4.12, and the bottom plot is clearly Helmholtz motion. Both have the same value of β, as stated in Figure 4.17.

4.3.2 GUETTLER DIAGRAM: PRE-HELMHOLTZ DURATION IN N-a PLANE

The second parameter space to be considered is the bow force versus bow acceleration plane. The study of the motion of the string in this plane was suggested by Guettler [45] as being intuitively important to a player, as discussed on page 21.

RESULTS, FOR DIFFERENT VALUES OF β

With the bow accelerated from rest at a uniform rate a, and the bow force held at a constant value N by the bowing machine as described in Chapter 3, the algorithm described in Section 4.2.3 was used to deduce the time delay between the first slip and the onset of Helmholtz motion. For each measurement, a and N were each assigned one of twenty linearly spaced values, to investigate a 20×20 grid of points in the N vs. a plane. For each grid of 400 measurements, the distance βL of the bow from the bridge was kept the same. In the spirit of Guettler himself [45], who was solely concerned with the occurrence of a single stick and slip per period, the vibration identification algorithm does not discriminate between Helmholtz motion and S-motion, as both of these types of motion only involve a single slip per period.

The results are shown, for eight different values of β, in Figure 4.20. Using the same convention as Guettler [45], the duration of the pre-Helmholtz motion transient at a given combination of N and

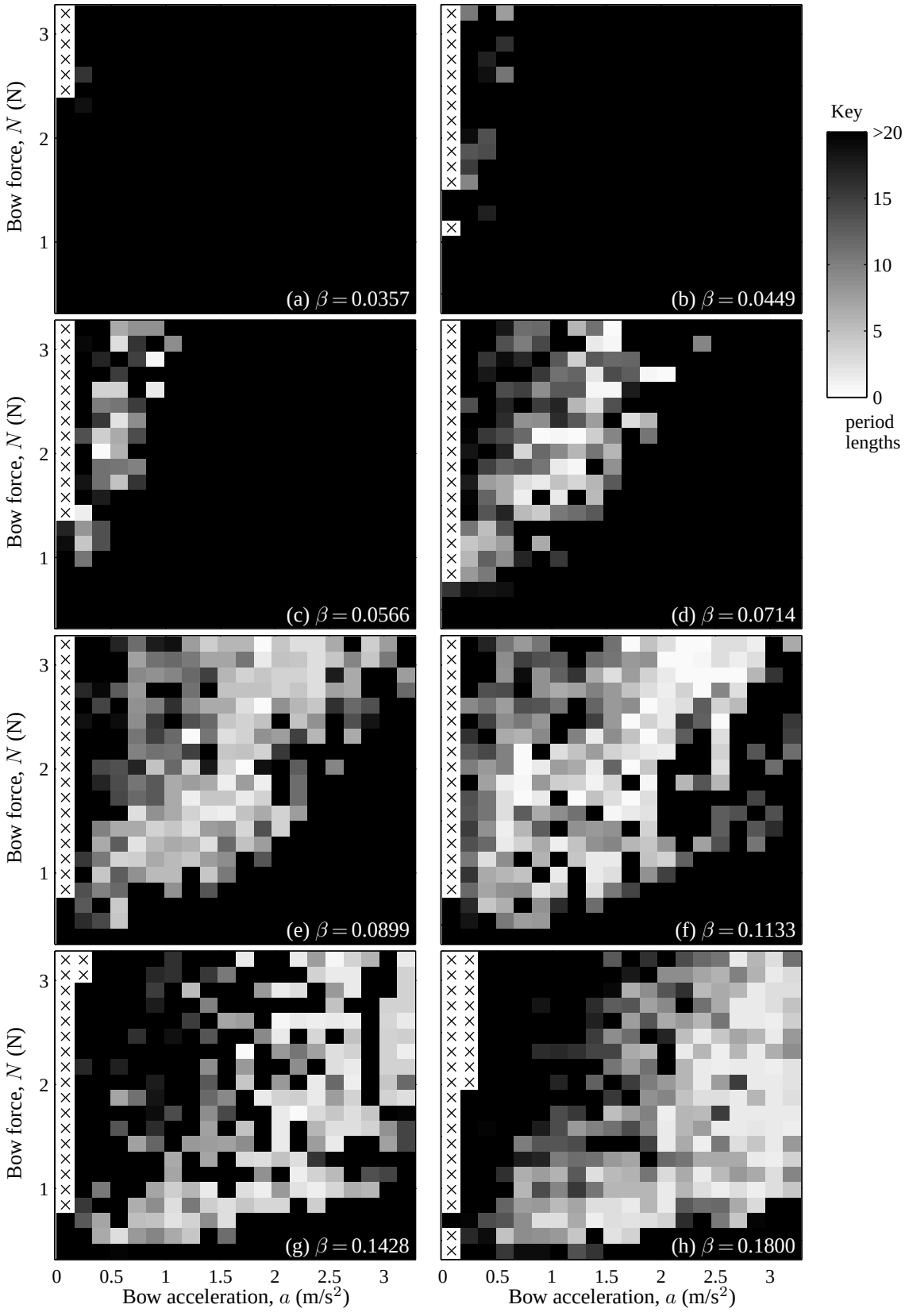

Figure 4.20: Experimentally measured "Guettler diagrams", for eight different values of β. In each plot, the time taken to achieve Helmholtz motion relative to the time of the first slip at a given combination of bow force and acceleration is given by the shade of the pixel at the corresponding location in the N vs. a plane. White pixels indicate "perfect transients", black pixels indicate that it took twenty or more period lengths to achieve Helmholtz motion, and grey pixels indicate intermediate pre-Helmholtz motion transient durations. White pixels with crosses ("$\times$") indicate unsuccessful measurements, as described in the text. The vertical and horizontal scales of each plot are the same.

a is indicated by the darkness of the pixel at the corresponding location in the N vs. a plane. White pixels indicate "perfect transients" (i.e. no delay between the first slip and the onset of Helmholtz motion), black pixels indicate that there was a delay of twenty period lengths or more between the first slip and the time when Helmholtz motion was permanently established (twenty period lengths equals 0.136 s for the cello D-string), and grey pixels indicate an intermediate pre-Helmholtz motion delay. However, occasionally the force was sufficiently large and the acceleration sufficiently small that the first slip would not occur until less than twenty period lengths before the end of the bridge force measurement. In such cases, there is not enough bridge force data to deduce whether the delay between first slip and Helmholtz motion lasted twenty period lengths. All such cases are indicated in Figure 4.20 by white pixels with black crosses ("$\times$"). The horizontal and vertical scales of all eight plots are the same.

The pattern which emerges from Figure 4.20 is that all white or grey pixels, i.e. occurrences of Helmholtz motion, lie within a "wedge"-like region, whose vertex is somewhere close to the origin. In general, the black pixels below the "wedge" (i.e. at smaller values of N) are caused by multiple or constant slipping, and the black pixels above the wedge (i.e. at larger values of N) are caused by raucous motion. Comparing the appearances of Figures 4.20(a)–(h), which are presented in ascending order of β, it is clear that as β decreases towards zero the size of the wedge shrinks, and its position shifts upwards. For values of β less than 0.0357, where 0.0357 is the smallest value shown in Figure 4.20, there are no occurrences of Helmholtz motion at all; for this reason, Guettler diagrams for $\beta < 0.0357$ are not shown.

The notable exception to the gradual upwards shift and steepening of the upper and lower boundaries of the light-colored regions as β decreases is the upper limit in Figure 4.20(f). In this case, the upper limit of the light-colored region is as high as it was in any of the other cases shown in Figure 4.20, even though the value of β is the third largest of the eight values shown. The reason for this is that the value of β used in Figure 4.20(f), 0.1133, is close to the integer ratio 1/8, which encourages the growth of S-motion; and as seen already in Section 4.3.1, occurrences of S-motion cause the maximum allowable bow force to increase. Indeed, the middle one of the three "columns" of S-motion in the Schelleng diagram of Figure 4.12 was centered around $\beta = 0.1133$. In the Guettler diagrams, the vibration classification algorithm did not distinguish between S-motion and Helmholtz motion, and as such many of the light-shaded pixels in Figure 4.20(f) are caused by a mixture of Helmholtz motion and S-motion.

Another conspicuous feature of Figure 4.20 is that Figure 4.20(g) appears to be more "speckly" than its neighbors, with the light-shaded region interspersed with several black pixels. The vast majority of these black pixels are caused by an interesting waveform that appears to be a mixture of S-motion and multiple flyback motion. The bridge force waveforms for this case and for others are presented in the next section.

EXAMPLES OF BRIDGE FORCE WAVEFORMS

A typical example of the bridge force waveform corresponding to the mixture of S-motion and multiple flyback motion seen commonly when $\beta = 0.1428$ is shown in Figure 4.21. This particular waveform was generated with $N = 1.579$ N, $a = 2.215$ m/s^2, and $\beta = 0.1428$, and hence corresponds to one of the black pixels near the centre of Figure 4.20(g). Once it has settled into a steady state, this pattern of bridge force is similar to many of the cases that appear as black pixels in Figure 4.20(g), and as such is evidently prone to occurring when $\beta = 0.1428$. The exact pattern itself, shown at a greater level of magnification in Figure 4.21(b), has large ripples that are often associated with S-motion, but can be seen to slip twice per period. During the shorter of the two sticking periods, the ripples are larger, causing the waveform to look similar to a multiple flyback waveform.

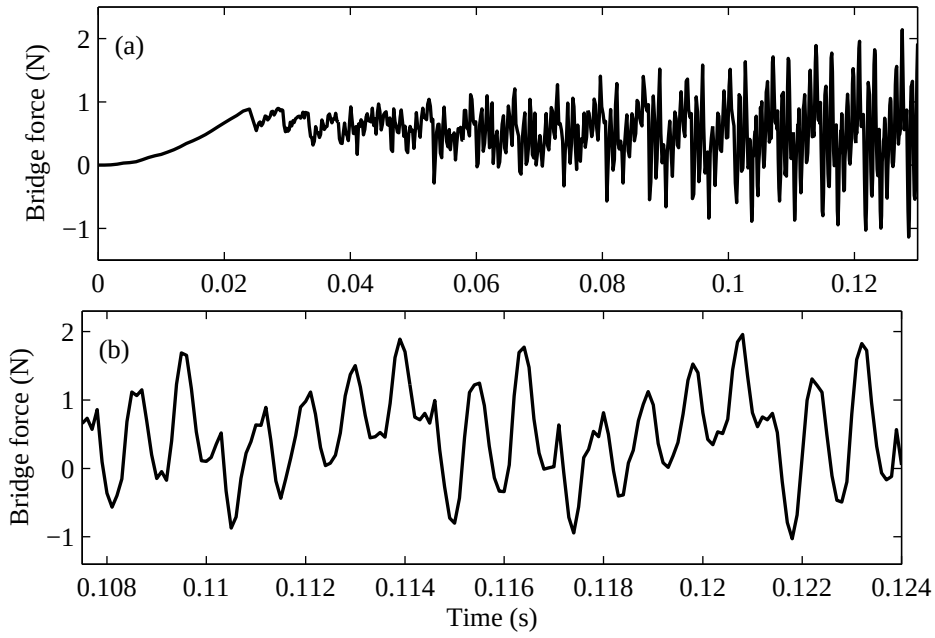

Figure 4.21: Bridge force waveform measured with bow force equal to 1.579 N, bow acceleration equal to 2.215 m/s^2, and β equal to 0.1428. As was observed with a surprising proportion of the vibration transients when β was set to 0.1428 and the bow was accelerated from rest, this waveform shows evidence of a mixture of S-motion and multiple flyback motion (or in this particular case triple flyback). The string is evidently slipping twice per period, since the ripples in (b) are underpinned by a double saw-tooth wave — indeed, multiple flyback causes two slips per period.

Other significant bridge force waveforms are shown in Figures 4.22 (a)–(d). These show, respectively: a "perfect transient", in which Helmholtz motion is achieved immediately after the first slip; a "perfect" S-motion transient, in which S-motion is seen to occur starting almost immediately after the first slip; a raucous transient, in which the second sticking period clearly lasts for longer than one period length (which, in all cases, is 0.0068 s); and a multiple slipping transient. In all cases, the bridge force is seen to rise parabolically before the first slip, indicating that the string

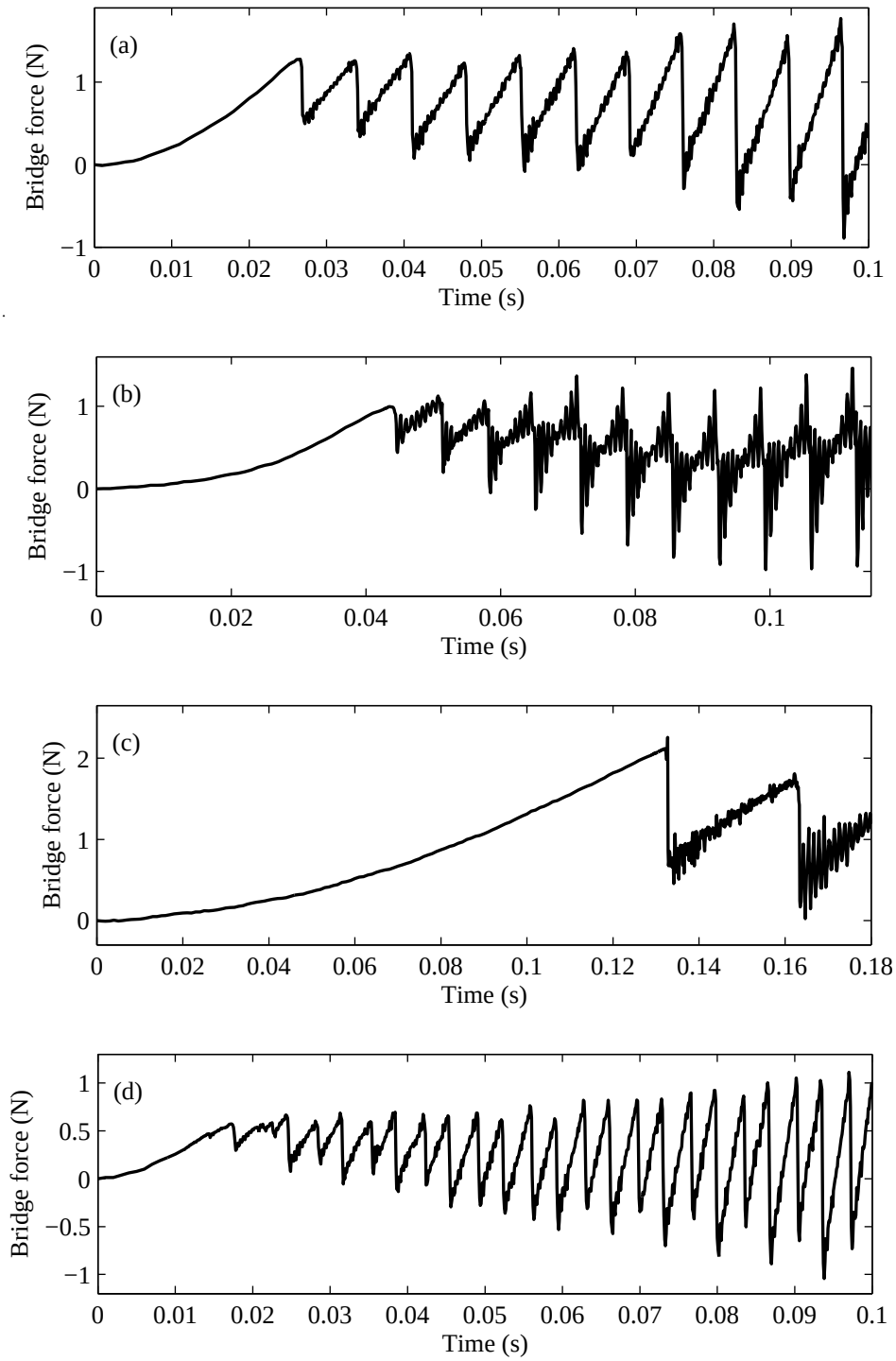

Figure 4.22: Examples of bridge force waveforms from various regions of the Guettler diagrams. The values of N, a and β for each example are, respectively: (a) 1.874 N, 1.230 m/s^2, and 0.0714; (b) 1.726 N, 0.901 m/s^2, and 0.1133; (c) 2.758 N, 0.244 m/s^2, and 0.1800; (d) 1.137 N, 1.722 m/s^2, and 0.0566. In this figure, the horizontal and vertical axes ranges are different in every plot, although the string's natural period is 0.00680 s in all cases.

is displacing quasi-statically during that period: the constant acceleration causes a string displacement proportional to $1/2\,a\,t^2$, and the lack of other waves on the string means that the bridge force, which is proportional to the slope of the displacement of the string near the bridge, also increases in proportion to $1/2\,a\,t^2$.

GUETTLER'S "PERFECT TRANSIENTS", AND TRENDS IN THE GUETTLER DIAGRAM

Guettler's motivation [45] for exploring the N vs. a plane was to determine the positions of regions containing only "perfect transients", in the sense defined on page 21. It is interesting to note, therefore, that perfect transients — indicated by white pixels in Figures 4.20, 4.25 and 4.29 — do not appear to be confined to a single coherent region. Anecdotal evidence from cellists suggests that open (i.e. unfingered) strings of cellos are more difficult to make "speak" than fingered strings, and all of the results in this chapter are generated using the open D-string of a cello. As such it is possible that a different conclusion would be reached if the measurements in this chapter had been made with the cello string stopped by a finger. However, such measurements remain a topic of future research.

It is encouraging that the regions in Figures 4.20 (a)–(h) containing "good transients" (i.e. grey pixels) are roughly wedge-shaped, which is the shape that Guettler predicted [45] for regions of white pixels. It is possible, therefore, that a generalization of Guettler's four conditions (see page 21) could describe the general behaviour of the bowed string seen in the N vs. a plane.

Indeed, given these wedge shapes, one might guess that waveforms generated at operating points that lie along the same radial line in the N vs. a plane, for example along the maximum bow force line, would bear some degree of similarity to each other. This has proven to be true in several cases, for example in the two pairs of waveforms shown in Figures 4.23 and 4.24, which show the results from two pairs of radially linked operating points in the N vs. a plane. These two examples demonstrate that the waveform can stay essentially unchanged if the ratio N/a is held constant.

REPEATABILITY: CONSISTENCY OF RESULTS AT A SINGLE β VALUE

Even when the bowing machine performs an apparently identical bowing gesture a number of times, the resulting pattern of transient string motion can often differ considerably, due to imperceptibly small differences in experimental conditions. In this sense, the bowed string exhibits considerable "twitchiness". This twitchiness may prevent contours of constant pre-Helmholtz duration showing up more clearly in the experimental results of Figure 4.20. If, say, contours of constant pre-Helmholtz duration are closely spaced and their positions are influenced by ambient conditions, then any small deviation of the operating point from a line of constant N/a in the N vs. a plane, or a slight change in the laboratory environment, may cause an anomalous vibration transient, and create "speckly" appearance in the results.

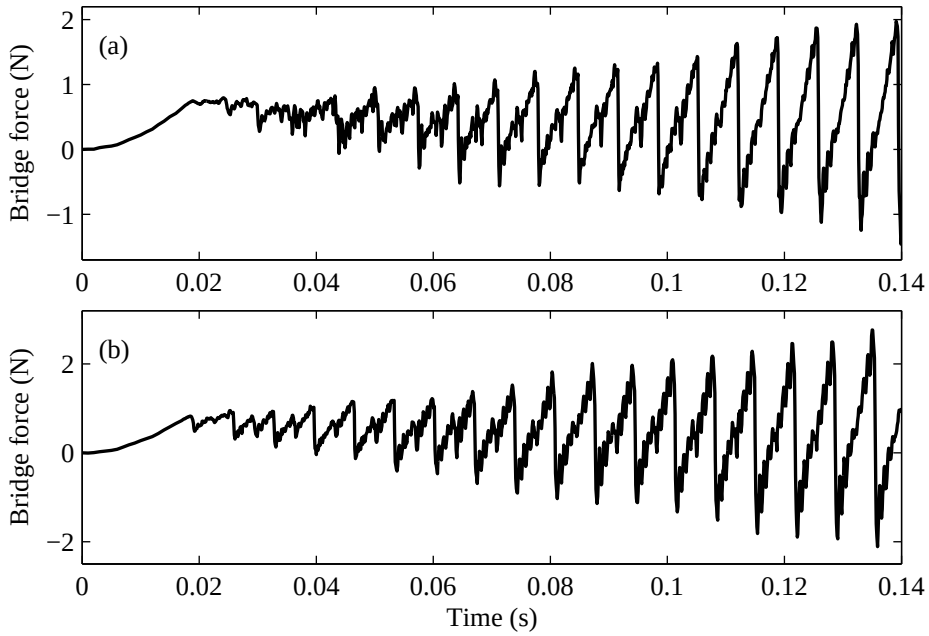

Figure 4.23: An example of two similar bridge force transients from operating points along the same radial line in the N vs. a plane. Here, the string's motion is seen to follow similar trends at both operating points: double slipping gradually gives way to Helmholtz motion. The values of N, a and β are, respectively: (a) 1.137 N, 2.215 m/s^2, and 0.1133; (b) 1.579 N, 3.036 m/s^2, and 0.1133. Hence, these are both taken from near the minimum bow force line in Figure 4.20(f).

To illustrate the repeatability of the experimental results, a Guettler diagram was measured a total of twelve times with $\beta = 0.08$ each time. The results are shown in Figure 4.25.

Figure 4.25 demonstrates the nature of the bowed string's twitchiness. Whereas the general border of white and grey pixels in the Guettler diagram — sketched in Figure 4.26 — remains fairly fixed, the detailed pattern of dark and light pixels varies chaotically between the twelve different measurements. This variation is apparently due to imperceptibly small variations in experimental conditions: as demonstrated in Chapter 3, the force and acceleration are controlled to within around $\pm\,2\%$ under all conditions.

It is revealing to combine the twelve plots in Figure 4.25, to see the shortest and longest transients at each point in the N vs. a plane. This is done in Figure 4.27: the top two plots show the effect of combining the first two sets of measurements, the next two plots show the effect of combining the first four sets of measurements, the third row shows the effect of combining the first eight sets of measurements, and the bottom two plots show the effect of combining all twelve sets of measurements. In each case, the overall shortest transients are shown on the left, and the overall longest transients are shown on the right. As previously, transient lengths are indicated by the darkness of the pixels, and the white pixels with black crosses ("$\times$") indicate that a measurement at the corresponding operating point was unsuccessful in one of the sets of measurements under consideration.

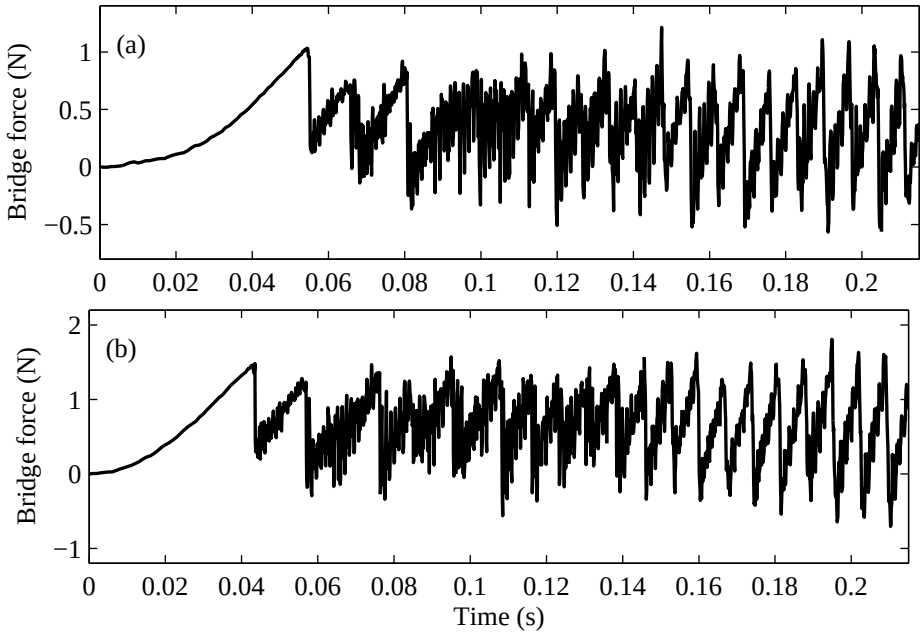

Figure 4.24: Another example of two bridge force transients that are similar, having been generated at different points along the same radial line in the N vs. a plane. The values of N, a and β are, respectively: (a) 1.432 N, 0.901 m/s^2, and 0.1800; (b) 2.316 N, 1.394 m/s^2, and 0.1800. Hence, these are both taken from near the maximum bow force line in Figure 4.20(h).

In Figure 4.27, the plots of shortest transients (on the left) are gradually filled in as more and more sets of measurements are included, and the plots of longest transients (on the right) gradually become more and more sparse. Additionally however, the region in the N vs. a plane in which the longest transients are still less than twenty period lengths (i.e. the region containing light pixels in the right-hand plots of Figure 4.27) becomes progressively narrower as more sets of data are included; conversely, the region in which the shortest transients are less than twenty period lengths (i.e. the region containing light pixels in the left-hand plots of Figure 4.27) becomes progressively wider. This suggests that the most "reliable" operating points are nearest the centre of the light-shaded region, whereas the most "unreliable" operating points are towards the edges.

In addition to shedding additional light on the location of operating points that can lead to Helmholtz motion, Figure 4.27 also shows that when the entire twelve sets of measurements are combined, the maximum and minimum bow force lines are blurred. Visibly, this is apparent by the gradual transition from white to black at both the upper and lower edges of the light-shaded region of the bottom left plot of Figure 4.27.

Figure 4.28 provides an alternative insight into the repeatability of the bowed string in experiment. It shows ten bridge force waveforms that were measured under the same conditions in immediate succession, in the order in which they are shown. The values of N and a were chosen to be close to the minimum bow force limit, with $\beta = 0.08$. Demonstrating the unreliability of the string's behaviour near the minimum bow force, the saw-tooth wave of Helmholtz motion is observed

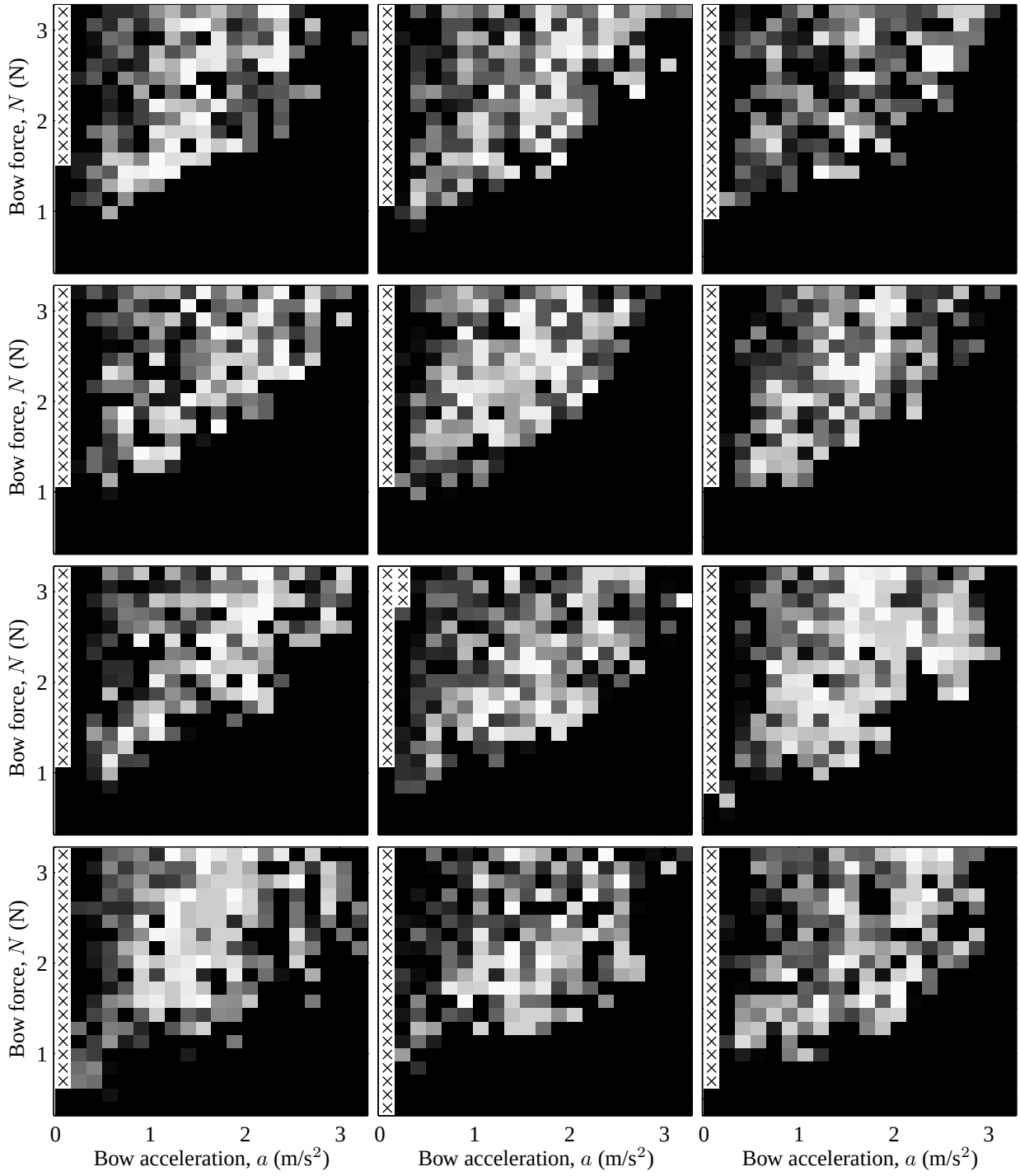

Figure 4.25: Twelve separate experimental measurements of the Guettler diagram, each with $\beta = 0.08$. As with Figure 4.20, the shade of each pixel indicates the time delay between the first slip and the onset of Helmholtz motion, with white pixels indicating no delay, and black pixels indicating a delay of twenty period lengths or more. White pixels with black crosses ("×") indicate that the first slip occurred less than twenty period lengths before the end of the bridge force measurement, making it impossible to deduce whether the transient time was twenty period lengths. The vertical and horizontal axes ranges of all of the above plots are the same as they were in Figure 4.20.

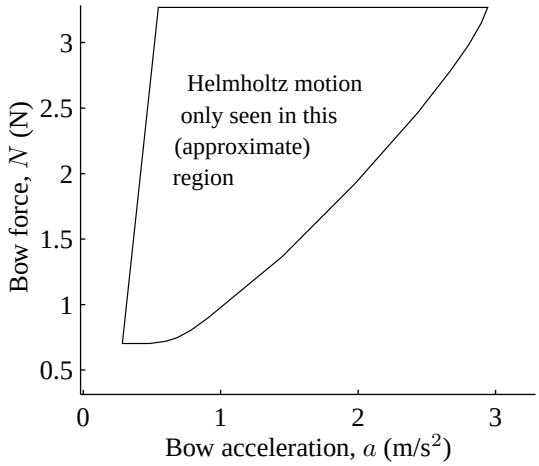

Figure 4.26: Sketch of region of N-a plane containing all experimentally observed cases of Helmholtz motion, when $\beta = 0.08$. Although the detailed location of occurrences of Helmholtz motion in the N vs. a plane varies, the position of the overall region containing them is roughly constant.

to occur only in Figures 4.28 (b), (c), (h) (and at the very end of Figure 4.28 (i)), whereas the double saw-tooth waveform of double slipping is observed in the other six cases. Indeed, no two waveforms are exactly alike in detail; the closest matches are probably Figures 4.28 (b) and (h).

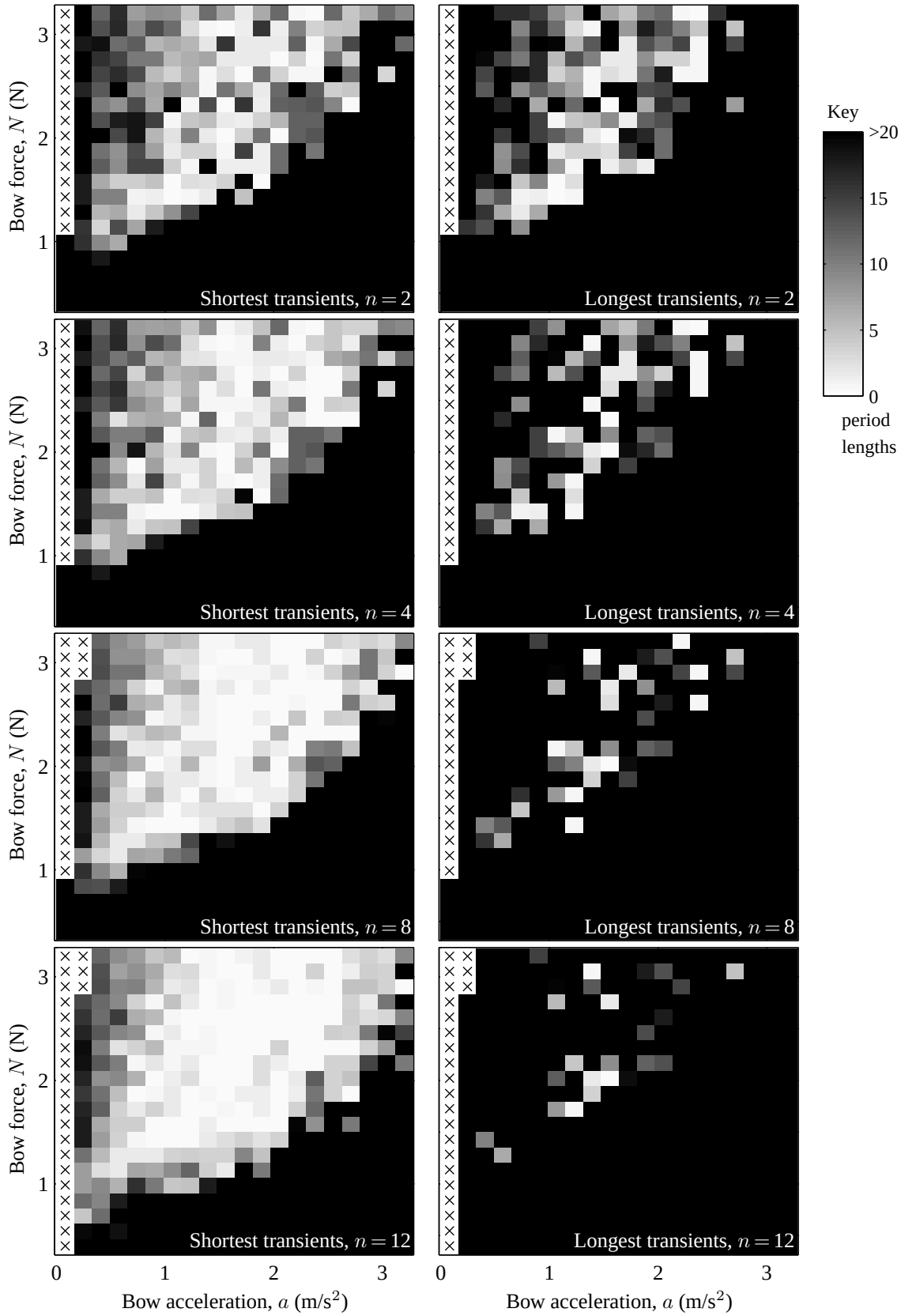

Figure 4.27: Shortest and longest transients in the first n plots (out of a total of twelve) shown in Figure 4.25. Transient lengths at a given combination of N and a are again given by the darkness of the pixel at the corresponding location in the N vs. a plane. β is 0.08 in all cases here. The shortest (and hence best) transients in the first n cases are shown in the left column, the longest transients (and hence worst) transients are shown in the right column, and each row corresponds to a different value of n.

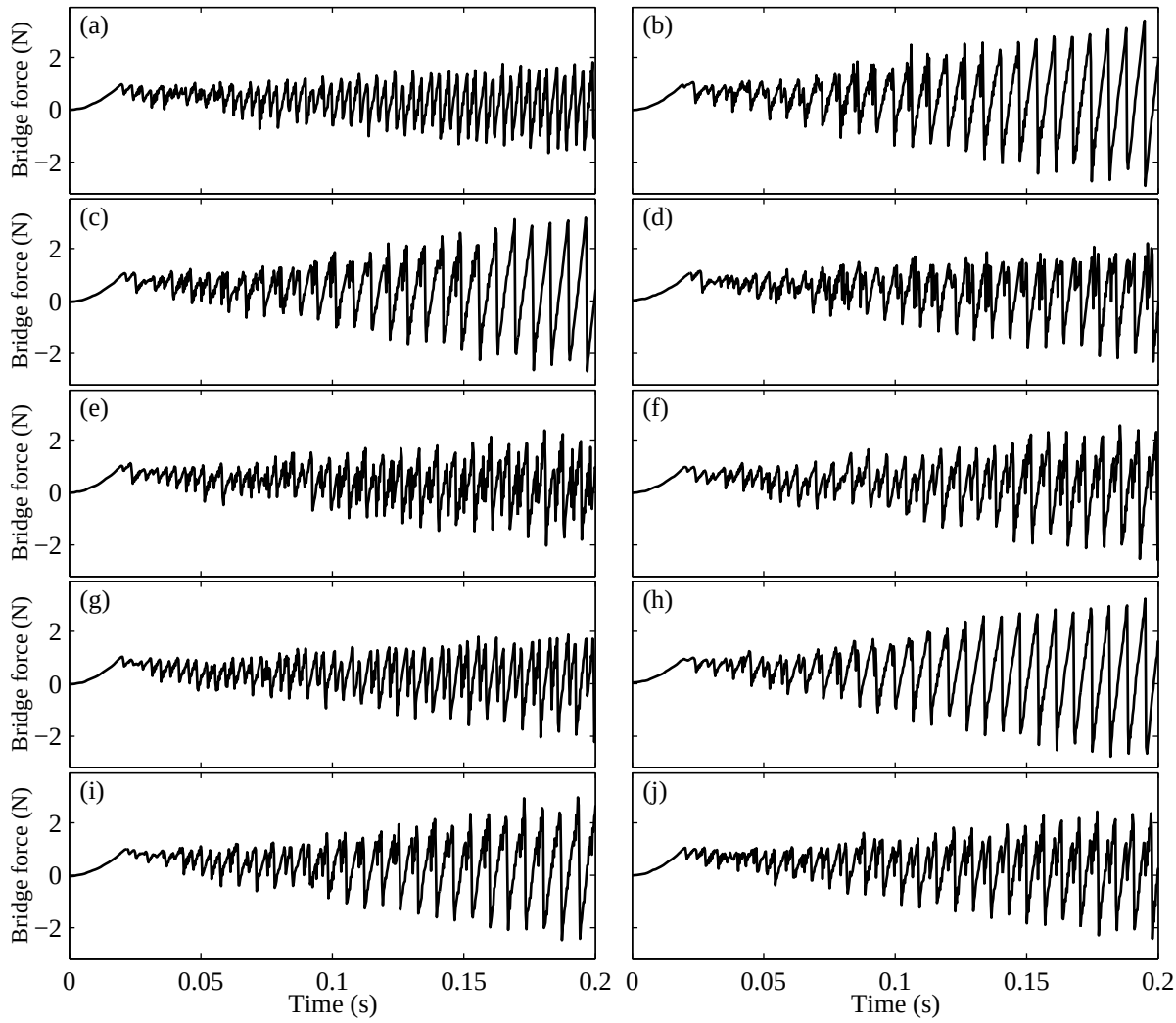

Figure 4.28: Ten bridge force waveforms, measured in immediate succession, each under the same experimental conditions. Due to the chaotic nature of the bowed string, no two of these waveforms look alike in every detail.

REVERSING THE ORDER OF MEASUREMENTS

Each array of 400 measurements in Figure 4.25 was obtained in the same order: the twenty values of acceleration were tested in ascending order, and at each acceleration the twenty values of force were tested in ascending order. On the premise that the initial conditions of a given measurement may be influenced by the details of the previous bowing gesture, due to long thermal time lags for example, the same Guettler diagram was repeated in the reverse order, seven times. Thus, at each value of acceleration the force was decreased, and the values of acceleration were tested in descending order: the results are shown in Figure 4.29.

It is apparent, from Figure 4.29, that reversing the order of the measurements certainly does not drastically change the general appearance of the Guettler diagram, although the lower boundary of

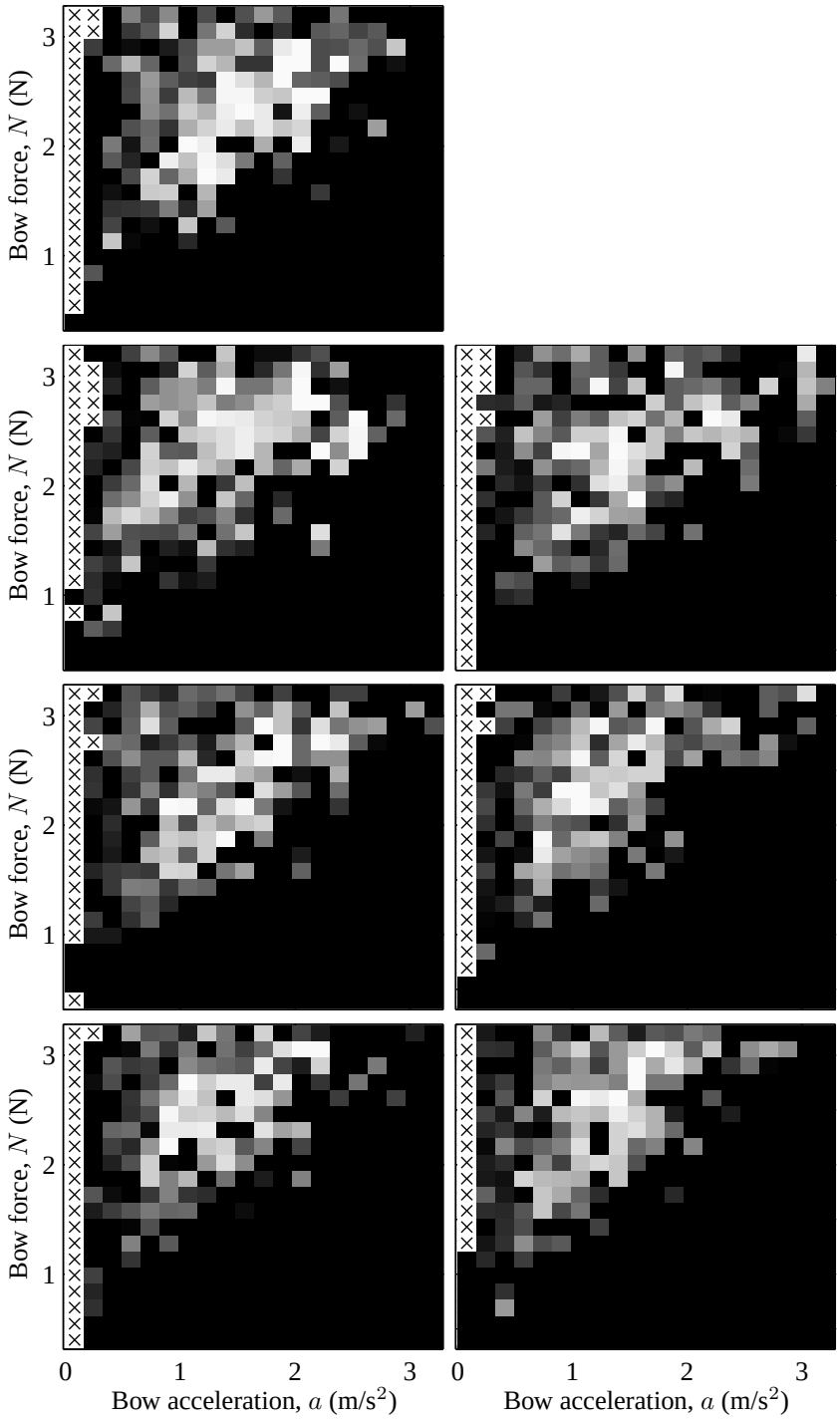

Figure 4.29: Seven additional experimental measurements of the Guettler diagram, but with the N vs. a parameter space traversed in the opposite order from previously (including Figures 4.20 and 4.25). Thus, the twenty values of acceleration were tested in descending order; and at each acceleration, the twenty values of force were tested in descending order.

the light-shaded regions has shifted upwards slightly. This corresponds to a slight increase in the minimum bow force required to produce Helmholtz motion.

FRICTION JUST BEFORE FIRST SLIP

As discussed before, when the bow accelerates smoothly from rest, the string is effectively devoid of high frequency waves until the time of the first slip. Therefore, if one assumes that there exists a maximum possible coefficient of friction μ_s associated with limiting static friction, then a simple equilibrium force balance reveals that the bridge force just before the first slip must equal $(1-\beta)\mu_s N$. It is straightforward, then, to deduce the limiting coefficient of friction μ_s by dividing the bridge force just before first slip by $(1-\beta)N$.

The result of performing this calculation on each of the bridge force signals that were used to construct the twelve Guettler diagrams of Figure 4.25 is shown in Figure 4.30. The darkness of each pixel in Figure 4.30 indicates the average value of μ_s from the corresponding operating point in the twelve plots in Figure 4.25; thus each value of μ_s is the average of twelve measurements. The surprising feature of Figure 4.30 is that μ_s depends much more strongly on the bow's acceleration than on the bow force, with μ_s around twice as large at low values of acceleration than at high values. Thus, although the fact that μ_s is independent of N supports the notion that $f \propto N$, it would appear that additional friction is created somehow at low accelerations.

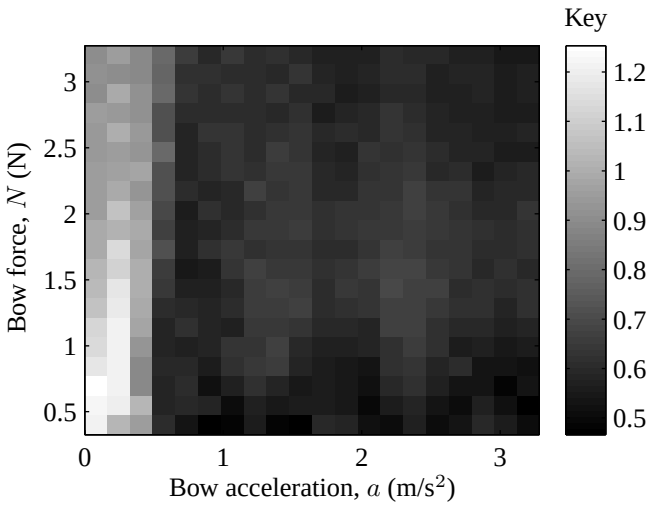

Figure 4.30: The value of coefficient of friction between bow and string shortly before the first slip, based on the same data used to generate the twelve plots in Figure 4.25. The darkness of each pixel indicates the average of the twelve results obtained by calculating μ_s for each of the twelve sets of data in Figure 4.25. As illustrated by the guide on the right, white pixels denote the largest value of μ_s seen, and black pixels denote the smallest. μ_s is seen to double as the acceleration is brought towards zero.

To further illustrate the relative strength of the dependence of μ_s on acceleration compared with force, the average value of μ_s for each column of Figure 4.30 is shown plotted in Figure 4.31(a)

against the corresponding values of acceleration. This again shows the doubling of friction coefficient at low accelerations. For comparison, the average value of μ_s for each row of Figure 4.30 is shown plotted in Figure 4.31(b) against the corresponding values of force: μ_s stays within 7% of the mean value of 0.66.

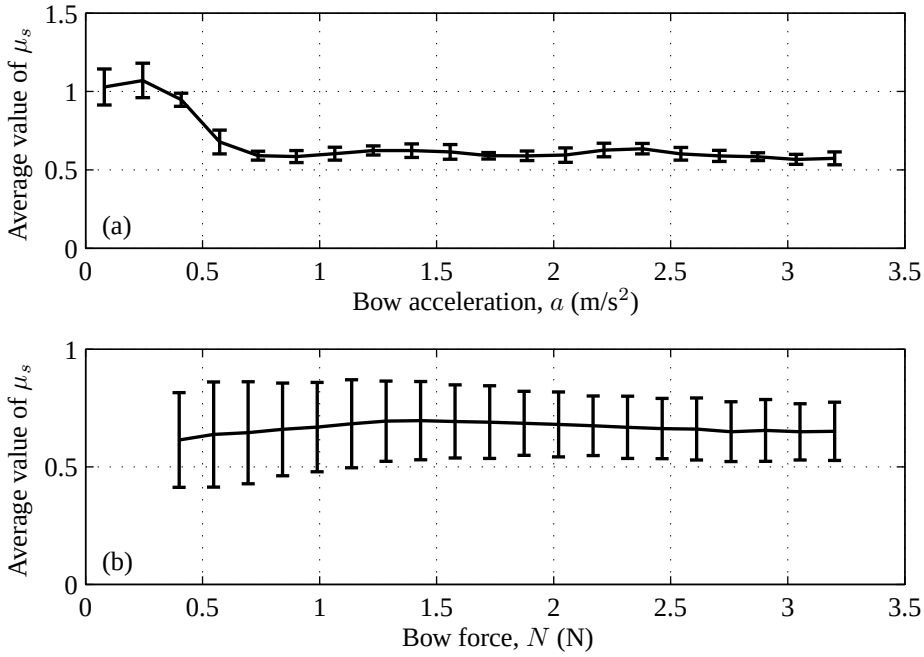

Figure 4.31: Limiting static coefficient of friction, μ_s, plotted as a function of acceleration in (a) and of force in (b). Each of the data points in (a) is an average of the values from one of the columns of Figure 4.30, and each of the data points in (b) is an average of one of the rows of Figure 4.30. The error bars indicate the standard deviation of each average. Conspicuously, μ_s is seen to increase by a factor of two when a is less than approximately 0.6 m/s^2.

This result is supported by repeating the same calculation on the data used to generate Figure 4.29; the results are shown in Figures 4.32 and 4.33. The dependence of μ_s on N and a is almost indistinguishable from that seen previously in Figures 4.30 and 4.31, demonstrating that the limiting static coefficient of friction is larger at low accelerations regardless of the order in which the data is gathered.

"Spike" Observed In Cases with Larger Friction

A clue as to the reason for this increase in limiting friction coefficient before first slip at low acceleration may be found by careful examination of the bridge force at first slip. Interestingly, in all observed cases in which the friction is significantly larger than normal, an apparent "spike" can be seen at the start of the first flyback. An example of this feature — which is presumably linked to the increase in friction — is shown in Figure 4.34. Indeed, a similar "spike" can be seen in one of the bridge force waveforms shown previously, in Figure 4.22(c).

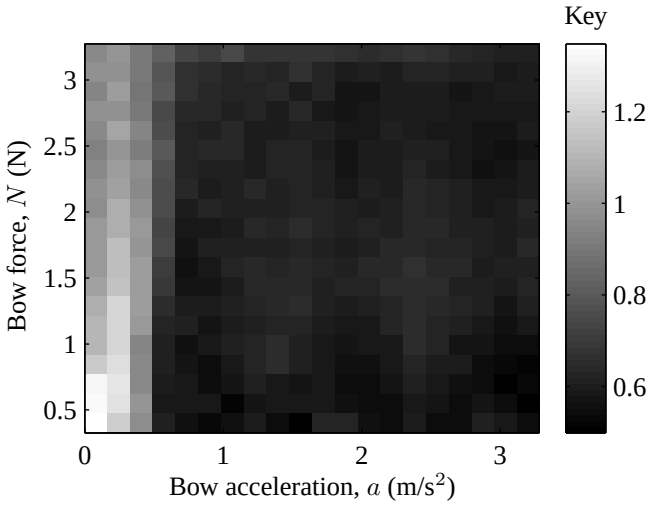

Figure 4.32: Coefficient of friction just before the first slip, based on the same data used to generate the seven plots in Figure 4.29. As with Figure 4.30, the darkness of each pixel indicates the value of coefficient of friction according to the bar on the right. The pattern of light and dark pixels is very similar to before, confirming that the friction just before first slip is repeatedly larger at smaller values of acceleration.

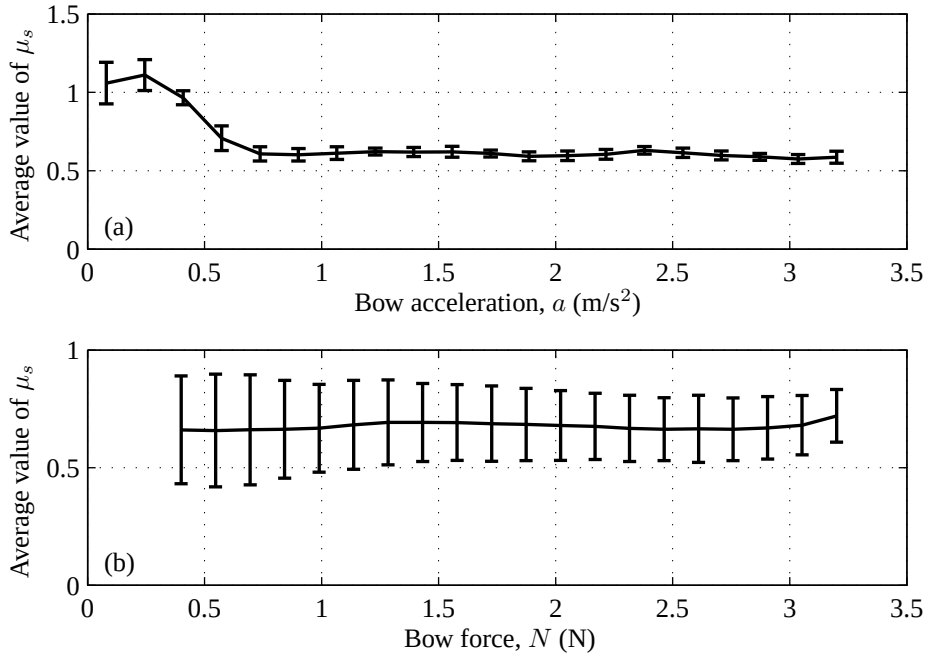

Figure 4.33: Limiting static coefficient of friction, μ_s, plotted as a function of acceleration in (a) and of force in (b), based on the data used in Figure 4.32. These are plotted in the same manner as, and look very similar to, Figures 4.31(a) and (b). Thus, the result that μ_s depends heavily on a is unchanged by reversing the order of gathering the data.

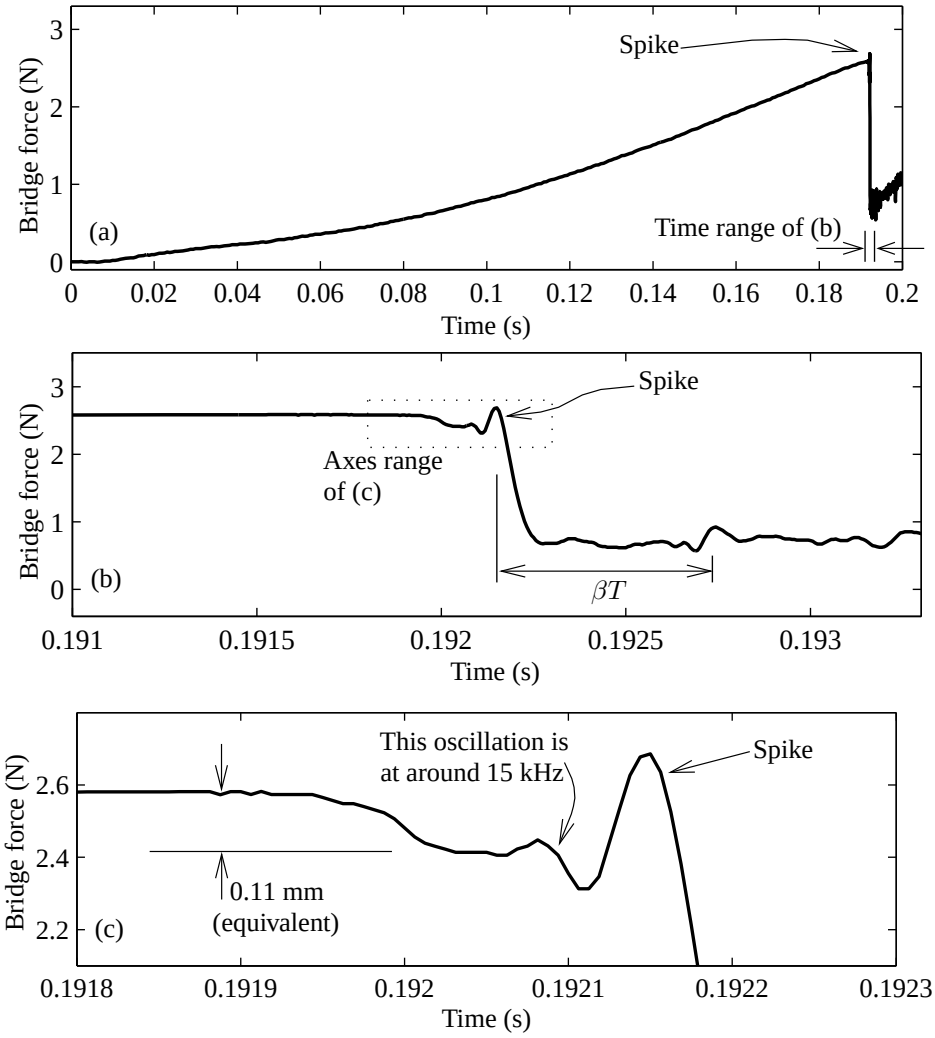

Figure 4.34: The "spike" seen in the bridge force as described in the text, (a) in the context of the rest of the transient, and (b) and (c) considerably magnified (note the different time scales). In all cases containing a "spike", the shape of the spike is very similar to the one shown here: the bridge force drops by around 0.15 N, rises back up in what appeared to be the "spike" in (a), and then falls considerably further due to the first large slip. The small oscillation in bridge force at and slightly before the spike has a frequency of approximately 15 kHz, which is around one seventh of the high-pass 3 dB cut-off frequency of the charge amplifier used, as quoted by the manufacturer (see page 67), suggesting that this feature of the waveform has been captured accurately. The vertical scale of the "spike" is 0.15 N as already mentioned, corresponding to approximately 0.11 mm of string displacement at the bowing point. This is of the right order of magnitude to be associated with the (0.97 mm diameter) string jumping clear of an accumulation of rosin. The reflection of the spike off the bow can, incidently, be observed in (b) a time βT after the original spike itself, as indicated.

In the case shown in Figure 4.34 as in every other case where it has been observed, when this "spike" is looked at more closely it turns out to be the final part of an oscillation following a *drop* in bridge force; the drop is so brief that it was initially masked by the rest of the bridge force, and as such is almost invisible in Figure 4.34(a). In every instance in which it was observed, this drop in bridge force occurred immediately before the first slip, or flyback in bridge force. Its shape is essentially the same each time: the bridge force drops by around 0.15 N, before an oscillation of about 15 kHz grows — the original "spike" in Figure 4.34(a) itself appears to be part of this oscillation.

One explanation for this feature, and the concurrent increase in limiting coefficient of friction, could be that at low accelerations there is enough time between the start of the bow movement and the first slip that either: (1) the string is given enough time to "plough up" an accumulation of rosin into its path as sketched in Figure 4.35, or (2) "junction growth" [82] (i.e. an increase in contact area between the string and the perspex rod, or "bow", due to the deformation of surface asperities). In either case, there would be an increased resistance to slipping, since a greater area of rosin would need to be fractured; if the shear yield strength of rosin is k_y, and the area of contact between the bow and string is A, then the friction required to induce slipping is $k_y A$. As such, the increase in friction seen at low accelerations in Figures 4.30–4.33 is attributable to the physical barrier presented by the increased contact area, and the oscillatory feature seen in the bridge force is attributable to the string jumping clear at the start of the first slip. Promisingly, the overall scale of the feature in the bridge force is 0.15 N, corresponding to a string displacement at the bowing point of the order of 0.1 mm (c.f. Figure 4.2); it seems natural therefore to conclude that this is the result of the string (which is 1 mm in diameter) breaking free from a patch of rosin.

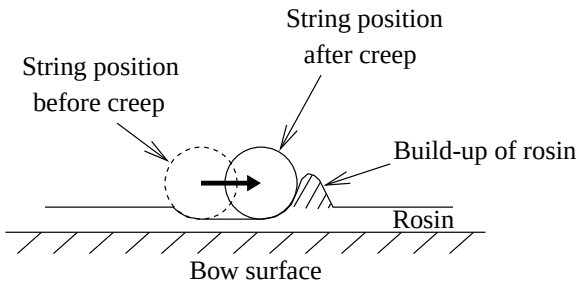

Figure 4.35: Material build-up in front of the string, caused by "ploughing" (not drawn to scale). This figure is drawn in the frame of reference of the bow; relative to the string, the bow is moving to the left.

If this feature of the bridge force is indeed the result of the string suddenly jumping clear from an obstacle, then it is worth reviewing the theoretical response of a string to a step change in displacement (i.e. jump) at a point along the string. As a first approximation, we neglect the bending stiffness of the string, so that the motion of the string may be described by d'Alembert waves [22, Ch.2]. Consequently, a jump in displacement of unit magnitude causes step-like displacement waves of equal magnitude to travel in each direction away from the bow. Using the method of im-

ages, the condition of (approximately) zero displacement at the bridge gives rise to the existence of equal and opposite waves on the other side of the string terminations that cancel out the actual waves impinging on the string terminations.

Figure 4.36 shows these waves travelling along the string, although the waves are shown rounded (because the string cannot jump instantaneously). As shown in the figure, the slope of the string is briefly smaller during the reflection, which would cause a brief drop in bridge force. It seems plausible therefore that the brief drop in bridge force seen in Figure 4.34 was caused by the string jumping clear of an accumulation of rosin.

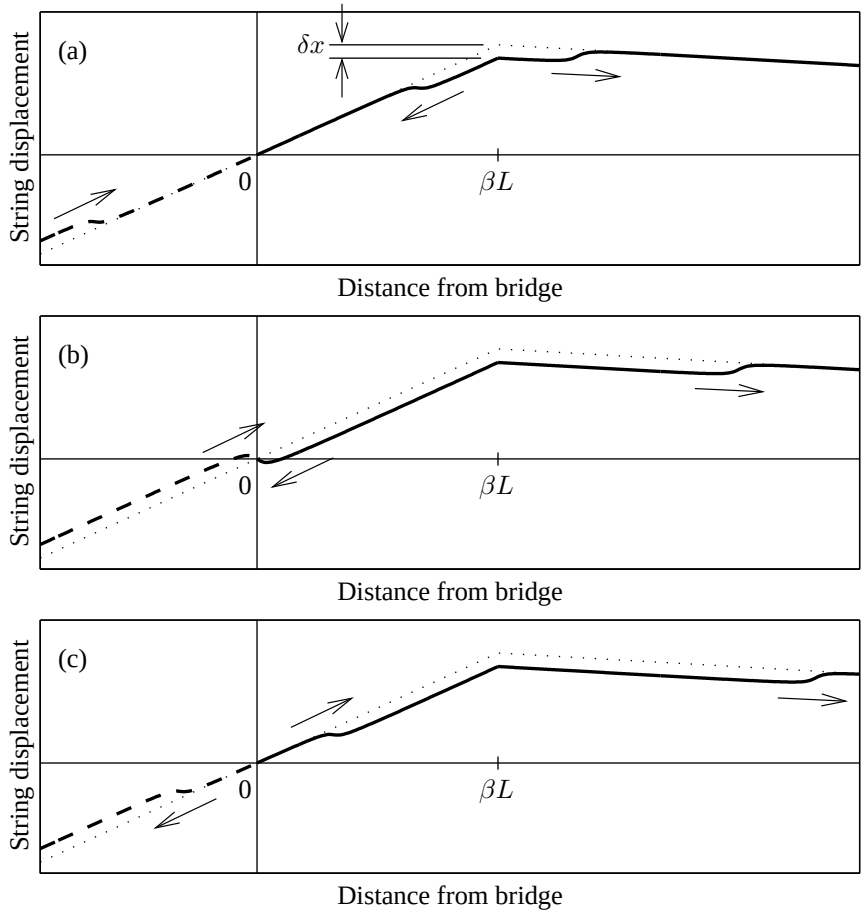

Figure 4.36: Waves generated by a quick change in displacement, not drawn to scale. The waves are of magnitude δx, and have only travelled a short distance from the bow in (a), but have travelled a distance βL in (b), and slightly further in (c). The string is indicated with a solid line, the "virtual wave" on the far side of the bridge is indicated with a dashed line, and the string's shape before the wave was generated is indicated by a dotted line. At the moment the wave travelling towards the bridge impinges on the bridge, the bridge force decreases briefly as the slope of the string temporarily dips.

4.3.3 VIBRATION REGIME IN THE N-v_b PLANE

The third and final parameter space to be investigated is the bow force vs. bow speed plane. In this section, the bowing machine is used to perform "switch on" transients: with the bow and string initially at rest, the velocity of the bow is abruptly increased to some value v_b while the bow force is held at a constant value N.

MAP OF PERFORMANCE CAPABILITY OF BOWING MACHINE IN THE N-v_b PLANE

As discussed in Chapter 1, several past investigators have performed simulations where the force stays constant and the bow speed instantaneously changes from zero to a non-zero constant value. In practice, achieving an instantaneous change in bow velocity requires an infinite amount of thrust for an infinitesimal period of time, which is impossible. In the last chapter however, it was demonstrated that a combination of feedback control and open-loop compensation has enabled the bowing machine to change velocity in only around 0.01 s. Following this, two pre-requisites may be defined when using the bowing machine to actuate a switch on transient:

1. The bow speed must reach at least 95% of the required speed v_b by the time the string slips for the first time.

2. The impulsive thrust used by the bowing machine to achieve a rapid change in bow speed must not disturb the normal force exerted by the bow on the string. More precisely, the bow force must not oscillate with an amplitude of more than 5% of the required force N.

For a range of values of v_b and N, the success of the bowing machine at passing these criteria was evaluated. The resulting performance envelope is shown in Figure 4.37: the grey region indicates conditions in which one or other of the above two tests failed, and the white area indicates the region where the bowing machine succeeded in both tests. It was found that boundary of the grey region is well approximated by a straight line, as shown.

While the thresholds that define the above two tests were chosen somewhat arbitrarily, the results are similar if different thresholds are chosen.

RESULTS: PRE-HELMHOLTZ MOTION TRANSIENT DURATION IN THE N-v_b PLANE

With the bowing machine made to actuate an approximately step-like change in bow velocity, the bridge force was measured and analyzed in the same manner as it was for the Guettler diagrams in the previous section, to give the time taken to achieve Helmholtz motion relative to the first slip for a range of values of N and v_b. The results are shown in Figure 4.38 with $\beta = 0.08$, plotted with the same convention as the Guettler diagrams previously. The combinations of N and v_b that the bowing machine could not successfully actuate are covered by the grey region.

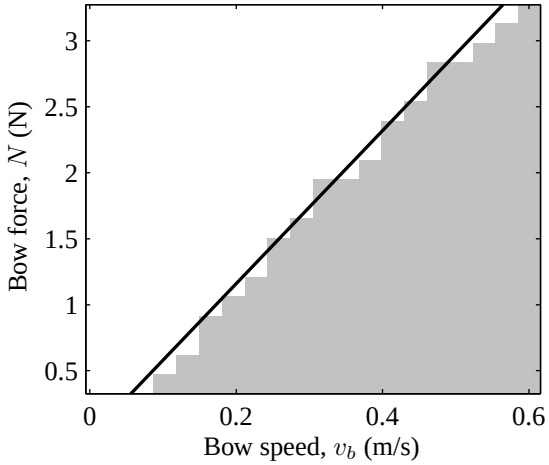

Figure 4.37: The white pixels indicate the region in the bow force vs. bow speed plane in which the bowing machine is capable of achieving "switch on" transients. The grey pixels indicate that the bowing machine either failed to accelerate to within 5% of the required bow speed by the time of the first slip, or that the bow force fluctuated by more than 5% of its nominal value during the bowing gesture. The results shown here strictly only apply when $\beta = 0.08$.

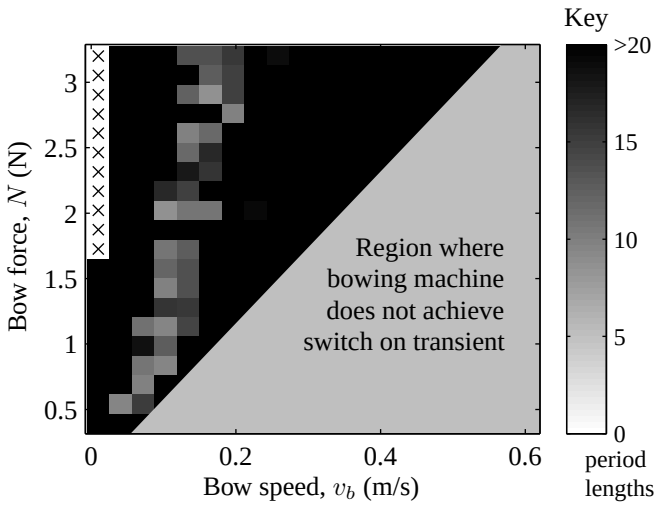

Figure 4.38: Time taken to produce Helmholtz motion, relative to the first slip, in the N vs. v_b plane, for $\beta = 0.08$. As with the Guettler diagrams of the previous section, the delay between the first slip and the onset of Helmholtz motion at a given combination of bow force and velocity is indicated by the shade of the pixel at the corresponding location in the N vs. v_b plane, according to the guide on the right. White pixels with crosses ("$\times$") indicate that the first slip occurred less than twenty period lengths before the end of the bridge force measurement, making it infeasible to deduce whether or not the pre-Helmholtz motion delay lasted twenty period lengths. The grey shaded region indicates the combinations of N and v_b that the bowing machine could not achieve, as discussed in Figure 4.37.

The lack of white pixels in Figure 4.38 suggests that, at least when $\beta = 0.08$, switch on bowing gestures are not conducive to the rapid production of Helmholtz motion. This observation is in accordance with Guettler [45], who argued that switch on bowing gestures could *never* produce "perfect transients", in the sense defined previously.

COMPARISON WITH SCHELLENG'S LOWER BOW FORCE LIMIT

In Section 4.3.1, the lower boundary of the region of the Schelleng diagram containing occurrences of Helmholtz motion was found to be well represented by $0.00086/\beta^2$ (or $0.017 v_b/\beta^2$), i.e. by Schelleng's minimum bow force with $Z^2/2\lambda_b(\mu_s - \mu_d)$ set to 0.017 Ns/m. Schelleng's minimum bow force limit pertains to the stability of a pre-existing Helmholtz motion at low bow forces, and for this reason the Schelleng diagram in Section 4.3.1 contains the results from producing Helmholtz motion as an initial condition. The results in the N vs. v_b plane in this section on the other hand were obtained with the string initially at rest. With the string started from rest, one would expect to require more force to *create* Helmholtz motion that one would to *sustain* it.

It is no surprise, then, that the best fit line given by $N_{min} = 0.017 v_b/\beta^2$ (the best fit minimum bow force limit from the Schelleng diagram) is around four times lower than the lower limit of the Helmholtz motion region in Figure 4.38. In Figure 4.39, $0.017 v_b/\beta^2$ is superimposed on the results shown in Figure 4.38. The considerable gap between the region containing Helmholtz motion and the lower limit obtained from the Schelleng diagram underlines the importance that initial conditions make to the string's vibration waveform: in this large gap, both Helmholtz motion and multiple slipping motion are stable, and can be achieved given different initial conditions

INDIVIDUAL BRIDGE FORCE WAVEFORMS

It is more revealing, however, to review aspects of the appearance of individual bridge force waveforms from this family of constant bow speed bowing gestures.

Figure 4.41 contains four basic waveforms, with the values of N and v_b used for each waveform given by Figure 4.40. The first waveform, in Figure 4.41(a), illustrates the effect of the 0.01 s response time of the bowing machine: the bridge force takes around 0.01 s to obtain the required slope (as indicated by the dotted line). The waveform shown in Figure 4.41(b) shows one of the few vibration transients in which Helmholtz motion was produced. The waveform shown in Figure 4.41(c) shows raucous motion, and the waveform in Figure 4.41(d) shows double slipping.

In Figure 4.41(c), we can again see the "spike-like" feature at the start of the first slip that was discussed on page 100. The fact that the spike coincides with an increase in limiting static coefficient of friction is evident from the fact that the bridge force is seen to rise to a larger value before the first slip (at around 0.039 s) than before any of the other slips (at 0.054 s, 0.074 s, 0.095 s and 0.115 s): in each case the bridge force rises to a value of $(1 - \beta)\mu_s N$; clearly therefore μ_s is largest

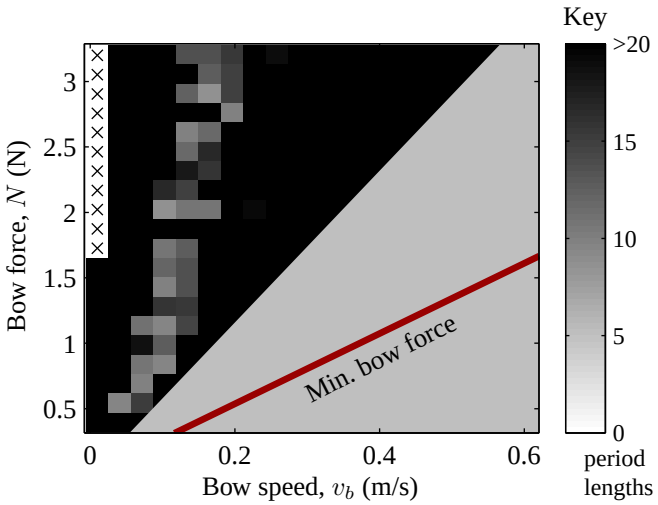

Figure 4.39: The results from Figure 4.38, superimposed with the minimum bow force limit derived in Section 4.3.1 for cases in which the string's initial condition was Helmholtz motion. The nonlinearity of the bowed string is clearly demonstrated by the large gap between the previous minimum bow force limit for Helmholtz motion (indicated by a solid line) and the region (indicated by grey pixels) in which Helmholtz motion was observed.

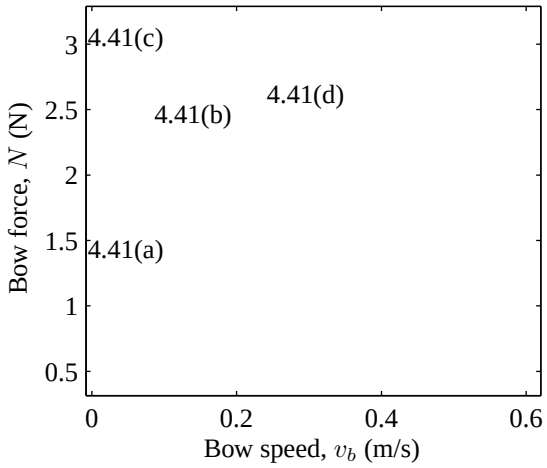

Figure 4.40: Location in the N vs. v_b plane of the force and velocity used to generate the individual bridge force waveforms shown in Figures 4.41. Each label in this figure is vertically and horizontally centered over the coordinates of the corresponding waveform. β was 0.08 in all of the above cases.

before the first slip. (In fact there are smaller spike-like features at the start of each of the slips, which are only visible if magnified.)

Also in Figure 4.41(c), once the bridge force first reaches a value of around 1.6 N before the first slip, its slope decreases by around 30%; this is made visible by the dotted line, whose slope equals the theoretical value during sticking, $2Z_T v_b/\beta T$. This decrease in slope suggests that there is

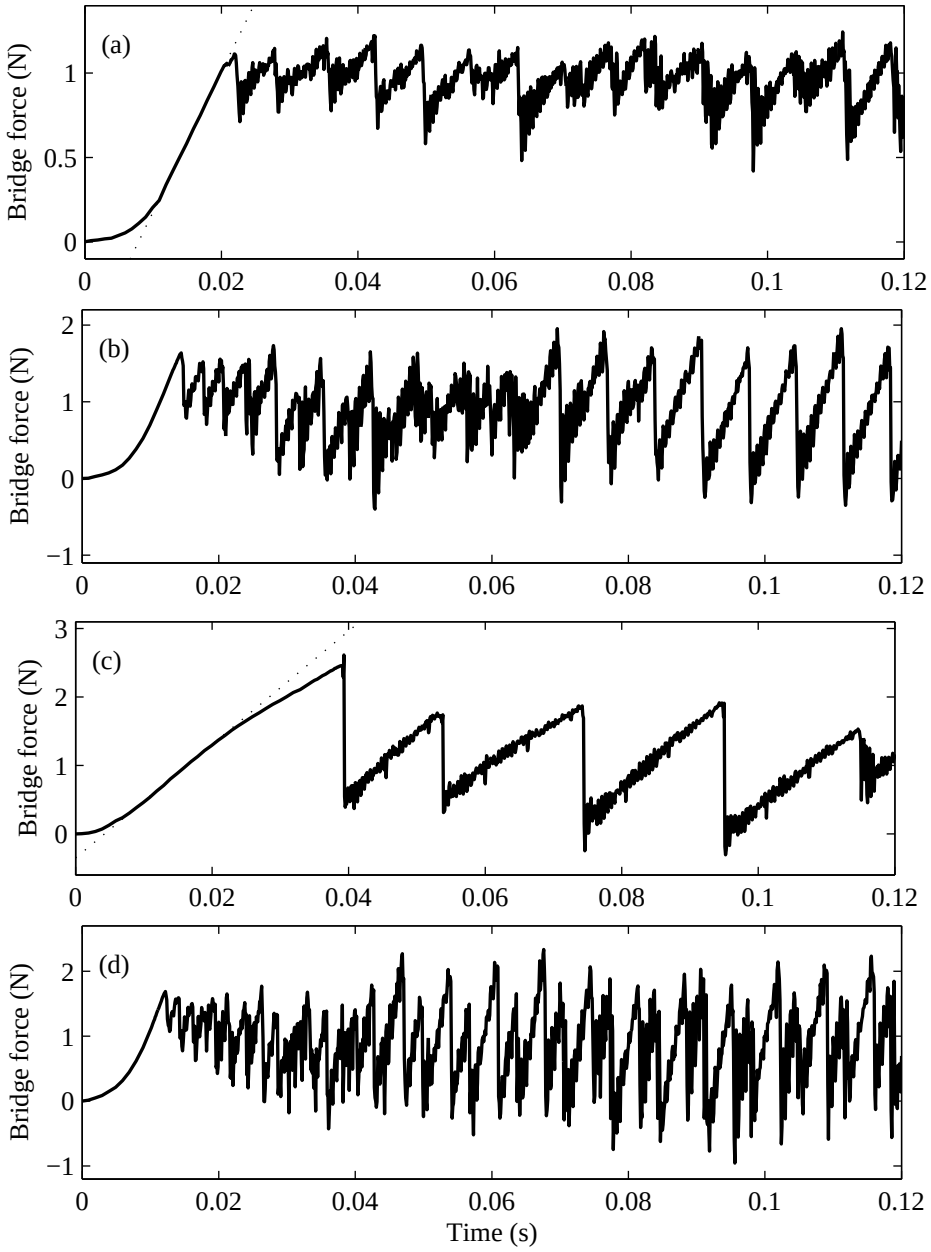

Figure 4.41: Examples of bridge force waveforms generated by "switch on" transients. The operating point in the N vs. v_b plane for each waveform is shown in Figure 4.40, and β is 0.08 in all cases. In the top plot, a dotted line has been superimposed on the waveform to show the theoretical slope of the bridge force during sticking. By about 0.01 s the bridge force has straightened out and almost exactly acquired this slope; the first slip is not until around 0.021 s, indicating that the bow speed has reached its target value well before the first slip. The lower three plots are typical examples of different types of motion: (b) Helmholtz motion (after 0.085 s); (c) raucous motion; (d) multiple slipping motion. The horizontal scale is the same for all four plots.

some relative motion between the perspex rod (or "bow") and the string. Indeed, the fact that this decrease in slope approximately coincides with the time when the bridge force has risen above the peak values from subsequent sticking periods suggests that while μ_s increases (through junction growth or ploughing, as discussed on page 103), the string creeps along the surface of the rod.

At even lower bow speeds than that used to produce Figure 4.41(c), this slow relative motion between the bow and the string, or creep, was observed frequently. A typical example is shown in Figure 4.42, where again the theoretical value of bridge force and the actual bridge force are indicated by dotted and solid lines, respectively. In Figure 4.42, the bridge force is seen to fall below the value of $(2Z_T v_b/\beta T) \times t$ by some 1.4 N by the time of the first slip; this corresponds to a relative displacement of around 0.7 mm at the bowing point. It should be noted that this deficit in bridge force could not have been caused by a bandwidth limitation of the charge amplifier used to amplify the bridge force signal, for two reasons: (1) the low-pass cutoff frequency of the amplifier is 0.53 Hz, which means that the 0.25 s of data shown in Figure 4.42 is too short to be affected; and (2) the effect of low-pass filtering a ramp-like signal is to cause its slope to gradually decrease and curve downwards, where as in Figure 4.42 the slope of the bridge force is approximately constant — the bridge force certainly does not curve downwards.

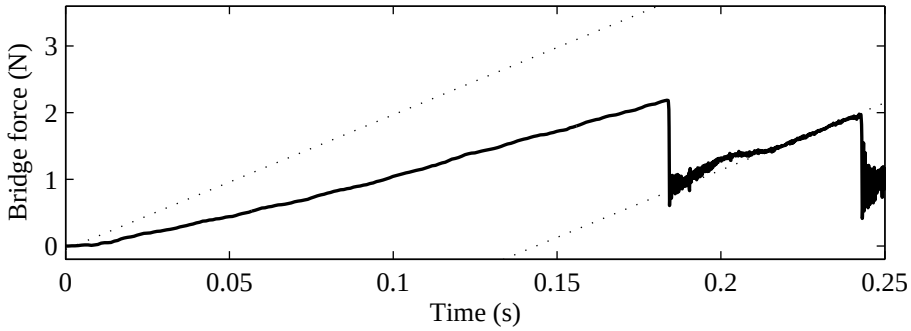

Figure 4.42: Bridge force waveform generated with $N = 3.2$ N, $v_b = 0.01$ m/s, and $\beta = 0.08$. The dotted lines have the slope that the bridge force would theoretically have during sticking when the bow speed is 0.01 m/s; as is typical at low bow speeds and large bow forces, the bridge force gradually drops considerably below this line, suggesting a slow creep-like relative motion between the bow and the string. By the time of the first slip, the gap between the top dotted line and the actual bridge force is around 1.4 N, which corresponds to a relative displacement of around 0.7 mm, between the bow and the string. Also visible in this figure, the bridge force is seen to form a "hump"-like shape just after the first slip, at around 0.2 s. This often follows long periods of creep. The "spike-like" feature at first slip is not captured in this case, because the data acquisition sampling rate was too low.

Another feature of Figure 4.42 that is frequently seen at low bow speeds and high bow forces is the "surge" in bridge force immediately after the first slip, at around 0.2 s. This surge is highlighted by the lower of the two dotted lines shown, which again has a slope of $2Z_T v_b/\beta T$. The reason for this surge is not clear, although it is apparently due to a viscoelastic "springing back", following the prolonged period of sticking. This springing back could be due to the viscoelasticity of the rosin layer (rosin is a polymer, and so one would expect it to exhibit some viscoelasticity [83]),

although it could alternatively be due to movement of the entire cello itself. Aside from the surge, the bridge force has the same slope as the dotted line during the second sticking period.

Occasionally, this surge in the bridge force following the first slip has been observed to be sufficiently vigorous that it causes the string to slip in the "forwards" direction, i.e. in the same direction as the bow's movement. An example of this otherwise unusual occurrence is shown in Figure 4.43.

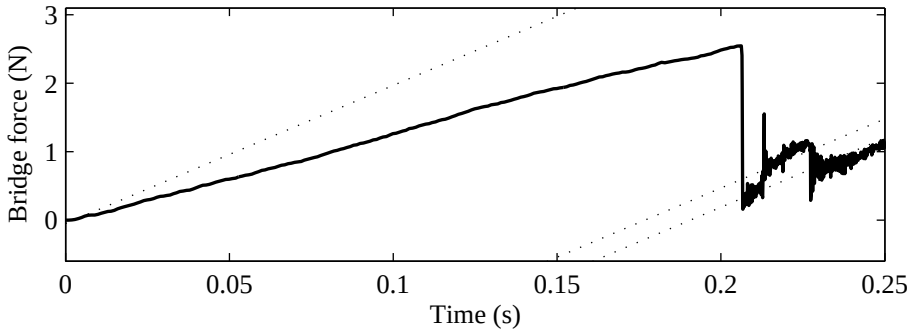

Figure 4.43: Same as Figure 4.42, but with a more pronounced surge in the bridge force just after the first slip. In this case, the surge causes a "forwards slip" as well as a backwards slip, causing the bridge force to jump upwards as well as downwards. The dotted lines again show the theoretical slope for the bridge force with $v_b = 0.01$ m/s.

FRICTION JUST BEFORE FIRST SLIP

As previously, the value of limiting static coefficient of friction μ_s was deduced from the bridge force by dividing the change in bridge force between the start of each bowing gesture and the first slip by $(1-\beta)N$. The results are shown in Figure 4.44. As was seen in Figures 4.32 and 4.30, μ_s can be seen to be slightly larger at lower bow speeds. Figure 4.45 shows the average of each column and row of the data in Figure 4.44 plotted against v_b and N respectively, reiterating the increase in μ_s at low bow speeds.

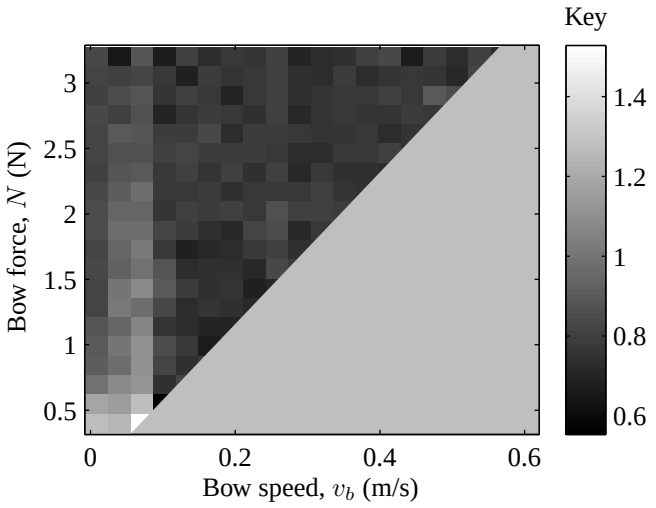

Figure 4.44: Limiting static coefficient of friction μ_s just before the first slip, based on the same data used to generate Figure 4.38. The darkness of each pixel indicates the value of μ_s according to the guide on the right. The grey shaded region again indicates combinations of N and v_b that the bowing machine could not achieve, as discussed in Figure 4.37.

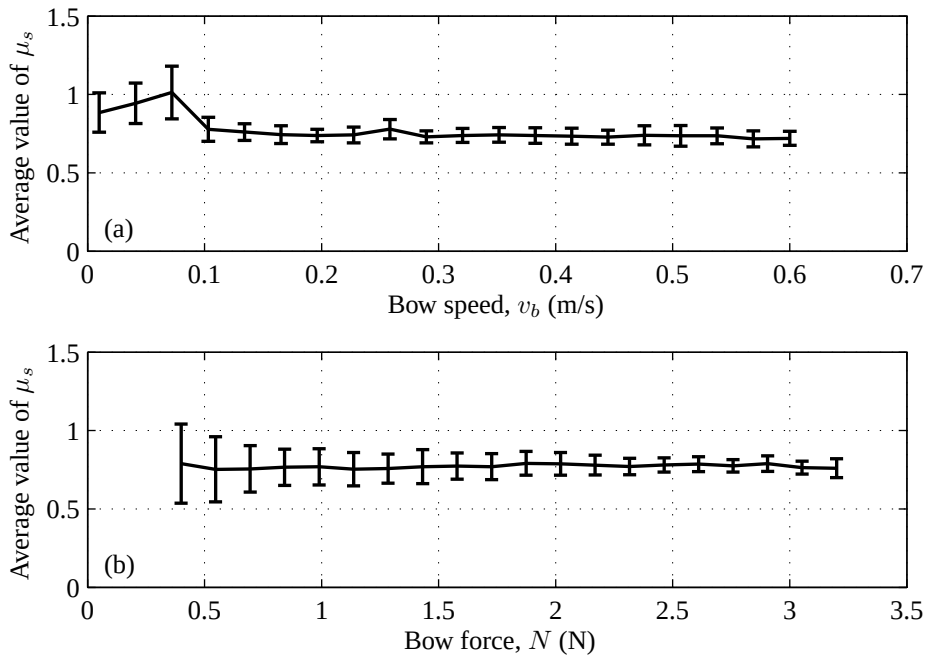

Figure 4.45: Limiting static coefficient of friction, μ_s, plotted as a function of bow speed in (a) and of force in (b), based on the data used in Figure 4.44. Each of the data points in (a) is an average of the values from one column of Figure 4.44, and each of the data points in (b) is an average of one of the rows of Figure 4.44. The error bars indicate the standard deviation incurred in the averaging process. μ_s is seen to be roughly equal to 0.74, except at low bow speeds. For convenience, all 400 data points in Figure 4.44 were included in the averages, but the result is almost unchanged by excluding the operating points which the bowing machine could not actuate.

RECONSTRUCTING A FRICTION CURVE FROM BRIDGE FORCE FLYBACK MEASUREMENTS

From Equation (1.9a) on page 11, the change in string velocity at the first slip, $(\Delta v)_{\text{first slip}}$, is equal to $1/2Z_T$ times the concurrent change in friction, $(\Delta f)_{\text{first slip}}$, and hence $(1/2Z_T N)$ times the change in coefficient of friction, $(\Delta\mu)_{\text{first slip}}$. Therefore, because the magnitude of the flyback in bridge force at first slip, $\Delta(\text{Bridge force})_{\text{first slip}}$, is equal to $(\Delta f)_{\text{first slip}}$, the values of $(\Delta\mu)_{\text{first slip}}$ and $(\Delta v)_{\text{first slip}}$ may be calculated according to:

$$(\Delta\mu)_{\text{first slip}} = \Delta(\text{Bridge force})_{\text{first slip}}/N, \tag{4.2a}$$

$$(\Delta v)_{\text{first slip}} = \Delta(\text{Bridge force})_{\text{first slip}}/2Z_T, \tag{4.2b}$$

Hence, because μ_s has already been measured, the absolute value of μ during the first slip can be calculated as $\mu_s - (\Delta\mu)_{\text{first slip}}$, and plotted with respect to $(\Delta v)_{\text{first slip}}$ to obtain a "reconstructed friction curve". The possibility of such a calculation was suggested by McIntyre et al. [34], and provides a novel alternative method for measuring the f vs. v characteristics of rosin.

To this end, the value of $\Delta(\text{Bridge force})_{\text{first slip}}$ for each operating point in the N vs. v_b plane is shown in Figure 4.46. The flyback at the first slip is apparently independent of bow speed, as seen also in Figure 4.47, which shows the result of averaging the results with respect to N and v_b. For this reason, the values of $\Delta(\text{Bridge force})_{\text{first slip}}$ were averaged with respect to v_b before being used to reconstruct a friction curve. The corresponding values of $\Delta(\text{Bridge force})_{\text{first slip}}/N$, after being averaged with respect to v_b, are shown in Figure 4.48: these values were used to reconstruct the friction curve.

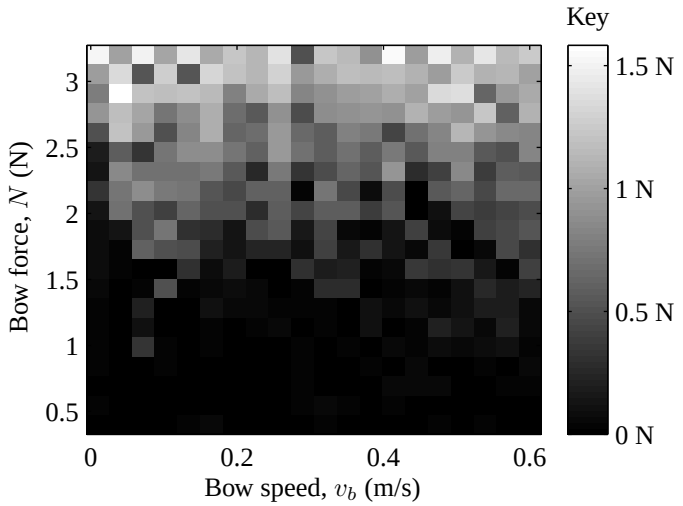

Figure 4.46: Magnitude of flyback in bridge force $\Delta(\text{Bridge force})_{\text{first slip}}$ due to the first slip, based on the same data used to generate Figure 4.38. The darkness of each pixel indicates the value of $\Delta(\text{Bridge force})_{\text{first slip}}$ according to the guide on the right.

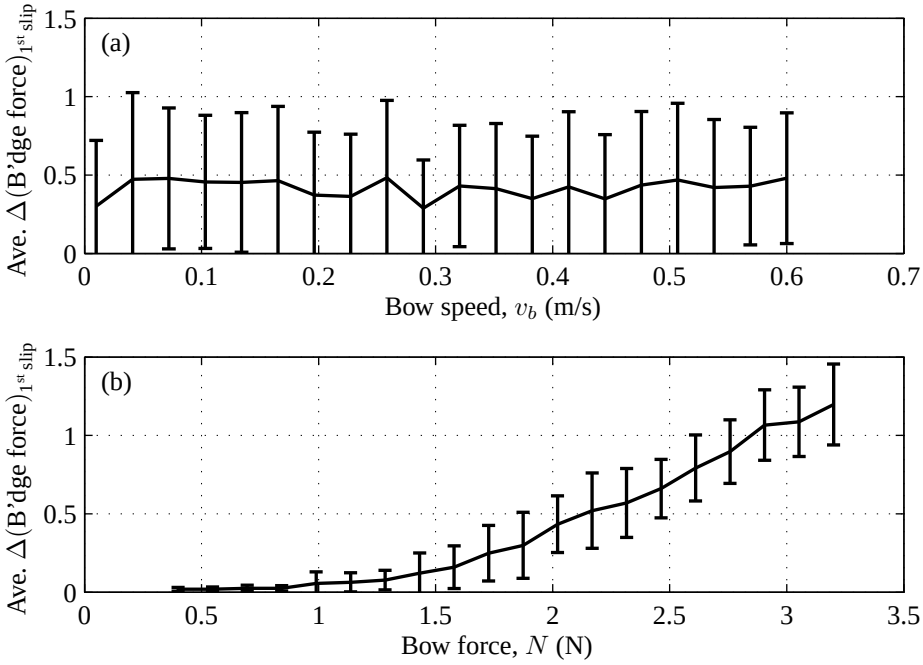

Figure 4.47: Magnitude of flyback in bridge force $\Delta(\text{Bridge force})_{\text{first slip}}$ due to the first slip, plotted as a function of bow speed in (a) and of force in (b), based on the data used in Figure 4.46. Each of the data points in (a) is an average of the values from one column of Figure 4.46, and each of the data points in (b) is an average of one of the rows of Figure 4.46. The error bars indicate the standard deviation incurred in the averaging process.

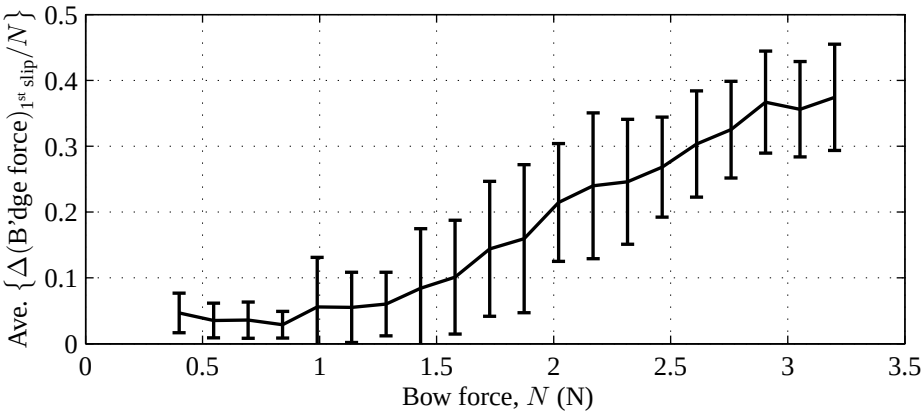

Figure 4.48: Magnitude of bridge force flyback divided by bow force, $\Delta(\text{Bridge force})_{\text{first slip}}/N$ at first slip. Each point represents the average value over the whole range of bow speeds, with the error bars indicating the standard deviation incurred in the averaging process.

The twenty pairs of values $(\Delta v, \mu_s - \Delta\mu)$ thus obtained using the results from Figures 4.45(b), 4.47(b) and Figure 4.48 and Equations (4.2b) and (4.2a) are hence shown in Figure 4.49 (as circles), along with a line of best fit (as a dotted line). For comparison, the friction curve obtained by Smith and Woodhouse [43] in steady sliding tests is superimposed over the results as a solid line.

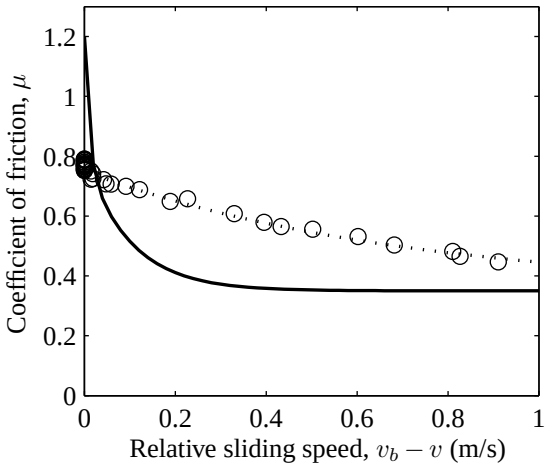

Figure 4.49: Measurements of points along the friction curve, indicated by circles. The measurements of μ plotted at $v_b - v = 0$ are those obtained under limiting static friction conditions. The measurements of μ and $v_b - v$ plotted at non-zero values of $v_b - v$ were obtained using the extent of the flyback in bridge force at first slip, as described in the text. Because the measurements of friction showed little variation with respect to v_b when $v_b > 0.08$ m/s, each data point shown in this plot is the result obtained after averaging the measurements of μ_s and flyback with respect to v_b; in doing so the shape of the friction curve becomes considerably clearer. A best fit through the measurements is shown with the dotted line, and Smith and Woodhouse's steady sliding measurements are shown with a solid line.

The best-fit line superimposed over the measurements in Figure 4.49 as a dotted line is given by the following relation:

$$\mu \;=\; 0.4\, e^{\,(v - v_b)/0.7} + 0.35. \tag{4.3}$$

For comparison, the equivalent equation of best fit given by Smith and Woodhouse [43], based on their steady sliding tests is as follows:

$$\mu \;=\; 0.4\, e^{\,(v - v_b)/0.01} + 0.45\, e^{\,(v - v_b)/0.1} + 0.35. \tag{4.4}$$

The reconstructed friction curve is clearly at odds with Smith and Woodhouse's measurements — as indeed were Smith and Woodhouse's own dynamic friction tests — reinforcing the suggestion that a friction curve, as measured under steady sliding conditions, is not relevant to the real bowed string with very short time scale changes in relative velocity.

4.4 SUMMARY OF FINDINGS

In this chapter, a variety of experimental results were shown in order to demonstrate the general behaviour of a cello string bowed by a rigid point-contacting bow. The scope of these results makes them the first of their kind, in that they show the vibration response of the string as it is bowed according to well-defined families of bowing gestures in three parameter spaces.

In various respects, the results agreed with the analytical and computational predictions of previous investigators:

- When the string was initialized with Helmholtz motion, the range of bow forces that could be used to sustain Helmholtz motion depended upon β approximately as proposed by Schelleng [16]: the maximum allowable bow force was approximately proportional to $1/\beta$, and the minimum allowable bow force was approximately proportional to $1/\beta^2$. If the bow force was too large, the string lapses into "raucous motion", and if the bow force was too small, then multiple slipping occurs.

- S-motion was seen to occur when the value of β was close to the reciprocal of an integer. Furthermore, the large slipping speed associated with S-motion was seen to cause S-motion to be sustainable at larger bow forces than Helmholtz motion; the maximum allowable bow force was considerably larger for S-motion than it was for Helmholtz motion.

- The amount of bow force required to produce Helmholtz motion when the string was initially at rest was several times larger than the amount of bow force required to sustain Helmholtz motion once it had been produced. Hence, the minimum bow force limit was much larger when the string was started from rest, compared to when it was initialized with Helmholtz motion.

- When the bow was accelerated from rest with a constant bow force, the region of force-acceleration parameter space in which Helmholtz motion was produced was wedge-shaped, as could be seen with the simulations of Guettler [45]. This wedge became narrower and moved upwards as β was decreased.

- Provided the bow speed was not too small (less than 0.1 m/s for constant velocity bowing gestures or less than 0.5 m/s^2 for constant acceleration bowing gestures), the limiting static coefficient of friction was found to be independent of N. This supports the common assumption that $f \propto N$.

However, several features of the experimental results have not been reported in previous theoretical or numerical analyses of the bowed string:

- The change in the appearance of the Guettler diagram as β was decreased was not gradual. Of the eight values of β tried, the value 0.1428 was shown to make the string surprisingly susceptible to multiple flyback motion, and 0.1133 was shown to make the string susceptible to S-motion.

- The bowed string is sufficiently "twitchy" that consecutive nominally similar measurements of transient string vibration were rarely alike in every detail. For example, the detailed pattern of short and long pre-Helmholtz motion transients in the Guettler diagram was different in consecutive measurements (although the general appearance was not).

- When the order in which the bow force and bow acceleration were varied when generating a Guettler diagram was reversed, the lower boundary of the region in the force-acceleration plane containing Helmholtz motion was observed to move upwards slightly. This corresponds to a small (but noticeable) increase in the minimum bow force required to produce Helmholtz motion using a constant acceleration bowing gesture, which may result from lengthy thermal time lags from previous bowing gestures.

- Whereas the vast majority of measurements of the vibration of the string show that its velocity during periods of apparent sticking is equal to the bow speed, some cases were shown in which the string's velocity was slightly less than the bow speed. In general, this "creep" only occurred in the time between the start of a bowing gesture and the first slip.

- At low bow speeds, the limiting static coefficient of friction was seen to become larger, sometimes by a factor of two, before the first slip. Detailed examination of the bridge force in such cases suggests that this may be caused by a growth of the contact area between bow and string as the string "creeps".

- A friction curve, or relationship between friction and relative sliding speed, was reconstructed from indirect measurements of the sliding velocity and coefficient of friction between the bow and the string during the first slip. This relationship was seen to be at considerable odds with the steady sliding friction measurements of Smith and Woodhouse [43], underlining the difference between steady sliding conditions and the dynamic conditions encountered in real bowing.

Results from computational simulations of the cello D-string being bowed by a rigid point-contacting bow are presented in the next chapter, in which the simulated string is bowed with the same range of bowing gestures used in experiment in this chapter. These results will be used to reflect how well existing simulation models predict the behaviour of real bowed strings.

Chapter 5

SIMULATION RESULTS

INTRODUCTION

Experimental results were presented in the last chapter to demonstrate the vibrational behaviour of the open D-string of a cello when bowed using a rigid point-contacting rod. In this chapter, equivalent results are shown from the simulation models described in Chapter 1: the first simulation model to be explored is based on the "friction curve" model; and the second simulation model uses Smith and Woodhouse's [43] "thermal plastic" rosin model. In the first case, two contrasting f-v relationships, or friction curves, are tested: that which Smith and Woodhouse [43] obtained from steady sliding tests; and that obtained in Section 4.3.3 from an analysis of bridge force flybacks. Maps of string vibration regime in various parameter spaces will be presented, and individual vibration waveforms shown, in an effort to understand the behaviour of the simulation model in the context of the experimental results of the last chapter. All simulated data is processed with the same algorithms used to process experimental data, to allow direct comparison of results.

Differences between the simulations of this chapter and the experiments of the last chapter, the causes of these differences, and suggestions for methods of alleviating them, will be discussed in the next chapter.

5.1 SIMULATIONS WITH STEADY SLIDING FRICTION CURVE

Simulations based on the existing friction curve model of rosin have been developed by previous authors [7, 26], and indeed in some detail in Chapter 1, and as such need not be introduced in great detail here. The string model used in this chapter uses the physical data for "Dominant" cello D-strings measured by previous investigators [21, 27], and the bow is assumed to be rigid and of an infinitesimal width. In this section, the coefficient of friction is assumed to depend on the relative sliding speed between the bow and the string according to Equation (4.4), which is a best fit through the steady sliding measurements of Smith and Woodhouse [43].

5.1.1 SCHELLENG DIAGRAM: VIBRATION REGIME IN THE N-β PLANE

The ability of the friction curve simulation model to predict the so-called "Schelleng diagram" is shown in Figures 5.1 and 5.2, which are nominally similar to the experimental data shown in Figures 4.12 and 4.13 respectively. As previously, in Figure 5.1 occurrences of Helmholtz motion are indicated by white pixels, occurrences of S-motion are indicated by grey pixels, and occurrences of all other types of string motion are indicated by black pixels. In Figure 4.13, the motion of the string is indicated through the use of symbols, with each symbol defined in the figure caption. In keeping with Schelleng's intentions [16], and with the method used in experiment, the simulated string was initialized with a "typical" Helmholtz motion waveform rather than started from rest, and bowed at a constant bow force and speed. The initial conditions comprise around 5 ms of transverse and rotational vibration data from a previous simulation that exhibited Helmholtz motion, scaled in proportion to v_b/β to match the nominal amplitude of Helmholtz motion at each operating point. The magnitude of bridge-bound velocity waves being sent from the bowing point (approximately equal to $1/2Z$ times the bridge force) during the "typical" Helmholtz motion waveform is shown in Figure 5.3.

In some respects, these results are similar to the experimental results shown in Figures 4.12 and 4.13: a central region of Helmholtz motion is bounded by multiple slipping at lower bow forces, and intermittent raucous motion and S-motion at larger bow forces. However, there are clear differences. Both the upper and lower boundaries of the Helmholtz motion region are lower than they were in experiment, and the region is generally wider than it was in experiment. Also, constant slipping motion was not predicted at any operating point within this range, with multiple slipping motion occurring even in the lower left corner of Figure 5.2. Instances of S-motion are predicted, although they do not appear to fall into three clear columns as they did in experiment.

It is noted in passing that the "patchy Helmholtz" region, as described on page 82, has not appeared; instead Helmholtz motion continues robustly into the lower right corner of the Schelleng diagram. It is not possible, however, to attribute this to a defect in the simulation model because the patchiness could instead be an artefact of experimental results. This is because, at large β

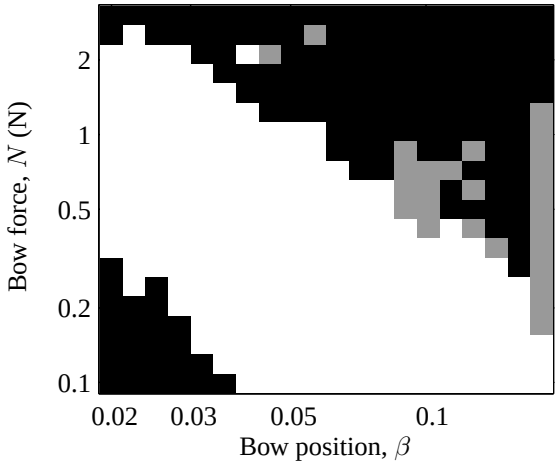

Figure 5.1: Schelleng diagram, from simulations based on the friction curve rosin model, with Smith and Woodhouse's [43] steady sliding friction curve. Here, as with the experimental equivalent in Figure 4.12, the shade of a given pixel indicates whether Helmholtz motion was sustainable at the combination of force and position corresponding to the position of the pixel. White pixels indicate that Helmholtz motion was still in evidence at the end of the two seconds of steady bowing; black pixels indicate that it was not; and grey pixels indicate that S-motion was observed. Further information about the individual operating points within the black regions is given in Figure 5.2. The bow speed is 0.05 m/s in all cases.

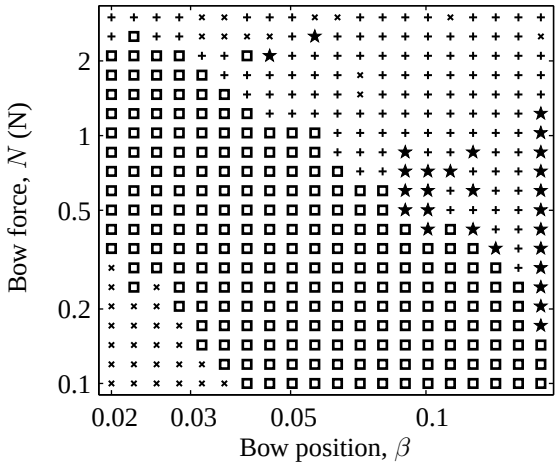

Figure 5.2: Schelleng diagram from simulations based on the friction curve rosin model, with Smith and Woodhouse's [43] steady sliding friction curve. Here, as with the experimental equivalent in Figure 4.13, squares (□) indicate that Helmholtz motion was sustained throughout the period of steady bowing; crosses (×) indicate that the string lapsed into multiple slipping motion; pluses (+) indicate raucous motion; dots (·) indicate constant slipping; and stars (★) indicate S-motion.

the amplitude of the Helmholtz motion is small, and as such the motion of string is more likely to be disrupted by small perturbations to the bowing machine, of which there were none in the simulations. The lack of a "patchy Helmholtz" region in simulation is, however, the only differ-

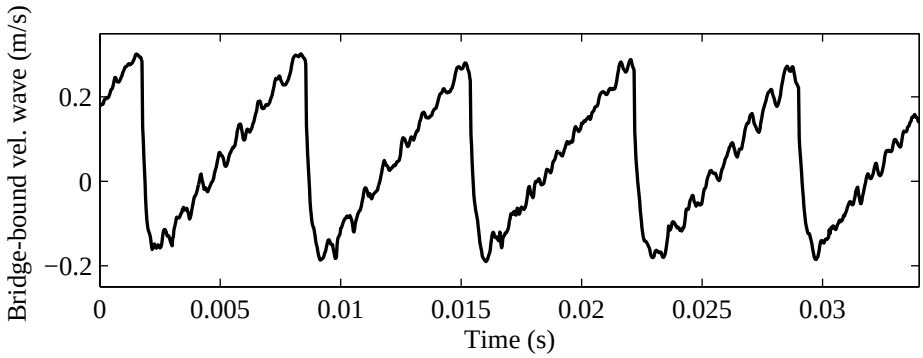

Figure 5.3: Excerpt of transverse vibration data used as part of the initial condition for the simulated Schelleng diagram. This shows the magnitude of transverse velocity waves sent towards the bridge from the bowing point, approximately equal to $1/2Z$ times the "bridge force", and hence comparable with for example Figure 4.18(a). This data was used along with excerpts of torsional waves concurrently sent towards the bridge, and transverse and torsional waves sent towards the finger. All initial conditions were scaled to be of the same magnitude as the theoretical Helmholtz motion waveform at each value of β.

ence between simulation and experiment reported here that could be attributable to experimental inaccuracy; the large gaps between the boundaries of the other regions in the experimental and simulated Schelleng diagrams are not within the bounds of experimental error.

SUPERIMPOSING THE UPPER AND LOWER FORCE LIMITS FROM EXPERIMENT

In Section 4.3.1, best fit approximations for the edges of the Helmholtz motion region of the experimentally measured Schelleng diagram were found. Following Schelleng, the upper edge of the Helmholtz motion region was approximated by a line proportional to $1/\beta$, and the lower edge was approximated by a line proportional to $1/\beta^2$. These limits have been superimposed on the data in Figures 5.1 and 5.2, in Figures 5.4 and 5.5 respectively.

These figures reiterate the difference between the upper and lower bounds of the Helmholtz motion region in the Schelleng diagrams from friction curve simulation and from experiment. The upper force limit in simulations is too low by a factor of around three, and the lower force limit in simulations is too low by a factor of around five. Therefore, with reference to Equations (1.15) and (1.16), if the mechanisms of the breakdown of steady state Helmholtz motion are as proposed by Schelleng [16], this would indicate that the values of $Z/(\mu_s - \mu_d)$ and $Z^2/\lambda_b(\mu_s - \mu_d)$ are too low by factors of three and five, respectively. Theoretically, the first of these limits could be corrected by performing simulations with a smaller value of $(\mu_s - \mu_d)$ (i.e. a "flatter" friction curve), and the second limit could be corrected by reducing λ_b (i.e. a more flexible string termination).

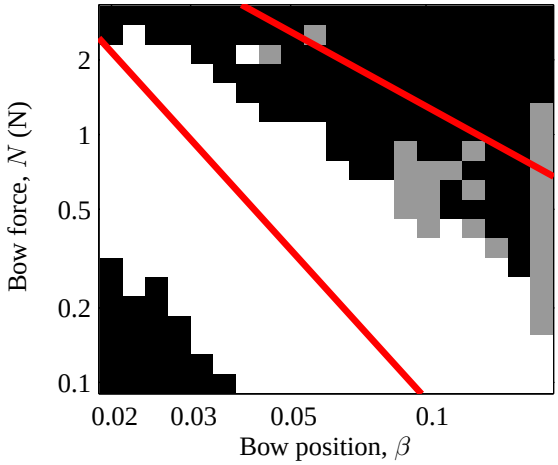

Figure 5.4: Schelleng diagram according to simulations based on Smith and Woodhouse's [43] steady sliding friction curve (same as Figure 5.1), with Schelleng's force limits superimposed as diagonal lines. The upper force limit, $0.13/\beta$, and the lower force limit, $0.00086/\beta$, were chosen to match the edges of the Helmholtz motion region in experiment, as shown in Figure 4.15.

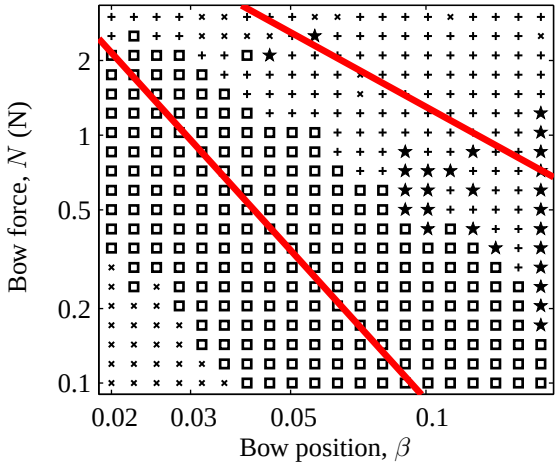

Figure 5.5: Symbolic representation of the Schelleng diagram, as simulated using Smith and Woodhouse's [43] steady sliding friction curve (same as Figure 5.2), with Schelleng's force limits superimposed as diagonal lines. The limits were chosen to match experimental data, as shown in Figure 4.16

INDIVIDUAL BRIDGE FORCE WAVEFORMS

Individual vibration waveforms corresponding to each type of motion predicted by simulations in the Schelleng diagram are shown in Figure 5.7. The locations of the operating points (i.e. values of N and β) for each waveform are shown in Figure 5.6. In each case the bridge force is calculated as $2Z$ times the magnitude of bridge-bound transverse velocity waves being sent from

the bowing point. Figure 5.7(a) shows an example of Helmholtz motion, generated at the same operating point as the experimental example in Figure 4.18(a): the two are similar in detail. Figure 5.7(b) shows an example of multiple slipping motion, which was generated at a different operating point to the experimental example of multiple slipping in Figure 4.18(b). Figure 5.7(c) shows an example of raucous motion from the same operating point as the experimental example of Figure 4.18(c); in this case, because the upper bow force limit has shifted downwards, the simulated example is "more raucous" than the experimental example (meaning, in this case, that not only is the motion non-periodic, but the duration of sticking is also considerably prolonged). Figure 5.7(d) shows an example of S-motion which is reasonably similar to the experimental example shown in Figure 4.18(e), although they were generated at different operating points. No example of constant slipping is shown, because it was not predicted at any operating point in the Schelleng diagram.

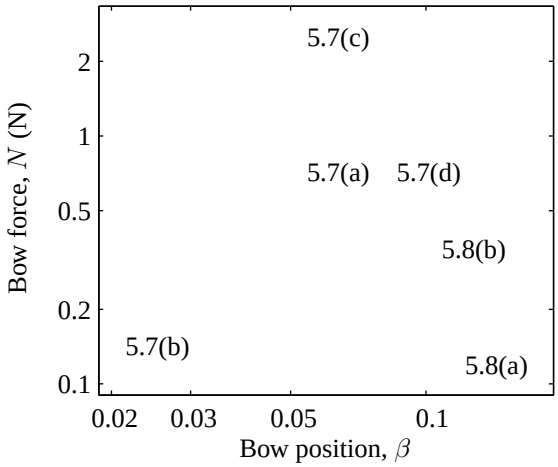

Figure 5.6: Location in the N vs. β plane of the force and position used to generate the individual bridge force waveforms shown in Figures 5.7 and 5.8. Each label in this figure is vertically and horizontally centered over the coordinates of the corresponding waveform. The bow speed was 0.05 m/s in all of the above cases.

As a final comparison with the experimental results from Section 4.3.1, the simulation's predictions from operating points inside and above the "patchy Helmholtz" region of the experimental Schelleng diagram are shown in Figures 5.8(a) and 5.8(b) respectively. The operating point used to generate Figure 5.8(a) is the same as that used to generate the experimental example shown in Figure 4.19(a), but the operating point for Figure 5.8(b) is slightly different to that used for Figure 4.19(b), since it was slightly above the upper boundary of the Helmholtz motion region of the simulated Schelleng diagram. Helmholtz motion is seen to persist in these cases, as it did in all cases in the lower right corner of the Schelleng diagram with the friction curve simulation model; the "patchy Helmholtz" region was not reproduced in these simulations.

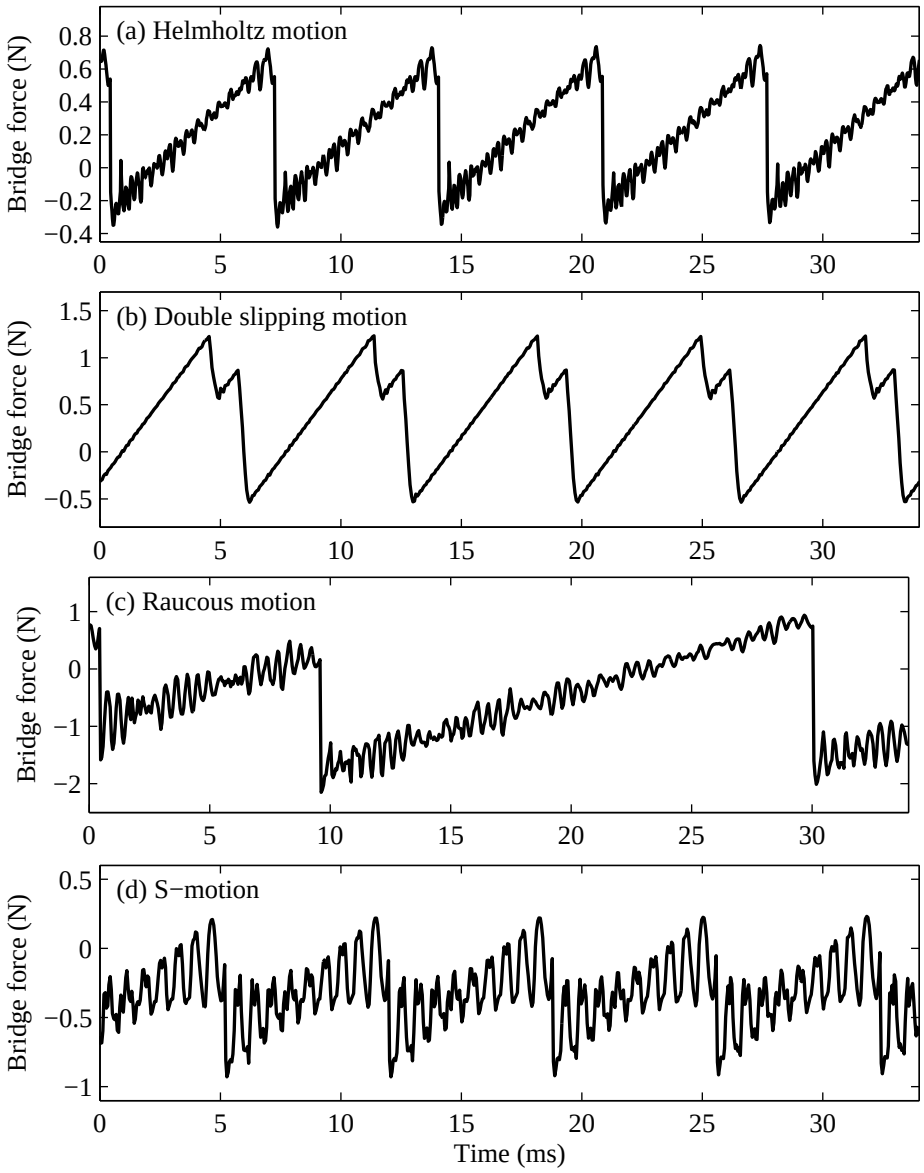

Figure 5.7: Example of a bridge force waveform corresponding to one of each of the symbols shown in Figure 5.2. The values of bow force and position for each waveform are given in Figure 5.6, and the bow speed is 0.05 m/s in all cases. (Note, constant slipping motion is omitted here because it was never predicted by the friction curve simulation model, when using Smith and Woodhouse's [43] steady sliding friction curve.)

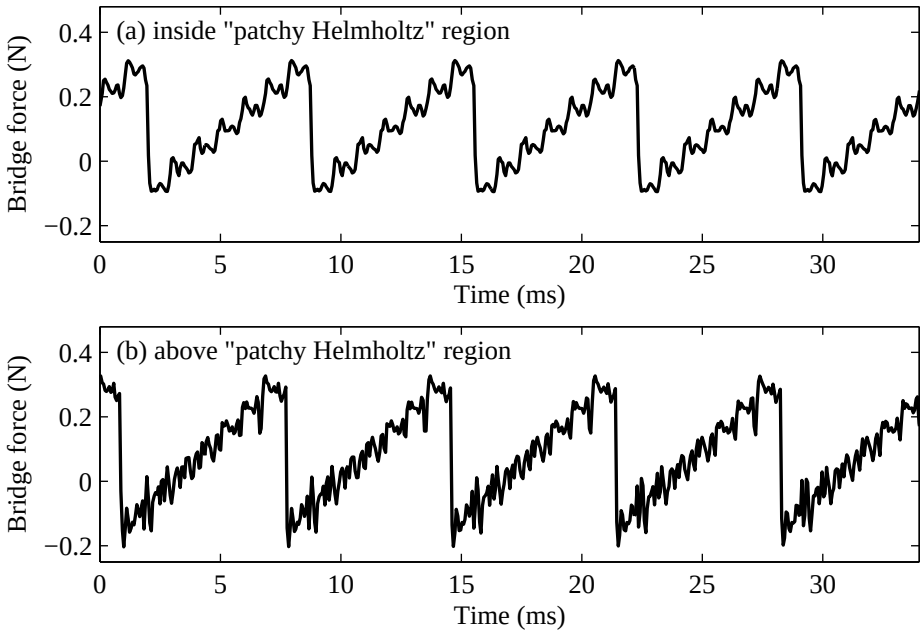

Figure 5.8: Simulated equivalent of the bridge force waveforms shown in Figures 4.19(a) and 4.19(b). The operating points for these waveforms were, respectively, within and above the region labelled "patchy Helmholtz" in Figure 4.14. Clearly, Helmholtz motion has remained intact in both of these cases with the friction curve simulation model, as it did throughout the entire region deemed to be "patchy" in experiment.

NUMERICAL CONVERGENCE OF SIMULATION

All of the simulated cases shown used a sufficiently short time step that numerical convergence was achieved, in as much as convergence is ever achievable to friction curve simulations; as discussed for example by Schumacher and Woodhouse [51, §III.C], small changes in a friction curve simulation — such as a small reduction in the sampling rate — can cause the string to begin slipping when it otherwise would not quite have done so (or of course vice versa). The string must then undergo the hysteresis loop discussed in Section 1.1.1 before it can resume sticking, by which time the motion may have changed sufficiently for the subsequent development of transient vibration to be altered. Ignoring this nonlinear chaotic behaviour, the simulations presented in this section were numerically stable.

5.1.2 GUETTLER DIAGRAM: PRE-HELMHOLTZ DURATION IN N-a PLANE

Turning now to the transient behaviour of the friction curve simulation model, the time taken to produce Helmholtz motion using bowing gestures with constant force N and acceleration a is examined in this section. Guettler diagrams are shown in Figure 5.9 for each of eight different values of β, in which the time delay between the first slip and the onset of Helmholtz motion with a given combination of N and a is indicated by the shade of the pixel at the corresponding

location in the N vs. a plane. White pixels indicate "perfect transients", i.e. Helmholtz motion ensued immediately following the first slip, and black pixels indicate that the delay between the first slip and Helmholtz motion was twenty period lengths or more. White pixels filled with black crosses ("$\times$") indicate that the first slip occurred less than twenty period lengths before the end of the simulation, making it impossible to deduce the true length of the pre-Helmholtz motion transient. The pre-Helmholtz motion delay was determined using the same algorithm, described in Section 4.2.3, that was used for experimental data; the results in Figure 5.9 are hence directly comparable with the equivalent results from experiment shown in Figure 4.20. Each simulation (like each experimental measurement) was run until a quarter of a second of data was obtained.

A comparison of the simulated Guettler diagrams in Figure 5.9 with the experimental Guettler diagrams in Figure 4.20 does not reflect well on the friction curve simulation model used, because the grey pixels, which indicate occurrences of Helmholtz motion, are considerably more spaced apart in Figure 5.9 than they were in Figure 4.20. A real cello that behaved as predicted by the friction curve simulation model would be extremely "unplayable", as an unreasonable degree of precision would be required to elicit Helmholtz motion.

As an aside, an interesting feature of the Guettler diagrams shown in Figure 5.9 is the presence of lines passing through the origin which contain apparently similar transients. In Figure 5.9(d), for example, there are two diagonal lines formed by white — or almost white — pixels, which pass very close to the origin. Trends like this were not observed in experiment, although one might expect such trends to be obscured by experimental errors, such as slight disturbances to the bowing machine.

INDIVIDUAL BRIDGE FORCE WAVEFORMS

Examples of the bridge force waveforms — calculated as $2Z$ times the magnitude of bridge-bound transverse velocity waves — with various combinations of N, a and β are shown in Figure 5.10. Figure 5.10(a) shows an example of a "perfect transient", i.e. one in which Helmholtz motion was seen to occur immediately following the first slip. Figure 5.10(b) shows an example of raucous motion, and Figure 5.10(c) shows an example of multiple slipping; the non-periodicity of the latter two examples is typical of nearly all waveforms in which a periodic Helmholtz motion or S-motion were not achieved.

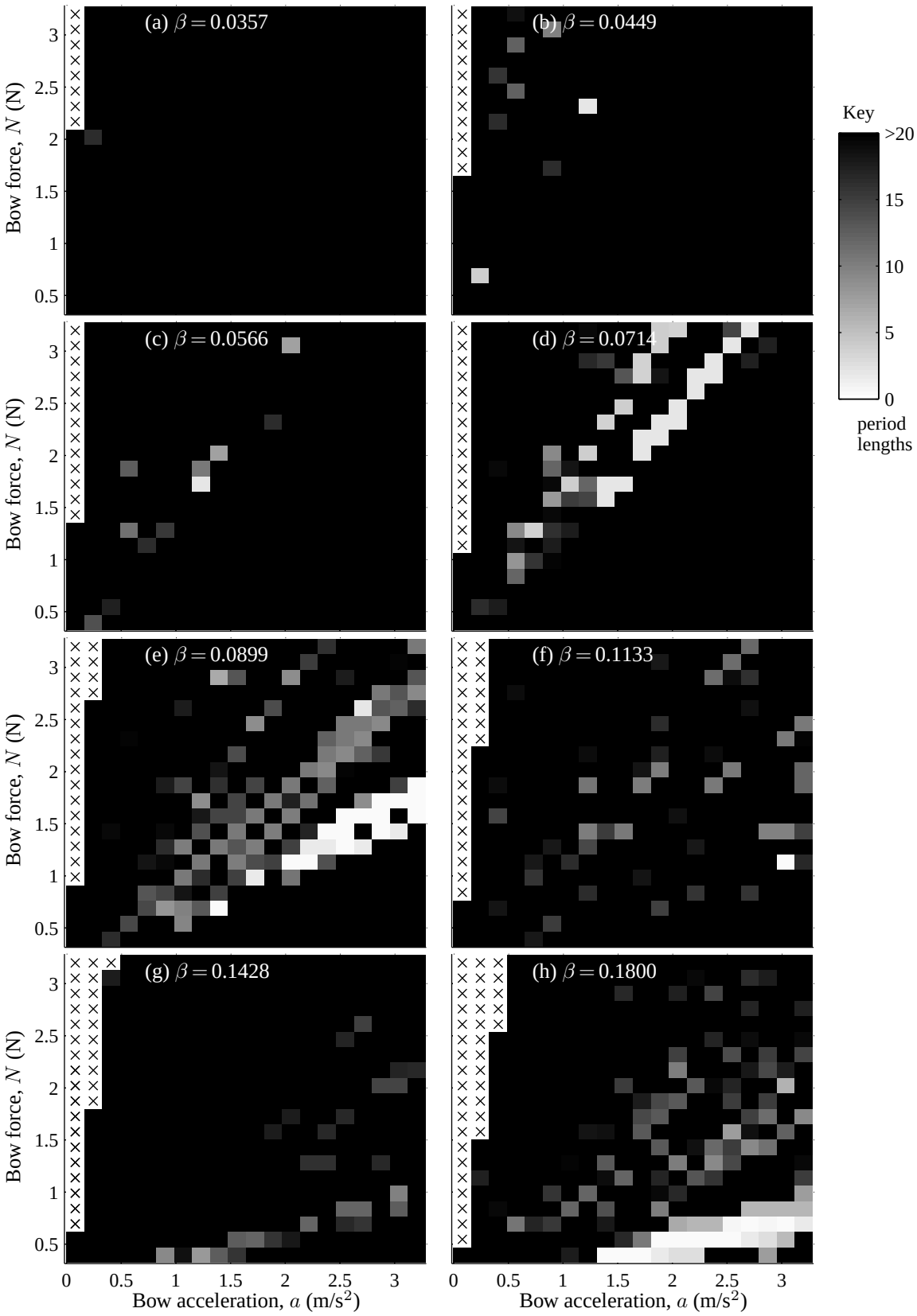

Figure 5.9: Simulated "Guettler diagrams", for eight different values of β, with the old friction curve model. In each plot, the time taken to achieve Helmholtz motion relative to the time of the first slip at a given combination of bow force and acceleration is given by the shade of the pixel at the corresponding location in the N vs. a plane, according to the guide on the right. This may be compared with the equivalent experimental measurements in Figure 4.20, which were plotted using the same convention.

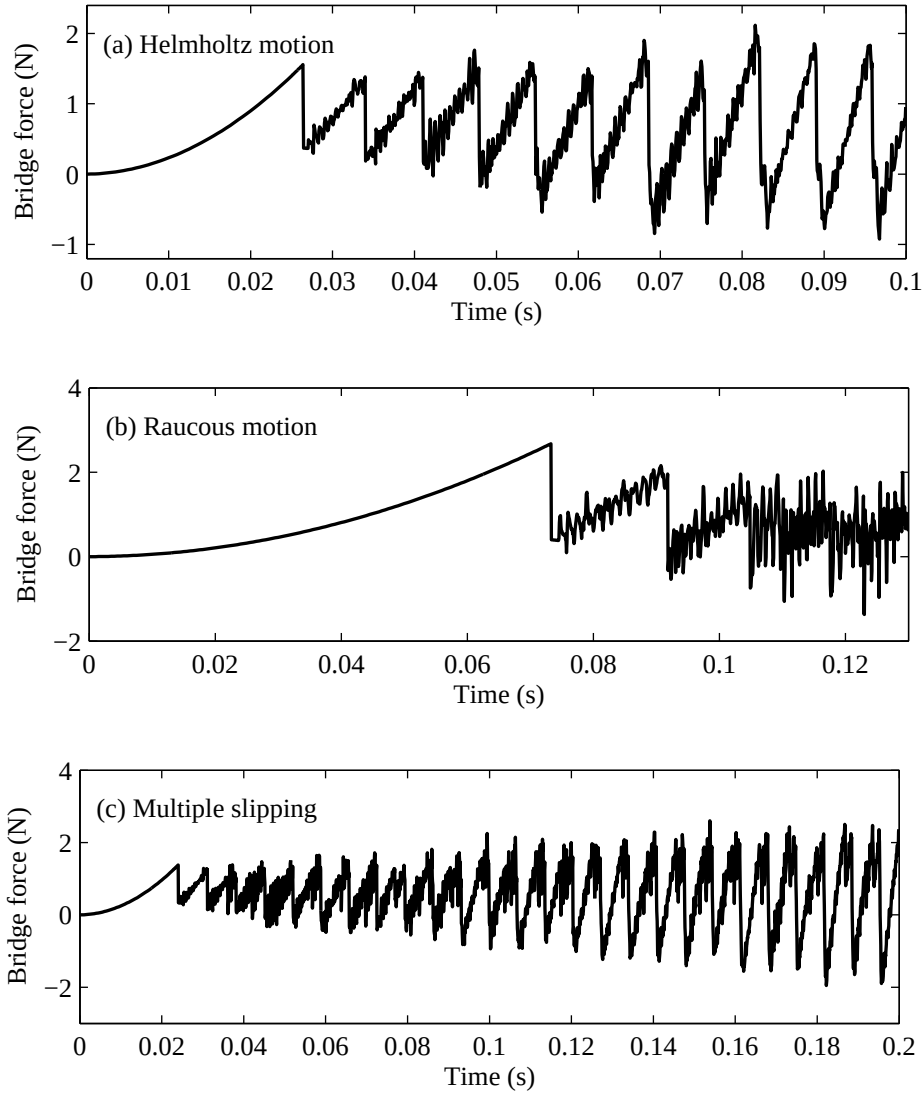

Figure 5.10: Examples of bridge force waveforms from various regions of the Guettler diagrams, when simulated using the "old" friction curve model. The values of N, a and β for each example are, respectively: (a) 1.284 N, 2.379 m/s^2, and 0.0899; (b) 2.463 N, 1.065 m/s^2, and 0.1800; (c) 1.137 N, 2.543 m/s^2, and 0.0899. The horizontal and vertical axes ranges are different in every plot, although the string's natural period is 0.00680 s in all cases.

"TROUGH" IN BRIDGE FORCE AT FIRST SLIP DUE TO FRICTION CURVE JUMP

A trademark of the friction curve simulation model is revealed by a closer examination of the bridge force just after the first slip, such as the example shown in Figure 5.11. The instantaneous jump in friction caused by the hysteresis rule at the first slip (which was described as the "solution of Friedlander's ambiguity", on page 6) induces an instantaneous change, Δv, in string velocity. From Equation (1.9a), this jump in string velocity and friction force causes the magnitude of the transverse velocity wave travelling towards the bridge to drop by an amount $(\Delta v)Z/Z_T$. Because changes in the magnitude of v_h are relatively slow until the wave sent towards the bridge returns to the bowing point, the conditions at the bowing point do not change until shortly before sticking resumes a time βT after the start of the first slip. This results in a "lull" lasting βT seconds immediately after the first slip, in which the outgoing velocity waves, and hence the bridge force, are constant. This "lull" is indicated in the example shown in Figure 5.11, which is unlike any experimental measurement.

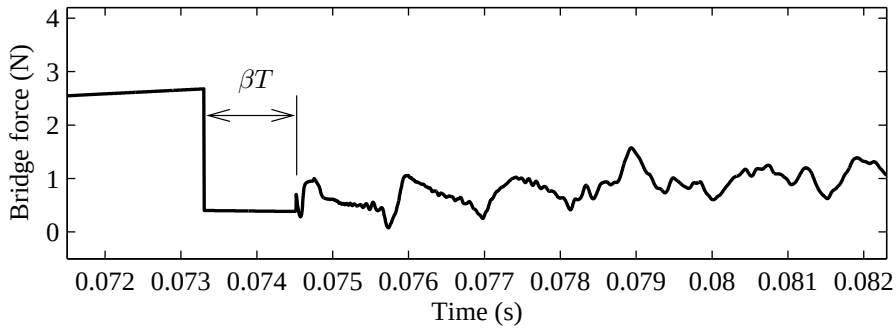

Figure 5.11: A close-up view of a typical bridge force waveform at first slip. The jump in string velocity and friction force caused by the "friction curve jump", and the subsequent delay of βT seconds before any significant change in v_h, causes a sudden drop in bridge force followed by a period of βT during which it is constant. The bridge force shown in this figure is a close-up view of that shown in Figure 5.10(b).

SIMILARITY BETWEEN TRANSIENTS WHEN N/a IS CONSTANT

Another trademark of the friction curve simulation model, when the Smith and Woodhouse steady sliding f-v relationship is used, is that when the ratio N/a is held constant the motion of the string remains self-similar, with only its amplitude changing. In the Guettler diagrams in Figure 5.9 this caused the visible diagonal trends in transient length, with similarly-shaded pixels generally lying along a straight line given by $N \propto a$. A vivid, but not at all unusual, example of this similarity is shown in Figure 5.12. The waveform shown in Figure 5.12(a) was generated with N and a equal to 0.842 N and 0.901 m/s^2 respectively, and the waveform shown in Figure 5.12(b) was generated

with N and a equal to 2.021 N and 2.215 m/s^2 respectively; and β was 0.0899 in both cases. The reason for this trend will be discussed in Section 6.1.

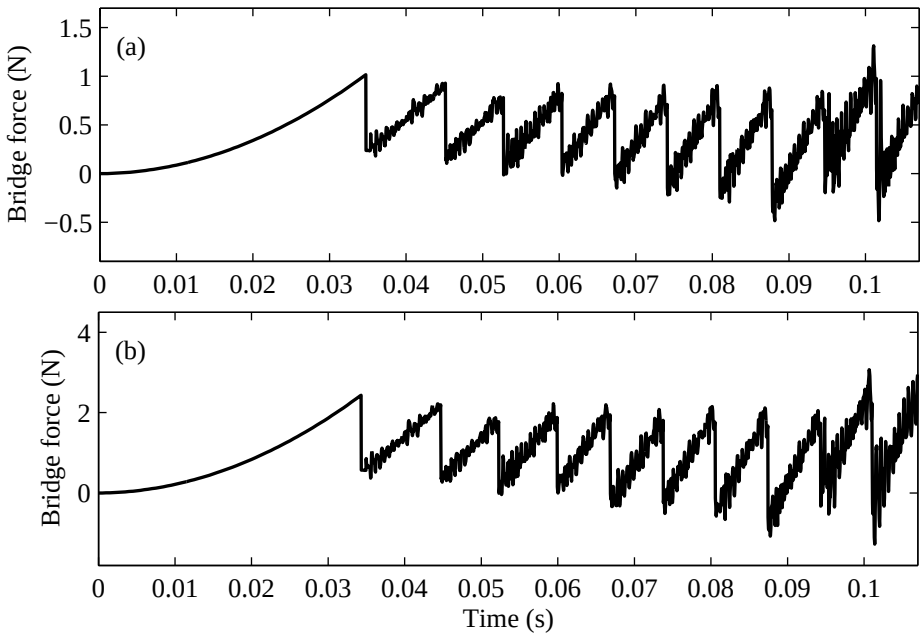

Figure 5.12: A typical example of two nearly identical bridge force transients from operating points along the same radial line in the N vs. a plane; only the magnitudes of the two waveforms are different (note the different vertical scales). The values of N, a and β are, respectively: (a) 0.842 N, 0.901 m/s^2, and 0.0899; (b) 2.021 N, 2.215 m/s^2, and 0.0899.

5.2 "RECONSTRUCTED FRICTION CURVE" SIMULATIONS

In Section 4.3.3, a relationship between coefficient of friction and relative sliding velocity was obtained, using only information from experimental bridge force measurements. This relationship, approximated by the best fit solution shown in Equation (4.3), was shown to be markedly different to the friction curve obtained by Smith and Woodhouse [43] from steady sliding tests. The difference between the "reconstructed friction curve" and Smith and Woodhouse's friction curve underlines the irrelevance of steady sliding conditions to real bowing.

In this section, simulations based on the friction curve model of rosin with this new f-v relationship are explored. Results are presented that are nominally similar to those of Section 5.1, which were generated with the "old" f-v relationship from Smith and Woodhouse's steady sliding tests [43].

5.2.1 SCHELLENG DIAGRAM: VIBRATION REGIME IN THE N-β PLANE

The Schelleng diagram generated by the "new" friction curve is shown using white pixels to indicate Helmholtz motion in Figure 5.13, and using symbols to denote each type of string motion in Figure 5.14. The string was again initialized in this case with the same Helmholtz motion initial conditions used with the "old" friction curve Schelleng diagram; these were discussed in Section 5.1.1.

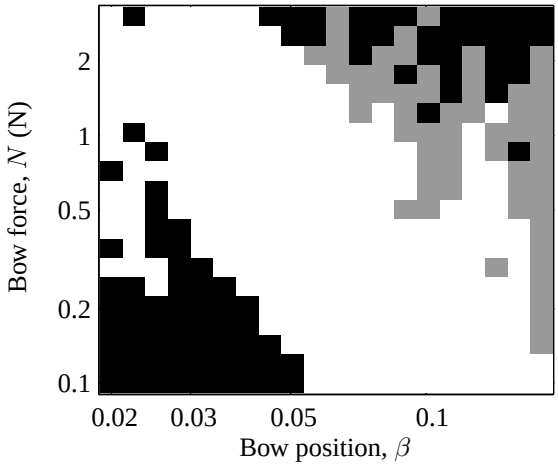

Figure 5.13: Schelleng diagram based on the reconstructed friction curve obtained in Section 4.3.3. Here, as with the experimental equivalent in Figure 4.12 and the steady sliding friction curve equivalent in Figure 5.1, the shade of a given pixel indicates whether Helmholtz motion was sustainable at the combination of force and position corresponding to the position of the pixel. White pixels indicate that Helmholtz motion was still in evidence at the end of the two seconds of steady bowing; black pixels indicate that it was not; and grey pixels indicate that S-motion was observed. Further information about the individual operating points within the black regions is given in Figure 5.14. The bow speed is 0.05 m/s in all cases.

Figures 5.13 and 5.14 are clearly different from those obtained using the steady sliding friction curve, which were shown in Figures 5.1 and 5.2. Many of the faults of the old friction curve have been, at least partially, corrected by using the new friction curve: the upper and lower limits of the white (i.e. Helmholtz motion) region in Figure 5.13 have moved upwards, as they should according to the experimental Schelleng diagram shown in Figure 4.12, and the region is narrower; also the occurrences of S-motion, while still not in the three clear columns seen in experiment, are visibly closer to the positions in the N-β plane where they were observed in experiment; in addition, Figure 5.14 shows that some occurrences of constant slipping motion were predicted with the new friction curve, whereas none were predicted previously. Not so encouragingly however, the new friction curve simulations predict an "offshoot" of Helmholtz motion occurrences in the two left-most columns (i.e. the two smallest values of β) of the Schelleng diagram; this feature was observed neither in the old friction curve simulations nor in experiment.

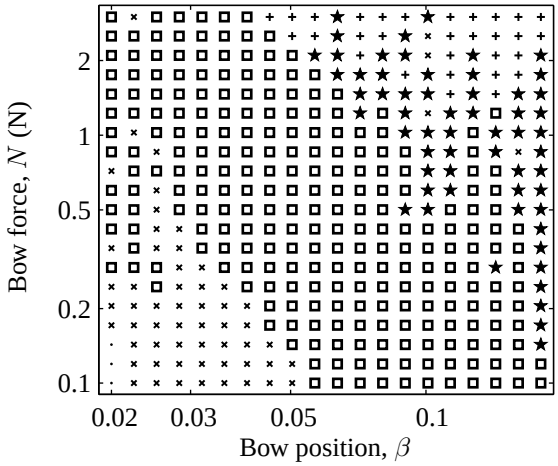

Figure 5.14: Schelleng diagram from simulations based on the reconstructed friction curve obtained in Section 4.3.3. Here, as with the experimental equivalent in Figure 4.13 and the steady sliding friction curve equivalent in Figure 5.2, squares (□) indicate that Helmholtz motion was sustained throughout the period of steady bowing; crosses ($\times$) indicate that the string lapsed into multiple slipping motion; pluses ($+$) indicate raucous motion; dots ($\cdot$) indicate constant slipping; and stars ($\star$) indicate S-motion.

In general, the agreement between Figures 5.13 and 5.14 and the experimental equivalents in Figures 4.12 and 4.13 is by no means perfect, but it is certainly better than it was with the friction curve used in Section 5.1.

SUPERIMPOSING THE UPPER AND LOWER FORCE LIMITS FROM EXPERIMENT

The upper and lower bow force limits, chosen in Section 4.3.1 to be as close as possible to the edges of the Helmholtz motion region of the experimental Schelleng diagram and proportional to $1/\beta$ and $1/\beta^2$, are shown superimposed over the Schelleng diagram obtained using the reconstructed friction curve simulations in Figures 5.15 and 5.16. Comparison with Figures 5.4 and 5.5 reinforces the assertion that the friction curve simulations were improved by replacing the steady sliding f-v relationship with Equation (4.3).

It was remarked on page 121 that the gap between the upper force limit predicted by the old friction curve simulations and that measured in experiment could be improved by using a "flatter" friction curve. The friction curve used in this section was calculated based on dynamic tests, and is indeed flatter; the result is a vast improvement in the position of the upper force limit. Referring to Equation (1.15), this suggests that the effective value of $(\mu_s - \mu_d)$ is in accordance with both the measurements in the N-v_b plane (from which it was obtained) and the measurements in the N-β plane.

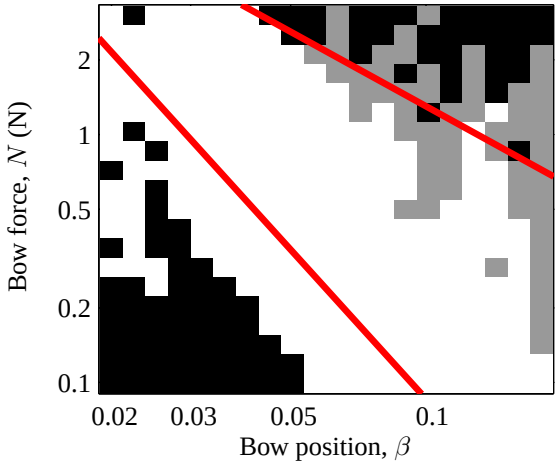

Figure 5.15: Schelleng diagram according to simulations based on the reconstructed friction curve of Section 4.3.3 (same as Figure 5.1), with Schelleng's force limits superimposed as diagonal lines. The upper force limit, $0.13/\beta$, and the lower force limit, $0.00086/\beta$, were chosen to match the edges of the Helmholtz motion region in experiment, as shown in Figure 4.15.

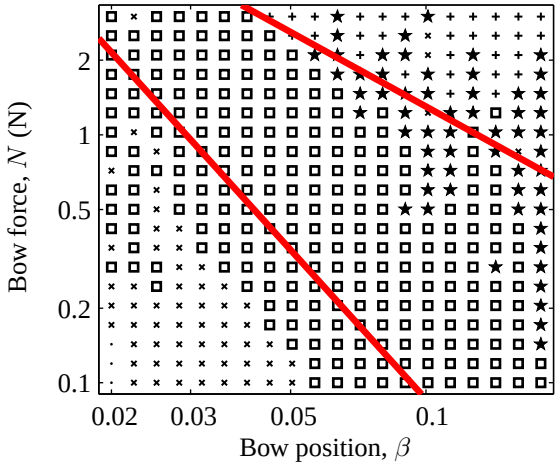

Figure 5.16: Symbolic representation of the Schelleng diagram, as simulated using the reconstructed friction curve of Section 4.3.3 (same as Figure 5.14), with Schelleng's force limits superimposed as diagonal lines. The limits were chosen to match experimental data, as shown in Figure 4.16

The lower edge of the Helmholtz motion region in Figures 5.15 and 5.16 has moved upwards, and is therefore improved, but is still too low by a factor of around two. From Equation (1.16), this suggests that the effective value of λ_b is too large, indicating that the simulated bridge should be more flexible.

INDIVIDUAL BRIDGE FORCE WAVEFORMS

An example of a bridge force waveform for each type of motion cited in Figure 5.14 is shown in Figures 5.18(a)–(e). The values of N and β used to generate each example is shown in Figure 5.17. They examples shown are, respectively: Helmholtz motion, generated at the same operating point as the experimental example in Figure 4.18(a); multiple slipping motion, generated with slightly smaller values of N and β than the experimental example in Figure 4.18(b); raucous motion, from the same operating point as the corresponding example shown in Figure 4.18(c); constant slipping motion, from near the bottom left corner of the Schelleng diagram; and S-motion, from a slightly smaller value of N but the same value of β as the experimental example in Figure 4.18(e).

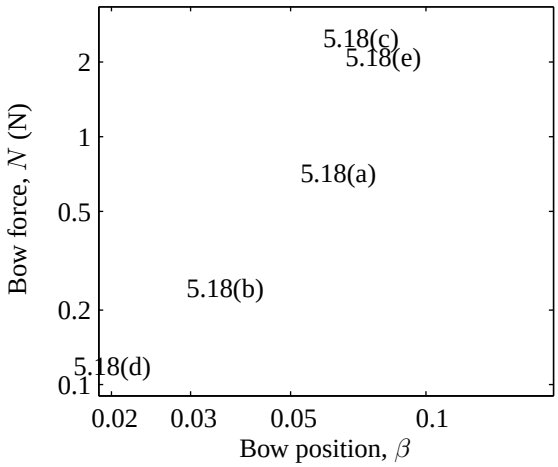

Figure 5.17: Location in the N vs. β plane of the force and position used to generate the individual bridge force waveforms shown in Figure 5.18. Each label in this figure is vertically and horizontally centered over the coordinates of the corresponding waveform. The bow speed was 0.05 m/s in all of the above cases.

The waveforms shown are generally very similar to the analogous experimental waveforms shown in Figure 4.18. The "Schelleng ripples" visible as small oscillations superimposed on the Helmholtz motion in Figure 5.18(a) are similar to the experimental example given from the same operating point. The small second slip in the example of double slipping in Figure 5.18(b) occurs shortly after the main slip, as it did in the experimental example shown in Figure 4.18(b). The principal difference between the simulated and experimental examples of raucous motion, in Figures 5.18(c) and 4.18(c), is the extent of the ripples during sticking periods; both are otherwise similar examples of non-periodic motion. The examples of constant slipping and S-motion shown in Figures 5.18(d) and 5.18(e) are both very similar to the experimental examples.

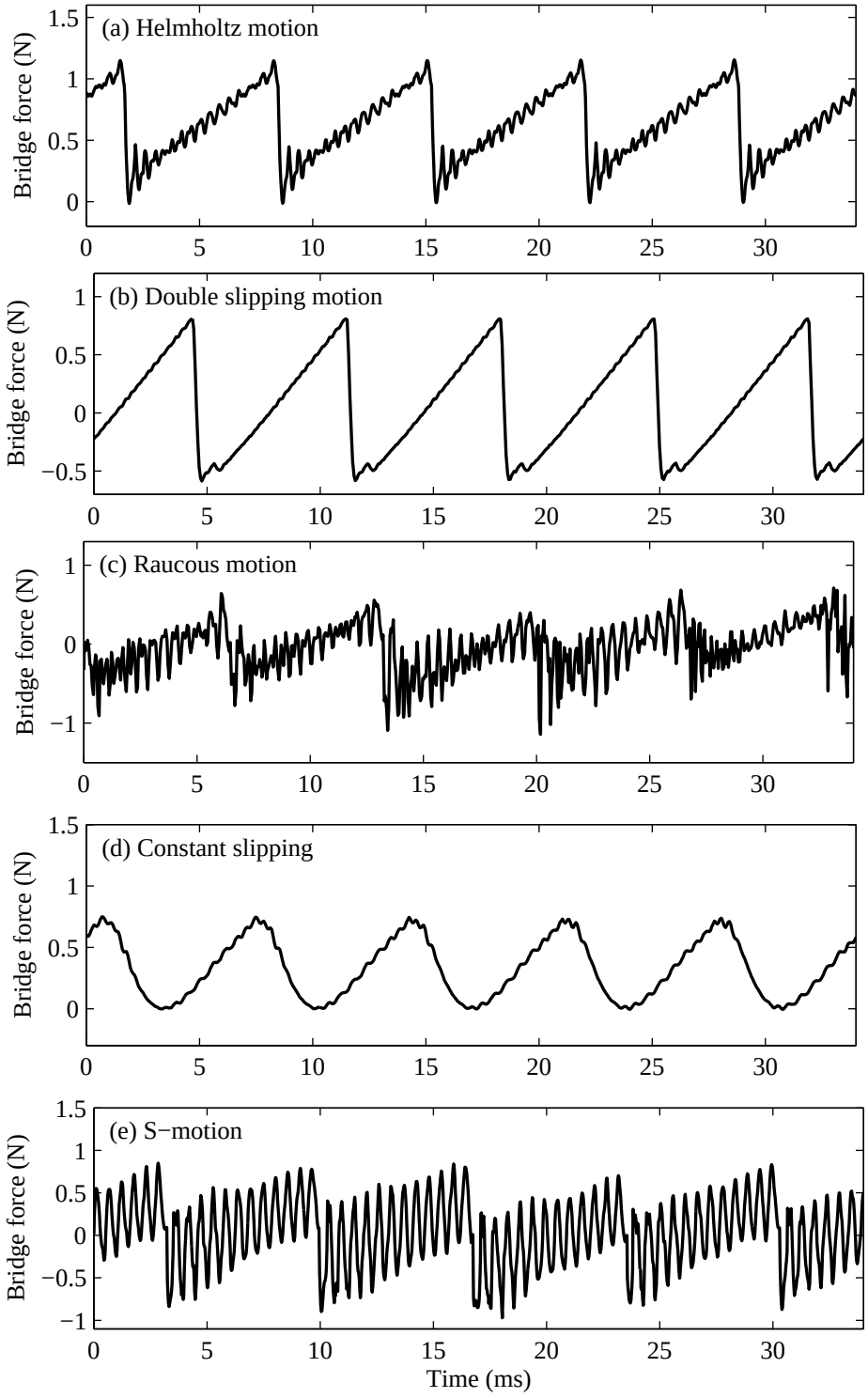

Figure 5.18: Example of a bridge force waveform corresponding to one of each of the symbols shown in Figure 5.2. The values of bow force and position for each waveform are given in Figure 5.6, and the bow speed is 0.05 m/s in all cases.

5.2.2 GUETTLER DIAGRAM: PRE-HELMHOLTZ DURATION IN N-a PLANE

The transient behaviour of the friction curve model with the new "reconstructed" friction curve from the last chapter is, however, not as encouraging as the steady state behaviour seen in Section 5.2.1. In this section, constant acceleration bowing gestures are investigated: "Guettler diagrams" which are nominally similar to those presented already are shown to be at odds with experiment, and the reason for this is revealed by consideration of the events immediately following the first slip.

GUETTLER DIAGRAMS AT DIFFERENT VALUES OF β

The time delay between the first slip and the onset of Helmholtz motion is plotted at a range of bow force and acceleration, for eight different values of β, in Figure 5.19. It is clearly apparent that the improvement seen in the Schelleng diagram prediction due to using a "flatter" friction curve is not reflected in the Guettler diagram prediction: the instances of Helmholtz motion are as sparse as they were when using Smith and Woodhouse's steady sliding friction curve, and the approximate boundaries of the regions containing occurrences of Helmholtz motion bear little resemblance to the boundaries observed in experiment, in Figure 4.20.

BEHAVIOUR AT FIRST SLIP, WITH LARGE AND SMALL BOW FORCES

In light of the improvements seen in the Schelleng diagram predictions due to changing the friction curve, it is surprising that the transient behaviour of the string, as indicated by Figure 5.19, is no better. With a plausible cause of this being the differences between initial conditions in the Guettler and Schelleng diagrams (the string was initialized with Helmholtz motion in the latter case), it is logical to review the motion of the string in the moments following the first slip.

With the new friction curve, the string was found to behave in two alternative ways, depending on the magnitude of the bow force, N. The slope of the friction curve at the start of the slipping portion (i.e. at $v = v_b^-$), which from Equation (4.3) equals $0.571 \times N$. If this slope is less than that of the load line, $2Z$, then there is no "ambiguous" region in the friction curve (see Figure 1.4). Hence if N is less than $3.5Z$, then the operating point does not "jump" during stick-slip transitions, but instead drops gradually. Hence, with Z being 0.421 Ns/m for the simulated string (according to measured data for Dominant cello D-strings [21, 27]), the string's motion is relatively benign if $N \leq 1.474$ N, whereas flybacks are observed in the bridge force if $N > 1.474$ N. Unexpectedly however, the cases where $N > 1.474$ N, in which the bridge force "flies back" at first slip, have an apparent tendency to "overshoot" at first slip. An example of bridge force waveforms for cases where N is both greater than and less than 1.474 N is shown in Figure 5.20. The cause of these overshoots will be discussed in Section 6.3.

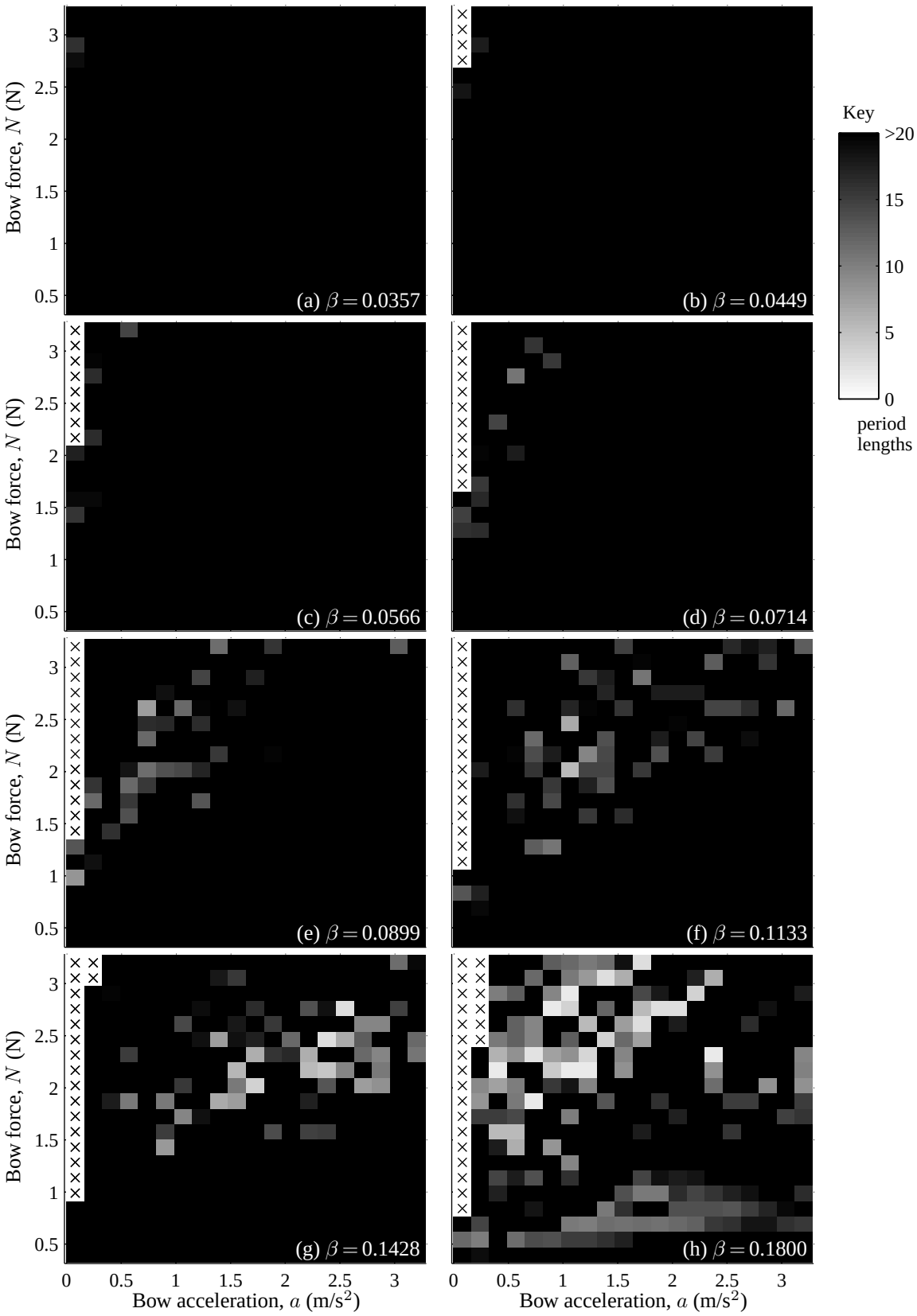

Figure 5.19: Simulated "Guettler diagrams", for eight different values of β, with the new friction curve model. In each plot, the time taken to achieve Helmholtz motion relative to the time of the first slip at a given combination of bow force and acceleration is given by the shade of the pixel at the corresponding location in the N vs. a plane, according to the guide on the right. White pixels with black crosses indicate that the quarter of a second of data was insufficient to deduce the length of the pre-Helmholtz motion transient. The experimental equivalent of this figure is Figure 4.20.

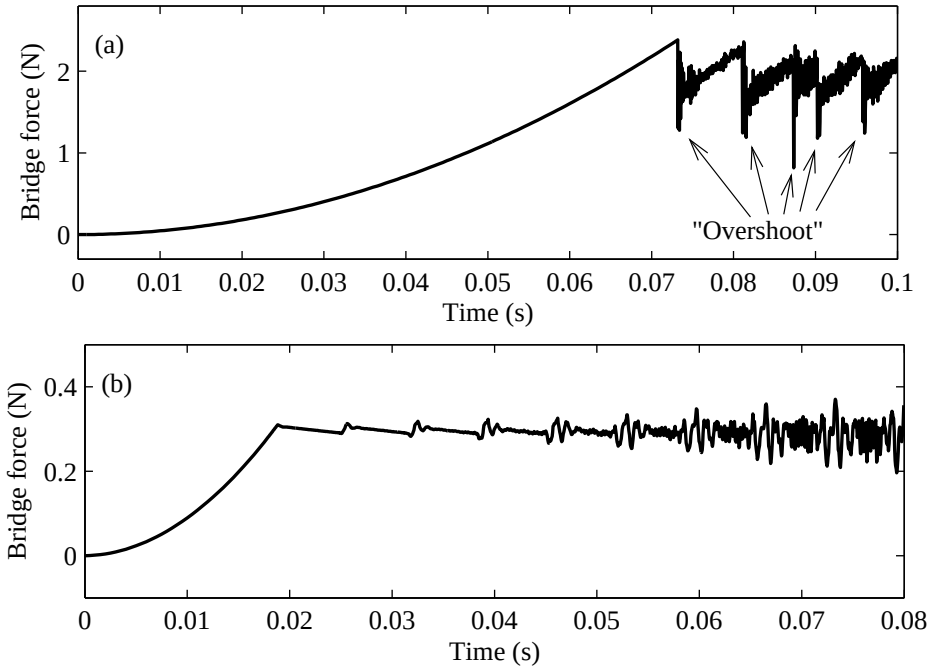

Figure 5.20: Bridge force waveforms from constant acceleration bowing gestures using the friction curve simulation model with the "reconstructed" friction curve. The top plot is typical of the bridge force waveforms when N is large enough to cause the operating point in the f vs. v plane to "jump", and the bottom plot is a typical result with N too small to cause a jump. The values of N, a and β for each example are, respectively: (a) 3.053 N, 0.244 m/s^2, and 0.0449; and (b) 0.400 N, 0.737 m/s^2, and 0.0714.

5.3 "PLASTIC THERMAL MODEL" SIMULATIONS

Having reviewed the behaviour of the friction curve model of rosin with both Smith and Woodhouse's friction curve and with the curve derived in the last chapter, the behaviour of the plastic thermal model is investigated in this section. The results presented in this section are directly comparable to those obtained from friction curve simulations and experiment.

5.3.1 SCHELLENG DIAGRAM: VIBRATION REGIME IN THE N-β PLANE

The Schelleng diagram, as obtained using the plastic thermal friction model, is shown in Figures 5.21 and 5.22, which are plotted using the same conventions as previously. The latter is similar to the results published by Woodhouse [21], except that the vibration identification algorithm used in this case is different (as described in Section 4.2.3), and the range of values of N and β is

different. Following Schelleng, who considered the conditions for the breakdown of a pre-formed Helmholtz motion under steady bowing conditions, and in the same spirit as the experimental Schelleng diagram in Section 4.3.1 and the friction curve results in Sections 5.1.1 and 5.2.1, the string was initialized with Helmholtz motion, rather than started from rest. The exact vibration waveform and thermal history used as the initial condition for the string are shown in Figure 5.23.

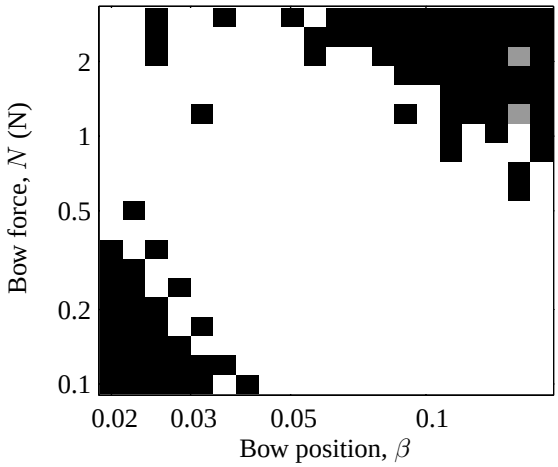

Figure 5.21: Schelleng diagram, from simulations based on the plastic thermal rosin model. Here, as previously, the shade of a given pixel indicates whether Helmholtz motion was sustained at the combination of force and position corresponding to the position of the pixel. White pixels indicate that Helmholtz motion was still in evidence at the end of two seconds of steady bowing; black pixels indicate that it was not; and grey pixels indicate that S-motion was observed. Further detail regarding the outcome of individual operating points within each black region is shown in Figure 5.22. The bow speed is 0.05 m/s in all cases.

The general appearance of Figures 5.21 and 5.22 is similar in some respects to the experimental equivalents in Figures 4.12 and 4.13: the central region of Helmholtz motion is adjacent to a region of raucous motion at larger bow forces (with some S-motion), and a region of constant or multiple slipping below. However, instances of multiple slipping and S-motion are far less frequent than they were in experiment, and the "patchy" region at low bow forces and large values of β is missing.

The rarity of S-motion occurrences may be due to a deficiency in the plastic thermal model, but alternatively could be due to the difference between initial conditions in experiment and simulation. As discussed on page 78, in experiment the string was initialized with a single stick and slip per period, but it was not always possible to establish a clear Helmholtz motion rather than S-motion. With the simulation model, the same initial condition of Helmholtz motion was always used, and as such instances of S-motion could not be caused by S-motion initial conditions. Hence, although the lack of S-motion in the simulated Schelleng diagram may be attributable to a fault with the plastic thermal simulation model — indeed, S-motion was predicted far more frequently by the friction curve models in Sections 5.1.1 and 5.2.1 — this cannot be proven on the basis of the Schelleng

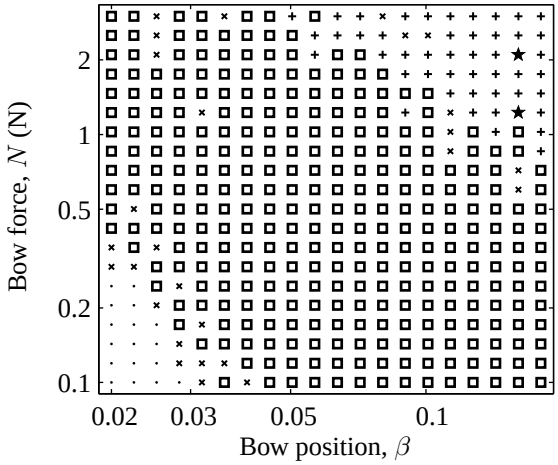

Figure 5.22: Schelleng diagram from simulations based on the plastic thermal rosin model. Here, as with the experimental equivalent in Figure 4.13, squares (□) indicate that Helmholtz motion was sustained throughout the period of steady bowing; crosses (×) indicate that the string lapsed into multiple slipping motion; pluses (+) indicate raucous motion; dots (·) indicate constant slipping; and stars (★) indicate S-motion.

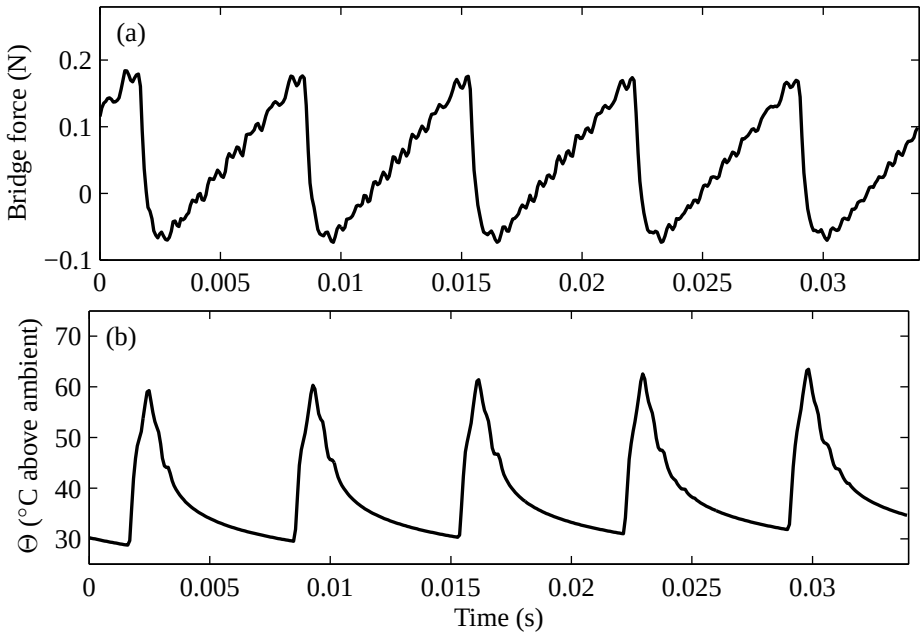

Figure 5.23: Excerpt of transverse vibration data used as part of the initial condition for the simulated Schelleng diagram. This shows the magnitude of transverse velocity waves sent towards the bridge from the bowing point, approximately equal to $1/2Z$ times the "bridge force", and hence comparable with for example Figure 4.18(a). This data was used along with excerpts of torsional waves concurrently sent towards the bridge, transverse and torsional waves sent towards the finger, and the temperature of the rosin in the contact patch.

diagram appearance alone. It should, however, be noted that the two reported occurrences of S-motion in the plastic thermal simulated Schelleng diagram are both at $\beta = 0.1603$, the second column from the right of the Schelleng diagram, which is the same location as one of the three "columns" of S-motion reported in experiment. It would seem, then, that both experiment and simulation are most sensitive to S-motion under the same conditions that Lawergren [60] suggested based on his original measurements of S-motion.

The lack of double slipping in the plastic thermal simulations, however, cannot be attributable to initial conditions. From Figure 5.22, it appears that as the bow force is decreased, Helmholtz motion degenerates almost directly into constant slipping motion, with a second slip appearing only occasionally. Instead of a second slip, the plastic thermal model predicts that the single slip per period of Helmholtz motion gradually grows, until it lasts for the entire period of the motion.

SUPERIMPOSING THE UPPER AND LOWER FORCE LIMITS FROM EXPERIMENT

In Section 4.3.1, best fit approximations for the edges of the Helmholtz motion region of the experimentally measured Schelleng diagram were found. Following Schelleng, the upper edge of the Helmholtz motion region was approximated by a line proportional to $1/\beta$, and the lower edge was approximated by a line proportional to $1/\beta^2$. These limits are reproduced, superimposed on the plastic thermal model simulated Schelleng diagrams, in Figures 5.24 and 5.25.

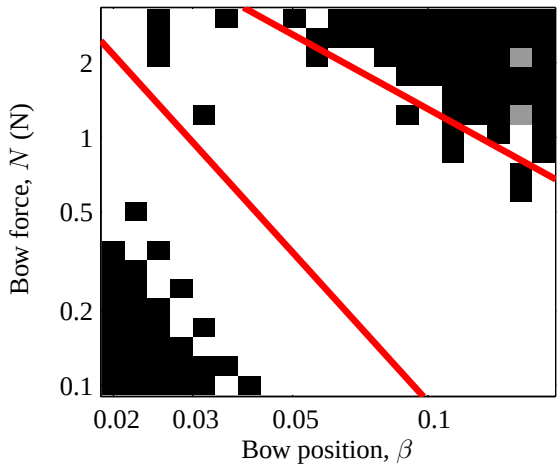

Figure 5.24: Schelleng diagram according to the plastic thermal simulation model (same as Figure 5.21), with Schelleng's force limits superimposed as diagonal lines. The upper force limit, $0.13/\beta$, and the lower force limit, $0.00086/\beta$, were chosen to match the edges of the Helmholtz motion region in experiment, as shown in Figure 4.15.

These figures demonstrate that the upper bow force line is well predicted by the plastic thermal model, but that the lower limit is almost an order of magnitude too low. This reinforces the earlier

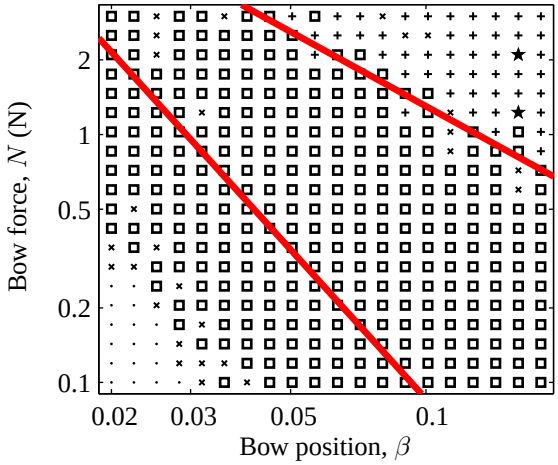

Figure 5.25: Symbolic representation of the Schelleng diagram according to the plastic thermal simulation model (same as Figure 5.22), with Schelleng's force limits superimposed as diagonal lines. The limits were chosen to match the Helmholtz motion region in experiment, as shown in Figure 4.16

assertion that the plastic thermal model is reluctant to predict the formation of double slipping motion at low bow forces.

EXAMPLES OF INDIVIDUAL BRIDGE FORCE WAVEFORMS

A typical vibration waveform corresponding to one of each of the symbols in Figure 5.22 is shown in Figure 5.27, and the corresponding thermal history of the contact patch is shown in Figure 5.28: Figure 5.27(a) shows Helmholtz motion, Figure 5.27(b) shows one of the rare occurrences of double slipping, Figure 5.27(c) shows raucous motion, Figure 5.27(d) shows constant slipping, and Figure 5.27(e) shows S-motion. Bridge force is calculated in each case as $2Z$ times the magnitude of transverse velocity waves being sent towards the bridge from the bowing point. The values of N and β used to generate each waveform are given in Figure 5.26, and v_b was 0.05 m/s in each case.

Of the five bridge force waveforms shown in Figure 5.27, the first, third and fourth were generated using the same values of N and β as the corresponding experimental examples in Figures 4.18(a), (c) and (d). In these three cases, the plastic thermal model predicts very similar motion to that observed in experiment. The operating points for the remaining two cases, double slipping motion and S-motion, had to be different from those of the corresponding experimental examples in Figures 4.18(b) and (e), because the regions containing double slipping and S-motion were different in the experimental Schelleng diagram.

The double slipping waveform shown in Figure 5.27(b) holds a clue as to the reason why the plastic thermal simulation model rarely predicts transition from steady state Helmholtz motion to double

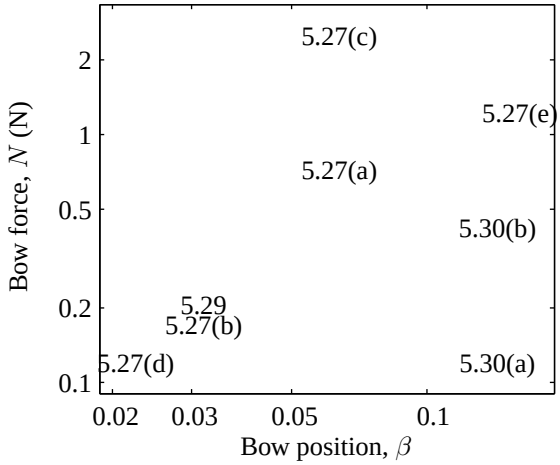

Figure 5.26: Location in the N vs. β plane of the bow force and position used to generate the individual bridge force waveforms shown in Figures 5.27, 5.30 and 5.29. Each label in this figure is vertically and horizontally centered over the coordinates of the corresponding waveform. The bow speed was 0.05 m/s in all of the above cases. Figures 5.27(a), 5.27(c), 5.27(d), 5.30(a) and 5.30(b) have the same operating point as the experimentally measured bridge force waveforms in Figures 4.18(a), 4.18(c), 4.18(d), 4.19(a) and 4.19(b).

slipping motion. In this case, as with waveforms at similar operating points in the N-β plane, the "flyback" in bridge force is more gentle; it is less steep than in experiment (see for example Figure 4.18(b)), and is slightly rounded at its end. This is symptomatic of an increase in the roundedness of the Helmholtz corner: by spreading the Helmholtz corner out over a finite length of string, the drop in bridge force that occurs when it reflects from the bridge is also spread out over over a finite period of time [12]. This roundedness appears to impede the growth, and indeed the creation, of a second slip at low bow forces. A separate example of the bridge force waveform at a low bow force is shown in Figure 5.29, which was generated at an operating point that gave double slipping in experiment.

As a final comparison with the experimental results from Section 4.3.1, the plastic thermal model predictions from the operating points used to generate Figures 4.19(a) and 4.19(b) — the waveforms from inside and above the "patchy Helmholtz" region of the experimental Schelleng diagram — are shown in Figures 5.30(a) and 5.30(b). Helmholtz motion is seen to persist in these cases, as it did in all cases in the lower right corner of the Schelleng diagram with the plastic thermal simulation model; the "patchy Helmholtz" region was not reproduced with the plastic thermal model.

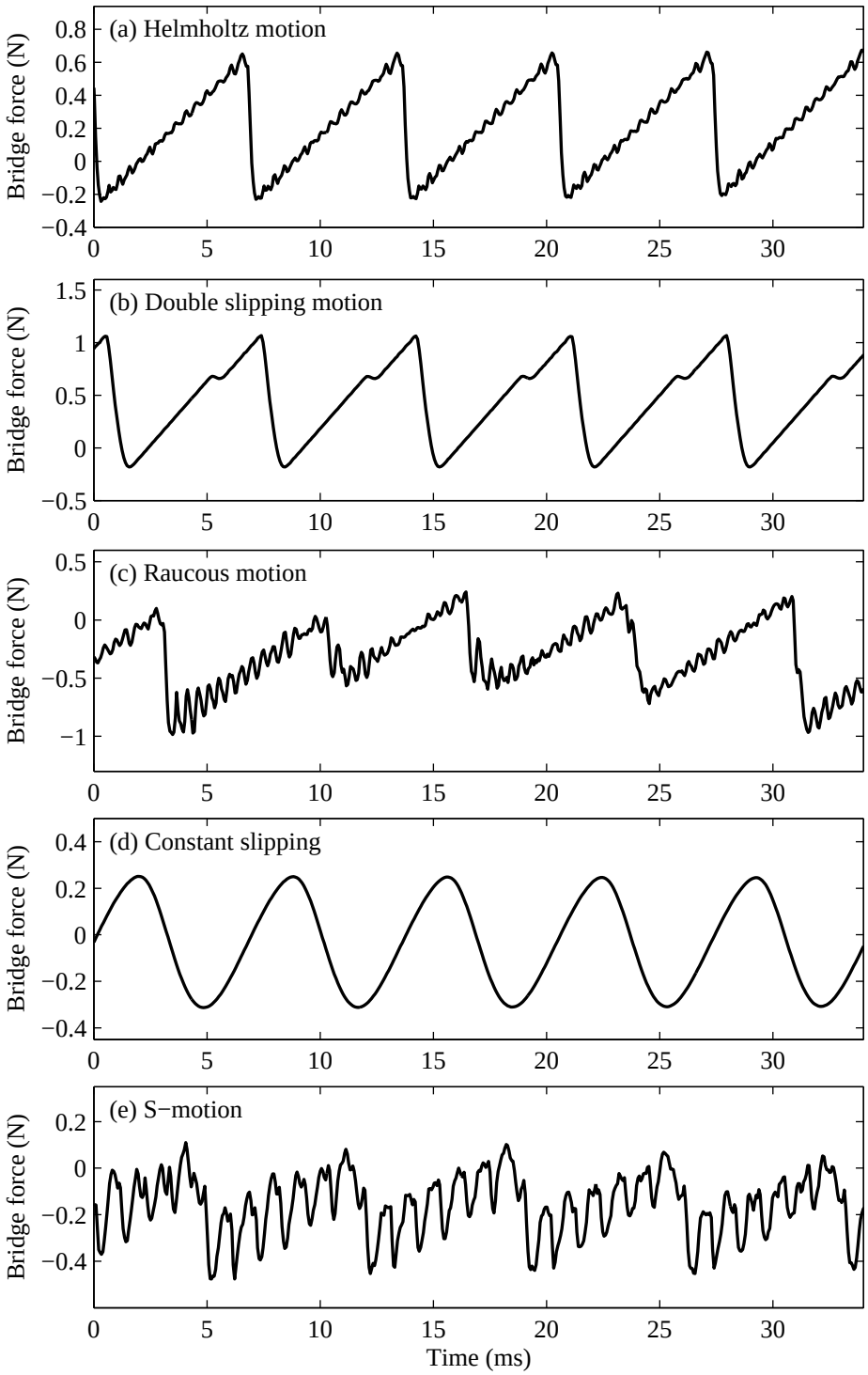

Figure 5.27: Examples of bridge force waveforms (calculated as $2Z$ times the magnitude of bridge-bound velocity waves) for each of the types of string motion indicated by symbols in Figure 5.22. The values of bow force and position used to generate each waveform are given in Figure 5.26, and the bow speed is 0.05 m/s in all cases. The waveforms shown in (a), (c) and (d) were generated at the same operating point as the analogous experimental waveforms, in Figures 4.18(a), 4.18(c) and 4.18(d); experiment and simulation produce quite similar results in these cases. The plastic thermal model was not seen to produce double slipping and S-motion (i.e. (b) and (e) above) at the same operating points as experiment, as discussed in the text.

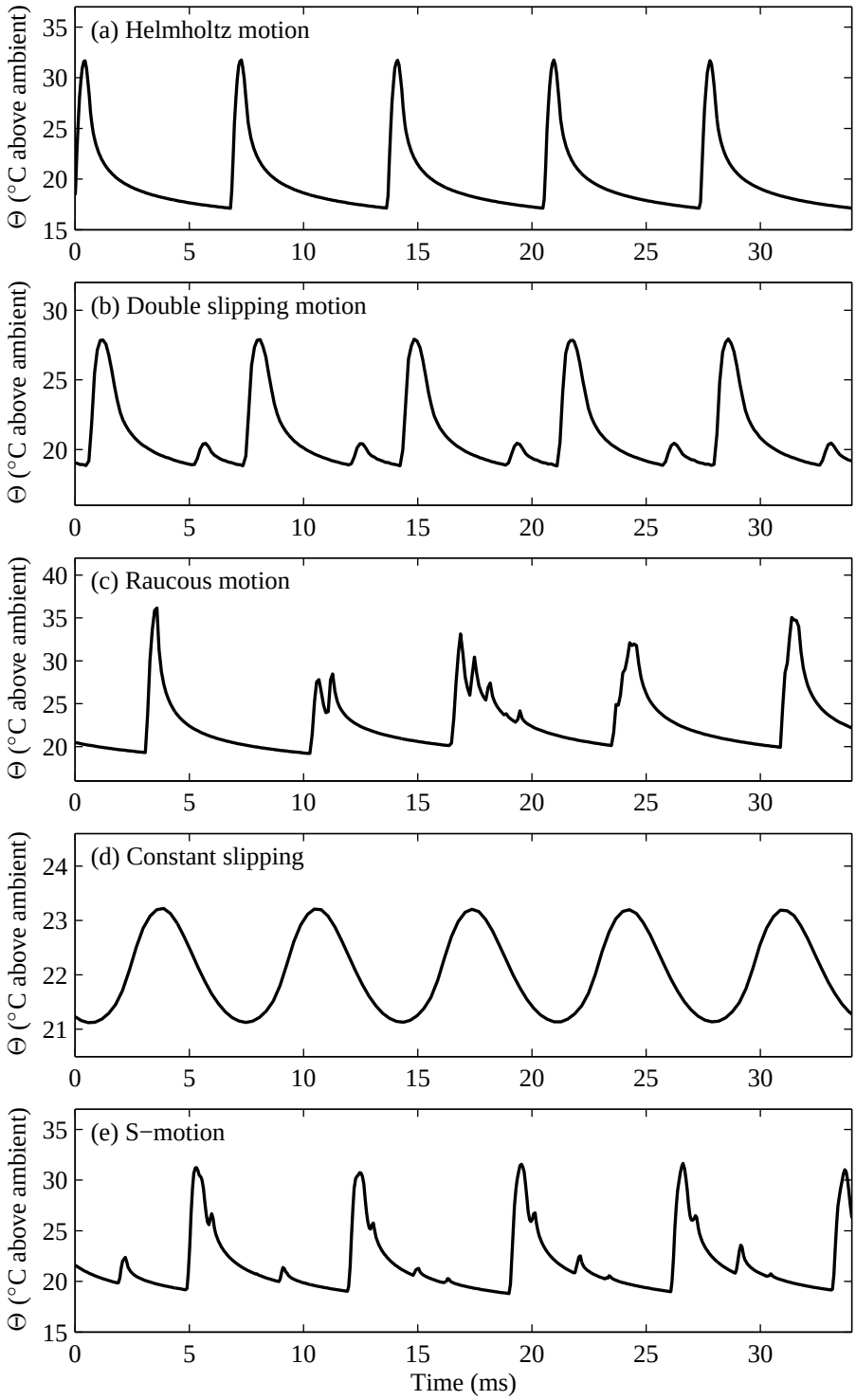

Figure 5.28: Temperature of the rosin in the bow/string contact patch, corresponding to the bridge force waveforms shown in Figure 5.27. Each flyback in bridge force, corresponding to a slip, causes a rise in temperature, each sticking period causes a gradual decrease. In the case of constant slipping, as shown in (d), the rosin is not given a chance to cool down.

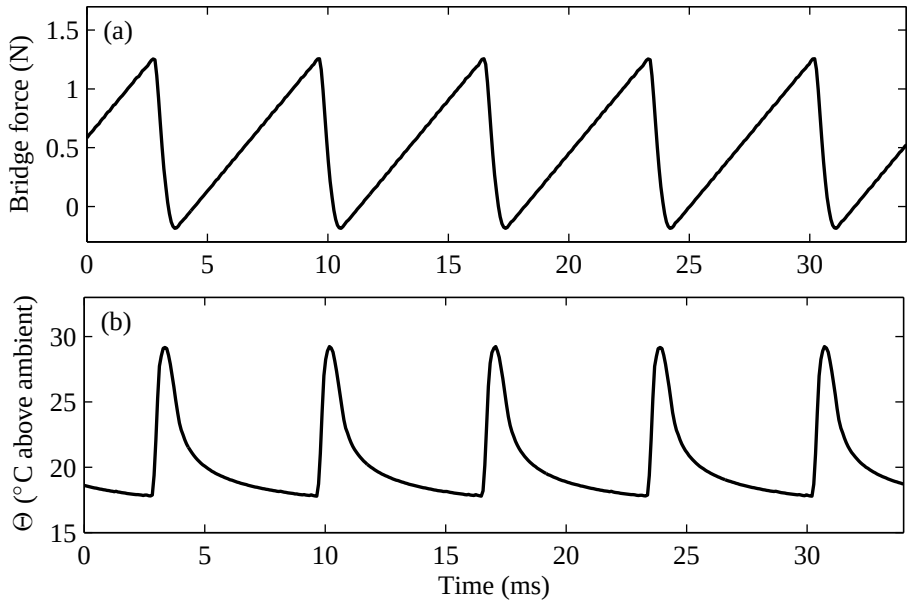

Figure 5.29: Example of bridge force waveform (equal to $2Z$ times the magnitude of transverse velocity waves travelling towards the bridge from the bowing point), and the corresponding temperature in the contact patch, in which the Helmholtz corner has been rounded. The flybacks in bridge force in the top plot are not as steep as they were in, for example, Figure 5.27(a).

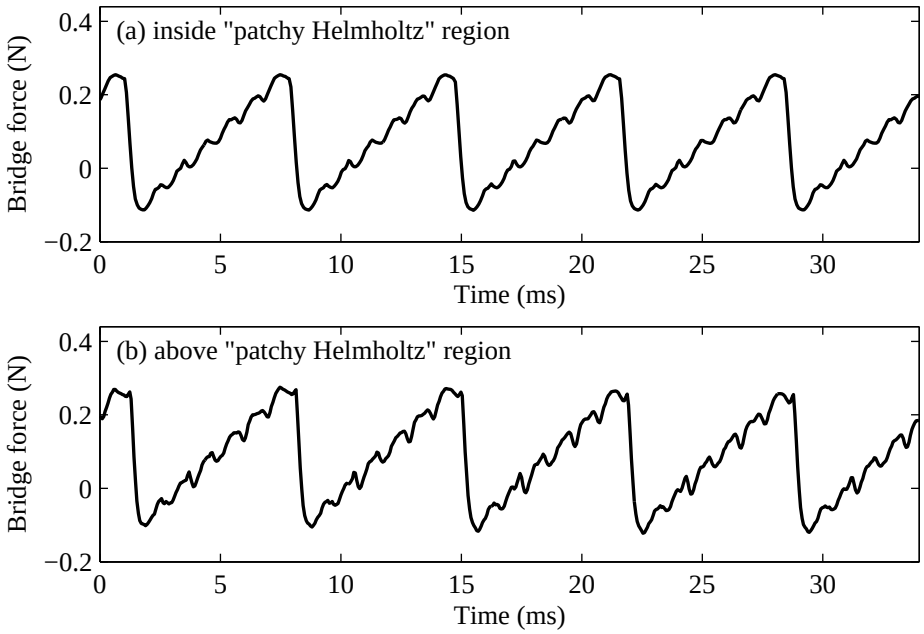

Figure 5.30: Simulated equivalent of the bridge force waveforms shown in Figures 4.19(a) and 4.19(b). The operating points for these waveforms were, respectively, within and above the region labelled "patchy Helmholtz" in Figure 4.14. Clearly, Helmholtz motion has remained intact in both of these cases with the thermal plastic simulation model, as it did throughout the entire region deemed to be "patchy" in experiment.

5.3.2 GUETTLER DIAGRAM: PRE-HELMHOLTZ DURATION IN N-a PLANE

The transient behaviour of the plastic thermal simulation model at a range of operating points in the force vs. acceleration plane is illustrated in Figure 5.31. These "Guettler diagrams" can be compared directly with the experimental equivalents in Section 4.3.2, and the old and new friction curve models in Sections 5.1.2 and 5.2.2 respectively.

It is encouraging to see that positions of the regions containing grey pixels, i.e. occurrences of Helmholtz motion, are qualitatively similar to the experimental measurements shown in Figure 4.20 — at least more so than the friction curve simulations. As in the experimental case, the upper and lower boundaries of the grey regions rotate in the anti-clockwise direction and become closer together as β is decreased, and in several places the data appears "twitchy", or visually speckly.

However, in all cases shown in Figure 4.20, the upper and lower borders of the Helmholtz motion region appears to intersect the N axis at some distance above the origin, with the distance increasing as β decreases. In experiment, the borders of the Helmholtz motion region appeared to pass through, or very near to, $(N, a) = (0, 0)$. Of even more concern however, in all cases shown in Figure 5.31, the region containing Helmholtz motion appears to terminate once a reaches a value of around 2.5 or 3 m/s^2 (the latter value is more appropriate for Figure 4.20(e), and the former is more appropriate for Figure 4.20(h)). This apparent limit in acceleration was not observed in experiment, and is therefore an artefact of the plastic thermal simulation model, whose cause will be discussed in the next chapter.

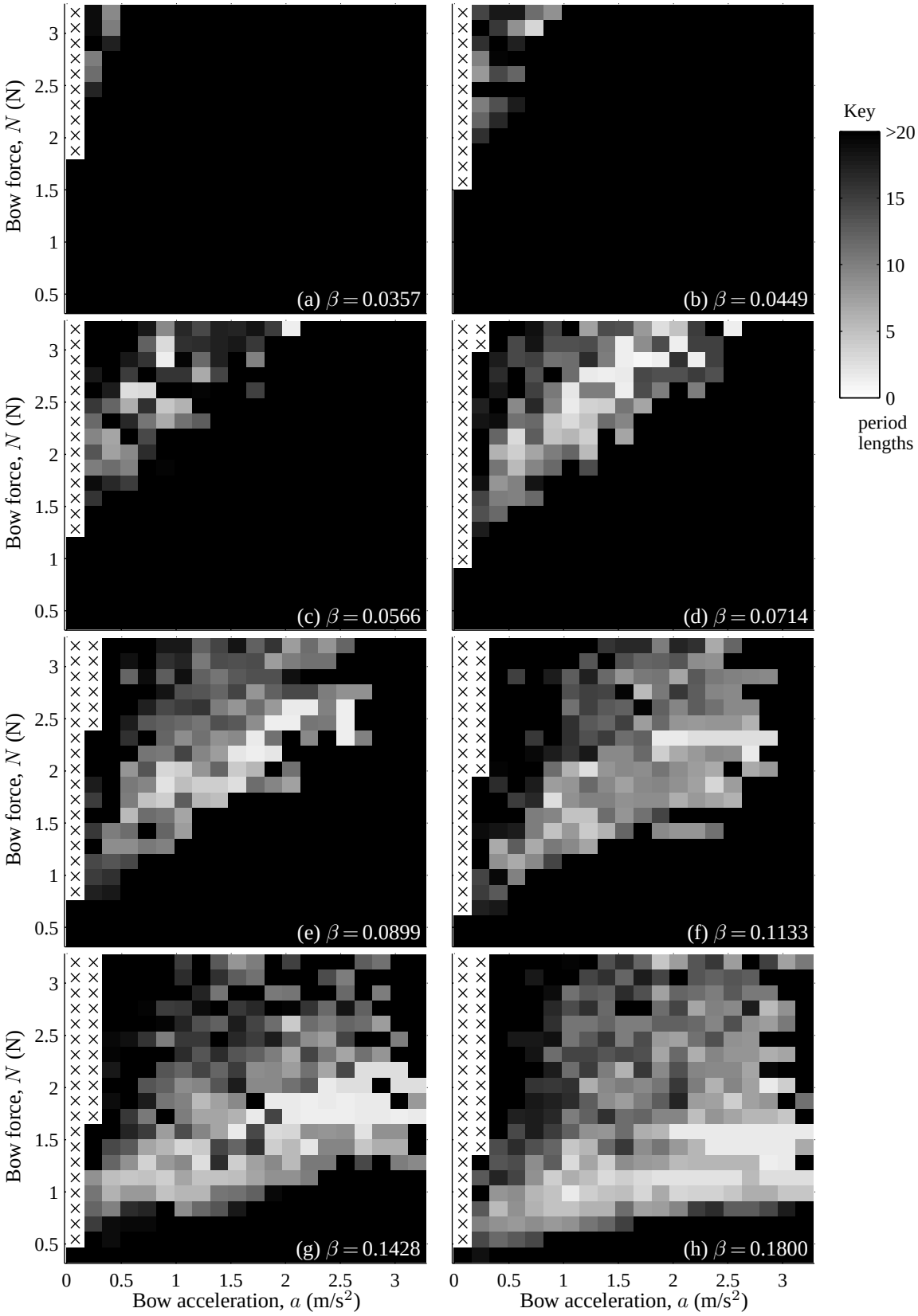

Figure 5.31: Simulated "Guettler diagrams", for eight different values of β, with the thermal plastic model of rosin. In each plot, as previously, the time taken to achieve Helmholtz motion relative to the time of the first slip at a given combination of bow force and acceleration is given by the shade of the pixel at the corresponding location in the N vs. a plane, according to the guide on the right. The experimentally measured equivalent, and the old and new friction curve simulated equivalents, are shown in Figures 4.20, 5.9 and 5.2.2 respectively.

INDIVIDUAL BRIDGE FORCE WAVEFORMS

Examples of the bridge force waveforms with various combinations of N, a and β are shown in Figure 5.32, and the associated thermal histories of the contact patch are shown in Figure 5.33. Figure 5.32(a) shows an example of a "nearly perfect" transient, i.e. one in which Helmholtz motion was achieved after a very short delay, and Figure 5.32(b) shows an example of raucous motion with clearly prolonged sticking periods. Figure 5.32(c) shows an example of double slipping motion; unlike in the steady state simulations used to construct the plastic thermal model Schelleng diagram previously, the plastic thermal model frequently predicts the formation of double slipping in transient waveforms. In each case, the eventual steady state waveform looks plausibly like an experimental equivalent.

The striking anomaly of all bridge force waveforms in Figure 5.32 is that the bridge force never "flies back", or drops, at the first slip. In all the experimental bridge force examples in Figure 4.22, the bridge force was seen to fly back at first slip; this was also seen to be the case in Figure 4.46. A direct comparison of Figures 5.32(b) and 4.22(c) exemplifies the difference observed at first slip between the vast majority of experimental and plastic thermal simulated "raucous" waveforms. The closest the plastic thermal simulation model comes to predicting an abrupt drop at the first slip is when the bow force and bow speed are both at their largest, but even then there is a delay between the start of the first slip (indicated by the instant when the bridge force stops rising) and the flyback: Figure 5.32(a) shows an example of this.

Besides predicting anomalous behaviour at first slip, the plastic thermal simulation model also predicts a "rounding" of the bridge force waveform at high bow speeds. In the case of constant acceleration bowing gestures, this occurs if the simulation is simply allowed to run for an extended length of time. The "rounded" pattern of behaviour seen at high bow speeds coincides with a failure of the string to resume sticking in the moments immediately following the passage of the Helmholtz corner past the bow towards the finger, as one would normally expect it to. An example of this behaviour is shown in Figure 5.34, which shows the effect of allowing the same simulation shown in Figure 5.33(a) to run for a quarter of a second: the saw-tooth wave in the bridge force has become rounded at the end of each flyback, and the velocity of the surface of the string at the bowing point (plotted in Figure 5.34(c)) does not rise up to the bow speed until the rosin temperature (plotted in Figure 5.34(b)) has cooled down to around 45°C.

The vibration identification algorithm described in Section 4.2.3 was designed to classify experimental bridge force signals. The "rounding" of the saw-tooth wave associated with Helmholtz motion observed with the plastic thermal simulation model never occurred in experiment, and as such the identification algorithm does not reliably class it as Helmholtz motion — indeed, perhaps the string can no longer be said to exhibit Helmholtz motion when the sticking time has diminished as much as it did, for example, in Figure 5.34. The apparent upper limit in acceleration seen in the Guettler diagrams in Figures 5.31(e), (f), (g) and (h), is caused by the vibration identification algorithm classifying this rounded Helmholtz motion as multiple slipping motion.

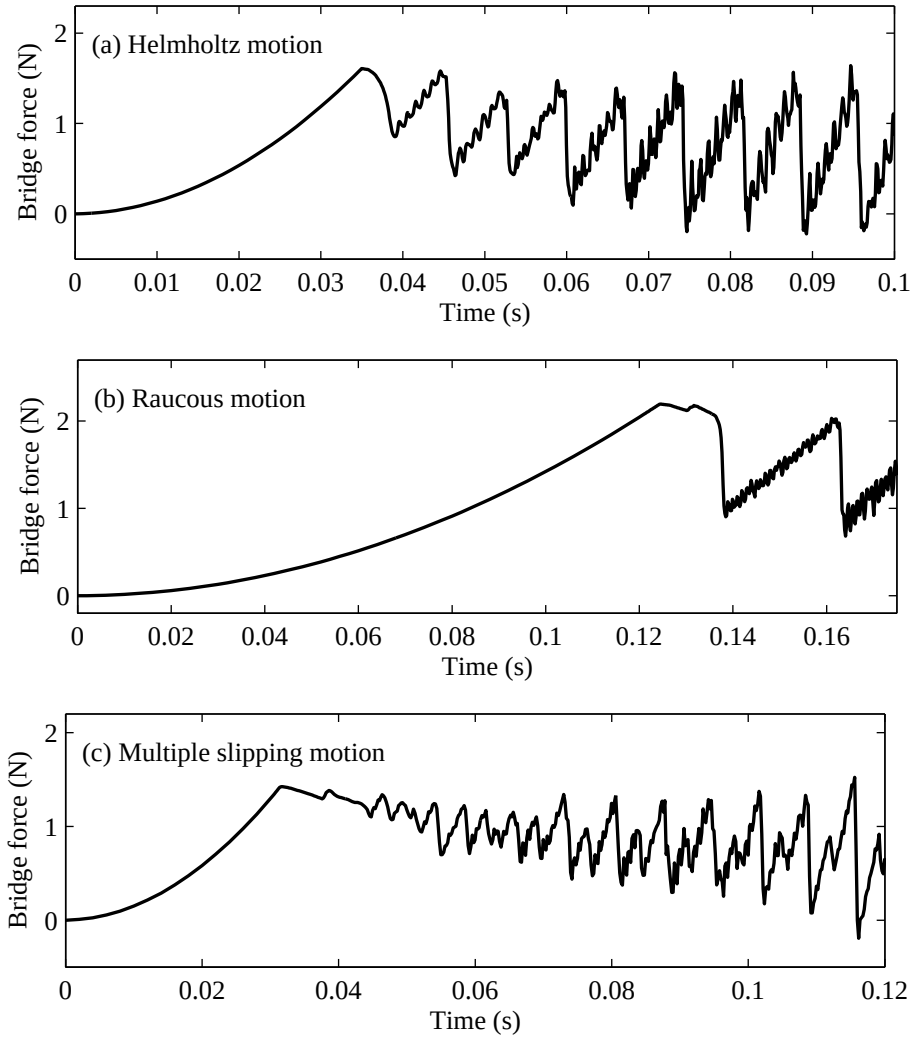

Figure 5.32: Examples of bridge force waveforms generated using constant acceleration bowing gestures, with the plastic thermal simulation model. The values of N, a and β for each example are, respectively: (a) 1.874 N, 2.215 m/s^2, and 0.1428; (b) 2.611 N, 0.244 m/s^2, and 0.1428; and (c) 1.579 N, 1.558 m/s^2, and 0.0899. the horizontal and vertical axes ranges are different in every plot, although the string's natural period is 0.00680 s in all cases.

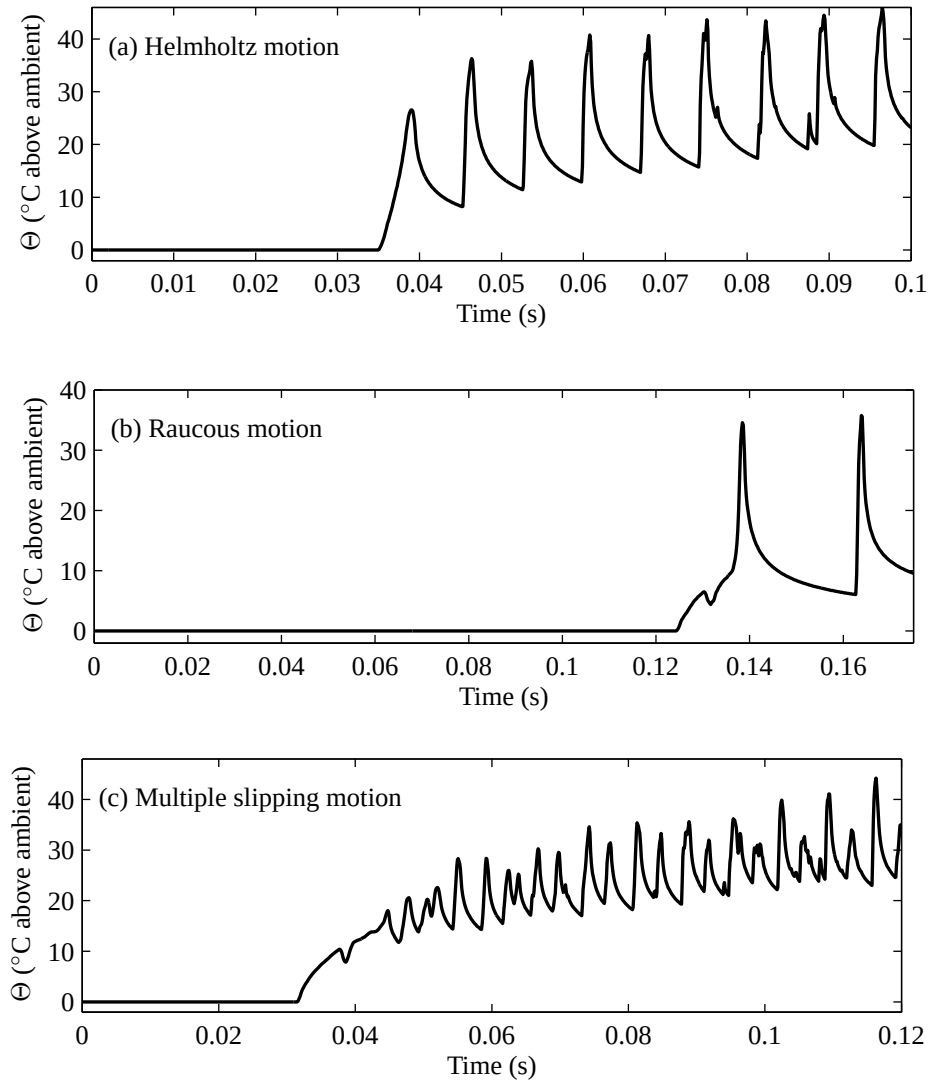

Figure 5.33: Temperature of the rosin in the bow/string contact patch corresponding to the bridge force waveforms in Figure 5.32.

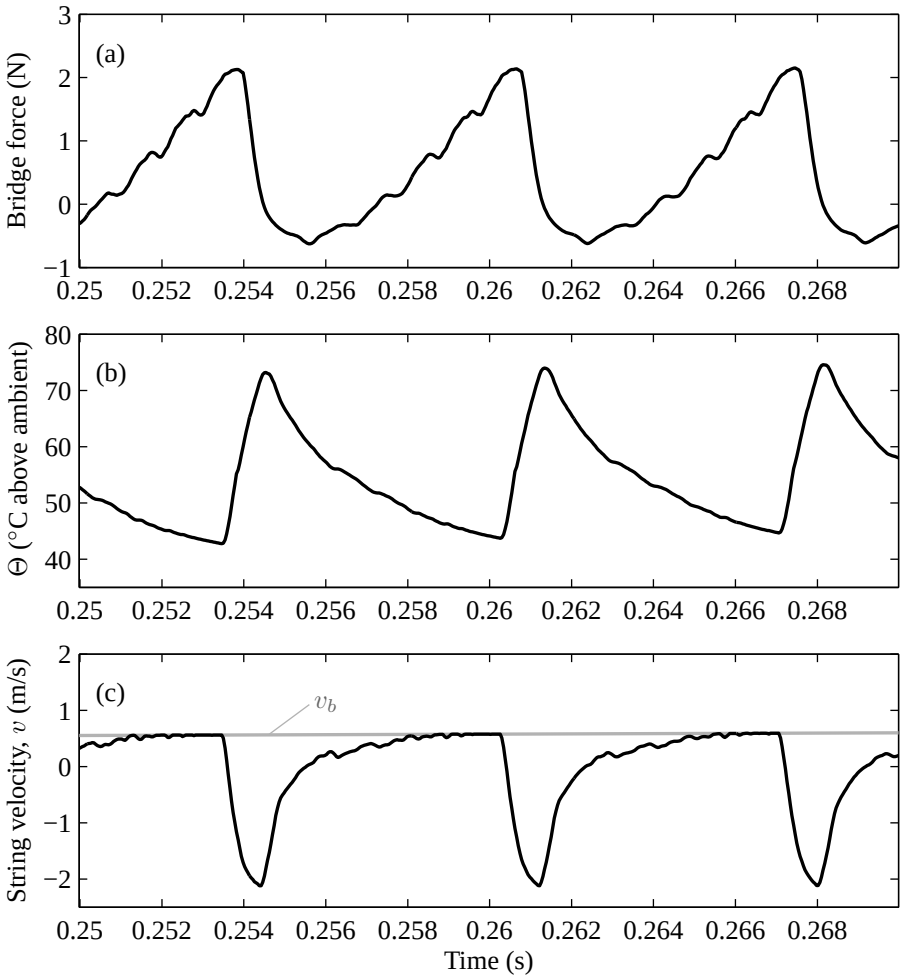

Figure 5.34: Example of the "roundedness" that occurs at high bow speeds with the plastic thermal model. (a) shows the bridge force, calculated as $2Z$ times the magnitude of the bridge-bound transverse velocity wave generated $\beta T/2$ seconds previously, (b) shows the temperature of the rosin in the contact patch, and (c) shows the velocity of the surface of the string. The bridge force is clearly rounded at the end of each fly-back, because the string does not stick to the bow until close to the time of the next slip. The values of N, a and β used to generate this data are 1.874 N, 2.215 m/s^2 and 0.1428 respectively, with the bow accelerated from rest starting at time $t = 0$ s.

5.4 SUMMARY OF FINDINGS

The ability of computational simulations of the bowed string based on both the friction curve and plastic thermal models of friction to predict the experimental results presented in the last chapter has been reviewed. Under certain conditions, each model showed at least qualitative agreement with experiment, although neither model was sufficiently consistent in this regard to warrant the type of playability investigations discussed in Chapter 1.

Each model successfully predicted that excessively large bow forces lead to the production of raucous motion or S-motion, and that excessively small bow forces lead to the production of multiple

or constant slipping. However, neither model succeeded in predicting the correct location of both the maximum and minimum bow force limits in the Schelleng or Guettler diagrams, although using the "reconstructed friction curve" from the last chapter in place of Smith and Woodhouse's steady sliding measurements was beneficial to the steady state vibration predictions from the friction curve simulation model.

The success of each simulation model at predicting the measured Schelleng diagram was not a consistently good indicator of its success at predicting measured Guettler diagrams. It is important, therefore, to recognize that the bow force limits for steady bowing that can be seen in a Schelleng diagram do not necessarily reflect the extent to which an instrument is conducive to short pre-Helmholtz motion transients. Certainly, noting that the duration of pre-Helmholtz motion transients is central to a player's perception of an instrument's playability, it is crucial that Schelleng diagrams should not be used as the *only* measure of playability.

Clues as to the source of differences between simulation and experiment were revealed by examining details of individual bridge force waveforms. Although the simulations occasionally predicted steady state vibration waveforms that were difficult to distinguish from those seen in experiment, various aspects of the transient vibration waveforms were highlighted that are at odds with experiment. These include:

- The precise transient vibration waveform predicted by the friction curve model with Smith and Woodhouse's steady sliding friction curve was almost unchanged as the bow force was varied by several times its original value, provided the ratio N/a was held constant. This similarity was not observed with the friction curve model when using the reconstructed friction curve, nor was it observed when using the plastic thermal model or in experiment. Similarity between transients generated using the same value of N/a caused trends in the Guettler diagrams predicted by the friction curve model with Smith and Woodhouse's steady sliding friction curve to coincide with radial lines in the N vs. a plane.

- In friction curve simulations based on the reconstructed friction curve, if the bow force is sufficiently large to cause a "flyback" in the bridge force at first slip, then the bridge force "overshoots" each saw-tooth wave associated with the slip-stick transition. This "overshoot" feature was not observed in experiment.

- Plastic thermal simulations generally fail to predict the transition of Helmholtz motion to double slipping at low bow forces, predicting instead that Helmholtz motion degenerates almost directly into constant slipping at low bow forces. In experiments there was a clearly defined range of bow forces that caused Helmholtz motion to degenerate into multiple slipping motion.

- In plastic thermal simulations, when the bow force and acceleration were both large, the saw-tooth wave associated with Helmholtz motion was observed to become rounded, and the slipping time elongated. This behaviour was not observed in experiments. Consequently,

the Helmholtz motion regions of the plastic thermal simulation Guettler diagrams did not extend into the top-right corner of the N vs. a plane.

- Whereas bridge force waveforms generated by the friction curve simulation model were frequently observed to "fly back" at first slip, those generated by the plastic thermal model did not under any conditions tested in this chapter. In experiment, "flybacks" at first slip were observed when the bow force exceeded a threshold value, which was generally around 1 N.

Causes of each of these anomalies and methods for preventing their occurrence are discussed in the next chapter.

Chapter 6

IMPROVING SIMULATIONS IN LIGHT OF EXPERIMENTS

INTRODUCTION

The wealth of experimental results presented in Chapter 4 was intended to provide a general understanding of the vibrational behaviour of the bowed string; the results from simulations of the bowed string shown in Chapter 5 exhibited different behaviour in several respects. In this chapter, possible reasons for these differences are discussed, and accordingly, remedies for the simulation model are suggested.

6.1 INTERPRETING EXPERIMENTS AND SIMULATIONS

NON-DIMENSIONAL GROUPS, AND SIMILAR VIBRATION TRANSIENTS

A striking degree of similarity was observed between different vibration transients generated using the friction curve model in Section 5.1.2 when the ratio N/a was kept the same, as seen for example in Figure 5.12. Contours of constant pre-Helmholtz motion time delay in Figure 5.9 clearly coincide with radial lines in the N vs. a plane. Holding the ratio N/a constant was also seen to cause some degree of similarity in experiment (Figures 4.20, 4.23–4.26, 4.29) and in plastic thermal model simulations (Figure 5.31), in that the regions in the N vs. a plane containing Helmholtz motion appeared to be wedge-shaped. A possible reason why contours of similar string motion would tend to coincide with lines of constant N/a in the Guettler diagram may be arrived at by considering the basic principles of the bowed string in non-dimensional form.

The input to the string is the friction force, which has the ability to grip the string with a force proportional to the normal force N, under the assumption that $f = \mu N$. Furthermore, noting from Equation (1.9) that $f = 2Z(v - v_h)$, the amount of friction that is required to vibrate the string is given by the magnitude of the outgoing velocity waves multiplied by $2Z$.

However, for a given waveform of motion, the velocity of every part of the string at all times scales with the bow speed v_b; i.e. the amplitude of the motion, and hence the magnitudes of outgoing velocity waves from the bow, scale with v_b. Therefore the amount of friction required to sustain a given vibration waveform is proportional to Zv_b. Consequently, the input to the string is characterized by the dimensionless group N/Zv_b, which will be denoted Π_{input}.

If the limiting static coefficient of friction μ_s and the coefficient of friction during sliding μ_d are assumed to be constant, then "similar" vibration transients (which differ only in magnitude) must share the same value of μ at any given time. The instantaneous value of μ would in such cases be determined at all times by the dimensionless quantity $(v_b - v_h)Z/\mu_s N$, where v_h is the combined magnitude of returning transverse and torsional velocity waves from the ends of the string: if this quantity is greater than unity then $\mu = \mu_d$; if it is less than μ_d/μ_s then $\mu = Z(v_b - v_h)/N$; otherwise μ equals either $Z(v_b - v_h)/N$ or μ_d depending on whether the string is sticking or slipping. The non-dimensional amplitude of returning velocity waves from the ends of the string is only dependent upon the the value of Π_{input}; hence if μ_s and μ_d are constants, then μ only depends on Π_{input}.

The input, friction, produces waves on the string by reacting to the waves already present on the string. As such, if the fundamental period $2L/c$ of the string is extended, then the reactions of the friction input will be delayed. Indeed, if we assume that β is fixed, the bow contacts the string at a point, wave dispersion can be ignored, and again that μ_s and μ_d are constants, then the extent of the delay is simply proportional to $2L/c$. Hence, if the time scale of interest is T_{scale}, which could

be for example the time taken to achieve Helmholtz motion, and all of these assumptions are made, then Π_{time}, the non-dimensional form of T_{scale} equal to $T_{scale}/(L/c)$, is only a function of Π_{input}.

Now, if the bow accelerates uniformly from rest, then $\Pi_{input}(t)$ equals N/Zat. As such, in order to compensate for an increase in bow force, one may increase the bow acceleration proportionally. Furthermore, if we again make the assumptions that μ_s and μ_d are constant, that β is fixed, and that wave dispersion can be ignored, then holding the quantity $N/Za(L/c)$ constant will produce the same vibration waveform for different values of N or a.

Hence, under these assumptions, as Π_{input} can be expressed as $N/Za(L/c)$, the time taken to produce Helmholtz motion is only a function of $N/Za(L/c)$. Equivalently, under these assumptions a player can not influence any aspect of the pre-Helmholtz motion transient (except its amplitude) without varying Π_{input}; this serves as an indication of the force being used by the player in dimensionless terms.

One would expect the player, through the use of N, v_b and β, to have more influence on the vibration pattern of the string than any other variable (including for example changes in the amount of energy dissipation or dispersion in the string). This means that, even for lightly damped and slightly stiff strings, Π_{time} should depend more on Π_{input} and β than on other physical quantities, provided that μ_s and μ_d are roughly constant. So for example, if Z, L and c are fixed, and the bow is accelerating uniformly from rest at a given value of β, then contours of constant pre-Helmholtz motion transient duration should lie approximately along contours of constant N/a. If either μ_s or μ_d do vary significantly, then this becomes an approximation.

This would appear to account for the strong similarity between waveforms generated at the same value of N/a using the friction curve model with Smith and Woodhouse's [43] steady sliding friction curve in Section 5.1.2: Smith and Woodhouse's steady sliding friction curve is so steep at low sliding speeds (see for example Figure 4.49) that the hysteresis rule described on page 6 forces the operating point to stay away from the steep part of the friction curve under nearly all sliding conditions, and hence the value of μ_d remains almost exactly equal to 0.35 at all times — see also [21, Fig.7(c)]. The uniformity of μ_s and μ_d means that the details of the transient string vibration are almost entirely determined by the quantity Π_{input}, or $N/Za(L/c)$.

The wedge-like appearance of the experimental Guettler diagrams in Section 4.3.2 and the plastic thermal simulation Guettler diagrams in Section 5.3.2, and the reasonable degree of similarity between measured waveforms with the same ratio N/a (see Figures 4.23 and 4.24), also probably reflects a relatively small degree of fluctuation of μ_s and μ_d under most conditions. The "reconstructed friction curve" on the other hand has very little curvature (see Figure 4.49), and hence the value of μ_d in simulations based on this the reconstructed friction curve constantly varies throughout the range 0.35–0.7. This may account for the apparent lack of structure in the reconstructed friction curve Guettler diagrams in Figure 5.19. In addition, all four of Guettler's conditions for the production of a "perfect transient" (see page 21) predict an upper or lower bound for bow force which is proportional to acceleration for constant values of μ_d.

6.2 FRICTION AT FIRST SLIP

It was seen in Figures 4.30, 4.32, and 4.44 that in experiment the limiting static coefficient of friction μ_s becomes larger before the first slip in cases where there is a long delay between the start of the bowing gesture and the first slip. Otherwise, if the delay is not so long, then μ_s is constant, and approximately equal to 0.65. This behaviour was not observed in simulations, as the value of μ_s before first slip was universally set to a single value.

This increase in μ_s is presumably an essential ingredient of any simulation model of the bowed string: by increasing the limiting static coefficient of friction and causing the string to be pulled further outwards before the first slip, the string's motion is initialized with additional potential energy. Additional potential energy would presumably impart extra "vigour" into the string's subsequent motion, which may indeed affect whether or not Helmholtz motion is achieved. Therefore a physical model, and a corresponding mathematical model, is developed in this section to govern the static friction properties of rosin.

6.2.1 INTERPRETING THE EXPERIMENTAL OBSERVATIONS

As a preparation for suggesting a physical model for this behaviour, it is illuminating to note that as the bow speed or acceleration is decreased towards zero, and the value of μ_s increases as discussed, it increases more at low bow forces than at high bow forces. This is evident from the fact that, while the left-most three columns of data in Figures 4.30, 4.32 and 4.44 contain lighter pixels (i.e. larger values of μ_s) than the other columns, the lightest pixels are confined to the bottom left corner of the plots.

This is further illustrated by plotting each individual measured value of μ_s for the first four columns of Figure 4.30, as shown in Figure 6.1 below. From Figures 4.30 and 6.1, it appears that the values of μ_s increase from a base level of around 0.6 to some upper limit that varies roughly in proportion to $N^{-1/3}$. The first column of data is particularly well approximated by a $N^{-1/3}$ dependence, although it is slightly obscured in Figure 6.1 by the second column.

However, the relation $\mu_s \propto N^{-1/3}$ is well known to occur when two bodies make intimate contact with each other, i.e. when all surface asperities have been flattened out and "Hertzian contact" has been achieved [82]. Conversely, situations where μ_s is independent of N are associated with problems where the two bodies only make contact with each other's surface asperities [84]; in such problems the total contact area between asperities on the two bodies may be referred to as the "real area of contact", A, whereas the overall cross-sectional area of the apparent contact patch may be referred to as the "area of contact", A_{tot}. Hence, in the case of Hertzian contact, $A = A_{tot}$. Slip is induced when the shear stress acting over the real area of contact reaches the shear yield stress k_y, such that $\mu_s N = k_y A$: for Hertzian contact in an elliptical contact patch (as for example between the perpendicular string and rod), $A \propto N^{2/3}$, whereas for "rough" contact, i.e. where contact is

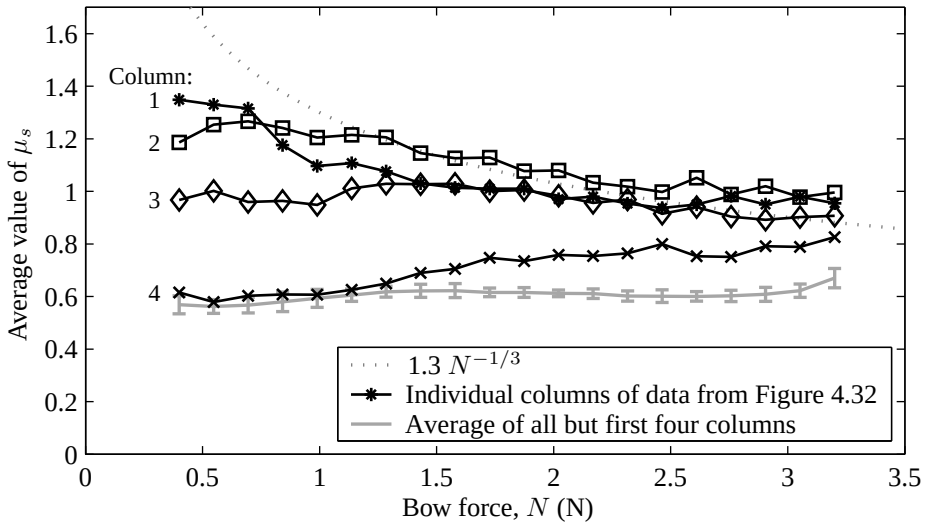

Figure 6.1: Same as Figure 4.33(b), but with the first four columns of the array of μ_s values shown separately, and with a grey dotted line showing the function 1.3 $N^{-1/3}$ for comparison. The first two columns of μ_s data appear to tend towards the $N^{-1/3}$ line, except at the lowest bow forces. The average of the remaining sixteen columns is shown as a grey line, with error bars indicating the standard deviation incurred in the averaging process.

made through surface asperities only, $A \propto N$; hence $\mu_s \propto N^{-1/3}$ in Hertzian contact problems, and $\mu_s \propto N^0$ (i.e. independent of N) for "rough" contact problems [82].

Therefore, from Figure 6.1 it would seem that if there is a sufficient time delay between the start of a bowing gesture and the first slip, then the asperities begin to flatten out, until the real area of contact A reaches the total area of the contact patch A_{tot}. The fourth column of values of μ_s from Figure 4.30, plotted with respect to N and labelled with a "4" in Figure 6.1, shows a gradual increase in μ_s with respect to N, suggesting that the value of bow acceleration, a, associated with the fourth column of μ_s values is just large enough for the growth in contact area, and hence μ_s, to be noticeable. The first two columns of values of μ_s from Figure 4.30, labelled as "1" and "2" in Figure 6.1, appear to indicate that the gap between A and A_{tot} is small enough that the entire contact area is filled out, and Hertzian contact — and hence $\mu_s \propto N^{-1/3}$ — is achieved. The third column of data, labelled "3" in Figure 6.1, apparently only exhibits this behaviour at large bow forces.

It is interesting to note, finally, that studies of seismic fault lines have reached a similar conclusion regarding the friction between rock surfaces under a shear load. Marone [85], for example, found that holding the shear load between two granite surfaces at a large constant value before increasing it to the point of slipping causes an increase in limiting static coefficient of friction. Marone found that the increase in μ_s was approximately proportional to $\log(\text{holding time})$.

6.2.2 INCORPORATING CONTACT AREA GROWTH INTO SIMULATIONS

Under the hypothesis that the real area of contact, A, between the perspex rod and the string increases if it is held under a shear load for any prolonged period of time, it is plausible that the following type of behaviour might occur:

$$\frac{dA}{dt} \propto \left(\frac{q}{dq/dt}\right)^z, \tag{6.1}$$

where q is the shear stress acting on the contact patch, equal to f/A, and z is a positive constant. As such, if $q/(dq/dt) \sim T_{1^{\text{st}}\text{ slip}}$, where $T_{1^{\text{st}}\text{ slip}}$ is the delay between the start of the bowing gesture and the first slip, then $dA/dt \sim (T_{1^{\text{st}}\text{ slip}})^z$.

Furthermore, it is logical that the real area of contact would stop growing once it has reached the total area of the contact patch. One way to ensure this would be to assume that the following behaviour also occurs:

$$\frac{dA}{dt} \propto \left(1 - A/A_{tot}\right)^y, \tag{6.2}$$

where y is a positive constant. Equation (6.2) ensures that the real area of contact is allowed to grow according to Equation (6.1), until the ratio A/A_{tot} approaches unity — i.e. until asperity contact fills the contact patch.

Hence, the following equations are suggested to predict the limiting static coefficient of friction:

$$q = f/A, \tag{6.3a}$$

$$\frac{dA}{dt} = c_{jg}\left(\frac{q}{dq/dt}\right)^z \left(1 - A/A_{tot}\right)^y, \tag{6.3b}$$

$$\text{and} \quad \mu_s = k_y A/N, \tag{6.3c}$$

where c_{jg} is a constant of proportionality and k_y is the shear yield strength of rosin. They are readily solvable numerically. The initial value, A_0, of the real area of contact A may be obtained from the experimental results: at large bow speeds, μ_s was seen to be approximately equal to 0.7, and hence $A_0 \approx 0.7N/k_y$. The value of A_{tot} may also be extrapolated from the experimental results: μ_s appears in Figure 6.1 to stop increasing once it reaches $1.3N^{-1/3}$, and hence $A_{tot} \approx 1.3N^{2/3}/k_y$.

6.2.3 RESULTS FROM SIMULATIONS WITH CONTACT AREA GROWTH

Using the candidate static friction model in Equations (6.3a) (6.3b) and (6.3c), and choosing $k_y = 10$ MPa, $c_{jg} = 22$ s^{-z}, $z = 3$ and $y = 2$, the results shown in Figures 6.2 and 6.3 are obtained. In both figures, the general appearance of the predictions are broadly similar to the corresponding results obtained in experiment, in Figures 4.30, 4.32 and 6.1. This supports the general idea of the junction growth model used to predict an increase in the real area of contact, although the values of k_y, c_{jg}, z and y were chosen in an ad-hoc manner.

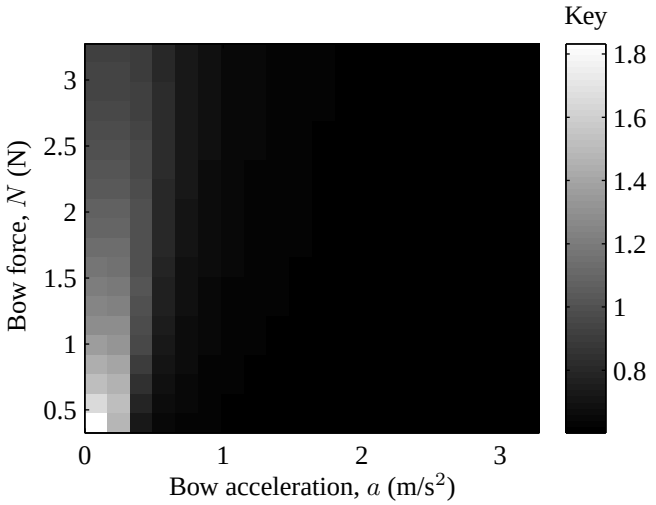

Figure 6.2: Theoretical equivalent of the experimental results shown in Figures 4.30 and 4.32 (on pages 99 and 101), based on the junction growth model in Equations (6.3b) and (6.3c). As in Figures 4.30 and 4.32, the darkness of each pixel indicates the value of limiting static coefficient of friction just before first slip, according to the color guide on the right. The general appearance of light and dark pixels is visibly similar to that of Figures 4.30 and 4.32, suggesting that the physical model used is plausible.

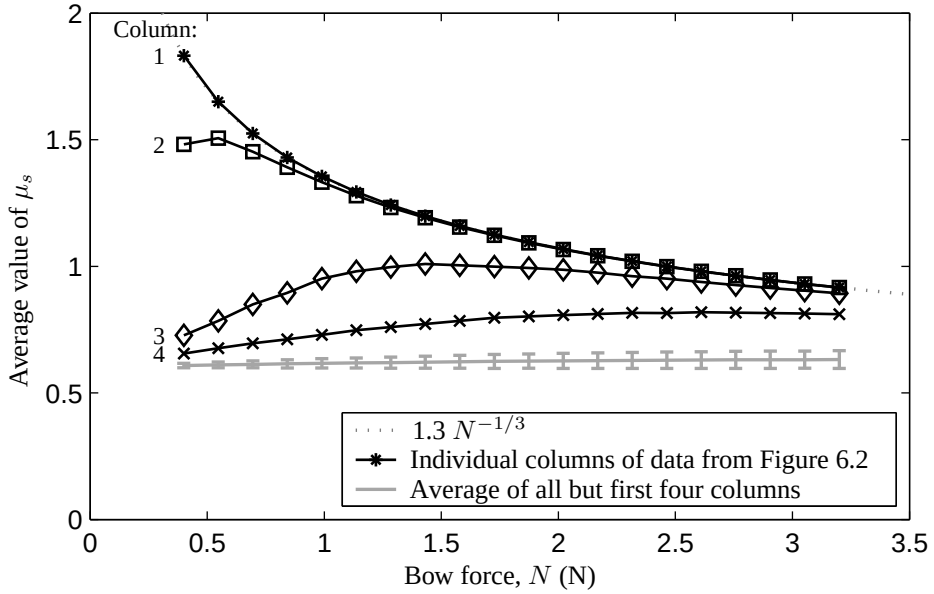

Figure 6.3: Theoretical equivalent of the experimental results shown in Figure 6.1, based on the junction growth model in Equations (6.3b) and (6.3c). The general rise in μ_s at low accelerations is predicted with qualitative accuracy, suggesting that the physical model used is plausible.

6.2.4 CREEP DISTANCE

A subtle but distinct feature of Figures 4.30, 4.32, 4.44 and 6.1 is that as the bow speed (or acceleration) decreases to very low values, well inside the range where the increase in μ_s was observed, the value of μ_s appears to drop slightly. This is apparent from the fact that points in the the left-most column in Figures 4.30 and 4.32 is slightly darker than those in the second column; the three left-most columns of Figure 4.44 are progressively darker at smaller bow speeds; and the first value of column-averaged μ_s in Figures 4.31(a), 4.33(a) and 4.45(a) is less than the second value. This is also apparent in Figure 6.1, in which the individual values of μ_s are plotted, column by column: the first column, as mentioned in the text, is well approximated by $1.2N^{-1/3}$, but the second column slightly obscures the appearance of the first by being larger at high values of bow force (but smaller at low values of bow force for the reasons discussed previously); the first and second column are the same at around $N = 0.75$ N.

This evidence is consistent, and suggests the existence of a secondary effect that also affects the value of μ_s, which was not captured by the simple junction growth model in Equation (6.3b). Two possible explanations for this are as follows:

1. As the shear stress increases before the first slip, the string may be seen to creep slowly along the bow (see for example Figure 4.42). It could be that at low bow speeds, the string is given enough time to creep before first slip that it moves beyond the edge of its original zone of contact with the bow. In the event of the string moving into a new contact zone, it would need to start the junction growth process afresh; similarly, if it is steadily moving beyond the edge of the existing contact zone, then the real area of contact will never reach A_{tot}, and so the value of μ_s will never reach $k_y A_{tot}/N$. Hence, if very low bow speeds enable the contact zone to move due to relatively large loading times, then one would expect μ_s to be smaller if the bow speed is very small.

2. It is alternatively possible that as the string creeps (albeit slowly), some amount of heat is generated, at a rate $\mu N(v_b - v)$, and that this heat softens the rosin and causes k_y — and hence μ_s — to decrease. As such, creep would again be responsible for the drop in μ_s.

6.3 "OVERSHOOTS" WITH RECONSTRUCTED FRICTION CURVE

In Section 5.2.2, it was seen that when using the reconstructed friction curve with the friction curve simulation model, if the bow force is large enough to make the string fly back at first slip, the bridge force appears to "overshoot" at most flybacks near the start of the bowing gesture. A typical example of a bridge force waveform containing several overshoots was shown in Figure 5.20(a).

HYSTERESIS LIMITS ARE TOO CLOSE FOR CLEAR TRANSIENTS

This "overshoot" in the bridge force at the first slip in cases where the bow force is sufficiently large is caused by the events immediately following the first slip. At first slip, provided the normal force is sufficiently large, the operating point in the f vs. v plane jumps from the tip of the vertical portion of the friction curve to the point along the curved section which has the same value of v_h. The resulting change, $(\Delta v)_{\text{slip}}$, in relative sliding velocity between the surface of the string and the bow causes transverse and torsional waves to be sent towards both ends of the string. From Equations (1.5), (1.9a) and (1.9c), the magnitude of the transverse waves equals $(\Delta v)_{\text{slip}} Z_\theta/(Z_T + Z_\theta)$, and the magnitude of the torsional waves, when referred to the tangential velocity $a\dot{\theta}$ of the surface of the string, equals $(\Delta v)_{\text{slip}} Z_T/(Z_T + Z_\theta)$. Using the notation of Figure 1.4, sticking will resume once v_h equals or exceeds v_2, i.e. the "upper limit" of the friction curve hysteresis cycle, whereafter sticking will persist until v_h falls below v_1, where v_1 is the "lower limit" of the hysteresis cycle (equal to $v_b - \mu_s N/2Z$). With the old friction curve model, the two limits v_1 and v_2 were sufficiently well separated that v_h did not increase by an amount equal to or exceeding $v_2 - v_1$ until the transverse velocity wave returned from the bridge.

Crucially, the reconstructed friction curve that predicted overshoots has relatively little curvature because the term $e^{(v-v_b)/0.7}$ in Equation (4.3) decays relatively slowly with respect to $v - v_b$; this can be compared with the two exponential terms in the "old" friction curve in Equation (4.4). This lack of curvature, or flatness, makes the two hysteresis limits v_1 and v_2 relatively close together, to the extent that even the bridge-side torsional wave is large enough to increase v_h by the amount $v_2 - v_1$ required to induce sticking. This is illustrated in Figure 6.4. Therefore, whereas the first slip lasted βT seconds in the vast majority of cases with the old friction curve, where stick-slip alternations were determined by transverse waves (as seen for example in Figure 5.11), the first slip only lasts for $2\beta L/c_\theta$, where c_θ is the propagation speed of torsional waves. Here, the ratio of the wave speeds for torsional and transverse waves is around 5:1, so the first slip lasts for only around a fifth of the time that it would ordinarily last with the old friction curve model.

When the first slip terminates prematurely due to slip-stick triggering by torsional motion, the string's sliding velocity jumps back to zero, approximately reversing the original $(\Delta v)_{\text{slip}}$ change in string velocity. This again causes transverse and torsional velocity waves to be sent outwards from the bowing point, this time of magnitudes $-(\Delta v)_{\text{slip}} Z_\theta/(Z_T + Z_\theta)$ and $-(\Delta v)_{\text{slip}} Z_T/(Z_T + Z_\theta)$ respectively. Therefore, when sticking resumes, a new torsional wave is sent towards the bridge which, when it returns to the bowing point, nearly restores v_h to v_1, its value just before the first slip. Only a small disturbance, typically from high frequency transverse waves that have travelled ahead of the main transverse wavefront due to the wave dispersion, is sufficient to perturb v_h beyond v_1 and induce slipping again.

The cycle of sticking and slipping repeats until the main part of the transverse wave sent towards the bridge at the start of the first slip returns to the bowing point. A typical example, and ample illustration, of these rapid stick-slip alternations is shown in Figure 6.5. For the example in Figure

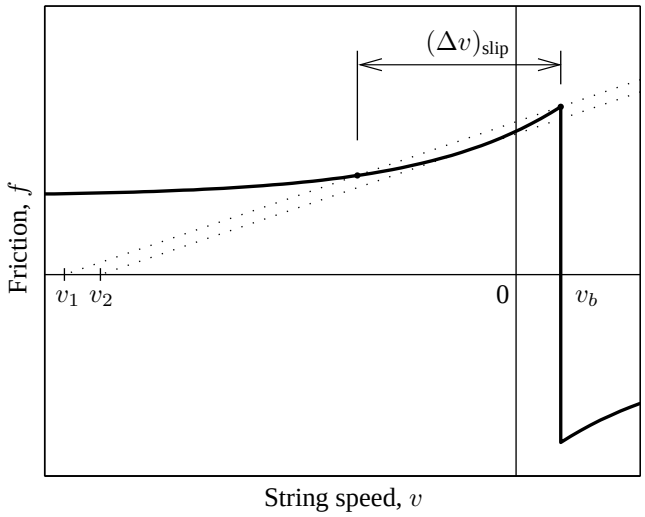

Figure 6.4: Illustration of the fact that the hysteresis limits v_1 and v_2 become closer together if the friction curve is flatter, or straighter. The friction curve shown is the "reconstructed" friction curve of Equation (4.3); for the values of v_b and N used to generate this plot, the difference between v_1 and v_2 is less than $(\Delta v)_{\text{slip}} Z_T/(Z_T + Z_\theta)$, and so the torsional wave sent towards the bridge at first slip will cause the premature resumption of sticking when it returns to the bowing point. (The quantity $Z_T/(Z_T + Z_\theta)$ is around 0.23 for a Dominant cello D-string.)

6.5, the quantity $Z_T/(Z_T + Z_\theta)$ is equal to 0.234 and the ratio of torsional to transverse wave speeds is 5.23. Hence the torsional wave generated at first slip, indicated by a solid line, is seen to be around 0.234 times the magnitude of the overall change in string surface velocity at first slip, $(\Delta v)_{\text{slip}}$; and the "nominal Helmholtz" slipping time βT is around five times the duration of the first "mini-slip".

This behaviour is responsible for the "overshoots" in bridge force, such as those shown in Figure 5.20(a). One would ordinarily expect slipping to cause the bridge force to rise gradually and then suddenly drop, forming the recognizable pattern of saw-tooth waves. The rapid stick-slip transitions just after the first slip create an additional oscillation that is superimposed on the saw-tooth wave for as long as the oscillations last. In the same way that secondary travelling waves create "Schelleng's ripples" [16, 22], the transverse waves created by the rapid changes in string velocity create the "overshoot" feature.

General Implications for Friction Curve Simulation Model

The preceding discussion does not bode well for the friction curve model of rosin: on one hand, measurements of the steady state vibration of the string, in the context of measuring a Schelleng diagram, demonstrate that a "flatter" friction curve is required; however, the effect of "flattening" the friction curve as such is to produce anomalous behaviour just after the first slip, caused by rapid

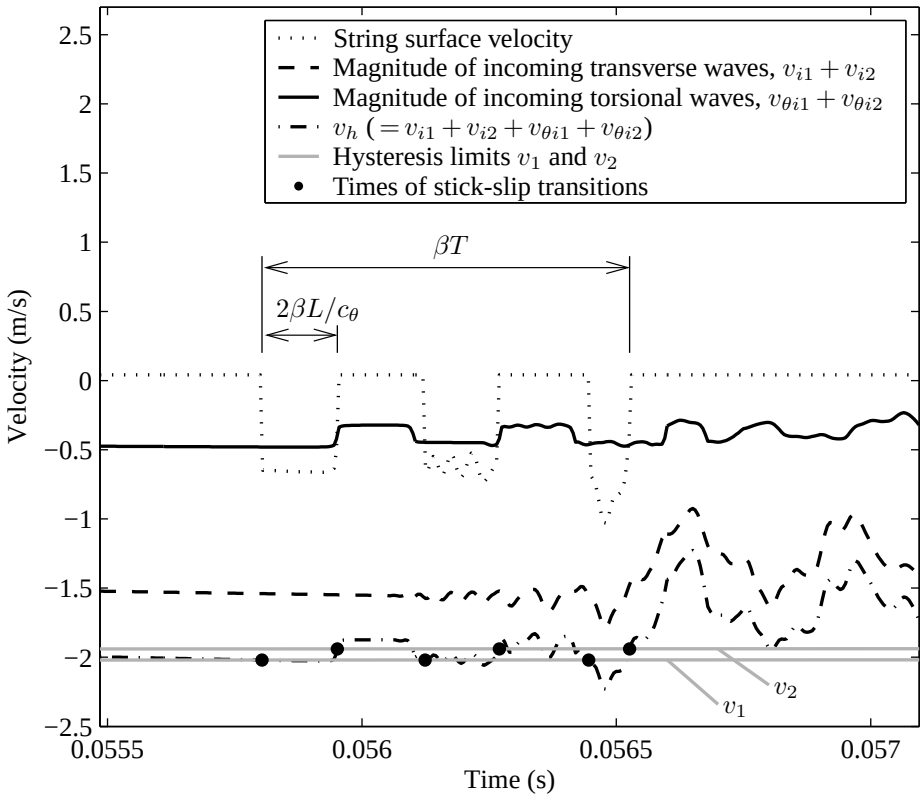

Figure 6.5: An example of the rapid stick-slip motion described in the text, that is frequently seen at the times of the first few slips in simulations based on "flat" friction curves. The dotted line shows the velocity of the surface of the string, which during times of sticking is equal to approximately 0.041 m/s, the velocity of the bow; the times of slipping are hence clearly seen as the times when the dotted line dips. The value of v_h is shown as a dot-dash line, and the hysteresis threshold values v_1 and v_2 are shown as grey lines; the black circles indicate times of stick-slip transitions, and are superimposed on whichever of the two hysteresis thresholds has been crossed. The torsional contribution to v_h, equal to $v_{\theta i1} + v_{\theta i2}$ using the notation of Figure 1.7, is plotted separately as a black solid line; the transverse contribution to v_h, equal to $v_{i1} + v_{i2}$, is plotted separately as a dashed line. The end of the first slip can be seen to coincide with the return of the torsional wave sent towards the bridge at the beginning of the first slip; the start of the second slip can be seen to coincide with the first high frequency transverse oscillation following the return of the torsional wave sent towards the bridge at the end of the first slip, and so on. This rapid stick-slip oscillation finishes when the lower frequency components of the original bridge-side transverse wave return to the bowing point, at a time βT after the start of the first slip, as shown.

torsion-induced stick-slip alternations. These results suggest that it may not be possible to use the friction curve simulation model, in its existing form, to obtain quantitatively accurate predictions of the motion of the bowed string.

From a wider perspective, the contrasting success of the friction curve simulation model when predicting the Schelleng diagram steady state behaviour and the Guettler diagram transient behaviour suggests that a good prediction of the Schelleng diagram is not equivalent to a universal guarantee of the playability of an instrument in every sense. Although information about bowing limits dur-

ing steady bowing is useful as information for players, or as a guide when assessing the accuracy of a simulation model, the appearance of Schelleng diagrams does not necessarily correlate with how conducive an instrument is to producing short pre-Helmholtz motion transients.

6.4 PLASTIC THERMAL MODEL: THE k_y VS. Θ CURVE

Having not directly measured the shear yield strength, k_y, of rosin as a function of temperature, Θ, Smith and Woodhouse [43] suggested that the relationship between k_y and Θ should be chosen such that the thermal plastic friction model predicts the same results, under steady sliding conditions, as were obtained in steady sliding experiments. The resulting curve, when the "real area of contact" A between bow and string is 0.79 mm^2, is shown in Figure 6.6. If the values of μ are multiplied by N/A (which Smith and Woodhouse found to equal 3.82 MPa), then Figure 6.6 is equivalent to a k_y vs. Θ curve.

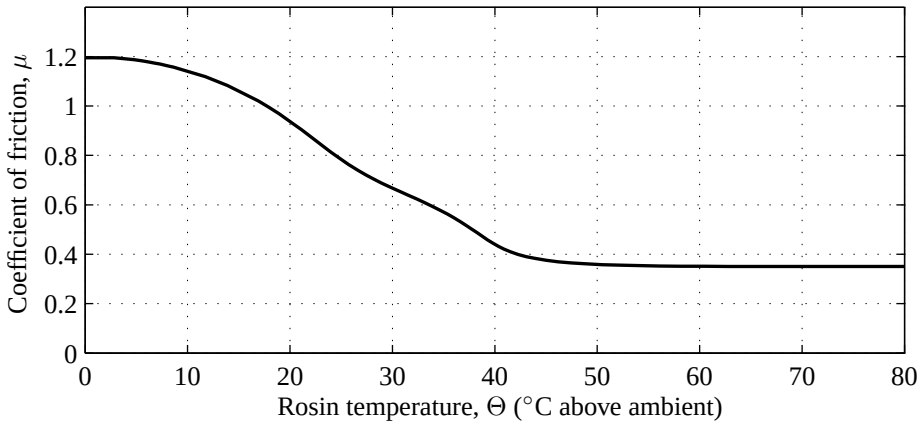

Figure 6.6: Variation of friction with temperature as proposed by Smith and Woodhouse [43] for the plastic thermal model. Multiplying the values of μ in this figure by N/A (which was reportedly equal to 3.82 MPa in Smith and Woodhouse's experiments), one obtains the variation of rosin's shear yield stress k_y with temperature. This thermal dependence uniquely ensures that the plastic thermal friction model predicts the same amount of friction during steady sliding as was measured in steady sliding tests by Smith and Woodhouse. Simulations conventionally start with the rosin at the ambient temperature.

However, in light of the measurements of μ_s shown in Chapter 4, and the discussion in Section 6.2, it seems unlikely that a k_y vs. Θ relationship based only on steady sliding measurements will be accurate, as steady sliding measurements may be prone to the junction growth phenomenon discussed previously. In addition, Smith and Woodhouse's steady sliding tests only include measurements of friction at sliding speeds of up to 0.3 m/s, whereas sliding speeds in practice are frequently an order of magnitude larger.

With this context in mind, some discrepancies between experiment and simulation that are attributable to the k_y vs. Θ curve are examined in this section, and methods of modifying the k_y vs. Θ curve in order to correct them are suggested.

6.4.1 μ_s AT FIRST SLIP IS TOO LARGE

Because the limiting static coefficient of friction μ_s was measured as being approximately 1.2 by Smith and Woodhouse [43], the highest value of k_y predicted by the plastic thermal model (at the lowest temperatures) is $1.2N_{st}/A_{st}$, where N_{st} and A_{st} are the normal force and contact area reported by Smith and Woodhouse in their steady sliding tests. However, in light of the discussion in Section 6.2 and the experimental measurements in Figures 4.30, 4.32 and 4.44, it seems that the value of k_y at low temperatures should not be so high when simulating bowing by a perspex rod. If $k_y A/N$ is assumed to be 0.65 instead of 1.2, then the value of k_y at low temperatures is almost halved. It is suggested that the value of k_y should not exceed $0.65\,N_{st}/A_{st}$ at any temperature, when simulating the contact between the string and the perspex rod.

It is noted in passing that the "reconstructed friction curve" in Figure 4.49 cannot be used in place of Smith and Woodhouse's steady sliding measurements to evaluate the k_y vs. Θ curve using the same method as Smith and Woodhouse, because they were not obtained under steady sliding conditions.

6.4.2 FLYBACKS IN BRIDGE FORCE AT FIRST SLIP

REASON FOR ABSENCE OF BRIDGE FORCE FLYBACK AT FIRST SLIP IN SIMULATIONS

It was seen in Section 5.3 that all bridge force waveforms obtained using the plastic thermal simulation model have a delay between the time of the first slip and the time when the bridge force drops from its value before first slip. However, in experiment, when the bow force was greater than some threshold value (around 1.3 N when $\beta = 0.08$ for instance), the bridge force was always observed to drop abruptly following the first slip before increasing again. Figures 6.7(a) and (b) show examples of experimental bridge force transients which have, respectively, no clear bridge force flyback at first slip, and a flyback of around 0.34 N; transients generated using the plastic thermal model are of a similar nature to the latter, as demonstrated for example in Figure 6.8. The difference that the flyback makes to the sound made by the cello is audible.

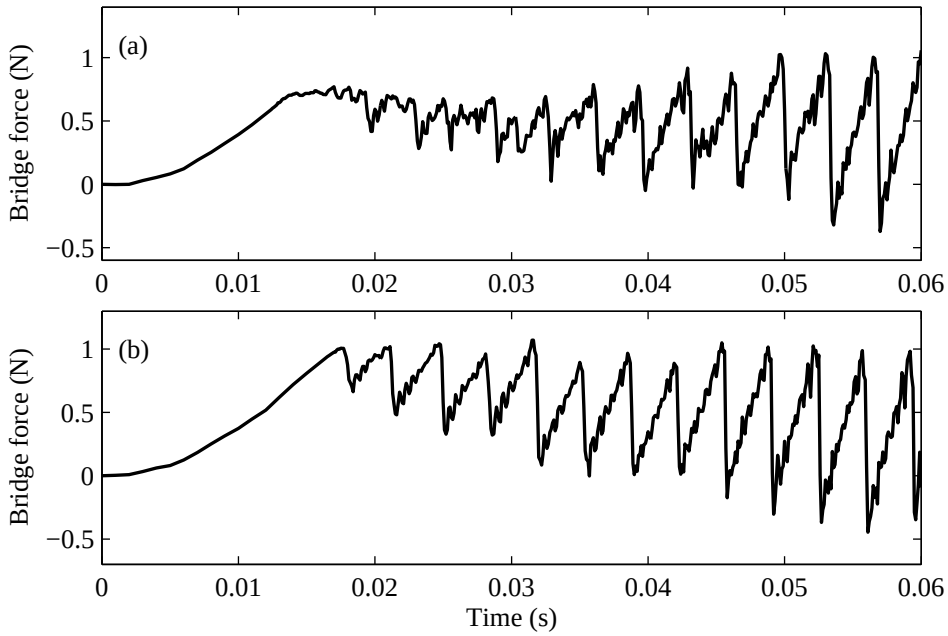

Figure 6.7: Examples of experimentally measured bridge force waveforms generated with slightly different values of N, but otherwise nominally similar bowing parameters. In (a), N is 1.137 N, and in (b) N is 1.432 N; these two values of N are very near to the limiting bow force required to generate a flyback. The bow acceleration a and β are respectively 2.543 m/s^2 and 0.0714 in this example.

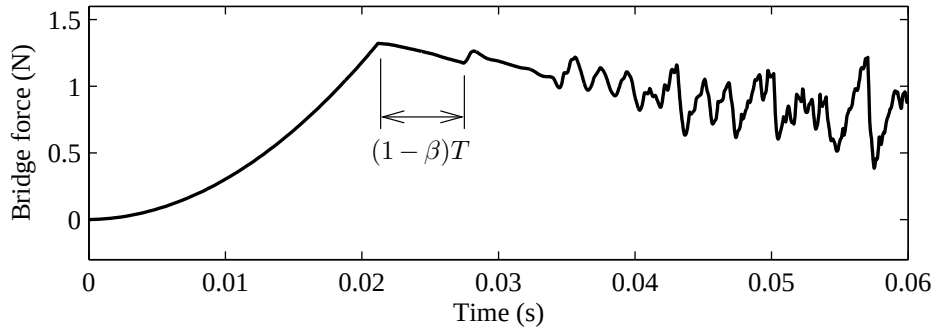

Figure 6.8: Plastic thermal simulation, at the same operating point as Figure 6.7(b), illustrating the $(1-\beta)T$ duration of the first slip. In this case, the second slip lasts for $(1-2\beta)T$ for similar reasons.

The cause of the plastic thermal model's reluctance to produce an abrupt "flyback" in the bridge force (or "jump back" in string displacement) at the time of the first slip is related to the time taken for the rosin to warm up to temperatures where, according to the k_y vs. Θ curve, the rosin is sufficiently compliant to allow rapid sliding movement. In order for the string to fly back and quickly start sticking again at the first slip, the hysteresis cycle comprising the following chain of events must occur:

1. The string slips, and in doing so sends transverse velocity waves towards the bridge and the finger (labelled "2" and "1" respectively in Figure 1.15(b)).

2. The relative sliding velocity between the bow and string during slipping generates heat, causing k_y, and hence also the coefficient of friction, to drop.

3. The velocity wave sent towards the bridge at the start of the first slip (labelled "2" in Figure 1.15(b)) reflects from the bridge and returns to the bowing point, reducing the relative sliding speed of the bow and string.

4. Because the coefficient of friction μ and the relative sliding velocity $v_b - v$ are both reduced, the rate of generation of heat through friction, equal to $\mu N(v_b - v)$, drops. This allows the rosin in the contact zone between the bow and the string to cool down.

5. As the rosin cools, μ increases, causing the sliding speed to diminish until it reaches zero; at this point sticking has resumed.

This chain of events is illustrated in Figure 6.9.

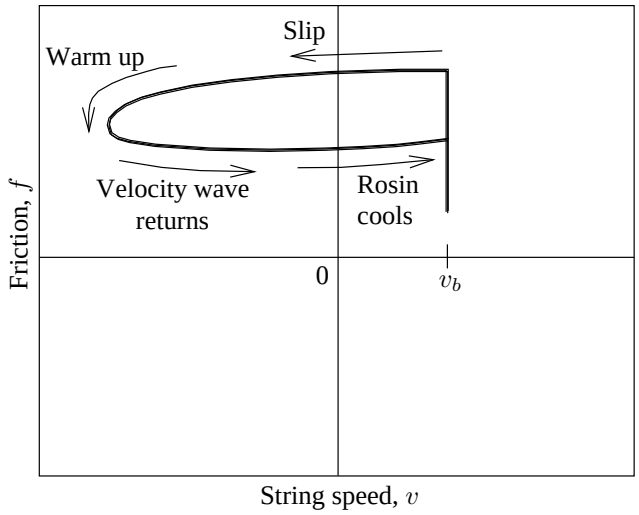

Figure 6.9: Illustration of the necessary chain of events for a short first slip (duration $\approx \beta T$), when the thermal plastic simulation model is used. At the start of the slip, the string acquires relative sliding velocity, causing the rosin to warm up and soften. When the velocity wave sent towards the bridge at the start of the slip returns to the bowing point, the slipping speed decreases. The resulting reduction in heat production allows the rosin to cool down, and sticking to resume. With the existing k_y vs. Θ curve, insufficient heat is generated at the start of the first slip for the rosin to soften, and hence for the hysteresis cycle to be completed. As such sticking only resumes once the velocity wave sent towards the finger at the start of the slip returns to the bowing point.

The existing k_y vs. Θ curve shown in Figure 6.6 is flat at low temperatures, and therefore while the rosin's temperature initially rises from ambient during slipping due to frictional heat generation, the friction μN does not immediately drop. As such, when the velocity wave sent towards the bridge at the start of the slip returns to the bowing point, the sliding velocity decreases, but the rate of generation of heat is not sufficiently low for the rosin to cool down, and hence for sticking to resume. In this situation, sticking only resumes once the second velocity wave (labelled "1" in

Figure 1.15(b)), sent from the bowing point towards the finger at the start of slipping, returns to the bowing point. Hence, if the k_y vs. Θ curve is too shallow, there is a delay of $(1-\beta)T$ between the beginning and end of the first slip. This can be seen to be the case in Figure 6.8, for example.

If more heat were generated during the first slip, or if the same heat were to cause a greater decrease in k_y, or indeed if the friction coefficient dropped by some other means, then the velocity wave sent towards the bridge at the start of slipping could reduce the sliding speed, causing the rosin to cool down, and sticking to resume more rapidly.

METHODS FOR ENABLING FRICTION JUMPS AT FIRST SLIP

With the k_y vs. Θ curve taking the shape shown in Figure 6.6, the temperature of the rosin in the contact patch must increase by around 10 or 15°C before the coefficient of friction will begin to drop significantly and allow cooling and sticking. If, however, the k_y vs. Θ curve was downwards-sloping rather than flat at ambient temperatures, then any frictional heat generation during the first slip would cause the coefficient of friction to start dropping as soon as the string started slipping. If this drop is sufficiently large, then the rosin will cool down sufficiently after the return of the velocity wave from the bridge to induce sticking, with little delay. And, as with experiment, this would require the normal force N to exceed some value depending on the value of β; the drop in friction coefficient is determined by the rate of heat generation, given by $\mu N(v_b - v)$.

The extent to which the k_y vs. Θ curve should slope downwards at ambient temperatures depends on the thermal heat capacity of the rosin inside the contact patch, as well as on the rate of conduction and convection of heat away from the contact zone. Using the parameter values relevant to each of these that Smith and Woodhouse originally suggested [43] — which were after all, unlike the k_y vs. Θ curve, based on direct measurements of the relevant physical properties — it is possible to deduce the required slope by ensuring that the bridge force flies back at first slip by the same amount as was measured in experiment.

6.4.3 OVERHEATING AT HIGH BOW SPEEDS

Another important instance in which the shape of the k_y vs. Θ curve was seen to cause anomalous behaviour in plastic thermal model simulations is at high bow speeds in the Guettler diagrams of Figure 5.31. It was shown on page 149 that Helmholtz motion tended to become "rounded" when the bow force and speed were large, because the string failed to resume sticking when the Helmholtz corner passes the bowing point travelling towards the nut.

In this case, as with the lack of flyback at first slip, the failure of the slipping to stop after βT seconds is due to a failure to complete the hysteresis cycle illustrated in Figure 6.9. At sufficiently large bow speeds, enough heat is generated during slipping to increase the rosin temperature be-

yond 45°C, the (approximate) temperature where the k_y vs. Θ curve becomes flat. A similar pattern occurs at high temperatures where the k_y vs. Θ curve becomes flat, compared with at first slip when the rosin is at ambient temperature, where the k_y vs. Θ curve is also flat. At first slip, the flatness of the k_y vs. Θ curve at low temperatures was shown to prevent μ from dropping during the first slip, and hence the frictional heat generation from being sufficiently small after the return of the bridge-side transverse wave to ensure cooling, and hence sticking. Similarly, if the rosin temperature becomes large due to large amplitude Helmholtz motion, the flatness of the k_y vs. Θ curve can prevent μ from dropping during the slipping portion of Helmholtz motion, and hence the frictional heat generation from being sufficiently small after the Helmholtz corner passes the bowing point after reflecting from the bridge to ensure that the rosin cools down and μ rises enough for the bow to "grip", or recapture, the string.

A typical example of this failure to complete the thermal hysteresis cycle quickly was shown in Figure 5.34. In that example, the string began slipping when the Helmholtz corner passed the bowing point on its way to the bridge, but the sliding speed did not decrease entirely back to zero when the Helmholtz corner passed the bowing point on its way back to the finger; this is clearly demonstrated in Figure 5.34(c). The temperature of the rosin in the contact patch is shown in Figure 5.34(b), and can be used to infer the position of the Helmholtz corner: the Helmholtz corner passes the bowing point on its way to the bridge at each of the moments where the temperature suddenly starts to rise (due to slipping); and the Helmholtz corner passes the bowing point on its way to the finger at each of the moments where the temperature starts to decrease again (due to the reduction in relative sliding speed). The bridge force is seen to drop (or "fly back") halfway between these times, which is the moment when the Helmholtz corner reflects from the bridge, but the end of the flyback is rounded. The end of the slip does not occur until the rosin temperature drops below about approximately 45°C, which can be seen in Figure 6.6 to be the start of the flat portion of the k_y vs. Θ curve.

Effect of Overheating on the Appearance of the Guettler Diagram

It was shown in Section 5.3.2 that there was an apparent upper limit in bow acceleration for the creation of Helmholtz motion in the Guettler diagram with the plastic thermal model, and that this limit was attributable to the saw-tooth waveform associated with Helmholtz motion becoming rounded. Furnished now with a knowledge that the rounding is caused by overheating, it is possible to derive an expression for this upper limit.

The rate of generation of heat is equal to the quantity $f \times (v_b - v)$, and hence the amount of heat generated per cycle of Helmholtz motion is equal to

$$\int_0^T \mu N (v_b - v)\, dt.$$

Assuming a "theoretical Helmholtz motion" [22, Ch.2], in which the string speed v equals the bow speed v_b during sticking, which lasts for $(1-\beta)T$ seconds per period, and $-v_b/\beta$ for the

remaining βT seconds, and in which the coefficient of friction is roughly equal to some constant μ_d during slipping, then this expression for the amount of heat generated per cycle of Helmholtz motion is approximately equal to

$$\mu_d N v_b \left(\frac{1+\beta}{\beta} \right) \beta T.$$

With the temperature rising gradually throughout each constant acceleration bowing gesture as the bow speed increases linearly with time, the point in each measurement where the simulation is most likely to have overheated, and hence where the motion is most likely to become rounded, is at the end of the measurement. All measurements lasted for a quarter of a second, and hence the value of v_b at the end of each measurement is equal to $0.25\,a$. Hence, the amount of heat being generated per cycle of Helmholtz motion, at the end of each simulation, is approximately:

$$\mu_d \, N \, (0.25\, a) \, (1+\beta) \, T.$$

The dependence of the rosin's temperature on the rate of heat generation means that the rosin will pass into the flat region of the k_y vs. Θ curve if this expression becomes too large. Assuming that μ_d is approximately constant (around 0.35 or 0.4 with the existing k_y vs. Θ curve at high temperatures), and bearing in mind that T is the same for all cases here, one finds that the string will overheat and its motion become rounded, if $Na\,(1+\beta)$ exceeds some value. Hence, the boundaries of the Helmholtz motion regions at the right-hand sides of Figures 5.31(e), (f), (g) and (h) are given by constant $Na(1+\beta)$, i.e. by

$$N \propto \frac{1}{a\,(1+\beta)}.$$

This expression predicts the behaviour in Figure 5.31 reasonably successfully, with the constant of proportionality roughly equal to ten.

How to Modify the k_y vs. Θ Curve to Avoid Overheating

The smallest value of coefficient of friction predicted by the current plastic thermal model, according to Figure 6.6, is 0.35. This value is sufficiently large that an appreciable quantity of heat can still be generated during slipping, at a rate equal to $\mu N(v_b - v)$, regardless of the temperature of the rosin. Consequently, the temperature can, and was frequently observed to when N and a were large, continue rising without bound as the bow speed increases. It was shown already that when the temperature of the rosin in the contact patch increases beyond 45°C above ambient, the thermal hysteresis cycle responsible for stick-slip motion becomes affected.

As a means of preventing the temperature of the rosin in the contact patch from rising into the flat region of the k_y vs. Θ curve at high temperatures, it is sufficient to extend the sloping portion of the k_y vs. Θ curve down to zero, or close to zero, i.e. to allow μ to drop to almost zero at high temperatures. This would force the rate of heat generation to drop to very small values as the temperature approaches the start of the of the flat region; and as the rate of generation of heat

becomes arbitrarily small, the temperature cannot traverse into the flat region. To generate enough heat to even approach the flat region would require a very large sliding velocity, to compensate for the very small quantity of friction resulting from a small value of μ.

Alternatively, the cooling rate during fast sliding could be increased, to reflect the increase in air cooling; this too would make it more difficult for the temperature to cross into the flat region.

6.4.4 HELMHOLTZ MOTION INTO DOUBLE SLIPPING

With the thermal plastic model, once a steady Helmholtz motion has been established with a single stick and slip per cycle, gradually reducing the bow force to zero does not cause a second slip to appear; rather, the existing slip becomes elongated, and the vibration waveform becomes generally rounded. This was observed to be the case in Section 5.3.1, in the context of the Schelleng diagram generated using the plastic thermal simulation model. An example of the bridge force for such a vibration waveform, where the slip has become elongated, is shown in Figure 5.29; the analogous operating point in experiments produced a double saw-tooth wave, like the one shown in Figure 4.18(b).

A reason why the plastic thermal model generally fails to predict the transition from single slipping to double slipping at low bow forces is again related to the thermodynamics of the hysteresis cycle sketched in Figure 6.9. At low values of N, the rate of heat generation, equal to $\mu N(v_b - v)$, becomes sufficiently small that μ does not decrease very much during slipping; as such, when the Helmholtz corner returns to the bowing point from the bridge and reduces the slipping speed (not quite to zero, because the Helmholtz corner is attenuated by the reflection), the rate of heat generation is not sufficiently less than it was at the start of slipping for the rosin to cool down quickly, and for sticking to resume without delay. Instead, this cooling process before recapture takes longer than it would under normal conditions; hence sticking is delayed and slipping lasts for a longer time. The corresponding shortening of the duration of sticking directly affects the mechanism, as proposed by Schelleng [16], for forming a second slip: the compliance of the bridge causes the friction force at the bowing point to fluctuate during sticking, with friction tending to rise and then fall from the start to the end of sticking; the peak value of the fluctuating component of friction is larger if the sticking time is larger, and if sufficiently large causes slipping. Thus at low bow forces, where Schelleng's mechanism for inducing a second slip is relevant, the shortened sticking time associated with the thermodynamics of the plastic thermal model reduces the fluctuation in friction, preventing a second slip from appearing.

This behaviour causes the bridge force to become rounded at the end of each flyback, in a similar fashion to the effect of overheating as discussed in Section 6.4.3. This type of roundedness was never observed in experiment under any circumstance, and should therefore be treated as a defect of the existing plastic thermal model.

COMPARISON WITH BEHAVIOUR OF FRICTION CURVE MODEL

It is interesting to review the behaviour of the friction curve simulation model as the bow force is decreased, when the string has been initialized with Helmholtz motion. Because the friction curve model involves a decrease in μ for any increase in relative sliding velocity, μ always increases and then decreases as it passes over the peak in the friction curve during the transition from sticking to slipping. Consequently, as illustrated in Figure 6.10, if the magnitude of the velocity wave (or Helmholtz corner) that induces slip is denoted $(\Delta v_h)_{\text{slip}}$, and the smallest allowable magnitude of the velocity wave that can restore sticking is denoted $(\Delta v_h)_{\text{stick}}$, then from Figure 6.10 $(\Delta v_h)_{\text{stick}} < (\Delta v_h)_{\text{slip}}$. Therefore, if the magnitude of the Helmholtz corner, treated as a transverse velocity wave, is $(\Delta v_h)_{\text{slip}}$, then sticking will resume when it returns from the bridge to the bowing point provided it has not been attenuated by more than the difference between $(\Delta v_h)_{\text{slip}}$ and $(\Delta v_h)_{\text{stick}}$.

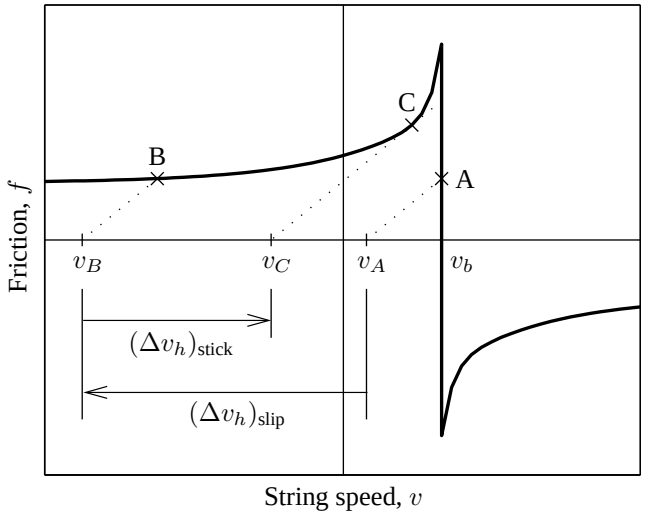

Figure 6.10: Diagram of the magnitude of transverse velocity wave required to induce sticking, compared with the magnitude of the transverse velocity wave that initially caused slipping. These are labelled $(\Delta v_h)_{\text{stick}}$ and $(\Delta v_h)_{\text{slip}}$ respectively. The difference between them causes the slipping time of Helmholtz motion, with the friction curve model, to remain equal to βT as the bow force is decreased. Helmholtz motion breaks down when a second slip appears somewhere near the middle of the sticking period.

As such, with the friction curve model, Schelleng's mechanism for the breakdown of Helmholtz motion as bow force is decreased occurs before the slipping time starts to increase. Unlike some cases with the plastic thermal model, once a steady Helmholtz motion has been established, if a Helmholtz corner succeeds in inducing slipping then it will succeed in inducing sticking a time βT later.

6.5 MODELLING CREEP

Examples from various situations in experiment were presented in Chapter 4, in which the string appeared to move slowly relative to the bow, or "creep", whilst apparently sticking (i.e. in between bridge force flybacks). An interesting test of the simulation models is whether they can predict this behaviour. Various situations in which creep may be important are considered in this section.

6.5.1 FLYBACKS AT FIRST SLIP THAT ARE NOT STEEP

In experiment, when the bow force N is only barely large enough to cause a flyback in the bridge force at first slip, the flyback has generally been observed to be not as steep as it was when the bow force was very large. A typical example of an experimental bridge force waveform generated using a bow force that was just barely large enough to cause a flyback at first slip was shown in Figure 6.7(b); in that case, the first flyback can be seen to be less steep than, say, in Figures 4.22(a) and 4.22(c). The slow slipping speed required to make the bridge force flyback rounded could be thought of as "creep".

The plastic thermal model, by nature, predicts a delay between the start and finish of the first bridge force flyback, since the first flyback requires a change in the temperature of the rosin. This delay was even shown to be too long when using the old μ vs. Θ curve shown in Figure 6.6, although it can be reduced by making the μ vs. Θ curve downwards-sloping at ambient temperatures, as already discussed. Hence, depending on the choice of slope of the μ vs. Θ curve at ambient temperature, the thermal hysteresis cycle will make the bridge force fly back quickly at large values of N, not fly back at small values of N, and fly back relatively gradually at intermediate values of N. In this respect then, the plastic thermal model is capable of predicting the detailed motion of the string at first slip, given a suitable k_y vs. Θ curve.

The friction curve model, on the other hand, either predicts an instantaneous change in the bridge force at first slip (provided the normal force is large enough to induce a "friction curve jump" as described on page 136) or no fly back at all. This behaviour is not in agreement with the observation that some flybacks do occur in experiment that are not steep. However, it is important to remember that the "friction curve jumps" responsible for instantaneous changes in string velocity (and hence vertical bridge force flybacks) only serve as a method for keeping the operating point in the f-v plane away from the "ambiguous" region of the friction curve. McIntyre and Woodhouse [7] proved that the string's bending stiffness causes these "jumps" to become spread out over a finite period of time, but does not otherwise change them when using the friction curve model; hence, for simplicity all friction curve jumps were assumed to be instantaneous in simulations based on the friction curve model. As such, although a close examination of the bridge force around the time of the first slip (see for example Figure 5.11) reveals unrealistic behaviour, it would not necessarily lead to a knock-on effect on the rest of the transient.

6.5.2 APPARENT CREEP BEFORE FIRST SLIP

It was demonstrated in Chapter 4 that the slope of the bridge force before the first slip sometimes dropped below its nominal value of $2Z_T v_b/\beta T$ during sticking. This was evident for example in Figure 4.41(c), by the deficit in the slope of the bridge force before the first fly back.

It is intuitive to treat this deficit in the slope of the bridge force as creep, and to include creep in simulations of the bowed string by inclining the vertical portion of the friction curve. If the vertical portion was rotated such that it was straight but no longer vertical, then the string would behave in a quasi-"viscous" manner during sticking (c.f. Figure 1.12); tangential loads applied to the string during sticking would cause a slow relative motion, which could be referred to as creep. This is equally feasible for the plastic thermal model as it is for the friction curve model: the vertical portion of the "perfectly plastic friction curve" in Figure 1.13(a) could be inclined in the same way. This is illustrated in Figure 6.11(a).

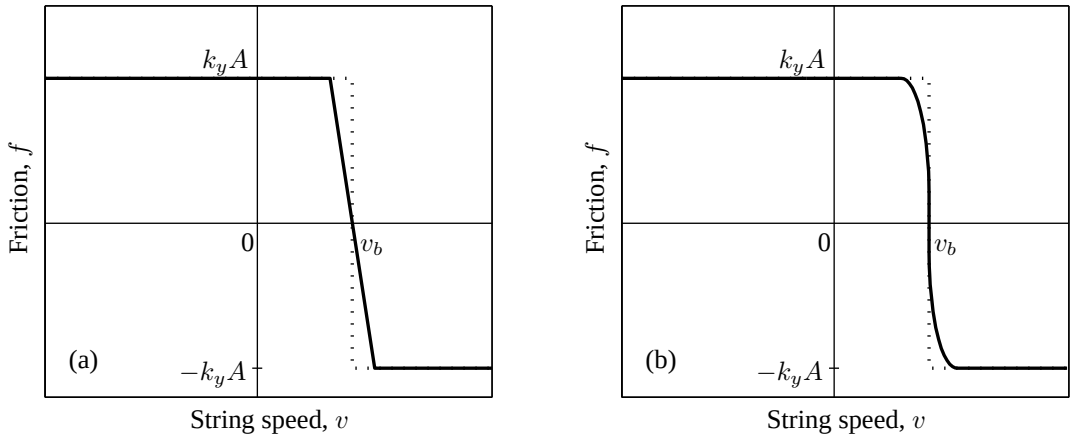

Figure 6.11: Two alternative, but essentially similar, methods for incorporating creep in to the plastic thermal friction model. In each case sticking, or vertical, portion of the "perfectly plastic friction curve" used to describe the dependence of friction f on relative sliding velocity $v_b - v$ at a given temperature is altered, such that any non-zero quantity of friction will cause some slipping. In (a), the rosin behaves like a viscous material until the friction reaches $k_y A$, and like a plastic material thereafter. In (b), the joins between the horizontal and vertical portions of the curve are rounded, to allow some slipping before the friction reaches limiting static conditions.

Various alternative, but essentially similar, modifications to the sticking portion of the friction curve could be attempted to produce a similar effect. For instance, making the join between the sticking and the slipping portion of the friction curve rounded as in Figure 6.11(b) would mean that slipping would begin before the shear stress in the contact patch had reached the shear yield stress. A demonstration that incorporating such a model into the plastic thermal simulation model can lead to much improved predictions is shown in Figure 6.12. The simulated bridge force waveform

in Figure 6.12(b) was generated by rounding the join between the horizontal and vertical portions of the "plastic friction curve" (as in Figure 6.11(b)), and also by incorporating the modifications to the k_y vs. Θ curve recommended in Section 6.4. The agreement between the simulated waveform in Figure 6.12(b) and the nominally similar experimental waveform in Figure 6.12(a) visibly demonstrates the potential of a "creep model".

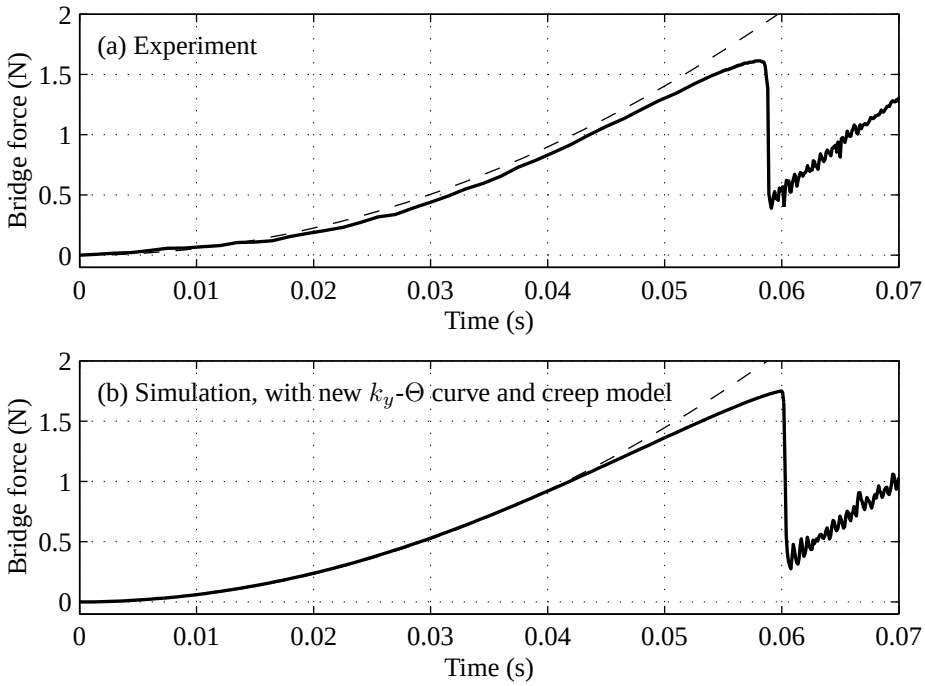

Figure 6.12: Example where rounding the vertical portion of the friction curve can lead to very successful predictions of the bridge force waveform. To produce the waveform in (b), the k_y vs. Θ curve was modified as described in Section 6.4 to achieve an appropriate value of μ_s and a flyback, and the method of rounding the vertical portion of the f-v curve shown in Figure 6.11(b) was used to model creep. The dashed lines have a slope of $2Z_T v_b/\beta T$, and hence indicate the theoretical value of bridge force during perfect sticking; the creep-like behaviour is evident in both (a) and (b) by the steadily increasing gap between the dashed line and the solid line. The values of N, a and β used in this example are 2.32 N, 0.573 m/s^2 and 0.08 respectively.

PROBLEMS WITH MODELLING CREEP, BASED ON EXISTING EXPERIMENTAL EVIDENCE

However, evidence was also presented in Chapter 4 that casts doubt on this method of including creep in simulations: in particular, Figure 4.42. Figure 4.42 shows the theoretical value of bridge force before first slip (given by $2Z_T v_b t/\beta T$) alongside the actual bridge force measurement, with the latter lagging behind the former, as indeed one would expect it to according to the model of creep developed above. However, the intriguing feature of Figure 4.42 — and for that matter Figure 4.43 — is that the measured bridge force does not start to curve downwards before the first fly-back, but instead continues to increase at a constant rate. The slope of the measured bridge

force before first slip is always approximately 50% less than that of the theoretical bridge force (this is well beyond the bounds of experimental error), and both are constant. This indicates that the creep rate was constant for the entire period leading up to the first slip, even as the shear stress acting on the contact patch changed from zero to the shear yield stress.

Simply inclining or rounding the vertical portion of the friction curve does not account for this behaviour; instead, the entire vertical portion would need to be shifted to the left by a uniform amount, to achieve a constant creep velocity. Shifting the vertical portion of the friction to the left as such would be counter-intuitive, and certainly at odds with the model used to produce Figure 6.12(b). It is likely therefore that some other physical effect is responsible for the large — and constant — deficit in the slope of the bridge force before first slip in the example shown in Figure 4.42.

As discussed in the context of Figure 4.42, the deficit in the slope of the bridge force could not have been caused by a bandwidth limitation of the data acquisition hardware, since this would have caused a gradual decrease, or curvature, of the slope. One possible alternative explanation is that the bridge of the cello, or indeed the entire cello itself, behaved in a compliant spring-like manner. As such, as the string was pulled outwards before the first slip, so too would the bridge have been to an extent proportional to the force. This could therefore account for the large constant deficit in the slope of the bridge force.

However, there is not sufficient evidence at the moment to prove whether bridge movement significantly influences some bridge force waveforms. To ascertain the definite cause of the deficit in bridge force before first slip will require further investigation, and is an interesting avenue for future work.

6.5.3 OTHER EVIDENCE OF CREEP

Although it is true that the behaviour seen in Figure 4.42 may not be due to creep, there are other instances of experimental data that do point far more strongly to the occurrence of creep. Three examples are as follows:

1. In numerous bridge force measurements, the slope of the bridge force was observed to start decreasing gradually before actually becoming negative. An example of this is shown in Figure 6.12(a), in which the bridge force is seen to begin curving downwards in the last few milliseconds before the flyback. This subtlety cannot be accounted for by any existing friction model, since they predict that the friction coefficient does not continue increasing after slipping starts, and hence that the bridge force increases according to a parabola (for constant acceleration) or a straight line (for constant bow speed) and then abruptly begins to drop. This can, however, be accounted for by a creep model like the one shown in Figure 6.11(b).

2. Occasionally, the bridge force waveform was seen to oscillate with the saw-tooth waveform associated with Helmholtz motion, but with a substantially reduced amplitude. This reduction in amplitude caused the slope of the bridge force during sticking to be reduced, and although this is not easily seen by simply looking at the original bridge force signal, it is readily apparent after "de-trending" the bridge force, i.e. subtracting from the bridge force the function $\int_0^t (2Z_T v_b/\beta T)dt$, whose slope equals the theoretical slope of the bridge force during sticking, as discussed in Section 4.2.3. An example of a reduced-amplitude saw-tooth wave is shown in Figure 6.13: the measured bridge force is shown in Figure 6.13(a), and the "de-trended" bridge force is shown in Figure 6.13(b). Whereas the de-trended bridge force was shown to be horizontal during sticking under the vast majority of experimental conditions — see for example Figures 4.4(a) and 4.5(a) — it is seen to be downwards-sloping during sticking in the two periods marked "A" and "B" in Figure 6.13(b). This deficit in slope is far beyond the bounds of experimental error, and suggests that the string fails to acquire the bow speed during the sticking portions of stick-slip motion. This creep-like behaviour was never predicted with the existing friction models, although it can be readily reproduced by modifying the models as described in Figure 6.11.

3. The ability of the string to creep along the bow while nominally sticking can also be demonstrated with ease by any reasonable violinist. With the bow pressed into the string near the frog (or heel) with a large bow force, pulling the bow with a force not quite large enough to induce slip will cause the string to slide slowly relative to the bow. This simple demonstration provides alternative evidence for the existence of creep, since both existing theoretical models of friction (the friction curve and plastic thermal models) predict that very slow sliding at large bow forces is unstable; in practice the this slow creeping can be sustained for any arbitrary amount of time.

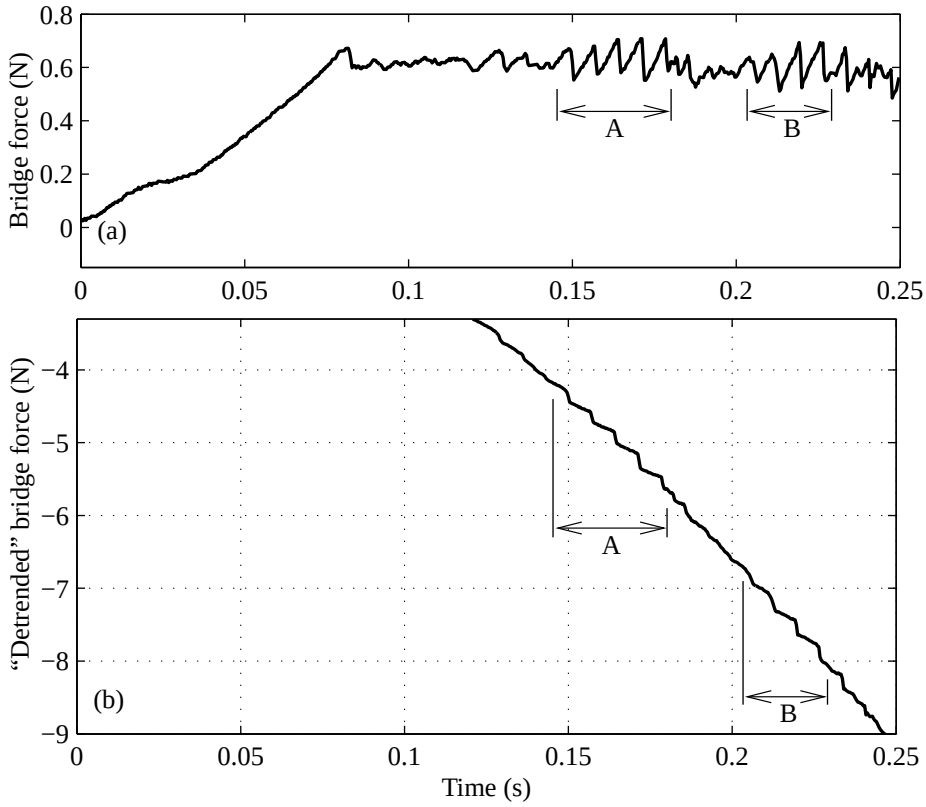

Figure 6.13: The bridge force waveform for an apparent stick-slip vibration in which the velocity of the string at the bowing point during sticking is considerably less than that of the bow. The top plot shows the original bridge force waveform, and the bottom plot shows the effect of subtracting off a line whose slope equals $2Z_T v_b/\beta T$ (the theoretical slope of the bridge force during sticking). In this case, the bridge force in the times marked "A" and "B" looks like the saw-tooth wave of Helmholtz motion, but turns out to have a smaller than expected amplitude; this is clear from the negative slope of the bridge force during sticking in the lower plot.

6.6 SUMMARY OF FINDINGS

Possible explanations and remedies for some of the differences between the experimental and simulated results presented in the previous two chapters are as follows:

- The striking similarity between vibration transients generated using the old friction curve model with the same value of N/a can be accounted for by the following rule: holding the dimensionless quantity $N/Za(L/c)$ constant results in vibration transients that differ only in amplitude, provided the quantities μ_s and μ_d are constant. The old friction curve model was sufficiently steep that μ_d was always well approximated by 0.35, and the value of μ_s was always equal to 1.2; hence the old friction curve model was well approximated by the assumption of constant μ_d and μ_s. The wedge-shaped appearance of the experimental and plastic thermal simulated Guettler diagrams can presumably be explained by a relatively small change in μ_s and μ_d, whereas the lack of any clear trends in the Guettler diagrams

generated using the friction curve model with the "reconstructed friction curve" in Section 5.19 is presumably due to large fluctuations in μ_d.

- The increase in limiting static coefficient of friction before first slip observed in experiment at low bow speeds could be due to a junction growth mechanism, whereby the real area of contact between bow and string gradually grows when subject to sustained tangential loads. Trends in experimental data suggest that this contact area growth stops once the the real area of contact fills the entire contact patch.

- The apparent "bridge force overshoots" observed in reconstructed friction curve model simulations were indirectly caused by the lack of curvature in the reconstructed friction curve. The closeness of the hysteresis limits resulting from this lack of curvature meant that torsional waves, whose wave speed is several times larger than that of transverse waves, cause stick-slip and slip-stick transitions. These transitions are rapid, and continue until the return from the bridge of the relatively large transverse wave generated at the first slip. This brief flurry of rapid stick-slip transitions causes the bridge force to fluctuate at the start of each new "saw-tooth" in the bridge force; these fluctuations appeared as overshoots. This behaviour was not observed in experiment, and may be inevitable for friction curves like the "reconstructed" friction curve, which is flat in order to reflect dynamic measurements of friction.

- A number of anomalies in the results from the plastic thermal friction model simulations were shown to be due to the function proposed by Smith and Woodhouse [43] to describe the variation of the shear yield strength k_y of rosin with temperature. In particular:
  - This function should not be flat at ambient temperatures; k_y should instead start decreasing as soon as the temperature is increased from ambient. Otherwise, the string will not "fly back" during the first slip, as it was seen to in experiment.
  - The value of k_y must drop to zero at high temperatures; otherwise the rosin will "overheat" in simulations based on the plastic thermal model, leading to behaviour that was never observed in experiment.
  - The largest value of k_y must be chosen to give a limiting static coefficient of friction no greater than that observed in experiment.

- "Creep" is likely to be responsible for various instances where the slope of the measured bridge force signal during sticking was less than the theoretical value for the same bow speed. One simple method for incorporating creep into the simulation model is to rotate the vertical portion of the friction curve in an anti-clockwise direction, following which any non-zero quantity of friction causes some relative motion between the bow and the string. Similarly, one could round the top of the vertical portion of the friction curve.

Chapter 7

EXPERIMENTS WITH REAL BOW

INTRODUCTION

All experimental and simulated data shown up to this point has been generated using a rigid point-contacting bow, rather than a real bow with a finite width of compliant horse-hair. As the behaviour of the string when bowed using a rigid point-contacting bow becomes better understood, it should be put into perspective by testing the difference made by using a real bow. In this chapter, results obtained using a real bow in place of the perspex rod are presented that aim to achieve this goal.

7.1 EXPERIMENTAL SETUP

In an effort to explore any general changes in the string's vibrational behaviour when it is bowed with a real bow instead of the stiffened perspex rod as previously, the same bowing machine described in Chapters 2 and 3 was adapted to use a real bow. The bow selected for use is a factory-made fiberglass violin bow, of little monetary value — designed for beginner violinists, and used instead by a beginner, and sometimes rather reckless, bowing machine. The general setup of the bowing machine is sketched in Figure 7.1. The bow is held in a custom-fitting spark-eroded aluminum alloy clamp, whose interior is lined with a thin layer of rubber for extra grip.

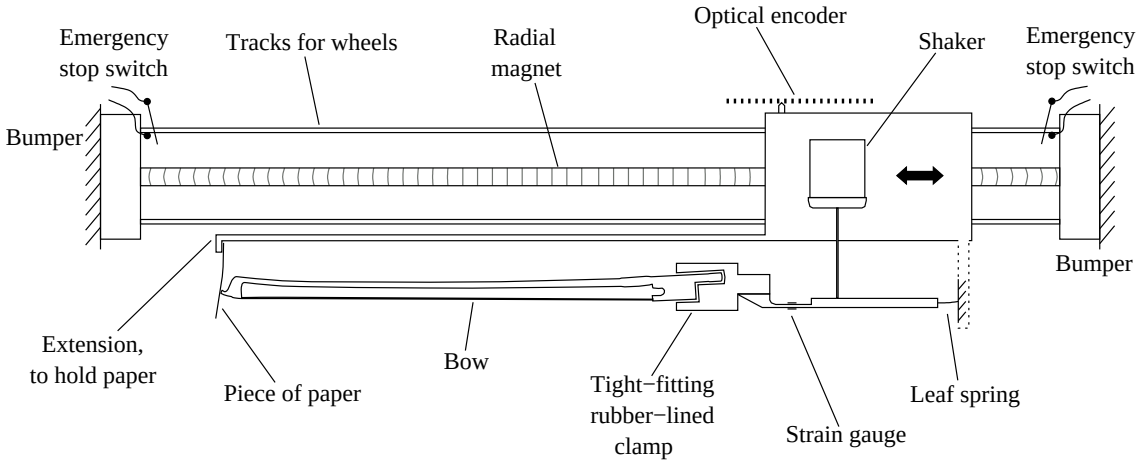

Figure 7.1: Drawing (not to scale) showing the essential features of the bowing machine with the real bow in place of the perspex rod, which can be compared with Figure 2.14 on page 43.

The bow is lighter than the steel-filled perspex rod used previously, but the natural frequency of the first vibration mode is lower due to the flexibility of the bow hair and the associated "bouncing mode". Consequently, the feedback control strategy of implementing an integrator controller, low-pass filtered below the first natural mode, gives an inadequate closed-loop bandwidth: it was found that with the controller designed for the perspex rod, the closed-loop bandwidth with a real bow is approximately 6 Hz. Consequently, oscillations in bow force caused by external disturbances (the sort that one would expect from a human with a shaky hand) are not damped.

A simple passive control scheme was used to suppress these oscillations, consisting of a light frictional contact between the tip of the bow and a piece of paper attached to the linear motor using an extension. This scheme was found to be sufficient to raise the damping of the bow's bouncing mode almost to critical: across the entire range of combinations of bow force and bow accelerations used to generate Guettler diagrams for example, the bow force was found not to fluctuate through bouncing by more than 3%.

The limiting static friction force required to cause relative movement between the bow and the paper was found, using a set of scales, to be less than 0.01 N. Therefore, estimating the distance

from the strain gauge to the tip of the bow to be five times greater than the distance from the strain gauge to the bow/string contact, the resulting error in bow force should never become greater than 0.05 N.

7.2 RESULTS

With the bowing machine effectively functioning as it did with the perspex rod, similar experimental tests can be undertaken to those in Chapter 4. Of the three parameter spaces explored in Chapter 4, the N vs. β plane, the N vs. a plane and the N vs. v_b plane, the second is the most relevant to playability. For this reason, bowing gestures in which the bow force is held constant while the bow is accelerates from rest are concentrated on in this chapter.

GUETTLER DIAGRAM AT A RANGE OF β VALUES

The Guettler diagram, indicating the time delay between first slip and the onset of Helmholtz motion, as measured with the real bow at eight different values of β, is shown in Figure 7.2. β is defined with a finite width bow as the distance from the centre of the bow hair to the bridge, divided by the length of the string. This Figure may be directly compared with Figure 4.20, which was generated with a perspex rod in place of the bow.

A quick comparison reveals that the results with the perspex rod and with the real bow, in Figures 4.20 and 7.2 respectively, are extremely alike — certainly more so than any of the simulation results and the perspex rod results: the general extent of the light-shaded regions in Figures 4.20 and 7.2 are similar at all values of β except arguably 0.0449 and 0.0566 (Figures 7.2(b) and (c) respectively); some of the "spottiness" of Figure 4.20(g) (where $\beta = 0.1428$), shown to be due to multiple flyback in Section 4.3.2, is preserved; and the boundaries of the light-shaded regions appear again to be approximately straight lines that pass somewhere near the origin.

However, there are some differences between Figures 4.20 and 7.2. Nearly all occurrences of Helmholtz motion in Figures 7.2(g) and 7.2(h) involve a delay of around ten period lengths, whereas in the corresponding cases with the perspex rod there were numerous cases in which Helmholtz motion followed straight from the time of the first slip. The results with the real bow at $\beta = 0.1133$, i.e. in Figure 7.2(f), are somewhat "smoother" than they were with the perspex rod; the light-shaded region appears to be white at its center, and fade gradually and uniformly into black. At $\beta = 0.0449$ and $\beta = 0.0566$, shown in Figures 7.2(b) and 7.2(c) respectively, there are fewer occurrences of Helmholtz motion than there were with the perspex rod.

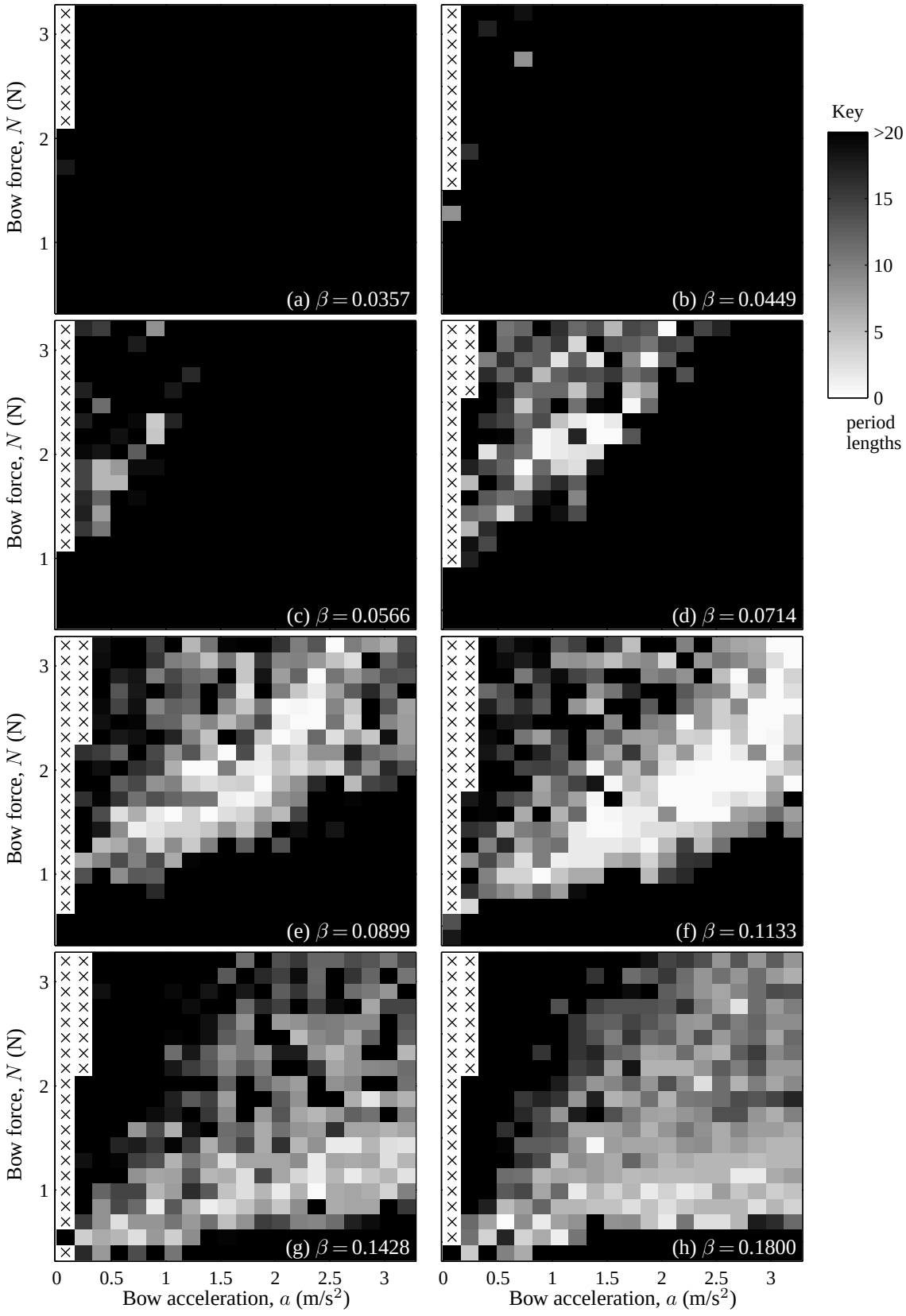

Figure 7.2: Experimentally measured "Guettler diagrams", for eight different values of β, using the real bow. In each plot, as previously when a perspex rod was used in place of a bow (see Figure 4.20 for comparison), the time taken to achieve Helmholtz motion relative to the time of the first slip at a given combination of bow force and acceleration is given by the shade of the pixel at the corresponding location in the N vs. a plane. White pixels indicate "perfect transients", and black pixels indicate that it took twenty or more period lengths to achieve Helmholtz motion. White pixels with crosses ("$\times$") indicate unsuccessful measurements.

EXAMPLES OF INDIVIDUAL BRIDGE FORCE WAVEFORMS

In general, the bridge force waveforms have a similar appearance when using the real bow compared to when using the perspex rod. Five examples of bridge force waveforms are shown in Figure 7.3: Figure 7.3(a) shows an example of a "perfect transient"; Figure 7.3(b) shows a case where multiple flyback motion was developed after a delay of a few hundredths of a second; Figure 7.3(c) shows an example of raucous motion, as characterized by the prolonged sticking periods and the lack of periodicity; Figure 7.3(d) shows an example of multiple slipping; and Figure 7.3(d) shows a bridge force waveform that is typical of the results at small β.

The example of multiple flyback motion in Figure 7.3(b) is one example of several multiple flyback motions observed at $\beta = 0.1428$. As with the perspex rod, the inconsistency, or visible "spottiness" in the $\beta = 0.1428$ Guettler diagram (Figure 7.2(g)) is due to a tendency for multiple flyback motion to form.

The "spike"-like feature discussed on page 100, seen in the bridge force at the end of prolonged periods of sticking with the perspex rod, was still observed to occur with the real bow. The example of raucous motion shown in Figure 7.3(c) contains a "spike", although it is partially obscured by the relatively low sampling rate used to acquire bridge force.

Two new features were seen in the bridge force with the real bow: differential slips and "overshoots". The first of these, differential slips, was illustrated in Figure 1.8, and refers to the small slips that occur at some points under the bow and not others, due to the kinematic incompatibility of finite-width bows during Helmholtz motion. At low values of β, where differential slipping was reported by McIntyre and Woodhouse to be most likely to occur [50], the bridge force was occasionally observed to jump downwards by a small amount during periods of otherwise uninterrupted sticking. Three examples of these small drops in bridge force are shown in Figure 7.3(e). It is plausible that these are caused by differential slipping, and indeed that this behaviour may be responsible for the relative lack of occurrences of Helmholtz motion in Figures 7.2(b) and (c). Differential slipping — if indeed these small slips are indicators of differential slipping — was rarely observed at larger values of β.

The second of the two new features observed in the bridge force with the real bow, referred to here as "overshooting", is an apparent tendency for the bridge force to fly back too far during slipping. Examples of these overshoots, which were again observed mainly at low values of β, are shown in Figure 7.3(e). Interestingly, this tendency to overshoot is visibly similar to the behaviour observed in friction curve simulations in Section 5.2.2, which was shown on page 163 to be due to rapid stick-slip alternations at times of slipping, caused by the ability of torsional waves to restore sticking when the friction curve is devoid of curvature. It seems possible, then, that these torsion-induced "overshoots", dismissed as being at odds with experiment when using a rigid point-contacting bow, do occur when using a real bow.

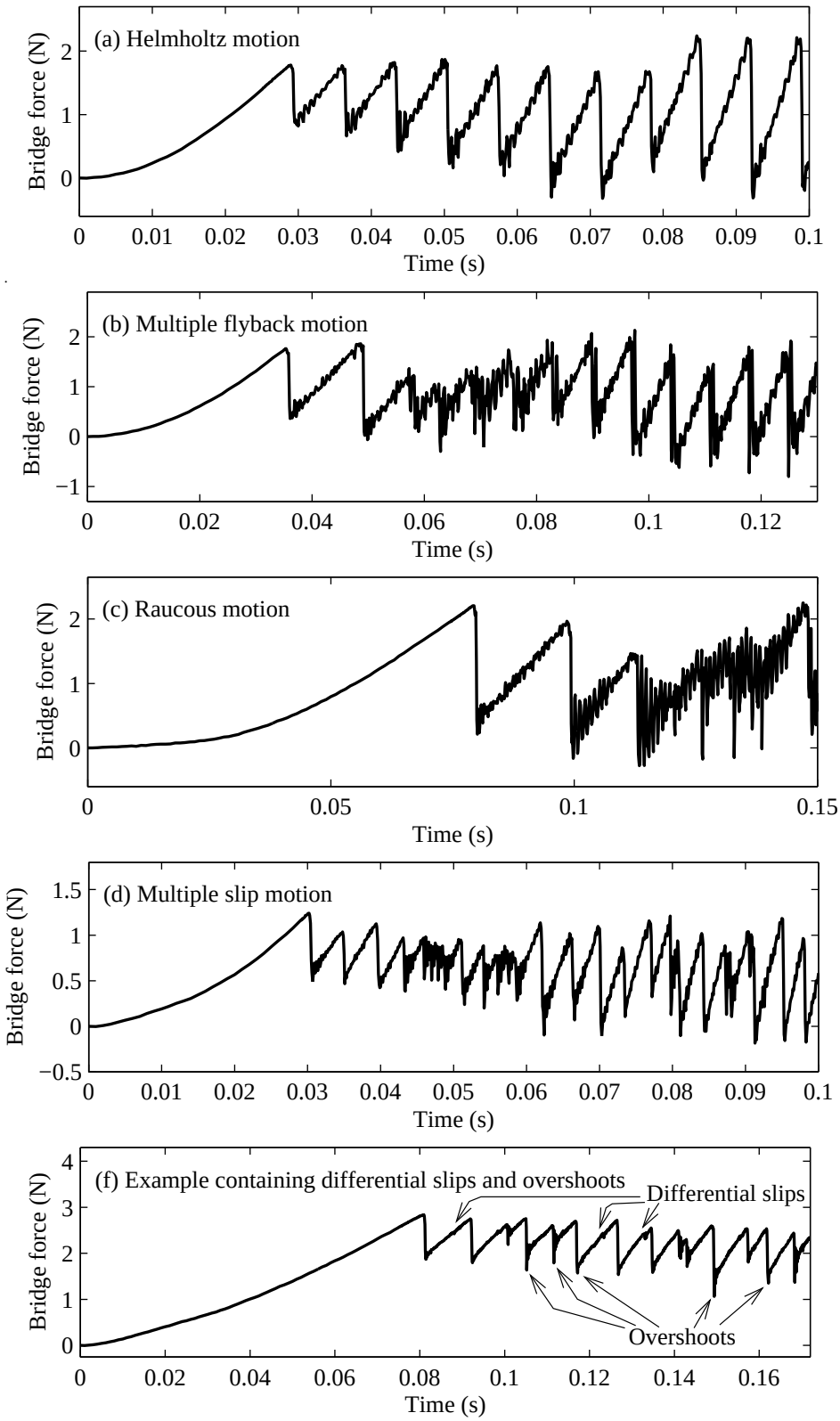

Figure 7.3: Examples of bridge force waveforms from various regions of the Guettler diagrams, with the cello bowed using the real bow. The values of N, a and β for each example are, respectively: (a) 1.874 N, 2.379 m/s^2, and 0.1133; (b) 2.316 N, 2.215 m/s^2, and 0.1428; (c) 2.758 N, 0.737 m/s^2, and 0.1428; (d) 1.579 N, 1.230 m/s^2, and 0.0566; (e) 2.021 N, 0.244 m/s^2, and 0.0449. In this figure, the horizontal and vertical axes ranges are different in every plot, although the string's natural period is 0.00680 s in all cases.

REPEATABILITY: CONSISTENCY OF RESULTS AT A SINGLE β VALUE

As a measure of the repeatability of the transient behaviour of the string when bowed using a real bow, four separate measurements of the Guettler diagram, with $\beta = 0.08$, were performed under nominally identical conditions. The results, shown in Figure 7.4, are analogous to the sets of data generated when using the perspex rod that were shown in Figures 4.25 and 4.29. A similar degree of consistency is observed in both cases: the exact pattern of light and dark pixels is not preserved from one set of data to the next, but the overall "spottiness" and approximate boundaries of the Helmholtz motion region are very similar.

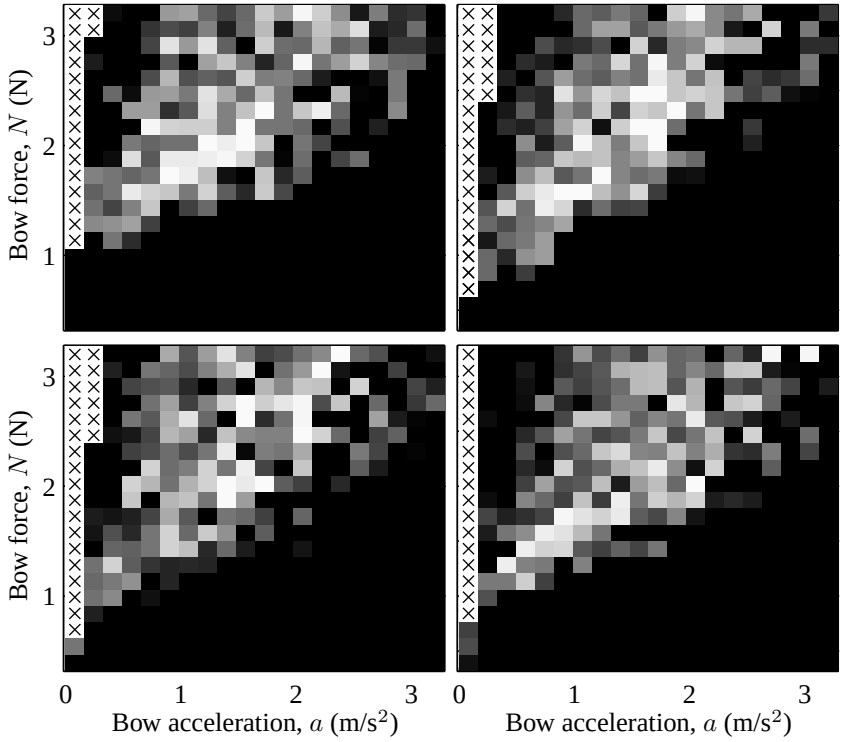

Figure 7.4: Four separate experimental measurements of the Guettler diagram, each obtained using a real bow with $\beta = 0.08$. As with the equivalent results shown in Figure 4.25 that were obtained using a perspex rod, the shade of each pixel indicates the time delay between the first slip and the onset of Helmholtz motion, with white pixels indicating no delay, and black pixels indicating a delay of twenty period lengths or more. White pixels with black crosses ("$\times$") indicate that the first slip occurred less than twenty period lengths before the end of the bridge force measurement, making it impossible to deduce whether the transient time was twenty period lengths.

To facilitate a direct comparison with Figure 4.27, which showed the shortest and longest pre-Helmholtz motion transient length from a number of nominally similar Guettler diagrams with the perspex rod, the shortest and longest transient lengths from the four sets of data used to make Figure 7.4 are shown in Figure 7.5. The overall appearance is the same: in the left-hand plots, which show the shortest (or "best") transients, the Helmholtz motion region is seen to become gradually filled in; the right-hand plots, which show the longest (or "worst") transients, the Helmholtz motion

region is seen to become gradually more sparse and narrower. The progressive narrowing of the region in which the longest pre-Helmholtz motion transients are still quite short illustrates the relative "reliability" of the centre of the Helmholtz motion region. Hence, as with the perspex rod, a player would presumably find operating points near the centre of the Helmholtz motion region most preferable.

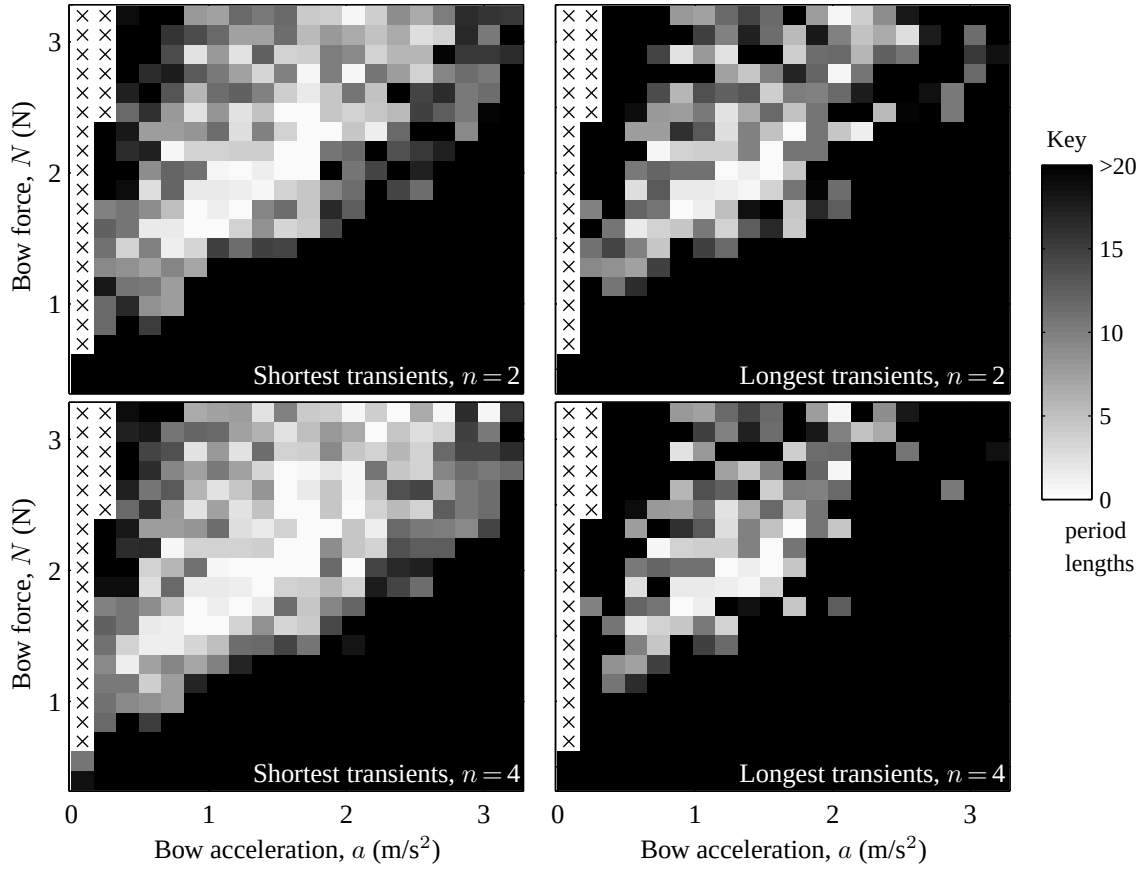

Figure 7.5: Shortest and longest transients in the first n plots (out of a total of four) shown in Figure 7.4. Transient lengths at a given combination of N and a are again given by the darkness of the pixel at the corresponding location in the N vs. a plane. β is 0.08 in all cases here. The shortest (and hence best) transients in the first n cases are shown in the left column, the longest transients (and hence worst) transients are shown in the right column, and each row corresponds to a different value of n. The results shown here can be directly compared with the equivalent results obtained using a perspex rod in Figure 4.27.

LIMITING STATIC COEFFICIENT OF FRICTION, MEASURED AT FIRST SLIP

It was pointed out in Chapter 4 that the limiting static friction coefficient μ_s, as measured just before the start of the first slip, becomes larger at low bow speeds. In the last chapter, a "junction growth" model was proposed that appeared to account for this behaviour reasonably successfully. The same measurement was repeated with the cello bowed using the real bow: the results are shown in Figure 7.6. Figure 7.6(a) shows the value of μ_s obtained at each operating point in the N

vs. a plane, if the four sets of data used previously to generate Figure 7.4 are averaged together. It is quickly apparent that the rise in μ_s at low accelerations is still seen with the real bow, with the exact pattern of variation of μ_s with respect to N at low accelerations discussed in Section 6.2.1 preserved.

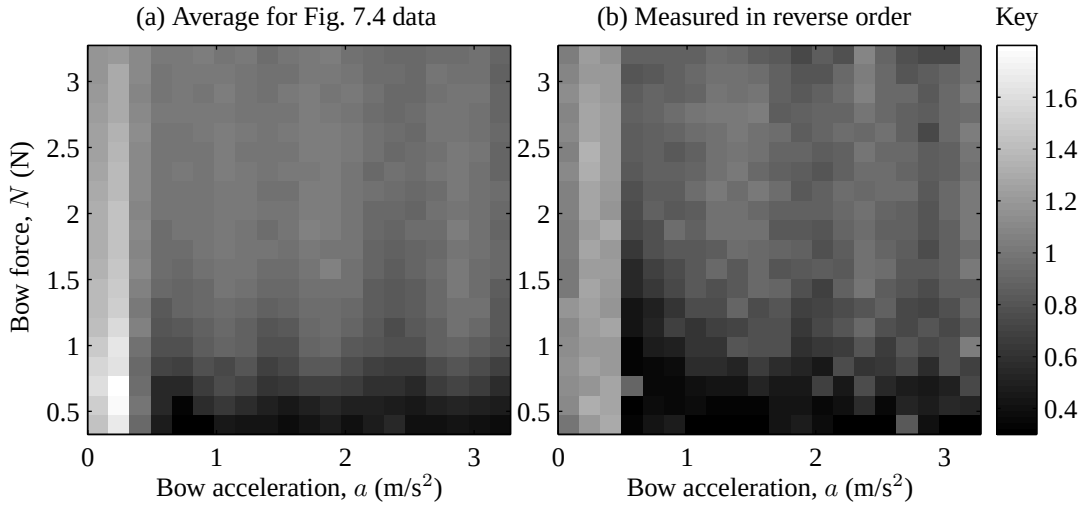

Figure 7.6: The value of coefficient of friction between bow and string shortly before the first slip. The data plotted in (a) is the average of the values obtained from each of the four sets of data used to obtain Figure 7.4; (b) shows the results obtained from a separate set of data in which the N-a parameter space was traversed in the opposite order. Hence, the twenty values of acceleration were tested in ascending and descending order in (a) and (b) respectively, and at each value of acceleration the twenty values of force were tested in ascending and descending order in (a) and (b) respectively. The results in both plots are similar to those seen with a rigid point-contacting perspex rod in Figures 4.30 and 4.32, in that the rise in μ_s at low accelerations is still in evidence in a very similar fashion. However, the interesting difference between both of these plots and Figures 4.30 and 4.32 is that μ_s drops towards zero at low bow forces here, except at low accelerations — with the point-contacting perspex rod it remained constant.

There is a surprising new feature of Figure 7.6(a) that was never observed when the cello was bowed by the perspex rod: the value of μ_s appears to drop towards zero as the bow force N is brought to zero. The increasingly dark appearance of pixels in the bottom few rows of data in Figure 7.6(a) indicates this decrease. If extrapolated beyond the lowest value of N in Figure 7.6(a), the value of μ_s appears to pass very near zero at $N = 0$. This decrease in μ_s at low bow forces appears not to occur at the left of the plot; at the lowest three values of acceleration, μ_s appears to behave as it did with the perspex rod, for all values of N.

To investigate whether this dependence of μ_s on N was related to the order in which the measurements were obtained, values of μ_s were calculated based on measurements obtained in the reverse order, with the values of acceleration tested in descending order rather than ascending order, and with the bow force varied in descending order rather than ascending order at each acceleration. The results are shown in Figure 7.6(b), and clearly demonstrate that the order in which the force and acceleration are varied is not responsible for the drop in μ_s at low bow forces. It seems,

then, that whereas the contact mechanics of the perspex rod and the string change from "rough" to "Hertzian" under a sustained tangential load, the contact mechanics of a real bow change from some other type of mechanics to Hertzian under a sustained tangential load, with the mechanism of the change still junction growth.

7.3 SUMMARY OF FINDINGS

The transient vibration response of the string to constant acceleration bowing gestures appears to be very similar when the perspex rod is replaced by a real bow. The overall appearance of the Guettler diagrams did not change, and various subtle details of the perspex rod Guettler diagrams were still observed when using the real bow: the maximum bow force was again disproportionately large when $\beta = 0.1133$ due to S-motion; and the string was still prone to exhibiting multiple flyback motion when $\beta = 0.1428$. Consecutive measurements of the Guettler diagram reflect a similar degree of "repeatability" to that observed with the perspex rod, and the evaluation of cumulative longest and shortest pre-Helmholtz motion transient lengths reveals again that the centre of the Helmholtz motion region is the most "reliable" to the player.

The few differences between the perspex rod and real bow Guettler diagrams were mostly seen at small values of β. Individual bridge force waveforms generated at small β suggest that this may be caused by occasional differential slipping and apparent "overshoots" in the bridge force flybacks. The cause of the latter is unclear, although it is strikingly similar to the rapid torsion-induced stick-slip alternations seen in the reconstructed friction curve simulations of Section 5.2.2.

Surprisingly perhaps, measurements of the limiting static friction coefficient at first slip reveal a somewhat similar pattern to that seen with the perspex rod: the limiting static coefficient of friction is larger at lower accelerations, and at low accelerations it is largest at low bow forces. However, at larger bow accelerations, the limiting static coefficient of friction was seen to decrease towards zero as the bow force decreases towards zero. This behaviour was certainly not observed with the perspex rod, and apparently indicates a different tribological behaviour for the contact between bow hair and strings.

Chapter 8

CONCLUSIONS AND FUTURE WORK

8.1 MAIN FINDINGS OF THESIS

Theoretical models of the bowed string developed by past investigators are sufficiently advanced that they can successfully predict most qualitative aspects of the motion of the bowed string, such as the existence of "Helmholtz motion". If these models were sufficiently accurate that they could predict the precise details of the string's vibration under any practical conditions, then they could be utilized by makers of violins and their component parts to predict and understand ways of improving the "playability" of a violin.

However, there is a surprising lack of detailed experimental validation of the theoretical models of the bowed string, limiting the potential usefulness of this type of design study at the moment. This thesis has presented experimental data from a real stringed instrument, and used it to asses the accuracy of the existing theoretical models of the bowed string and to suggest methods for improving them.

A bowing machine was constructed that controls the force and speed with which an instrument is bowed. Bow speed is controlled using a combination of feedback control and open-loop compensation, and measures were taken to limit the effects of controller windup. Bow force is controlled using a feedback controller, with a careful mechanical design used to avoid the need to resort to gain scheduling or switching. The response time of the speed controller to changes in speed demand signal is 0.01 s, which is of the order of a single period of transverse string vibration, and quicker than the response time of a human violin player. The force controller has a response time of 0.2 s when bowing with a real bow and around 0.1 s when using a perspex rod instead, but was only used in this project to maintain a constant bow force.

In the initial experimental tests described in this thesis, the bowing machine was used to bow a cello with a perspex rod rather than a real bow. This allowed the computational complexities of finite width ribbons of bow hair to be ignored in nominally similar computer simulations of the bowed string, which focussed instead on the behaviour of the string when bowed simply by a rigid point-contacting object. Simulated and measured Schelleng diagrams were used to compare the

steady state vibration behaviour of the bowed string in the N vs. β plane, whereas simulated and measured Guettler diagrams were used to compare the transient vibration behaviour of the bowed string in the N vs. a plane, and to understand how well simulations predict its "playability". The main findings from these comparisons, and from examinations of individual vibration waveforms, are as follows:

- Simulations based on neither the friction curve model nor the thermal plastic model succeeded in precisely predicting both the maximum and minimum bow force limits for sustaining Helmholtz motion during steady bowing, although the thermal plastic model was the more successful of the two. In the case of the friction curve model, it was demonstrated that these predictions could be manipulated by changing the details of the friction vs. relative sliding speed relation.

- In experiment, the string was observed to "fly back" during the first slip provided the bow force was sufficiently large. In plastic thermal model simulations, the string was apparently reluctant to do so, whereas in friction curve simulations based on Smith and Woodhouse's [43] steady sliding curve the string "flew back" regardless of the normal force. The extent of the flybacks in each case reflects the change in coefficient of friction incurred by slipping.

- When a new f-v relationship, derived from experimental data based on the extent of bridge force flybacks, was used in place of Smith and Woodhouse's [43] steady sliding measurements in the friction curve model, any bridge force flybacks that occurred during the initial transient part of the string's motion were obscured by apparent "overshoots". This was not observed in experiment.

- The thermal plastic friction model was found to be far more successful at predicting the appearance of the measured Guettler diagram than the friction curve model. Whether used in conjunction with Smith and Woodhouse's steady sliding friction curve [43] or with the new "reconstructed friction curve", Guettler diagrams predicted by the friction curve model were relatively sparse in their appearance.

- The success of the various simulation models at predicting the transient behaviour of the string was not reflected in their success at predicting the string's steady state vibration behaviour. In particular, improvements in the resemblance of simulated and experimental Schelleng diagrams did not appear to correlate with improvements in the appearance of the simulated and experimental Guettler diagrams. This suggests that the information about the bowed string contained in the Schelleng and Guettler diagrams is mutually exclusive, and that each diagram addresses a different aspect of an instrument's playability.

- Plastic thermal simulations predict that the slipping time within Helmholtz motion becomes elongated as the bow force is decreased with a constant bow speed, or as the bow speed is increased with a constant bow force. This resulted in an apparent reluctance of the plastic thermal simulation model to predict the formation of a second slip per period in situations

where there had previously only been a single slip per period. This is contrary to the behaviour seen in experiments, in which Helmholtz motion was frequently seen to degenerate into multiple slipping.

- Measured values of limiting static coefficient of friction between the string and the bow (or rod) just before the first slip in a vibration transient were consistently larger in cases with low bow speeds. All existing simulation models assume a uniform value for limiting static coefficient of friction.

- In some bridge force measurements, the speed of the string at the bowing point in between flybacks appeared to be slightly less than the speed of the bow. This behaviour was not observed in simulations, and suggests the possibility that the string can "creep" while apparently sticking.

Suggested explanations and remedies for some of these observations are as follows:

- The "overshoots" observed in the bridge force flybacks when the reconstructed friction coefficient vs. sliding velocity relation was used by the friction curve model are caused by rapid stick-slip alternations. These rapid stick-slip alternations are caused by torsional waves, which are able to induce sticking and slipping due to the proximity of the hysteresis limits associated with friction curves with relatively little curvature. The indication that experimental results require the reconstructed friction curve to have very little curvature therefore casts doubt on the friction curve simulation model itself: on one hand, experimental results suggest that the friction curve should have relatively little curvature; on the other hand, simulations based on a friction curve with little curvature are prone to exhibiting anomalous rapid torsion-induced stick-slip alterations.

- The function used to relate the shear yield strength and temperature of rosin in the plastic thermal simulation model should be modified in order to remove various differences between the appearance of bridge force waveforms predicted by the plastic thermal simulation model and those measured in experiment:
  - The slope of the function at ambient temperature should be negative rather than zero; the slope determines the extent to which the string "flies back" at first slip.
  - The shear yield strength should drop to zero at high temperatures, to prevent overheating.
  - The limiting static coefficient of friction should be adjusted to equal the value measured in experiment.

- Creep, which presumably accounts for various instances in which the string speed at the bowing point is apparently less than the bow speed during sticking, can be incorporated into bowed string simulations by inclining or rounding the vertical portion of the function used to relate friction to relative sliding velocity.

- The Guettler diagrams constructed from experimental data are approximately "wedge-shaped", with the vertex of the wedge near the origin. It was also found that experimental vibration waveforms generated with the same ratio N/a, or along the same radial line in the N vs. a plane, were generally similar to each other. This can be explained in general terms using a dimensional analysis rule, which states that if the coefficient of friction during sliding and the limiting static coefficient of friction are constant, then the pre-Helmholtz transient duration depends only on $N/aZ(L/c)$.

Subsequent experiments with a real bow in place of the rigid point-contacting perspex rod revealed that most of these observations are not affected by the presence of a finite width of bow hair. The only exceptions to this are the presence of "overshoots" in the bridge force similar to those seen in simulations with the reconstructed friction curve model, and a tendency for the coefficient of friction at first slip to vary roughly in proportion to the bow force at low values of bow force.

8.2 SUGGESTIONS FOR FUTURE INVESTIGATION

As stated in Chapter 1, the ultimate goal of this research is to develop the deterministic tools necessary to understand the extent to which the various properties of the strings, the bow and the violin influence playability. Until this goal is reached there is a clear need for further work. Promising avenues for further investigation in the short term include the following:

- The recommended changes to the relationship between shear yield strength and temperature were inferred from trends in experimental data. It would be more revealing to obtain direct measurements of the shear yield strength of rosin at a range of temperatures. In addition, the value of thermal heat capacity of rosin used in plastic thermal model simulations was reported to be subject to doubt by Cobbold and Jackson [86], who originally measured it. It would therefore be useful to obtain a new measurement of this quantity, and to compare it with the value obtained by Cobbold and Jackson.

- Further measurements of the contact properties of rosined surfaces are required to understand whether creep and contact growth, the mechanisms suggested to be responsible for various features in bridge force measurements, do indeed occur in the moments leading to the first slip. Direct measurements of friction, rather than indirect measurements deduced from the bridge force waveform, would presumably be more conclusive in this regard.

- Rosin is presumably not perfectly plastic at a given temperature, and as such the shear stress in the bow-string contact patch required for slipping may depend upon the relative sliding velocity at a given temperature. Combining the friction curve and thermal plastic models of rosin may therefore be fruitful, whereby the dynamic coefficient of friction depended on both the relative sliding velocity and the temperature of the contact patch.

- Evidence was presented in this thesis that paradoxically suggests that the function used to describe the variation of friction with respect to relative sliding velocity in friction curve simulations should not be too curved, but that unless it is curved will suffer from "overshoots" during slipping. As stated already, it is possible that there is no "middle ground" for the friction curve model, and that it should be discarded in preference of a simulation model that predicts hysteresis in the friction-velocity plane by some other mechanism. However, additional experimental data should be sought to confirm whether the friction curve, as deduced from dynamic testing, should indeed be as straight as the "reconstructed friction curve" used in Section 5.2. Also, there is some uncertainty, as reported by Woodhouse and Loach [27], as to the torsional wave impedance of cello strings, which is a crucial parameter for the "overshoot" behaviour. There would appear to be considerable scope for a more comprehensive testing of a family of candidate friction curves, using a nonlinear optimization technique.

- The reason for the decrease in limiting static coefficient of friction at first slip at low bow forces, observed with the real bow and not with the perspex rod, is unclear at present. An analysis of the contact mechanics of string/bow hair contact has not been attempted in this thesis, but would presumably cast considerable light on this behaviour.

- The bowing machine and the cello were subject to some degree of disturbance in the course of all experimental measurements shown in this thesis. In addition, the surface of the bow and perspex rod used by the bowing machine could not have been perfectly uniform. These sources of "noise" presumably account for the constant change in the detailed locations of light and dark pixels in the Guettler diagrams of Figures 4.25 and 4.29. It would be an interesting test of the simulation models, therefore, to attempt to include this type of noise in simulations and perform multiple simulations, to see whether the inconsistency in the detailed locations of light and dark pixels can be predicted by simulation.

- It was remarked that the minimum bow force limit in each simulated Schelleng diagram in Chapter 5 was too small, and that this could presumably be fixed by making the simulated bridge more flexible, i.e. by decreasing its effective dashpot rate λ_b. It would be revealing to see the resulting change in the minimum bow force limit. Alternatively, the the experimental Schelleng diagram could be remeasured with a heavy mute on the cello bridge.

- It would be straightforward to evaluate the admittance at the bridge notch of the cello used in experiment, and to use it in Woodhouse's [46] generalization of Schelleng's equation for the minimum bow force limit.

BIBLIOGRAPHY

[1] Helmholtz, H., *On the sensation of tone*, Dover Publications, NY, USA, 1954, (English translation of the German edition of 1877).

[2] Raman, C. V., "On the mechanical theory of bowed strings and of musical instruments of the violin family, with experimental verification of results: Part I." *Bulletin of the Indian Association for the Cultivation of Science*, Vol. 15, 1918, pp. 1–158, pages 1-27 of this publication are reprinted in [87].

[3] Friedlander, F. G., "On the oscillations of a bowed string," *Proceedings of the Cambridge Philosophical Society*, Vol. 49, 1953, pp. 516–530.

[4] Keller, J. B., "Bowing of violin strings," *Communications in Pure and Applied Mathematics*, Vol. 6, 1953, pp. 483–495.

[5] Woodhouse, J., "On the stability of bowed string motion," *Acustica*, Vol. 80, 1994, pp. 58–72.

[6] Woodhouse, J., "Idealised models of a bowed string," *Acustica*, Vol. 79, 1993, pp. 233–250.

[7] McIntyre, M. E. and Woodhouse, J., "On the fundamentals of bowed-string dynamics," *Acustica*, Vol. 43, No. 2, 1979, pp. 93–108, additional details regarding the pitch flattening process may be found in [88].

[8] Cremer, L., "Das Schicksal der 'Sekundärwellen' bei der Selbsterregung von Streichinstrumenten (Translated: The fate of 'secondary waves' arising from self-excitation of stringed instruments)," *Acustica*, Vol. 42, 1979, pp. 133–148, an English translation of this paper may be found in [32, 33], and much of its content appeared in [22, Ch.7].

[9] Reinicke, F. L. W., *Die Übertragungseigenschaften des Streichinstrumentensteges*, Ph.D. thesis, Technical University of Berlin, 1973.

[10] Cremer, L. and Lazarus, H., "Die Ermittlung der Richtcharakteristik von Streichinstrumenten bei Gegebener Schwingungsform des Körpen," *Proceedings of the 6th International Congress on Acoustics, Tokyo*, Vol. N-2-3, 1968, note the error in the expression for ΔR; the correct formula is Equation (4.37) of [22]. See also [12].

[11] Cremer, L. and Lazarus, H., "Der Einfluss des 'Bogendrucks' beim anstreichen einer Saite," *Proceedings of the 6th International Congress on Acoustics, Tokyo*, Vol. Sec. 9-12, 1968, see also [12].

[12] Cremer, L., "Der Einfluss des 'Bogendrucks' auf die selbsterregten Schwingungen der gestrichenen Saite," *Acustica*, Vol. 30, 1974, pp. 119–136, an English translation of this paper may be found in [14, 15], and much of its content appeared in Cremer's book [22].

[13] Lazarus, H., "Technischer Bericht des Heinrich-Hertz Institute," Tech. Rep. 117, Berlin-Charlottenburg, 1970.

[14] Cremer, L., "The influence of bow pressure on the movement of a bowed string," *Catgut Acoustical Society Newsletter*, Vol. 18, 1972, pp. 13–19.

[15] Cremer, L., "The influence of bow pressure on the movement of a bowed string," *Catgut Acoustical Society Newsletter*, Vol. 19, 1973, pp. 21–25, (continued from [14]).

[16] Schelleng, J. C., "The bowed string and the player," *Journal of Acoustical Society of America*, Vol. 53, 1973, pp. 26–41, his main results on bowing tolerance are given by his Equations (1a) and (2), with important additional detail in his Footnote 10. This paper is reprinted in [87].

[17] Kohut, J. and Mathews, M. V., "Study of motion of a bowed violin string," *Journal of Acoustical Society of America*, Vol. 49, 1971, pp. 532–537.

[18] Boutillon, X., "Analytical investigation of the flattening effect," *Journal of Acoustical Society of America*, Vol. 90, 1991, pp. 754–763.

[19] Faure, C.-A. and Boutillon, X., "Détermination et étude expérimentale de la fréquence d'oscillation d'une corde frotté," *Comptes Rendus de l'Académie des Sciences de Paris*, Vol. 317, 1993, pp. 1377–1382.

[20] Schumacher, R. T., "Measurements of some parameters of bowing," *Journal of Acoustical Society of America*, Vol. 96, No. 4, 1994, pp. 1985–1998.

[21] Woodhouse, J., "Bowed string simulation using a thermal friction model," *Acustica*, Vol. 89, 2003, pp. 355–368.

[22] Cremer, L., *The physics of the violin*, MIT Press, MA, USA, 1984.

[23] Woodhouse, J., *On the acoustics and mechanics of stringed musical instruments*, Ph.D. thesis, Cambridge University, 1977.

[24] Schumacher, R. T., "Self-sustained oscillations of the bowed string," *Acustica*, Vol. 43, No. 2, 1979, pp. 109–120.

[25] McIntyre, M. E., Schumacher, R. T., and Woodhouse, J., "On the oscillations of musical instruments," *Journal of Acoustical Society of America*, Vol. 74, No. 5, 1983, pp. 1325–1345.

[26] Woodhouse, J., "On the playability of violins. Part I: Reflection functions," *Acustica*, Vol. 78, 1993, pp. 125–136.

[27] Woodhouse, J. and Loach, A. R., "Torsional behaviour of cello strings," *Acustica*, Vol. 85, 1999, pp. 734–740.

[28] Gillan, F. S. and Elliott, S. J., "Measurements of the torsional modes of vibration of strings on instruments of the violin family," *Journal of Sound and Vibration*, Vol. 130, 1989, pp. 347–351.

[29] Woodhouse, J., "The transient behaviour of guitar strings," *Proceedings of the Stockholm Music Acoustics Conference, Stockholm, Sweden*, 2003.

[30] Valette, C., *The mechanics of vibrating strings*, in "Mechanics of musical instruments," ed. A. Hirshberg, J. Kergomard and G. Weinreich, Springer-Verlag, NY, USA, 1995, pp. 116–183.

[31] Pitteroff, R. and Woodhouse, J., "Mechanics of the contact area between a violin bow and a string. Part I: Reflection and transmission behaviour," *Acustica*, Vol. 84, 1998, pp. 543–562.

[32] Cremer, L., "The absorption of 'secondary correction waves' in the excitation of a string by bowing," *Catgut Acoustical Society Newsletter*, Vol. 31, 1979, pp. 12–16.

[33] Cremer, L., "The absorption of 'secondary correction waves' in the excitation of a string by bowing," *Catgut Acoustical Society Newsletter*, Vol. 32, 1979, pp. 27–32, (continued from [32]).

[34] McIntyre, M. E., Schumacher, R. T., and Woodhouse, J., "Aperiodicity in bowed-string motion," *Acustica*, Vol. 49, 1981, pp. 13–32, See also [89].

[35] Pitteroff, R. and Woodhouse, J., "Mechanics of the contact area between a violin bow and a string. Part II: Simulating the bowed string," *Acustica*, Vol. 84, 1998, pp. 744–757.

[36] Pitteroff, R. and Woodhouse, J., "Mechanics of the contact area between a violin bow and a string. Part III: Parameter dependence," *Acustica*, Vol. 84, 1998, pp. 929–946.

[37] Schumacher, R. T., "Some aspects of the bow," *Catgut Acoustic Society Newsletter*, Vol. 24, 1975, pp. 5–8.

[38] Weinreich, G. and Caussé, R., "Elementary stability considerations for bowed-string motion," *Journal of Acoustical Society of America*, Vol. 89, 1991, pp. 887–895.

[39] Fletcher, N. H. and Rossing, T. D., *The physics of musical instruments (2nd edition)*, Springer-Verlag, NY, USA, 1998.

[40] Heckl, M. A. and Abrahams, I. D., "Curve squeal of trains, part 1: Mathematical model for its generation," *Journal of Sound and Vibration*, Vol. 229, No. 3, 2000, pp. 669–693.

[41] Woodhouse, J., Schumacher, R. T., and Garoff, S., "Reconstruction of bowing point friction force in a bowed string," *Journal of Acoustical Society of America*, Vol. 108, No. 1, 2000, pp. 357–368.

[42] Lazarus, H., *Die Behandlung der selbsterregten Kippschwingungen der gestrichenen, Saite mit Hilfeder endlichen Laplacetransformation*, Ph.D. thesis, Technical University of Berlin (D-83), 1972, Cremer [22] cites this as containing a measured Schelleng diagram.

[43] Smith, J. H. and Woodhouse, J., "The tribology of rosin," *Journal of the Mechanics and Physics of Solids*, Vol. 48, 2000, pp. 1633–1681.

[44] Smith, J. H., *Stick-slip vibration and its constitutive laws*, Ph.D. thesis, Cambridge University, 1990.

[45] Guettler, K., "On the creation of the Helmholtz motion in bowed strings," *Acustica*, Vol. 88, No. 6, 2002, pp. 970–985.

[46] Woodhouse, J., "On the playability of violins. Part II: Minimum bow force and transients," *Acustica*, Vol. 78, 1993, pp. 137–153.

[47] Kar, K. C., Datta, N. K., and Ghosh, S. K., "Investigation on the bowed string with an electrically driven bow. (Part 1)," *Indian Journal of Physics*, Vol. 25, 1951, pp. 423–432.

[48] Saunders, F. A., "The mechanical action of instruments of the violin family," *Journal of Acoustical Society of America*, Vol. 17, No. 3, 1946, pp. 169–186, reprinted in [90].

[49] Guettler, K. and Askenfelt, A., "Acceptance limits for the duration of pre-Helmholtz transients in bowed string attacks," *Journal of Acoustical Society of America*, Vol. 101, No. 5, 1997, pp. 2903–2913.

[50] McIntyre, M. E. and Woodhouse, J., "A parametric study of the bowed string: the violinist's menagerie," *Journal of the Catgut Acoustical Society*, Vol. 42, 1984, pp. 18–21.

[51] Schumacher, R. T. and Woodhouse, J., "The transient behaviour of models of bowed-string motion," *Chaos (a journal of the American Institute of Physics)*, Vol. 5, No. 3, 1995, pp. 509–523.

[52] Schumacher, R. T. and Woodhouse, J., "Computer modelling of violin playing," *Contemporary Physics*, Vol. 36, No. 2, 1995, pp. 79–92, Figures 6(a) and 6(b) in this publication are both upside-down.

[53] Cremer, L., "Consideration of the duration of transients in bowed instruments," *Catgut Acoustical Society Newsletter*, Vol. 38, 1982, pp. 13–18, reprinted in [91].

[54] McIntyre, M. E. and Woodhouse, J., "The acoustics of stringed musical instruments," *Interdisciplinary Science Reviews*, Vol. 3, No. 2, 1978, pp. 157–173.

[55] Saunders, F. A., "The mechanical action of violins," *Journal of Acoustical Society of America*, Vol. 9, 1937, pp. 81–98, reprinted in [87].

[56] Bladier, B., "Contribution à l'étude des cordes du violoncelle," *Acustica*, Vol. 11, No. 6, 1961, pp. 373–384, reprinted in [87].

[57] Weinreich, G. and Caussé, R., "Electronic bows: digital and analog," *Proceedings of the 12th International Congress on Acoustics, Toronto*, Vol. III, 1986, pp. K3–7.

[58] Caussé, R. and Weinreich, G., "Simulation and further experiments with the digital bow," *Proceedings of the 13th Internation Conference on Acoustics*, Vol. 3, 1989, pp. 83–86.

[59] Weinreich, G., "Bowed-string research with the digital bow," *Proceedings of the International Symposium on Musical Acoustics, Mittenwald, Germany*, 1989.

[60] Lawergren, B., "On the motion of bowed violin strings," *Acustica*, Vol. 44, 1980, pp. 194–206.

[61] Pickering, N. C., "A new light on bow action," *Journal of the Violin Society of America*, Vol. 11, 1991, pp. 83–92, this paper is reprinted in [91] with new results on coefficient of friction.

[62] Raman, C. V., "Experiments with mechanically-played violins," *Proceedings of the Indian Association for the Cultivation of Science*, Vol. 6, 1920-21, pp. 19–36, reprinted in [87].

[63] Askenfelt, A., "Measurement of the bowing parameters in violin playing," *Journal of Acoustical Society of America*, Vol. 80, 1986, pp. 1007–1015.

[64] Askenfelt, A., "Measurement of the bowing parameters in violin playing. II: Bow-bridge distance, dynamic range, and limits of bow force," *Journal of Acoustical Society of America*, Vol. 86, No. 2, 1989, pp. 503–516.

[65] Turner, J. D. and Hill, M., *Instrumentation for Engineers and Scientists*, Oxford University Press, 1999.

[66] Ewins, D. J., *Modal testing: theory, practice and application (Second Edition)*, Research Studies Press Ltd., 2000.

[67] Wood, G. D. and Woodhouse, J., "An investigation into robust force control through a constained flexible beam," *International Journal of Control*, Vol. 68, No. 3, 1997, pp. 539–578.

[68] Zhou, K., Doyle, J. C., and Glover, K., *Robust and Optimal Control*, Prentice Hall, NJ, USA, 1995.

[69] Vinnicombe, G., *Uncertainty and feedback: $\mathcal{H}_\infty$ loop-shaping and the ν-gap metric*, Imperial College Press, 2000.

[70] Leith, D. J. and Leithead, W. E., "Survey of gain scheduling analysis and design," *International Journal of Control*, Vol. 73, No. 11, 2000, pp. 1001–1025.

[71] Kothare, M. V., Campo, P. J., Morari, M., and Nett, C. N., "A unified framework for the study of anti-windup designs," *Automatica*, Vol. 30, No. 12, 1994, pp. 1869–1883.

[72] Franklin, G. F., Powell, J. D., and Emami-Naeini, A., *Feedback Control of Dynamic Systems (Third Edition)*, Addison Wesley Publishing Company, 1994.

[73] Askenfelt, A. and Guettler, K., "The bouncing bow: an experimental study," *Journal of the Catgut Acoustical Society*, Vol. 3, No. 6 (Series II), 1998, pp. 3–8.

[74] Winter, D. A., *Biomechanics and motor control of human movement*, John Wiley & Sons, Inc, 1990.

[75] Crawshaw, S. and Vinnicombe, G., "Anti-windup synthesis for guaranteed $\mathcal{L}_2$ performance," *Proceedings of the 39th IEEE Conference on Decision and Control, Sydney, Australia*, Vol. (CD-ROM), 2000, this paper is available on the World Wide Web at `http://www-control.eng.cam.ac.uk/sc10003/cdc00.ps`.

[76] Hanson, R. J., Schneider, A. J., and Halgedahl, F. W., "Anomalous low-pitched tones from a bowed violin string," *Journal of the Catgut Acoustical Society*, Vol. 2, No. 6, 1994, pp. 1–7.

[77] Guettler, K., "Wave analysis of a string bowed to anomalous low frequencies," *Journal of the Catgut Acoustical Society*, Vol. 2, No. 6, 1994, pp. 8–14.

[78] Guettler, K., *The bowed string - on the development of Helmholtz motion, and on the creation of anomalous low frequencies*, Ph.D. thesis, Royal Institute of Technology, Stockholm, 2002.

[79] Lawergren, B., "Harmonics of S motion on bowed strings," *Journal of Acoustical Society of America*, Vol. 73, No. 6, 1983, pp. 2174–2179.

[80] Stough, B., "E string whistles," *Journal of the Catgut Acoustical Society*, Vol. 3, No. 7 (Series II), 1999, pp. 28–33.

[81] Meirovitch, L., *Elements of vibration analysis, second edition*, McGraw-Hill, Singapore, 1986.

[82] Johnson, K. L., *Contact mechanics*, Cambridge University Press, Cambridge, UK, 1985.

[83] Callister, W. D., *Materials Science and Engineering: An Introduction*, Wiley & Sons, Inc, 2003.

[84] Greenwood, J. A. and Williamson, J. B. P., "Contact of nominally flat surfaces," *Proceedings of the Royal Society, London*, Vol. Ser. A, 295, 1966, pp. 300–319.

[85] Marone, C., "The effect of loading rate on static friction and the rate of fault healing during the earthquake cycle," *Nature*, Vol. 391, 1998, pp. 69–72.

[86] Cobbold, P. R. and Jackson, M. P. A., "Gum rosin (colophony): a suitable material for thermomechanical modelling of the lithosphere," *Tectonophysics*, Vol. 210, 1992, pp. 255–271.

[87] Hutchins, C. M., editor, *Musical Acoustics, Part I: Violin Family Components*, Dowden, Hutchinson & Ross, PA, USA, 1975, Benchmark Papers in Acoustics, No.5.

[88] McIntyre, M. E., Schumacher, R. T., and Woodhouse, J., "New results on the bowed string," *Catgut Acoustical Society Newsletter*, Vol. 28, 1977, pp. 27–31.

[89] McIntyre, M. E., Schumacher, R. T., and Woodhouse, J., "Aperiodicity in bowed-string motion: On the differential-slipping mechanism," *Acustica*, Vol. 50, 1982, pp. 294–295.

[90] Hutchins, C. M., editor, *Musical Acoustics, Part II: Violin Family Functions*, Dowden, Hutchinson & Ross, PA, USA, 1976, Benchmark Papers in Acoustics, No.6.

[91] Hutchins, C. M., editor, *Research papers in violin acoustics, 1975-1993 (Volumes 1 and 2)*, Acoustical Society of America, NY, USA, 1997.